Study of particle production in hadron-nucleus interactions for neutrino experiments

Tomasz Jan Palczewski

Ph. D. thesis
written under supervision of
prof. dr hab. Joanna Stepaniak.

National Centre for Nuclear Research
2012

Dla mojego syna Mateusza i mojej żony Sylwii.
Dla mojej Mamy i mojego śp. Taty.

Abstract

The dissertation presents a study of hadron production in the NA61/SHINE large acceptance spectrometer at CERN SPS. The differential cross sections were obtained for the production of negatively charged pions, neutral Kaons, and Lambdas from the proton-Carbon interactions at 31 GeV/c. Methods of particle yields extraction from proton Carbon interactions were developed. An analysis chain of global correction method (h- method) was established for the thin carbon target and as well for T2K replica target and compared to the results obtained with full particle identification. The h- method permits to cover larger phase space region not otherwise accessible. In addition, a full chain of V^0 analysis was prepared to obtain neutral Kaon and Lambda results in polar angle and momentum variables (p, θ). Results on the differential production cross sections and mean multiplicities in production processes for negatively charged pions (in three sets of variables: (p, θ), (xf, p_T), (y, p_T)), neutral Kaons (in (p, θ) and (y,p_T)), and Lambdas (in (p, θ)) from proton Carbon interactions at 31 GeV/c in tabularized forms were obtained. In addition, an inclusive cross section for neutral Kaon production corrected to the whole phase space region was obtained:

$\sigma(K^0_S) = 28.58 \pm 1.85$ (stat) ± 1.72 (sys) mb

The final results obtained in this dissertation are crucial for the T2K long baseline neutrino experiment and also of value for future neutrino oscillation experiments, which will use conventional neutrino beams, and for existing and future cosmic-ray physics experiments. These are pioneer measurements in this energy region, which is the region of the overlap of low and high energy Monte Carlo Models. No other data are available at this energy and for this system. For lower interaction energies, proton Carbon interactions were studied by the HARP experiment and in the past by bubble chamber and single-arm spectrometer experiments. A scan with a few different proton energies was done by the MIPP experiment but only partial and preliminary results have been published.

The importance of the presented results was shown by the T2K collaboration. Namely, these results decreased significantly systematic error on the far-to-near ratio, which is important in the determination of the oscillation parameters. These results are also of interest on their own right as pioneer measurements in this energy region.

Acknowledgements

I would like to thank Profesor Joanna Stepaniak for substantive supervision, guidance, patience, and lots of inspiring remarks. Without her, this thesis would have never come into existence. Thank you!

I would like to thank NA61/SHINE Collaboration members, especially Marek Gaździcki for many suggestions; Peter Seyboth, who helped me a lot of times, who improved my abstracts and posters, and who had a lot of very precise and always shrewd observations; Michael Unger for help with CORSIKA predictions. I also want to express my gratitude to Alain Blondel, Alessandro Bravar, Alberto Marchioni, and Boris Popov for many fruitful discussions.

It was a great experience to be a part of the Warsaw Neutrino Group. I would like to thank Profesor Danuta Kiełczewska, Profesor Ewa Rondio, Profesor Maria Szeptycka, and others. I'm really pleased that I had this opportunity to work with you. Your comments enriched this thesis greately.

Cheers to Marcin Berłowski, Magda Posiadała, Paweł Przewłocki, Piotrek Mijakowski, Justyna Łagoda, and others for advises, help, collaboration, and also what is equally important for having good days and a lot of fun during my Ph.D. studies.

Finally, I would like to thank my FAMILY. Without the endless support of my wife I never would have reached this point. I also thank my Mom and Brother for all the Help and Love!

This Ph. D. Thesis was supported by Polish Ministry of Science and Higher Education (grant N N202 287838 (PBP 2878/B/H03/2010/38)).

Table of Contents

List of tables

List of figures

Chapter 1 Introduction

1.1 Motivation

Accelerator long baseline oscillation neutrino experiments are challenged to lower their systematic uncertainties to be able to obtain high precision nutrino oscillation parameters. The main task is to minimize systematic error connected with a poor knowledge of hadron production cross sections. This thesis is devoted to the analyses of data collected by NA61/SHINE experiment, which were collected to reduce these uncertainties. As discussed in many articles on future neutrino projects, such measurements are also valuable for optimizing the design of the neutrino factory. The knowledge of hadron production cross sections is also important in other fields of physics. These are the key ingredients in the simulations and modelling of hadron interactions, hadron detectors, and cosmic ray cascades. The developed methods are valid for ongoing and future p-A and A-A experiments, which are focused on the study of the onset of deconfinement and search for the critical point of the strongly interacting matter.

1.2 Layout of the thesis

Theoretical introduction is contained in chapters from 2 to 5. Chapter 2 presents basic information about theory and modeling of hadronic interactions. In addition, in this chapter existing hadronic interaction data are discussed. Chapter 3 provides information about theory of neutrino oscillations, current knowledge of oscillation parameters, and principles of oscillation parameters determination in long baseline neutrino oscillation experiments. In chapter 4 production of conventional neutrino beams is discussed. Chapter 5 presents the main background sources for measurements of neutrino interactions via two main detection techniques, namely Water Cherenkov and LAr based techniques. Detection based on the use of Liquid scintillator is not discussed in this thesis. The LAr method is used in the ICARUS detector. The author of thesis made simulation studies of the ICARUS T600 detector response and took part in the neutral pion analysis, which ended with the publication in the Acta Phys.Polon. B. In chapter 6, the NA61/SHINE experiment and its main goals are presented. The detection technique and main detectors are described in details. The knowledge of the detector and its components, operation conditions, and computer systems used for monitoring and data aquisition was crucial for author while supervising the detector work during data taking periods in 2007, 2009, 2010, and 2011. Moreover, in chapter 6 a new forward time-of-flight detector is discussed. Light guides for this detector were made in the National Centre for Nuclear Research and the author of this thesis took part in the preparation and polishing of these parts. In addition, the information on trigger, data acquisition, reconstruction chain, and normalization of the particle yields is described. Subchapter 6.6 describes modeling of the detector response. The studies of the geometrical acceptance and reconstruction efficiency are presented in subchapter 6.7. The extraction of the negatively charged pion yields based on the global correction method (h- method) is presented in chapter 7. The pion results were published in the Phys. Rev. C. The second analysis, which used invariant mass distribution studies to extract K^0_S and Λ hadrons, is discussed in chapter 8. Chapter 9 contains comparison of obtained results with Monte Carlo models. Chapter 10 summarizes the results.

The author of this thesis performed the following analyses:

- Preparation and development of the c++/fortran programs used in the analyses
- Preparation of the neutral pion simulations (FLUKA) in the ICARUS T600 detector
- Simulation of the ICARUS T600 detector response and studies of the electromagnetic showers induced by electrons and photons
- Analyses of the data collected in the ICARUS T600 detector during surface test run
- Validation of the official NA61/SHINE Monte Carlo chain
- Evaluation of the event and track cuts, finalized by the list of NA61/SHINE official 2007 cuts
- Studies of the negatively charge pion production (p+C at 31GeV/c) from the primary vertex based on the global correction method (h- method) made in three different sets of variables: (momentum, polar angle), (transverse momentum, rapidity), (transverse momentum, Feynman x)
- Analyses of the neutral strange hadrons (K^0_S and Λ) production (p+C at 31 GeV/c) in two sets of variables: (momentum, polar angle), (transverse momentum, rapidity)
- Preparation of the Monte Carlo model prediction based on the existing root trees from CORSIKA simulator.

1.3 List of talks, poster presentations, and publications

Publications:

1. Further Information Requested in the proposal Review Process CERN-SPSC-2007-019, June 2007. (N. Abgrall et al.)
2. Report from the NA61/SHINE pilot run performed in October 2007. Addendum-3 to the proposal P330. By NA61 Collaboration (N. Abgrall et al.). CERN-SPSC-2007-033, CERN-SPSC-P-330, Nov 2007. 17pp.
3. Report from the NA61/SHINE experiment at the CERN SPS. By NA61/SHINE Collaboration (N. Abgrall et al.). CERN-OPEN-2008-012, CERN-ANNUAL-REPORT-2007, Apr 2008. 18pp.
4. Calibration and analysis of the 2007 data. By NA61 Collaboration (N. Abgrall et al.). CERN-SPSC-2008-018, CERN-SPSC-SR-033, Jul 2008. 43pp.)
5. Energy reconstruction of electromagnetic showers from pi0 decays with the ICARUS T600 Liquid Argon TPC. By ICARUS Collaboration (A. Ankowski et al.). Dec 2008. 24pp. Published in Acta Phys.Polon.B41:103-125,2010. e-Print: arXiv:0812.2373 [hep-ex].
6. Pion Production Measurement in NA61/SHINE Experiment for High Precision Neutrino Oscillation Experiments. (T. J. Palczewski for the NA61/SHINE collaboration). Published in PoS EPS- HEP2009:412, 2009. e-Print: arXiv:0911.2800 [hep-ex].
7. Particle production cross-sections by 30 GeV protons on Carbon at the NA61/SHINE experiment (T. J. P alczewski, M. Z. Posiadała for the NA61/SHINE Collaboration). Prepared for The XXIV International Conference on Neutrino Physics and Astrophysics (Neutrino2010), Athens, Greece. Will be published in Nuclear Physics B – Proceedings Supplements (NUPHBP).
8. Measurements of Cross Sections and Charged Pion Spectra in Proton–Carbon Interactions at 31 GeV/c. By NA61/SHINE Collaboration (N. Abgrall et. al.). CERN-PH-EP-2011-005. e-Print: arXiv:1102.0983 [hep-ex] Published in Phys. Rev. C 84:034604, 2011.
9. Pion production measurement in NA61/SHINE experiment (T. J. Palczewski for the NA61/SHINE collaboration). 2011. 3pp. Prepared for 11th International Workshop

on Meson Production, Properties and Interaction (MESON 2010), Cracow, Poland, 10-15 Jun 2010. Published in Int.J.Mod.Phys.A26:754-756, 2011.

10. Underground operation of the ICARUS T600 LAr-TPC: first results. C. Rubbia et al. Jun 2011. 14pp. Published in JINST 6:P07011,2011. e-Print: arXiv:1106.0975 [hep-ex]
11. A Search for the analogue to Cherenkov radiation by high energy neutrinos at superluminal speeds in ICARUS. By ICARUS Collaboration. Oct 2011. 8pp. e-Print: arXiv:1110.3763 [hep-ex].
12. Measurement of Production Properties of Positively Charged Kaons in Proton-Carbon Interactions at 31 GeV/c. By The NA61/SHINE Collaboration. Dec 2011. 10pp. e-Print: arXiv:1112.0150 [hep-ex]. Submitted to Phys. Rev. C.
13. Hadron Production Measurement in the NA61/SHINE Experiment at the CERN SPS for Neutrino and Cosmic Ray Experiments (T. J. Palczewski for the NA61/SHINE collaboration), prepared for the 19th Particles and Nuclei International Conference (PANIC11), Cambridge, USA. American Institute of Physics I Conference Proceedings 1441. 468-470, 2012.
14. Measurements of hadron production from $p+C$ interactions at 31 GeV/c from NA61/SHINE at the CERN SPS (T. J. Palczewski for the NA61/SHINE collaboration). Prepared for 12th International Workshop on Meson Production, Properties and Interaction (MESON 2012), Cracow, Poland. Will be published in Int.J.Mod.Phys.

Talks and posters:

1. Tomasz Palczewski. Symposium of the Soltan Institute for Nuclear Research, 2010, Warsaw, Poland (talk)
2. Tomasz Palczewski. International Workshop on Meson Production, Properties and Interaction, **MESON 2010**, Cracow, Poland **(talk)**
3. Tomasz Palczewski. Particles and Nuclei International Conference, **PANIC11**, 2011, Cambridge MA, USA **(talk)**
4. Tomasz Palczewski. International Euro-physics Conference, **EPS-HEP 2009**, Cracow, Poland (poster)
5. Tomasz Palczewski, Nicolas Abgral, Sebastien Murphy, Magdalena Posiadala. **European Strategy for Future Neutrino Physics**, 2009, CERN, Switzerland (poster)
6. Tomasz Palczewski, Magdalena Posiadala. International Conference on Neutrino Physics and Astrophysics (**NEUTRINO 2010**), 2010, Athens, Greece (poster)
7. Tomasz Palczewski. **INSS 2010**, Yokohama-Tokai, Japan (poster)
8. Antoni Aduszkiewicz, Tomasz Palczewski. **Quark Matter** Conference, 2011, Annecy, France (poster).
9. Tomasz Palczewski. International Workshop on Meson Production, Properties and Interaction, **MESON 2012**, Cracow, Poland (poster).
10. Tomasz Palczewski, International Conference on Neutrino Physics and Astrophysics (**NEUTRINO 2012**), 2012, Kyoto, Japan (poster).
11. Tomasz Palczewski, The 1st symposium of the National Centre for Nuclear Resarch, 2012, Warsaw, Poland (2 posters)

Chapter 2 Hadronic interactions

2.1 Theory and modelling of hadronic interactions

The formalism of hadronic interactions is mainly based on the Quantum Chrono-Dynamic (QCD) theory. Unfortunately, due to the large coupling constant of this theory, direct calculations of numerous processes are not possible, i.e. of the quark-quark interaction at low momentum transfer. One can divide hadronic interaction phenomenology into two parts - a part connected with high momentum transfer and small impact parameter („hard“) and a part connected with low momentum transfer and large impact parameter („soft“). Whether the particles originate from the hard or soft part, can be seen by inspecting transverse momentum spectra (Figure 1). On the other hand, the Q^2 value also distinguishes between these two regimes. The exact value where transition appears is not known. Presumably, it is between 1 to 10 GeV^2.

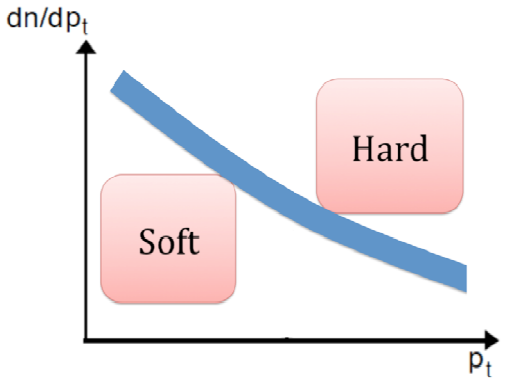

Figure 1. Transverse momentum distribution separating the soft and hard scattering. Own elaboration.

The hard part can be well described by perturbative QCD that is valid only if strong coupling constant is smaller than one. Up to now, no universally accepted theoretical model of the soft hadronic interaction part exists, mainly due to the fact that there is no complete picture of processes involved in hadronic interactions. A good understanding of hadronic interactions at low momentum transfer is of key importance to build and tune hadronic interaction models, which are a main component of neutrino flux and cosmic ray simulation models. The existing data, which are described in the chapter 2.3, do not cover important collision types and interaction energies. Moreover, a phase space region covered by many experiments is not sufficiently wide. This negatively influances a reliability of predictions in unmeasured kinematic regions. Regardless of the above, many models have been built, which describe the data well in particular kinematic regions.

In QCD the fundamental particles (quarks) interact via exchange of gluons. The gluons are eight color charged field quanta. The quarks are constituents of bound systems without net color charge. These systems are called hadrons. Forces between hadrons can be considered as residual color interactions in analogy to electron scattering (photon exchange) in Quantum Electro-Dynamics (QED). A simple picture of hadron hadron scattering is shown in Figure 2.

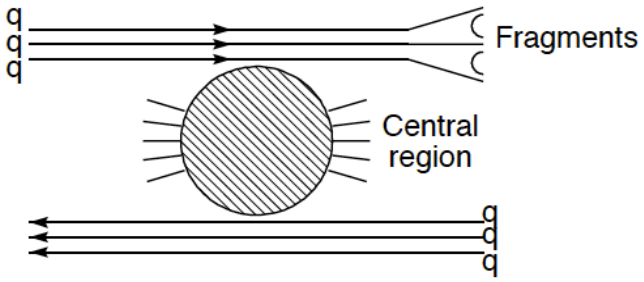

Figure 2. Simple picture of hadron hadron scattering [140].

The extension of virtual particle exchange theory, originally proposed by Yukawa in 1935 [183], was proposed by Tulio Regge in 1957. In this theory instead of virtual particles, the reggeon trajectories, which are representing particular quantum numbers, are exchanged [83]. This approach is commonly used in present theoretical models of soft hadronic interactions. These days, some semi-phenomenological models exist that quite well describe the main properties of the soft diffractive processes. These models are inspired by 1/N QCD expansion and take into account commonly accepted theoretical principles like duality, unitarity, Regge behavior, and parton structure [34]. Simulations of particle production in hadronic interaction can be divided into theoretical models, phenomenological models, or combined theoretical and parametrization approaches (semi-phenomenological models).
In addition, simulation models can be further divided into a few groups depending on different energy regions where those models are valid [126]:

2.1.1 Low energy region models

Up to about 4 GeV in c.m.s it is possible to calculate all exclusive channels through known hadronic resonances [116]. Above about 4 GeV the number of exclusive channels is getting too large and this approach becomes impractical. Some theoretical models valid at low energies (<10GeV) are based on the intranuclear cascade, such as Bertini Cascade model [64, 63], its extended version MICRES [10], and the Binary Cascade [98].

- Bertini intranuclear cascade model generates the final state for hadronic inelastic scattering by simulating the intra-nuclear cascade (INC). Serber first proposed the intra-nuclear cascade model in 1947 [163]. It was based on the fact that in particle-nuclear collisions the deBroglie wave-length of the incident particle is comparable to or shorter than the average intra-nucleon distance. Therefore, it is justified to describe the interactions in terms of particle-particle collisions. In Bertini model, incident hadrons collide with protons and neutrons in the target nucleus and produce secondaries, which in turn collide with other nucleons. The target nucleus is treated as an average nuclear medium to which excitons are added after each collision [178]. Bertini model is a solution to Boltzman equation on average. In this model scattering matrix is not calculated. This model is valid when $\lambda B/v << \tau c << \Delta t$, where λB is the deBroglie wavelength of the nucleons, v is the average relative nucleon-nucleon velocity, and Δt is the time interval between collisions. Bertini model breaks down at energies below 100-200 MeV and also at energies higher than 5-10 GeV.
- MICRES is the result of an attempt to improve Bertini INC model. The positive features of Bertini model are combined with the calculation of all resonances contributing more than 2% to the total cross-section in hadron-nucleus collsions. The nucleus evaporation is included in this code. An excited compound nucleus is formed from which, particles are emitted until evaporation is no longer energetically possible.

The calculation is based on a theory proposed by Weisskopf [182] and on a Monte Carlo code written by Dostrovsky [90, 91].

- Binary cascade is an INC model propagating primary and secondary particles in the nucleus. Interactions are between primary or secondary particle and an individual nucleon of the nucleus [177]. In this approach, a 3-dimentional model of the nucleus is constructed. It uses optical potentials to describe the time evolution of particles passing through the nuclear medium.

2.1.2 Intermediate energy region models

Data analysis in this region ($10\ GeV/c \leq p_{lab} \leq 100\ GeV/c$) showed that the total cross section is saturated by binary processes that are shown in Figure 3.

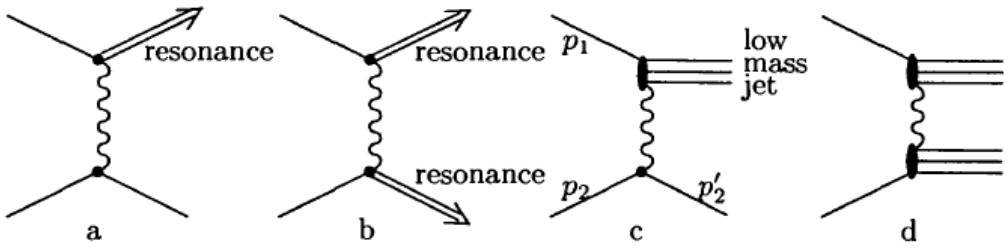

Figure 3. Characteristic binary processes in the intermediate energy region. (a) and (b) two body particle production diagrams, (c) and (d) quasi-two-body particle production diagrams. The figure is taken from [126].

This allows making successful description of the experimental data in this range by Regge phenomenology based models. Flexibility of this approach makes it possible to obtain very good description of data, but on the other hand makes predictive power of unmeasured systems limited. In this energy range, one needs to mention the following models: Fritiof [36, 142], Quark Gluon String Model (QGSM) [123], dual parton model [71].

String models are based on the assumption that in the interaction between partons strings are created.
The Fritiof model assumes that all hadron-hadron interactions are binary reactions like:
h1 + h2 → h'1 + h'2,
where h'1 and h'2 are excited states of the hadrons with continuous mass spectra [167]. This is presented in Figure 4.

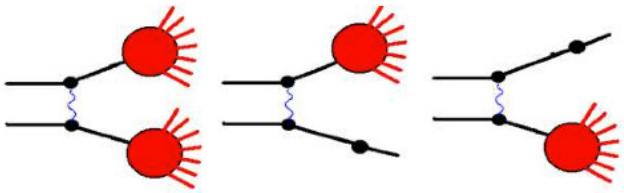

Figure 4. Double diffraction (left) and single diffraction reactions (right) considered in the Fritiof model [167].

If one of the hadrons after interaction remains in the ground state for example:
h1 + h2− > h1 + h'2

this type of reaction is called ”single diffraction dissociation”. If none of the hadrons remains in the ground state the reaction is called ”double diffraction dissociation”. The excited hadrons are considered as QCD-strings and the string fragmentation model is applied for a simulation of their decays. Hadronization models that are commonly used are: Lound string model, cluster model, and combination models.

Regge behavior and the parton structure of hadrons provide the basis for the dual parton model. This model has been extensively studied and developed over the past fifteen years. DPM and QGSM are closely related. They are based on the large-N expansion of non-perturbative QCD and on Gribov's Reggeon calculus [50].

2.1.3 High and super high-energy region models

High and super high-energy models (p_{lab} > 100 GeV/c) are not relevant to this thesis and will not be discussed.

2.1.4 Different classification of hadronic models

It is also possible to classify models according to different mechanisms of hadron production they propose [70]:

- The recombination models – Additive Quark Model (AQM) [65], Valon model [121].
- The perturbative QCD models based on Low and Noussinov ideas [132, 143, 113].
- String models – for example the Lund fragmentation model [35].
- Models based on the 1/N expansion in Dual Topological Unitarization (DTU) – the dual parton model [72].
- The Massive Quark Model (MQM) introduced by Preparata [170].

2.1.5. Main components of the hadronic event generators

A schematic view of the main components of hadronic model inventory is presented in Figure 5. Nowadays, most of these components (data-, parameter-, theory-driven) are included in hadronic event generators. Most often used hadronic event generators are FLUKA [175], GEANT3 [176], GEANT4 [179], and MARS [180].

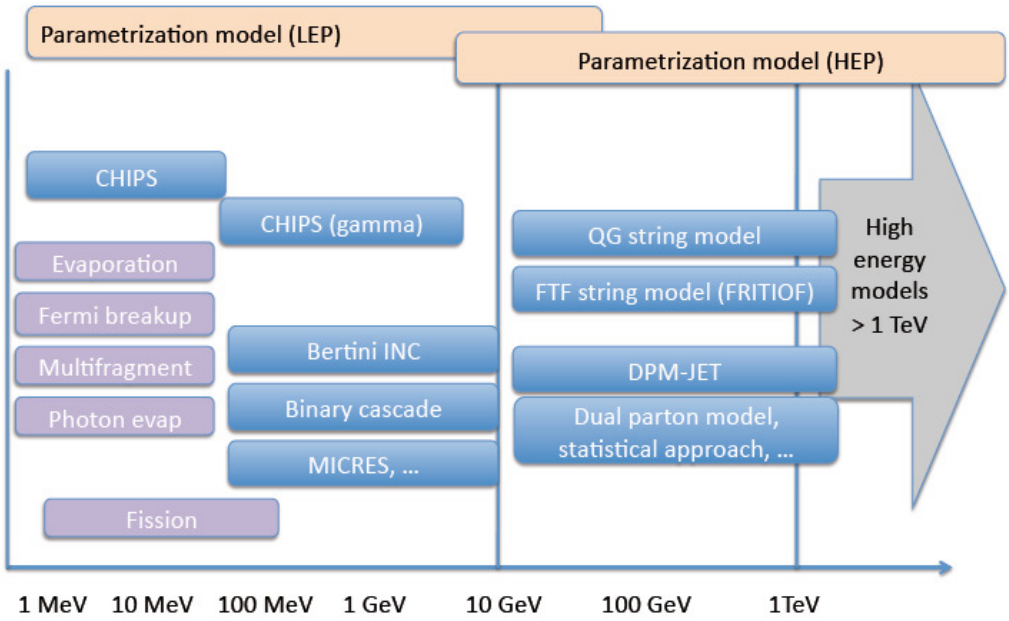

Figure 5. Schematic view of the main components of hadronic model inventory. Own elaboration.

Some parameterization models of hadron production that are based mainly on parameterization and extrapolation of existing data (not "theory driven") are presented in subchapter 2.4.

Almost all hadronic interaction models are based on the detailed description of proton-proton (pp) collisions and then extended to the other systems. The hadron-nucleus (hA) interactions can be understood in terms of many uncorrelated hadron-nucleon (hN) collisions. Such an approach is used in the wounded nucleon model. This simple approach is not sufficient to fully understand hadron-nucleus collisions.

Due to theoretical problems with description of the „soft" part of hadronic interactions, a study of the single particle inclusive cross sections in pp and pA interactions is crucial.

2.2 Cross-sections

In the hadronic interaction field, experiments study total or topological cross-sections. A topological cross-section refers to the production of a particular final state configuration or a particular process. The most commonly used topological cross-sections are:

- Elastic – projectile and target particles are emitted without change of their c.m.s energies and quantum numbers but in different directions.
- Inelastic – projectile and/or target particles are emitted with different momentum and/or quantum numbers.
- Quasi-elastic – a subset of inelastic cross-section without emission of new particles. An exemplary process of this type is target dissociation eg. (proton deuterium → proton proton neutron)
- Production – at least one new particle is produced (production = inelastic – quasi-elastic). This part can be further subdivided into: diffractive and non-diffractive

- In diffractive process target does not change its nature. In this process no quantum numbers are exchanged between the projectile and target system.

2.3 Existing hadronic interaction data

Before the nineties, a majority of the existing data concerning h-h and h-A were collected by bubble chambers or single-arm spectrometers. These detection techniques have specific limitations. In bubble chamber, separation between pions, kaons, and protons above a few hundred MeV/c is not possible. Furthermore, the number of events that can be collected and analyzed is limited. Single-arm spectrometers have small kinematic acceptance region but they can collect large number of events. Apart from bubble chamber and single-arm spectrometer experiments, some data collected in colliding beam were used in this field, for example the data on the rapidity distributions in the central region collected by UA5 experiment at the CERN super anti-proton proton collider [45]. Former experiments have explored only small fraction of the phase space and without sufficient precision needed these days. Recently, data have been collected by large acceptance multi-component spectrometers like HARP [74, 75], MIPP E907 [145], NA49 [17], and NA61/SHINE [39, 40]. HARP and NA49 experiments have finished data taking. MIPP and NA61/SHINE are at the halfway point of their operation.

The existing data were collected using incident proton beam with the momentum from 10 GeV/c to 450 GeV/c interacting with different target materials like beryllium, aluminum, copper, and lead. A compilation of p+Be and p+C target data in momentum and polar angle variables is shown in Figure 6. The box histograms show the importance of phase space regions for cosmic ray simulations. SPY/NA56 (NA52), MIPP E907, and NA61/SHINE data are not shown in this figure.

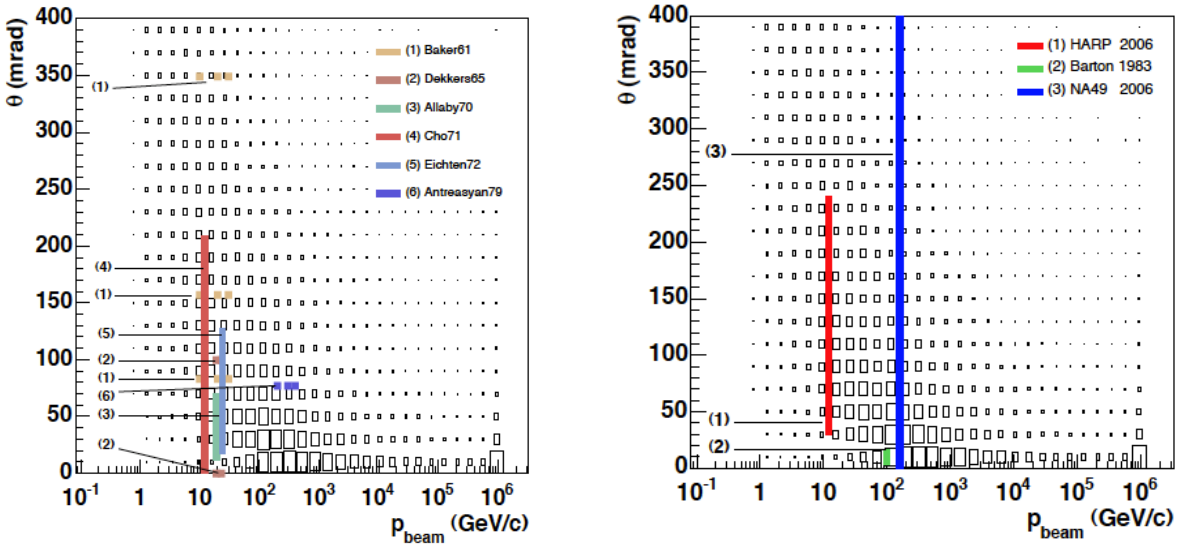

Figure 6. Compilation of p+Be (left) and p+C (right) target data in momentum and polar angle variables. The pictures are taken from [136] (left), [137] (right). More information in Table 2.

The compiled data were taken by:

- Single-arm spectrometer experiments at CERN, at Fermilab, at the Brookhaven Alternating Gradient Synchrotron (AGS), and at the Zero Gradient Synchrotron (ZGS) at the Argonne National Laboratory.
- NA49 and HARP large acceptance spectrometers at CERN.

In the bubble chambers liquid serves a double purpose. It forms target and detector medium. Bubble chambers were invented by Glasser who earned the Nobel Prize in 1960 for the invention of this detection technique. The improvements of this technique by Alvarez were also awarded the Nobel Prize in 1967. The functionality of the bubble chamber is based on the principle that a pressurized liquid heated to boiling point and suddenly expanded will begin to boil where charged particles pass through it. After the expansion, pictures are taken from three stereo angles. The three projections enable to produce a reconstruction of the geometry of the charged particle tracks in each event. Above a few hundred of MeV/c, the identification of secondary charged particle is not possible, protons appear the same as pions and kaons. The other limitation is the number of events that can be collected and analyzed. These limitations play an important role and lead to huge restrictions in usefulness of bubble chamber data. Bubble chambers allow to measure negatively charged mesons and pions, providing that other particle contamination is taken into account, up to a few tens of GeV. Bubble chambers also allow measuring the cross section of some neutral particles using secondary vertex resulting from the decay of those particles. A limitation to this approach is the restricted possibility to distinguish distance between primary and secondary vertex. In hydrogen chambers, it is almost not possible to measure photons due to a large radiation length.

Single-arm spectrometer detectors are placed along the single trajectory in some distance from the target. In this setting, the acceptance region is only a small fraction of available phase-space region. The momentum of secondary particle is selected by spectrometer magnet. The measurements are done as a function of the laboratory angle and momentum. To convert data collected by this kind of experiments into other variables, model corrections must be done. This introduces uncertainty, which due to the lack of clear description of soft hadronic interaction, can be large. In this type of experiments, counting of incoming protons was very often problematic, which influanced the precision of normalization. Typically, uncertainty connected with normalization ranged from about 10% to 25% [128].

The colliding beam experiments made another contribution to the hadronic interactions field. Those experiments studied almost exclusively $p-p$ or $\bar{p}-p$ collisions. Due to the fact that those experiments were operated in c.m.s their acceptance for forward going particles is limited. The UA5 experiment in CERN had important contribution to this field. The main components of the UA5 detector were two large stream chambers placed about 5 cm above and below the collision point. The trigger was provided by signal from two scintillation hodoscopes placed at the end of chambers. Among others, multiplicity distributions of charged particles produced in single-diffractive $\bar{p}-p$ collisions at c.m.s energies of 200 and 900 GeV were measured. These data were used to examine and tune different Monte Carlo models like Dual Parton, the Fritiof, and the Pythia models [37].

In the last group of experiments, large acceptance spectrometers were used to study hadronic interactions. Representatives of this group are NA49, HARP, MIPP E907, and NA61/SHINE experiments. The NA49 collected data mainly in heavy-ion collisions at 158 GeV/A but they also collected proton-proton, proton-lead, and proton-carbon data. The HARP was the first experiment purposely constructed to study hadron interactions needed to understand predictions of atmospheric neutrino fluxes and possible solutions for neutrino factory designs. The HARP collected data using proton and pion beams interacting with different nuclear targets in the energy range from 3 to 15 GeV. HARP results were used by the K2K [26] and MiniBooNE [20] in the neutrino flux calculations. Double differential production cross-sections of pions from p+C collisions at 12 GeV/c as a function of momentum (p) in different polar angle slices (θ) as measured by the HARP are shown in Figure 7. The HARP did not have full phase space acceptance therefore parameterization was used in unmeasured regions.

The MIPP E907 experiment at Fermilab was constructed to study hadron interactions for the use of neutrino experiments such as NOνA [27] and MINOS [138]. Preliminary results for 120 GeV and 60 GeV proton interactions with different nuclear targets were published in 2008 [145]. The most up to date results on pion, kaon, and proton cross sections from interactions of proton with different nuclear targets at 60 GeV were presented in the PhD thesis written in 2009 [112].

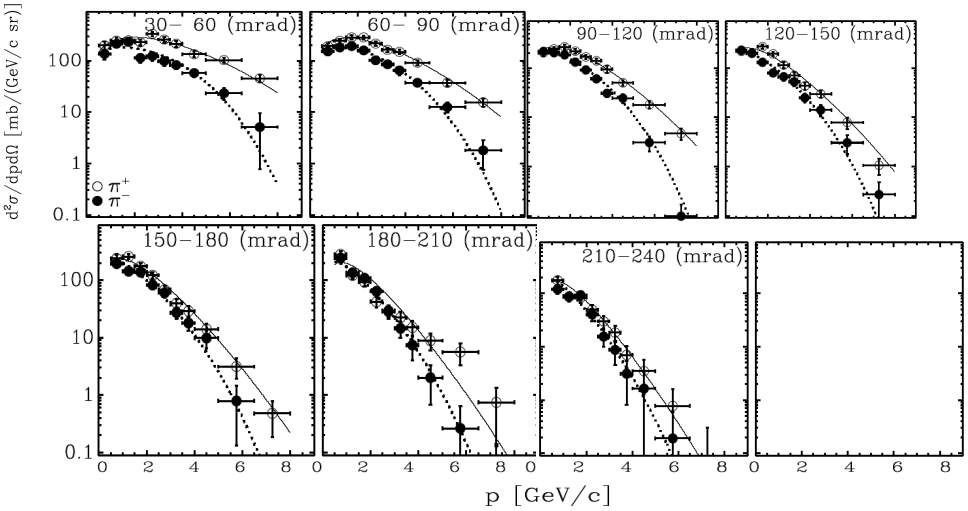

Figure 7. Double differential production cross-sections of pions from p+C collisions at 12 GeV/c as a function of momentum (p) in different polar angle slices (θ) as measured by HARP. Solid lines show Sanford-Wang parameterization [77].

As one can see from this short overview up to now region between 24 to 60 GeV was not covered by measurements. Information about published p + A data is gathered in Table 1 and in Table 2 for the low-energy region and high-energy region, respectively.

The region between 24 to 60 GeV is important for a better understanding of neutrino flux and cosmic ray simulations. The T2K experiment produces neutrino beam using proton carbon interactions at 31 GeV/c. The closest available data from proton Carbon interactions are from the HARP experiment. With closer energy to T2K needs, experiment in CERN were performed but with different nuclear targets (Be, B_4C, Al, Cu, Pb, and others) and with limited acceptance to angles from 17 to 127 mrad and momenta from 4 to 18 GeV/*c* [94].

Experiment or reference (beam)	p beam (GeV/c)	Target material	t/λint (%)	Secondary coverage
Baker (AGS)	10, 20, 30	Be, Al	Unknown	1 < p < 17 GeV/c, θ = 4.75°, 9°, 13°, 20°
HARP (PS)	3, 5, 8, 12, 15	Be, C, Al, Cu, Sn, Ta, Pb, N, O, H, D	2, 5, 100	0.75 < p < 6.5 GeV/c, 30 < θ < 210 mrad and 0.1 < p < 0.8 GeV/c, 350 < θ < 2150 mrad
Marmer (ANL)	12.3	Be, Cu	10	p =0.5, 0.8, 1.0 GeV/c, θ = 0◦, 5◦, 10◦
Cho (ANL)	12.4	Be	4.9, 12.3	2 < p < 6 GeV/c, 0° < θ < 12°
Lundy (ANL)	12.4	Be	25, 50, 100	1 < p < 12 GeV/c,

				$2^\circ < \theta < 16^\circ$
Asbury (ANL)	12.5	Be	4.9, 12.3	p =3, 4, 5, $\theta = 12^\circ, 15^\circ$
Abbot (AGS)	14.6	Be, Al, Cu, Au	1 – 2	0 < p < 8 GeV/c, $\theta = 5^\circ, 14^\circ, 24^\circ, 34^\circ, 44^\circ$
Allaby (PS)	19.2	Be, Al, Cu, Pb, B_4C	1 – 2	p =6, 7, 10, 12, 14 GeV/c, θ =12.5, 20, 30, 40, 50, 60, 70 mrad
Eichten (PS)	24	Be, B_4C, Al, Cu, Pb	1-2	4 < p < 18 GeV/c, 17 < θ < 127 mrad

Table 1. Compilation of the p + A hadron production data. The low-energy region.

Experiment or reference (beam)	p beam (GeV/c)	Target material	t/λint (%)	Secondary coverage
MIPP E907 (Fermilab)	60, 120	C	0.9 – 3.5	cos θ [0.79, 0.99]
NA49 (SPS)	158	C	1.5	$0.05 < p_T < 1.8$ GeV/c, $-0.1 < x_F < 0.5$
Baker (FNAL)	200, 300	Be	50	θ = ~3 mrad, 60 < p < 370 GeV/c
Baker (FNAL)	400	Be	75	θ = 3.6 mrad, 23 < p < 197 GeV/c
Barton (FNAL)	100	C, Al, Cu, Ag, Pb	1.6 – 5.6	0.3 < xF < 0.88, 0.18 < pT < 0.5 GeV/c
Atherton (SPS)	400	Be	10, 25, 75, 125	xF =0.15, 0.30, 0.50, 0.75, pT =0, 0.3, 0.5 GeV/c
NA56/SPY (SPS)	450	Be	25, 50, 75	xF =0.016, 0.022, 0.033, 0.044, 0.067, 0.089, 0.15, 0.30, pT=0, 75, 150, 225, 375, 450, 600 MeV/c

Table 2. Compilation of the p + A hadron production data. The high-energy region.

2.4 Parameterizations of hadron production data

A few attempts were made to parameterize hadron production data and to provide approximated information in unmeasured regions. Basic information about some of these parameterization models are presented below:

- Malensek parameterization [133]

  The parameterization of the Atherton data with included extrapolation for different beam energies. The production cross-section in this model is parameterized by this formula:

  $$\frac{d^2N}{dpd\Omega} = Kp(1-x_F)^A \frac{(1+5e^{-Dx_F})}{(1+p_T^2/m^2)^4}$$

  with separate parameters sets A, B, m, D for pions, kaons, and protons. In this approach, scaling to different nuclear targets is done using Eichten data and scaling to different target lengths is done by the simple absorption model.

- BMPT parameterization [67]

  The extension of Malensek parameterization that fits not only the Artherton data but also the NA56/SPY data. It takes into account evaluation of $<p_T>$ with x_F found by NA56/SPY [31]. Invariant cross-section in this method is parameterized by this formula:

  $$(E \times \frac{d^3\sigma}{dp^3}) = A(1-x_R)^{\alpha}(1+Bx_R)x_R^{-\beta}(1+a'(x_R)p_T + b'(x_R)p_T^2)e^{-a'(x_R)p_T}$$

  where x_R is the ratio of the particle's energy to its maximum possible energy in the central mass frame. Functions control the scale breaking of p_T. Separate parameters were fitted to positively and negatively charged pions and kaons. Scaling to other nuclear targets is done using Barton scaling equation [54]

  $$E\frac{d^3\sigma}{dp^3} = \sigma_0 A^{\alpha}$$

  In this parameterization, an improved absorption model was used for scaling to different target lengths.

- Sanford-Wang parameterization [173]

  Production cross-section is parameterized by this formula:

  $$\frac{d^2N}{dpd\Omega} = Ap^B(1-p/p_0)\exp[-\frac{cp^D}{p_0^E} - F\theta(p - Gp_0\cos^H\theta)]$$

  where p_0 is the proton momentum, p is the pion or kaon momentum, θ is the pion or kaon production angle. Parameters from A to H were fitted to experimental data separately for positively and negatively charged pions and kaons. Parameterization is valid only for thin target. Wang published variation of this parameterization valid for high energies [174].

- CKP parameterization [81]

  Production cross-section is parameterized by this formula:

  $$\frac{d^2\sigma}{dpd\Omega} = Ap^2(p_0 - p)e^{-(p-a)(b+c\theta)}$$

  This approach is valid for thin target. It was motivated by cosmic ray data. Therefore, the effective exponential dependence is present in this approach.

To minimize model uncertainty of T2K neutrino beam predictions, the NA61/SHINE made dedicated measurements using thin carbon target and T2K replica target. The NA61/SHINE program and results on negatively charged pion and neutrally charged kaon meson and lambda hyperon production from proton at thin carbon target interactions at 31GeV/c are discussed in this thesis.

Chapter 3 Neutrino oscillations

3.1 Formalism of the neutrino oscillations

In 1930 Wolfgang Pauli wrote his famous letter to "Dear Radioactive Ladies and Gentlemen". In this letter he proposed the existence of light neutral particle with spin ½ to explain a continuous energy spectrum of electrons produced in beta decay [96]. This new particle was needed to save conservation of energy and angular momentum in radioactive decays. In 1934, Enrico Fermi published theory in which he took into consideration Pauli's postulate [148]. He formulated a dynamical theory of weak particle interactions, in which this new extremely light particle plays a crucial role. Enrico Fermi proposed "neutrino", means a little neutral one, as the name for Pauli's postulated particle. Fermi's framework laid foundations for the Glashow-Weinberg-Salam (GWS) model of electroweak interactions. It was first formulated by Weinberg in 1967 and independently by Salam in 1968. Nowadays, the GSW model together with the model of strong interactions constitute the basis of the Standard Model of particle physics [84], in which processes in terms of gauge interactions between quarks, charged leptons, and neutrinos are portrayed. In the Standard Model, neutrino is massless and bounded by lepton number and flavor lepton number conservations. It means that the total number of leptons in any reaction and also number of leptons of a given flavor has to stay constant. To sum up, the Standard Model describes neutrinos as massless, left-handed, flavor-conserving particles. However, the recent data from atmospheric and solar neutrino experiments [99, 32, 79, 115, 1, 28, 24] are interpreted in terms of neutrino oscillations. It implies that not all neutrinos are massless. Besides that, direct measurements of neutrino mass have been performed by precise measurement of decay kinematics and by cosmological data, which provide stronger constraints on the total neutrino mass than particle physics experiments [95]. The best upper limits at present on the mass of the three neutrino species are summarized in the Table 3.

Neutrino type	Mass Limit	Experiment type / Confidence Level
ν_e	< 2 eV	Tritium beta decay / 95
ν_μ	< 190 keV	pion decay / 90
ν_τ	< 18.2 MeV	tau decay / 95
Total neutrino mass	< 0.28 eV	Cosmology / 95

Table 3. Upper limits on neutrino mass from direct measurements [110].

Neutrino oscillations were proposed in 1950s by Bruno Pontecorvo in analogy with kaon oscillations [152]. The modern theory evolved from this concept and was formulated in 1970s, among others, by Pontecorvo and Bilenky [66]. Neutrino oscillations, a quantum mechanical phenomenon, explain experimental results from atmospheric and solar neutrino experiments by allowing neutrino flavor transitions. Oscillations occur because it is assumed that physically interacting flavor eigenstates (ν_e, ν_μ, ν_τ) are combinations of mass eigenstates (ν_1, ν_2, ν_3). Mass eigenstates describe evolution in time and space. While these states propagate through space with different velocities as they have different masses, the change of neutrino flavors takes place. This change has periodical character.
The unitary transformation relating the flavor and mass eigenstates can be written as:

$$\left|\nu_\alpha\right\rangle = \sum_i U_{\alpha i}\left|\nu_i\right\rangle$$

The U is a lepton mixing matrix, also referred to as Pontecorvo–Maki–Nakagawa–Sakata matrix (PMNS matrix) or sometimes simply the MNS matrix. In the tree neutrino case mixing matrix is described by 3 x 3 unitary matrix:

$$U=\begin{pmatrix} c_{13}c_{12} & c_{13}s_{12} & s_{13}e^{-i\delta} \\ -c_{23}s_{12}-s_{13}c_{12}s_{23}e^{+i\delta} & c_{23}c_{12}-s_{13}s_{12}s_{23}e^{+i\delta} & c_{13}s_{23} \\ s_{23}s_{12}-s_{13}c_{12}c_{23}e^{+i\delta} & -s_{23}c_{12}-s_{13}s_{12}c_{23}e^{+i\delta} & c_{13}c_{23} \end{pmatrix} \times \begin{pmatrix} 1 & & \\ & e^{i\alpha} & \\ & & e^{i\beta} \end{pmatrix}$$

where $c_{ij}=\cos\theta_{ij}$ and $s_{ij}=\sin\theta_{ij}$, δ is Dirac phase and α, β are Majorana phases. These phases are zero if CP symmetry is not violated. If one assumes that neutrinos are Dirac particles then Majorana phases are equal to zero and one can disregard the right hand side matrix.
Now, mixing matrix can be split into three matrices, which describes mixing between specific mass eigenstates:

$$U=\begin{pmatrix} 1 & 0 & 0 \\ 0 & c_{23} & s_{23} \\ 0 & -s_{23} & c_{23} \end{pmatrix} \begin{pmatrix} c_{13} & 0 & s_{13}e^{-i\delta} \\ 0 & 1 & 0 \\ -s_{13}e^{i\delta} & 0 & c_{13} \end{pmatrix} \begin{pmatrix} c_{12} & s_{12} & 0 \\ -s_{12} & c_{12} & 0 \\ 0 & 0 & 1 \end{pmatrix}$$

The left hand side matrix corresponds to the atmospheric sector (sector 23). Experiments studying atmospheric neutrinos and long baseline accelerator neutrino experiments contribute to the results on oscillation angle θ_{23} and Δm_{23}. This sector was so far explored by the water Cherenkov detectors – IMB [104], and Kamiokande, and Super-Kamiokande [102]; and by tracking detectors – Frejus [87], NUSEX [19], MACRO [33], and Soudan-2 [160], and by long-baseline accelerator experiments – K2K [26], MINOS [138], and OPERA [18]. Right hand side matrix is related to solar sector (sector 12). The θ_{12} and Δm_{12} were studied so far by solar neutrino experiments by chloraine and gallium radiochemical detectors – Homestake [79], SAGE [3], GALLEX [115], GNO [29]; and water cherenkow detectors using light water and heavy water – Kamiokande [118], Super-Kamiokande [120], SNO [22]; and liquid scintilator detector – Borexino [43]; and long baseline reactor experiments – KamLAND [93]. The middle matrix (sector 13) is not well explored so far. Nowadays, search for the precise determination of the oscillation angle θ_{13} is ongoing. Dirac phase is also unknown. If it is different from zero, CP symmetry violation in lepton sector will occur. The strongest limits, before publication of Daya Bay results, to θ_{13} came from the CHOOZ reactor experiment. Sector 13 is now explored by long baseline accelerator experiments – T2K [122], NOνA (in preparation) [30]; and reactor experiments – Daya Bay [114], Double CHOOZ [42], RENO [25]. This thesis was prepared before reactor experiments have measured osicillation angle $\theta_{13,}$ therefore these results will not be discussed in detail. The current best-fit values are summarized below:

$$\sin^2\vartheta_{12} = 0.318\ ^{+0.019}_{-0.016}$$
$$\sin^2\vartheta_{23} = 0.50\ ^{+0.07}_{-0.06}$$
$$\sin^2\vartheta_{13} = 0.092 \pm 0.016$$ (θ_{13} is non-zero with a significance of 5.2 standard deviations)
$$0 \le \delta \le 2\pi$$
$$\left|\Delta M^2\right| = (2.40\ ^{+0.12}_{-0.11}) \times 10^{-3}\, eV^2$$
$$\Delta m^2 = (7.59\ ^{+0.23}_{-0.18}) \times 10^{-5}\, eV^2$$

where ΔM is equal Δm_{32} (assuming normal hierarchy) or Δm_{13} (assuming inverted hierarchy) and Δm is equal Δm_{21}

In vacuum, the propagation of neutrino flavor eigenstates is described by:

$$\left|\nu_\alpha(t)\right\rangle = \sum_{i=1}^{3} e^{-iE_i t} U_{\alpha i} \left|\nu_i\right\rangle$$

It shows that a neutrino produced with one specific flavor eigenstate after some time becomes a superposition of all possible flavor states. In proper conditions, a neutrino produced at the origin in the flavor eigenstate $|\nu_\alpha\rangle$ oscillates into different flavor eigenstate $|\nu_\beta\rangle$. The probability for such a neutrino oscillation in vacuum can be described by the following formula (in natural units):

$$P_{\nu_\alpha \to \nu_\beta} = \left|\left\langle \nu_\beta \left| \nu_\alpha(t) \right\rangle\right|^2 = \left| \sum_i U^*_{\alpha i} U_{\beta i} e^{-i m_i^2 L / 2E} \right|^2 =$$

$$\delta_{\alpha\beta} - 4 \sum_{i>j} \Re\left(U^*_{\alpha i} U_{\beta i} U_{\alpha j} U^*_{\beta j}\right) \sin^2\left(\frac{\Delta m^2_{ij} L}{4E}\right)$$

$$+ 2 \sum_{i>j} \Im\left(U^*_{\alpha i} U_{\beta i} U_{\alpha j} U^*_{\beta j}\right) \sin\left(\frac{\Delta m^2_{ij} L}{2E}\right)$$

where

$$\Delta m^2_{ij} \equiv m^2_i - m^2_j$$

is the difference of two squared masses, L is the oscillation distance, and E the neutrino energy.

The main term that is responsible for oscillation is often written as (with *c* and ħ restored) [119]:

$$\frac{\Delta m^2_{ij} L}{4E} \approx 1.267 \frac{\Delta m^2_{ij}(eV^2) L(km)}{E(GeV)}$$

The oscillation probabilities depend on the L/E, differences of squared masses, and elements of the mixing matrix (three mixing angles and Dirac phase).

In some experiments, only two neutrino types participate in the mixing. This simplifies presented picture to mixing matrix that depends only on the single oscillation-mixing angle:

$$U = \begin{pmatrix} \cos\theta & \sin\theta \\ -\sin\theta & \cos\theta \end{pmatrix}$$

Let us consider neutrino oscillations of two flavors (ν_e, ν_μ,). In this case equations for oscillation probabilities are described by:

$$P(\nu_\mu \to \nu_\mu) = 1 - \sin^2 2\vartheta \sin^2\left(\frac{1.267\,\Delta m^2 L}{E}\right)$$

$$P(\nu_\mu \to \nu_e) = 1 - P(\nu_\mu \to \nu_\mu)$$

Oscillation angle (ϑ) and difference of squared masses (Δm^2) control the strength of oscillations and oscillation periodicity, respectively. Two other parameters, distance L and neutrino energy E, are associated with a specific experimental situation.
Small value of θ13 allows in first approximation to study oscillations associated with sector 12 and sector 23 separately, as two flavor transitions. For sector 23, after neglecting contribution related with Δm^2_{12} oscillation, probabilities can be expressed by these formulas:

$$P\left(\nu_\mu \to \nu_e\right) = \sin^2 2\vartheta_{13} \sin^2 \vartheta_{23} \sin^2\left(\frac{1.267\Delta m^2_{23} L}{E}\right)$$

$$P\left(\nu_\mu \to \nu_\mu\right) = 1 - \sin^2 2\vartheta_{23} \cos^4 \vartheta_{13} \sin^2\left(\frac{1.267\Delta m^2_{23} L}{E}\right) - P\left(\nu_\mu \to \nu_e\right)$$

$$P\left(\nu_e \to \nu_\tau\right) = \sin^2 2\vartheta_{13} \cos^2 \vartheta_{23} \sin^2\left(\frac{1.267\Delta m^2_{23} L}{E}\right)$$

$$P\left(\nu_e \to \nu_e\right) = 1 - \sin^2 2\vartheta_{13} \sin^2\left(\frac{1.267\Delta m^2_{23} L}{E}\right)$$

These oscillation probabilities reduce to two flavors formulas if θ_{13}. We have the same situation in the sector 12. To conclude, the two-flavor approximation describes well situation in the sector 23 (atmospheric mixing $\nu_\mu \to \nu_\tau$ when ν_e is neglected) and as well in the sector 12 (solar sector $\nu_e \to \nu_x$)

3.2 Current knowledge of oscillation parameters

Neutrino oscillation parameters were explored by several experiments, which can be categorized into four types according to the neutrino sources: solar, atmospheric, reactor, and accelerator neutrino experiments. In this subchapter, brief overview of these four types of experiments and current knowledge of oscillation parameters obtained by them are presented. The current limits on oscillation parameters from experimental data are shown in Figure 8. The recent results on θ_{13}, namely results from the T2K, Daya Bay, RENO, and Double CHOOZ are not included. As it was mentioned, this thesis was prepared before non-zero results on osicillation angle θ_{13} were published. Therefore, detailed discussion of these results will not be presented.

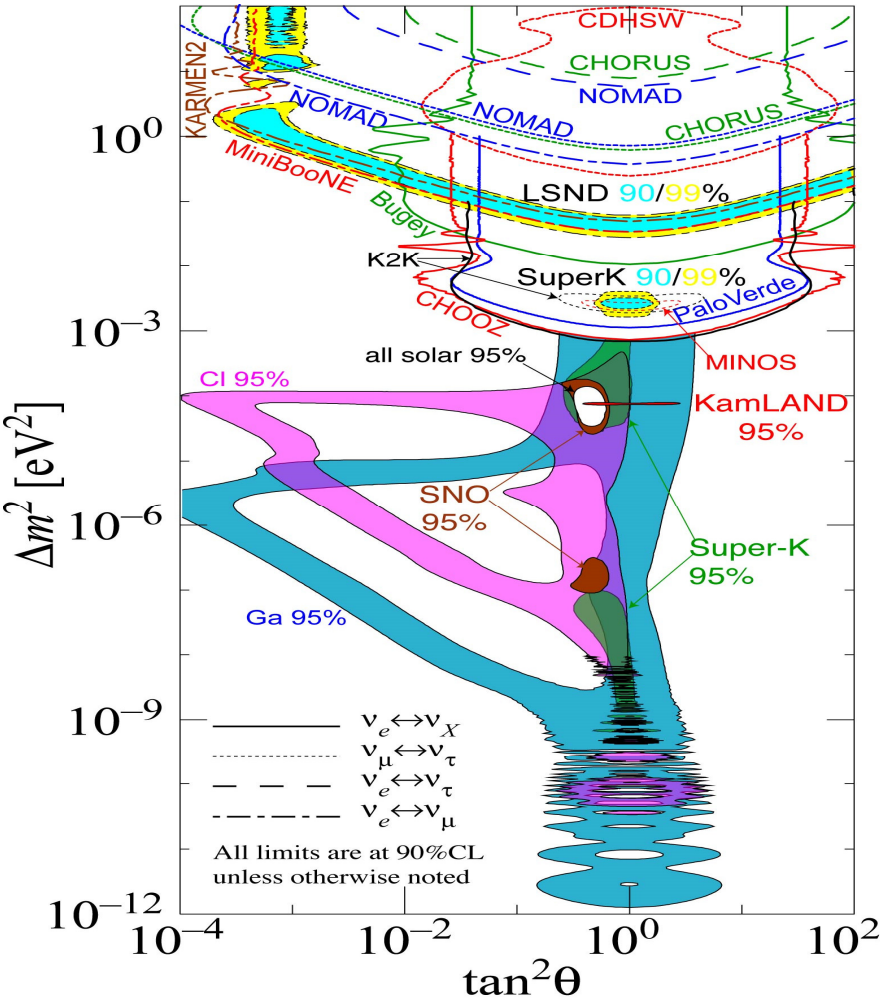

Figure 8. Current limits on oscillation parameters from existing experimental data [110]. Upper-middle part shows allowed region for atmospheric sector. Middle part shows allowed region for solar region. LSND and MiniBoone (which excludes LSND interpretation of electron neutrino appearance effect) results are placed in upper-part.

Main experiments contributing to Fig. 8 are discussed in the following subchapters. The LSND effect that is excluded by MiniBoone results (in neutrino mode) will not be discussed in this thesis.

3.2.1 Atmospheric neutrino experiments

As it was mentioned before, the Kamiokande, IMB, Super-Kamiokande, Frejus, NUSEX, MACRO, and Soudan-2 experiments provided the main contribution to the constraints on the atmospheric neutrino mixing parameters.

Cosmic ray interactions with air nuclei in the Earth's atmosphere lead to the production of hadrons, leptons, and neutrinos. Neutrinos are produced in the atmosphere mainly from the pion and muon decays. When the primary particles, mainly protons, interact with atmosphere's gasses, mainly pions and some kaons are produced. Then pions decay to neutrinos and muons that also decay, among others, to neutrinos:

$$\pi^+ \rightarrow \mu^+ + \nu_\mu$$

$$\mu^+ \rightarrow e^+ + \bar{\nu}_\mu + \nu_e$$

$$\pi^- \rightarrow \mu^- + \bar{\nu}_\mu$$

$$\mu^- \rightarrow e^- + \nu_\mu + \bar{\nu}_e$$

In these decays, muon neutrinos and electron neutrinos are produced. Produced neutrinos have wide energy spectrum from ~100 MeV up to TeV range with a peak at ~ 1 GeV. If we take into consideration that not all pions and muons decay before reaching Earth's surface and also the fact that not only pions lead via decays to neutrinos production, one can find the flavor ratio

$$R = (\nu_\mu + \bar{\nu}_\mu)/(\nu_e + \bar{\nu}_e)$$

that should be equal ~2.1 [103]. As an example the different flavor ratio calculations at the Super-Kamiokande are shown in Figure 9.

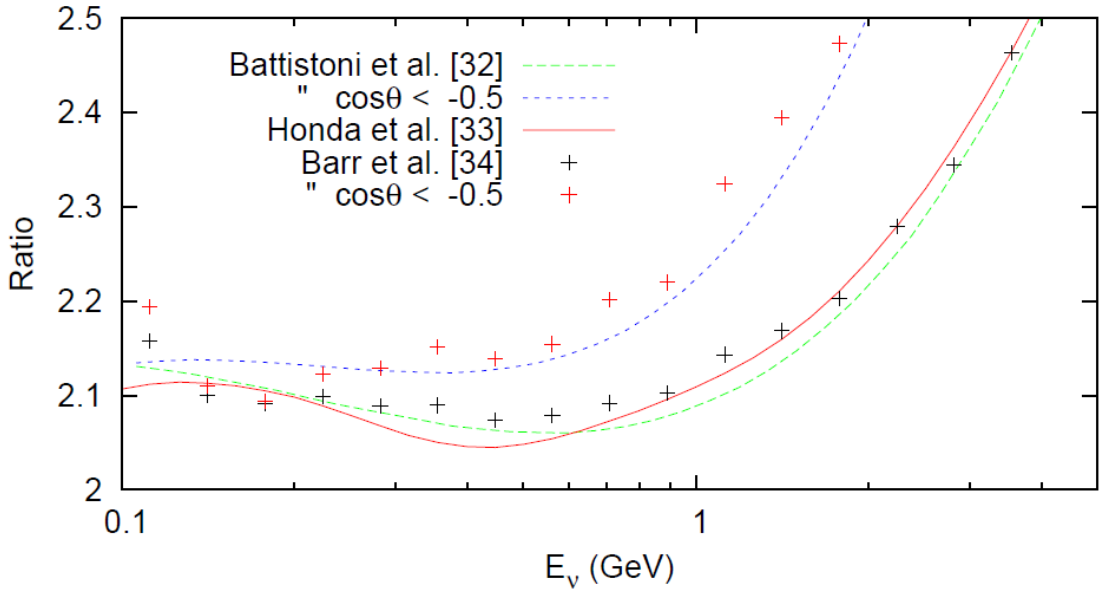

Figure 9. Three different calculations of flavor ratios at the Super-Kamiokande [103].

Starting from 1960s, several experiments, among others the Kamiokande and IMB, have obtained lower fluxes of muon neutrinos than expected. This deficit was called atmospheric

neutrino anomaly. This anomaly was confirmed and explained by Super-Kamiokande Collaboration in 1998 [46]. The atmospheric neutrino oscillation phenomenon was proposed as an explanation. The Super-Kamikande detection technique and background sources for measurement of neutrino interaction are discussed in detail in chapter 5.1.1. The Super-Kamiokande measured the zenith angle distribution of the muon and electron-like events. The reconstructed number of upward going muon neutrinos was found to be smaller than what was expected by predictions in the absence of neutrino oscillations. Therefore it affects flavor ratio. The observed angular asymmetry of atmospheric muon neutrinos is well described with the two-flavor oscillations. The measured asymmetry was also confirmed by the MACRO and Soudan-2 experiments. The ratio of data to Monte Carlo predictions without neutrino oscillations as a function of the neutrino flight length (L) over the neutrino energy (E) is shown in Figure 10. The shape of this distribution favours neutrino oscillation as a description of this phenomenon and disfavors different models like neutrino decay [51] and decoherence [131] as they do not reproduce the shape in whole L/E region.

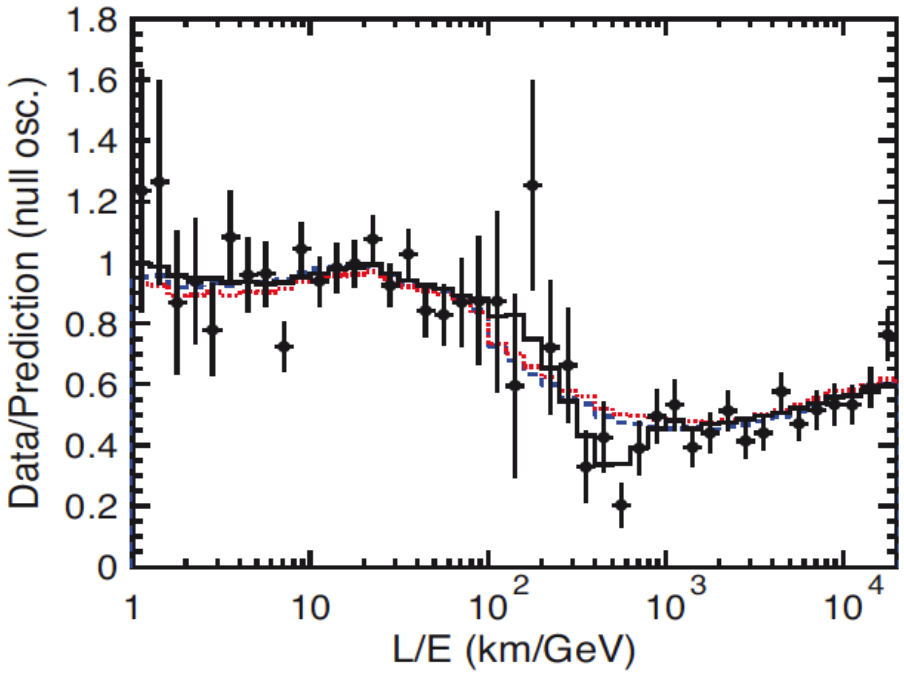

Figure 10. Ratio of data to the Monte Carlo predictions without neutrino oscillations as a function of neutrino flight length (L) over neutrino energy (E) as obtained by Super-Kamiokande [46].

3.2.2 Accelerator neutrino experiments

As it was mentioned before, the K2K, MINOS, and OPERA experiments plays the main role in this field.

To study $\nu_\mu \to \nu_\tau$ oscillations, accelerator based neutrino oscillation experiments were designed. Principles of long baseline neutrino experiment measurements are discussed in chapter 3.3. The KEK to Kamioka (K2K) and Main Injector Neutrino Oscillation Search (MINOS) experiments are both neutrino oscillation experiments, which were studying muon neutrino disappearance in accelerator-produced muon neutrino beams. In both experiments, near detectors were used to study unoscillated neutrino beam spectrum and composition. After the distance of 250 km in the K2K and 735 km in the MINOS, interactions of neutrinos were registered in far detectors. The distance of far detectors and average beam energy (~1.4 GeV in the K2K and ~4 GeV in the MINOS) were chosen to be with L/E in a first oscillation

maximum of atmospheric neutrinos. The results of the MINOS experiment, which are considered the most precise measurement in this field, are shown in Figure 11 together with the K2K and Super-Kamiokande results.

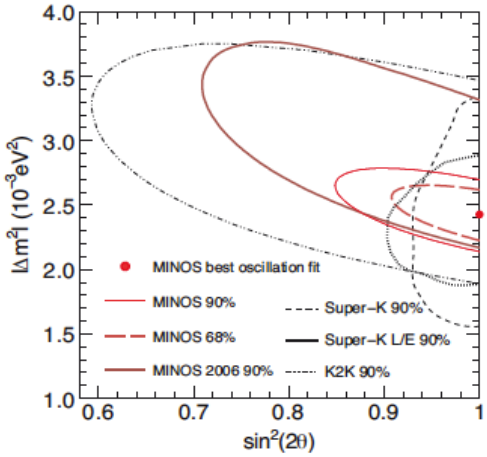

Figure 11. Contours of the two-flavor oscillation fit to the data from MINOS, Super-Kamiokande, and K2K [12].

The Oscillation Project with Emulsion-Tracking Apparatus (OPERA) experiment is aiming at the first direct detection of neutrino oscillations in appearance mode. The OPERA detector is placed in the CNGS 730 km away from the neutrino source. The analysis of a sub-sample of the data taken in the 2008-2009 runs was completed. In this sample the first ν_τ CC candidate was found with a background expectation 0.018±0.007 (syst). The probability to observe one event due to a background fluctuation is 1.8%, which corresponds to 2.36 σ [18]. The analysis of the 2008 and 2009 full sample will be completed soon.

The second subject covered by long baseline neutrino oscillation experiments is the study of the last unknown oscillation angle θ_{13} via $\nu_\mu \rightarrow \nu_e$ appearance approach. The long-baseline experiments did not found oscillations in this mode before June 2012. Therefore, they set limits on θ_{13}. However, the best constraint was set by the reactor experiment, which will be discussed in chapter 3.2.4. Recently, the T2K experiment has shown that the oscillation angle θ_{13} is different from zero with 3.2 σ.

3.2.3 Solar neutrino experiments

The main contribution to the constraints on the solar neutrino mixing parameters was provided by the Homestake, SAGE, GALLEX, Kamiokande, Super-Kamiokande, and Sudbury Neutrino Observatory experiments.

The nuclear processes that power the Sun produce only electron neutrinos. Therefore, solar neutrino experiments are sensitive to $\nu_e \rightarrow \nu_x$ oscillation. The main neutrino producing reactions in the proton – proton chain are listed in the Table 4.

Reaction	Label	Flux (cm^{-2} s^{-1})
$p + p \rightarrow {}^{2}H + e^{+} + \nu_e$	Pp	$5.95 * 10^{10}$
$p + e^{-} + p \rightarrow {}^{2}H + \nu_e$	Pep	$1.4 * 10^{8}$
${}^{3}He + p \rightarrow {}^{4}H + e^{+} + \nu_e$	Hep	$9.3 * 10^{3}$
${}^{7}Be + e^{-} \rightarrow {}^{7}Li + \nu_e$	${}^{7}Be$	$4.77 * 10^{9}$
${}^{8}B \rightarrow {}^{8}Be + e^{+} + \nu_e$	${}^{8}B$	$5.05 * 10^{6}$

Table 4. Main neutrino producing reactions in the proton – proton chain [108].

Most of the neutrinos produced in the Sun come from pp reaction but their energy is very low, which makes them hard to detect. The easiest neutrinos to detect come from ^{8}B reactions. They have maximum energy of approximately 15 MeV. Neutrinos are also produced in the secondary cycle of solar energy generation (CNO cycle). The neutrino energy spectrum from all nuclear fusion processes as predicted by the Solar Standard Model (SSM) is shown in Figure 12.

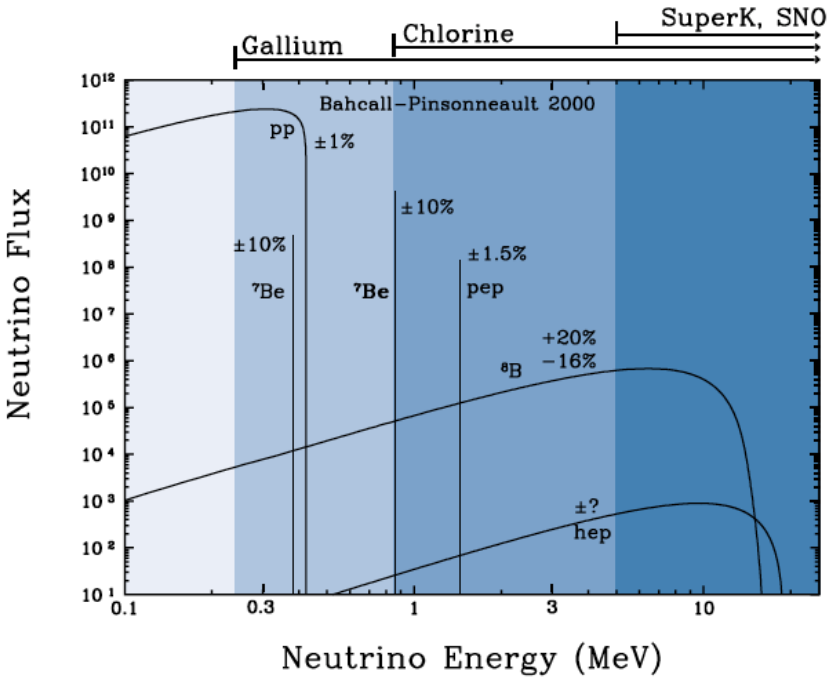

Figure 12. Solar neutrino spectra predicted by the SSM. The neutrino fluxes at one astronomical unit from continuum sources are given in units of cm−2 s−1 MeV−1, and the line fluxes are given in cm−2 s−1. The figure is taken from [61].

For over forty years, solar neutrino experiments have observed significantly lower electron neutrino fluxes than expected from neutrino production calculations. This discrepancy was known as Solar Neutrino Problem. It was for the first time observed by the Ray Davis's Homestake Experiment in the late 1960s. The detector was based on a concept first proposed

by Bruno Pontecorvo at Chalk River in 1946. The detection is based on the fact that neutrinos interacting with chlorine can produce an isotope of argon through the inverse beta reaction, $\nu_e + {}^{37}Cl \rightarrow e^- + {}^{37}Ar$, with an energy threshold of 0.814 MeV. Those argon atoms need to be extracted before they decay back to chlorine. The chlorine experiment took data until 1995 [79]. The final result for the neutrino capture rate was 2.56 ± 0.16 (statistical) ± 0.16 (systematic) $*10^{-36}$ per target atom s^{-1} (Solar Neutrino Unit ≡ SNU), while the rates predicted with SSM, depending on the opacity and equation of states used, were within the range of {5.8, 9.3} * SNU [61]. Clearly, the rate observed by the Homestake experiment is much lower than that predicted. The distance between the Sun and the Earth is ~1.5 * 10^8 km. If the Mikheyev-Smirnov-Wolfenstein (MSW) effect is taken into account, Solar Neutrino Problem can be explained by the neutrino oscillations. The MSW effect is defined as the shift of neutrinos' effective mass eigenvalues as they travel through matter [139]. In the 2001, the Sudbury Neutrino Observatory (SNO) experiment provided a clear evidence of electron neutrino flavor change. If neutrino oscillations are assumed, the Homestake experiment results can be transformed to the constrains on the oscillation parameters. The allowed region of Δm^2 and $\tan^2\theta$ is obtained from the comparison of the predicted and measured neutrino fluxes. The obtained constraints are presented in Figure 13.

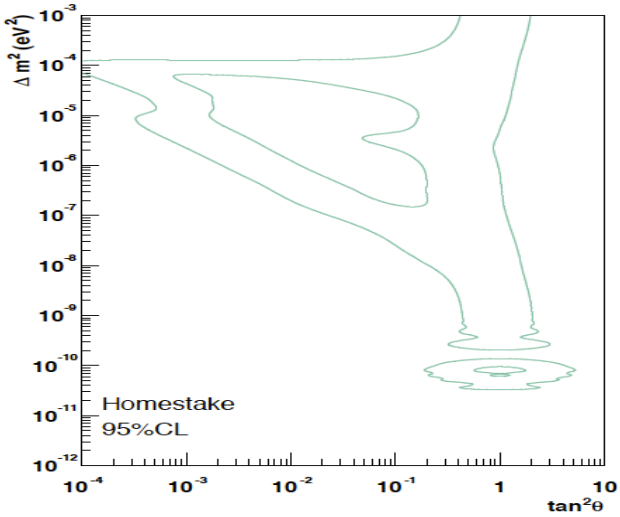

Figure 13. Mixing plane constraints obtained by the Homestake chlorine experiment [61]. The inside of the covariance regions is allowed at the 95% CL. $\tan^2\theta < 1$ correspond to the normal hierarchy, $\tan^2\theta > 1$ corresponds to the inverted hierarchy.

Two other radiochemical experiments, the SAGE at the Baksan laboratory [1] in Russia and the GALEX/GNO at the Gran Sasso laboratory [28] in Italy, which were using gallium as a detector medium also observed a solar neutrino rate that was lower than predicted. The gallium detector detection technique is based on the reaction $\nu_e + {}^{71}Ga \rightarrow e^- + {}^{71}Ge$ with the energy threshold of 0.233MeV. This technique allows detecting neutrinos from pp, ^{7}Be, ^{8}B, and pep reactions. The final GALEX/GNO result on the neutrino rate is 70.8 ± 4.5 (statistical) ± 3.8 (systematic) SNU [2], while SSM predicted rates are within {125, 134} * SNU. The constraints obtained from the GALEX/GNO and SAGE experiments on the oscillation parameters are shown in Figure 14.

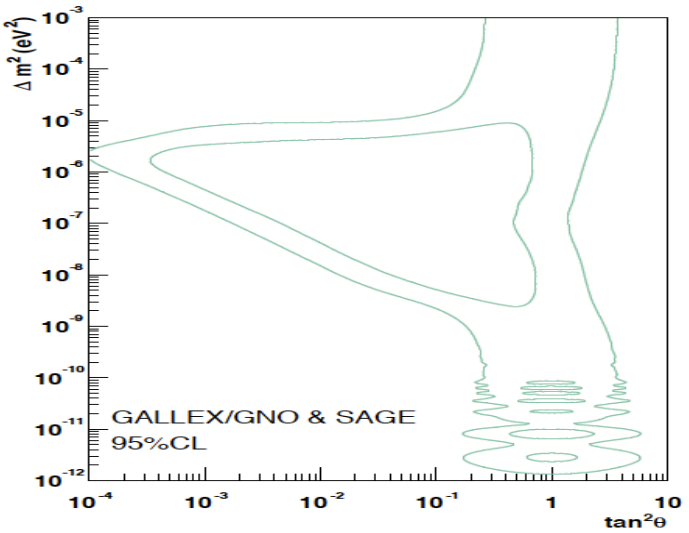

Figure 14. Mixing plane constraints obtained by GALLEX/GNO and SAGE gallium experiments [61]. The inside of the covariance regions is allowed at the 95% CL. $\tan^2\theta < 1$ correspond to the normal hierarchy, $\tan^2\theta > 1$ corresponds to the inverted hierarchy.

Other experimental technique was used in the Kamiokande and Super-Kamiokande detectors located in Kamioka mine in Japan [101]. These experiments measured solar neutrino flux in the higher energy region using water as a detector medium. This detection system allows determining not only energy of the particle but also its direction. Solar neutrino can interact in the detector via neutrino-electron scattering (ES) reaction, $\nu_e + e^- \rightarrow \nu_e + e^-$, and Cherenkov light emitted by recoil electron can be detected. The direction of recoil electron is correlated with direction of incident neutrino. The Super-Kamiokande obtained ES neutrino rate, 2.35 ± 0.02 (statistical) $\pm$ 0.08 (systematic) * 10^6 cm^{-2} s^{-1}, which was also smaller than SMM predicted rate. The obtained constraints from the Super-Kamiokande experiment on the oscillation parameters are shown in the Figure 15.

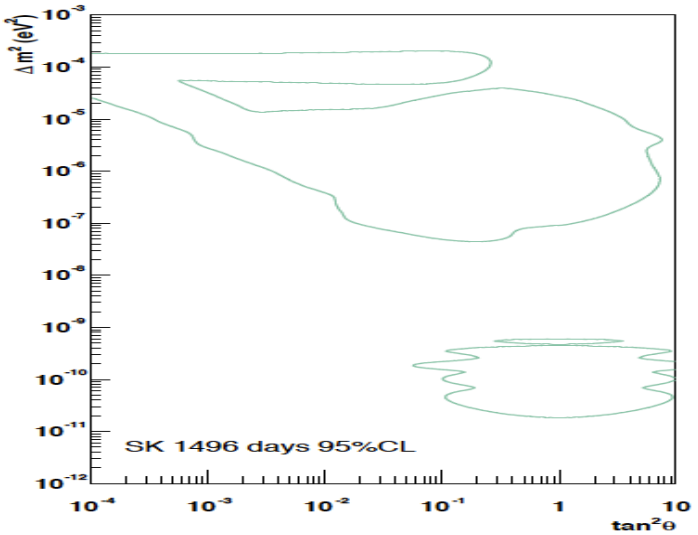

Figure 15. Mixing plane constraints obtained by Super-Kamikande experiment [61]. The inside of the covariance regions is allowed at the 95% CL. $\tan^2\theta < 1$ correspond to the normal hierarchy, $\tan^2\theta > 1$ corresponds to the inverted hierarchy.

The same tendency was observed in all experiments presented above. The observed rate was smaller than the predicted one. The ratios of observed and expected rates for different experiments are presented in the Table 5.

Experiment	Observed/expected rate
Homestake	0.27±0.04
GALLEX	0.56±0.07
SAGE	0.53±0.08
SuperKamiokande	0.39±0.06

Table 5. Ratios of observed to expected rates obtained by different solar neutrino experiments, typical SSM model used for expected rates calculations [150].

The explanation of these discrepancies was proposed by the SNO experiment. The experiment is located 2 km underground in the INCO's Creighton mine in Ontario, Canada. The detector is a 1000-ton heavy water Cerenkov detector. The heavy water is in an acrylic vessel (12 m diameter and 5 cm thickness) viewed by 9456 PMTs. The use of heavy water allows the flux of all three neutrino types to be measured. The SNO experiment sees solar neutrinos via three reactions:

$$CC: \nu_e + {}^2H \rightarrow p + p + e^-$$

$$NC: \nu_x + {}^2H \rightarrow p + n + \nu_x$$

$$ES: \nu_x + e^- \rightarrow \nu_x + e^-$$

where $x = e, \mu, \tau$, CC means Charge Current reaction, NC means Neutral Current reaction, ES means Elastic Scattering on electrons reaction. The results from SNO phase II, in which NaCl was dissolved in the heavy water to enhance the sensitivity to NC reactions through higher neutron capture efficiency, are presented in Figure 16.

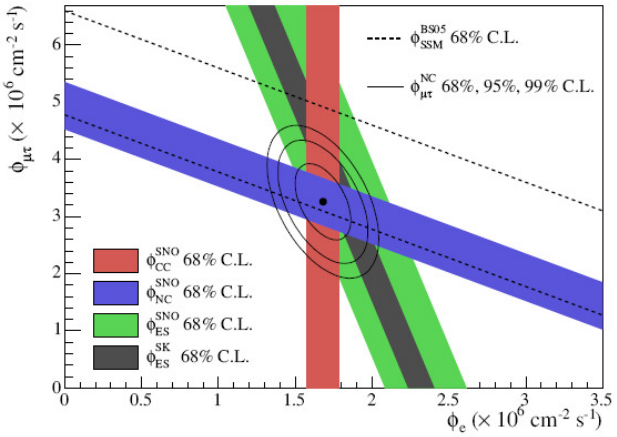

Figure 16. SNO results after Phase II. Combined flux of ν_μ and ν_τ versus ν_e. Black dot indicates the best fit point. The total ^{8}B solar neutrino flux predicted by the SSM is shown as dashed lines. The narrow band parallel to the SNO ES result corresponds to the Super-Kamiokande result [100]. The figure is taken from[21].

The combined $\nu_{\mu\tau}$ flux versus ν_e flux is shown. The results are as follows [21]:

$$\Phi_{CC} = 1.68 \pm 0.06^{+0.08}_{-0.09} \times 10^6 \, cm^{-2} s^{-1}$$
$$\Phi_{NC} = 4.94 \pm 0.21^{+0.38}_{-0.34} \times 10^6 \, cm^{-2} s^{-1}$$
$$\Phi_{ES} = 2.35 \pm 0.22 \pm 0.15 \times 10^6 \, cm^{-2} s^{-1}$$

The Φ_{NC} flux agreed with SNN expectations while Φ_{CC} and Φ_{ES} were smaller than expected. Clearly, a deficit in electron neutrino flux is observed. Presented results can be used to determine oscillation angle via determination of average survival probability (Φ_{CC}/Φ_{NC}). The Deficit in electron neutrino flux and observed non-zero value of combined $\nu_{\mu\tau}$ flux are interpreted as a result of the MSW-enhanced oscillation inside the Sun. Results from all three phases, in phase III an array of proportional counters was deployed in the heavy water, showing the two-flavor oscillation contour are presented in the Figure 17.

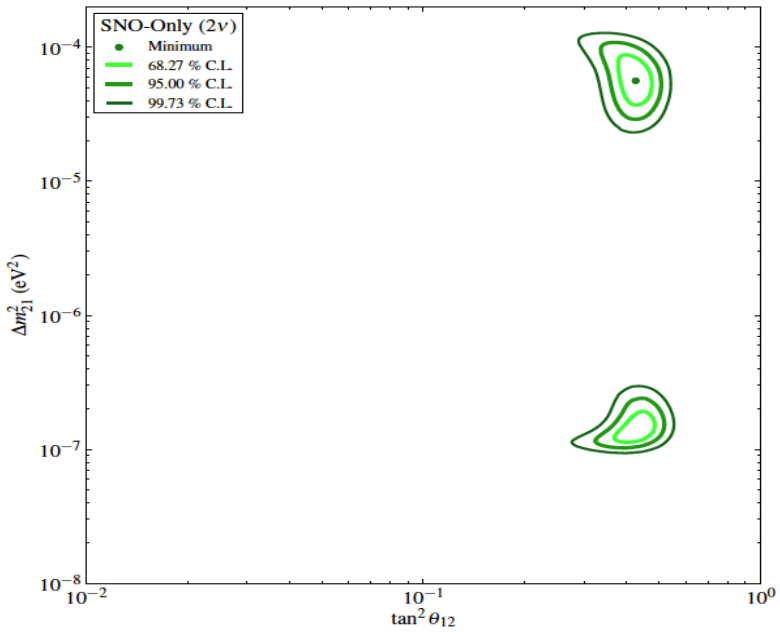

Figure 17. Two-flavor neutrino oscillation analysis contour obtained from the combined the SNO data of all three phases [23].

SNO data cannot distinguish between the upper and bottom region. The combination of the SNO results with the results of the other solar neutrino experiments eliminates the bottom region and higher values of Δm^2_{21} in the upper region. The other constrains for the allowed region come from the reactor neutrino experiments.

3.2.4 Reactor neutrino experiments

One type of the reactor neutrino experiments is a long baseline (L ~ 100 km) experiment. The interpretation of solar neutrino observations implies that oscillation of electron antineutrinos should appear after the distance larger than a hundred kilometers (CPT invariance assumed). The Kamioka Liquid Scintillator Anti-Neutrino Detector (KamLand) in Japan is an example of the long baseline reactor experiment [92]. The antineutrinos coming from nuclear reactors in the region (53 power plants in Japan and Korea) have energy, of the order of a few MeV, similar to the energy of the solar neutrinos. The detection technique is based on the inverse beta decay process:

$$\bar{\nu}_e + p \rightarrow e^+ + n$$

The KamLAND detector is a spherical plastic balloon filled with oil mixed with liquid scintillator and surrounded by photomultiplier tubes. It consists of about a kiloton of scintillator allowing for low energy detection thresholds of a few MeV. An effective

background rejection allowed the threshold for observing a neutrino to reach 1.8 MeV in the last phase of the experiment. The KamLAND was the first experiment that observed reactor neutrino oscillation. A global fit to both the solar and KamLAND data strongly constrains the oscillation parameters (Figure 18).

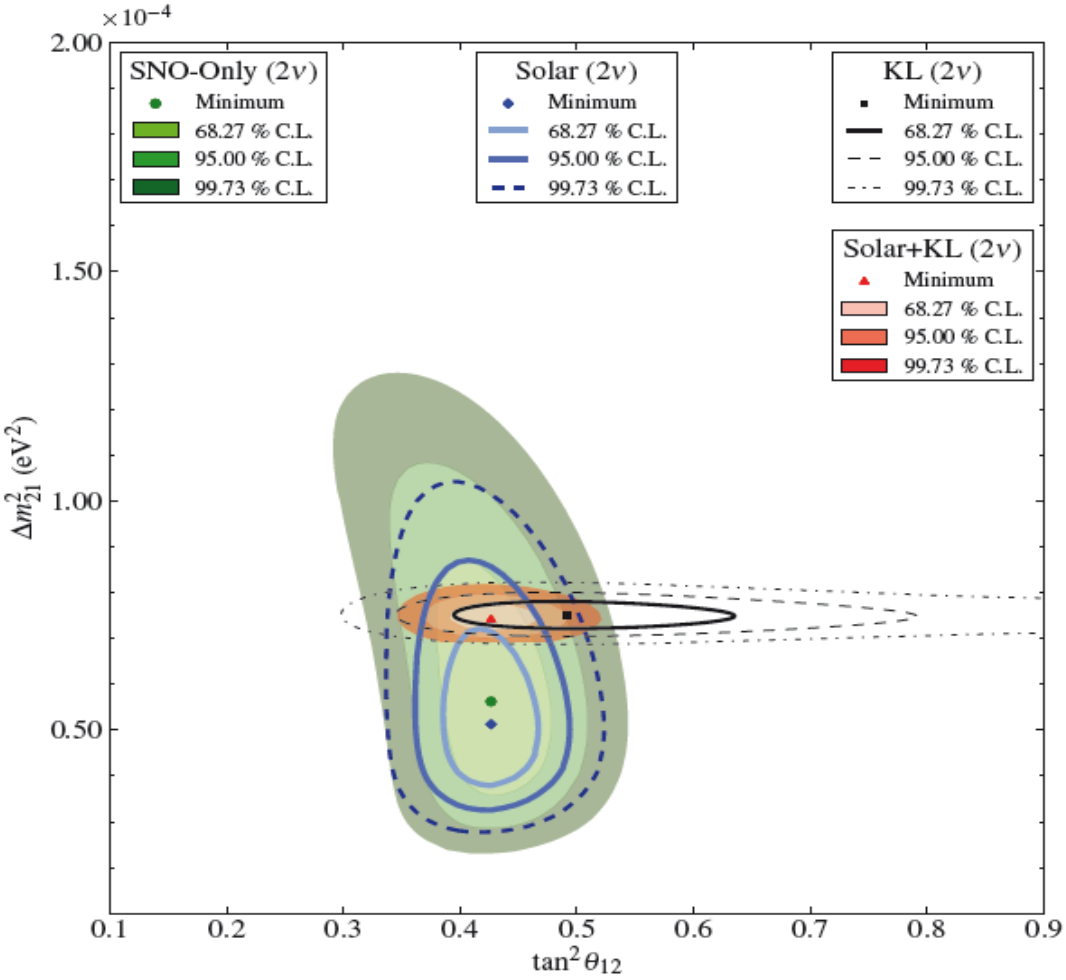

Figure 18. Two-flavor neutrino oscillation analysis contour using both solar neutrino and KamLAND results [23].

The second type of the reactor experiments is a short baseline experiment (L ~ 1 km) that looks for suppression of anti electron neutrinos. The atmospheric neutrino results and solar neutrino results imply oscillation of the νe → νx type at the Δm^2_{atm} region. No evidence of such an oscillation has been found before June 2012. In the region of $\Delta m^2 > 3*10\text{-}3eV^2$ an upper limit was found to be equal $\sin^2 2\theta < 0.1$ at 90% CL [41, 88] by the CHOOZ collaboration. The CHOOZ experiment is based on the liquid scintillator technique. The observed ratio of measured $\bar{\nu}_e$ versus the expected ones in the CHOOZ experiment was equal to 1.01 ± 2.8% (stat) ± 2.7% (sys). The CHOOZ null oscillation result was combined with other atmospheric and long baseline accelerator experiments. As a result, the upper limit on θ_{13} was found. The search was continued by the Double-Chooz experiment [42]. The recent results from the Double-Chooz, Daya Bay, and Reno experiments have shown that oscillation angle θ_{13} is none-zero with 3.1 σ, 5.2 σ, 4.9 σ, respectively.

3.3 Principles of the long baseline oscillation neutrino experiment measurements

The long baseline neutrino oscillation experiments are based on the basic idea to sample unoscillated neutrino beam close to the production point and at a few hundred kilometers when oscillations are apparent. This basic idea is shown by simple graph in Figure 19.

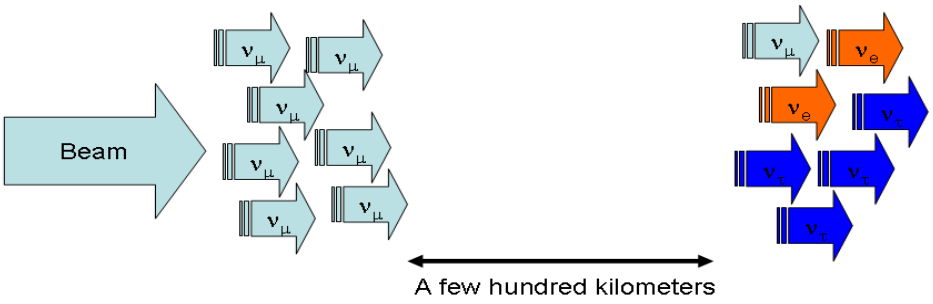

Figure 19. Schematic view of the idea of the long baseline neutrino oscillation experiment. Own elaboration.

The distance from the near to the far detector (L) is chosen accordingly to maximize oscillation probability. The second parameter, which can be used, is a neutrino energy (E). To be able to measure neutrino oscillations in long baseline experiment one needs to tune L/E ratio to maximize oscillation probability for a neutrino scale which is going to be studied (Δm^2). For example, to study neutrino oscillations from solar neutrino scale (Δm^2 ~10^{-4} eV^2) with neutrino beam with maximum energy ~1 GeV, baseline would need to be of order of the Earth's diameter. To study atmospheric neutrino scale (Δm^2 ~2.5 * 10^{-3} eV^2) with the same neutrino beam baseline of a few hundreds of km need to be used. For example for MINOS baseline is equal to 735 km, therefore for Δm^2 equal to 2.5 * 10^{-3} eV^2 oscillation maximum is achieved by neutrinos with energy equal to ~ 1.5 GeV. In the T2K experiment, the baseline is equal to 295 km, therefore in order to reach the oscillation maximum neutrinos need to have 0.7 GeV.
The parameters of the five main long baseline neutrino oscillation experiments are presented in Table 6.

Experiment	Data taking period	Neutrino energy peak	Baseline
K2K	1999 – 2004	1.4 GeV	250 km
MINOS	2005 – 2011	3 GeV	735 km
OPERA	2008 –	17 GeV	735 km
T2K	2010 – March 2011 (interrupted due to earthquake); restart in January 2012 –	0.7 GeV	259 km
NOνA	2013 – (construction will be complete in January 2014) - first run will last 6 years	1.8 GeV	810 km

Table 6. Parameters of the five main long baseline neutrino oscillation experiments.

The conventional neutrino beam production is described in chapter 4.

In the long baseline neutrino oscillation experiments, neutrinos are measured in near and far positions. There are two approaches used in the construction of detectors:

- near and far detectors are functionally identical e.g the MINOS experiment
- near and far detectors are different e.g the T2K experiment.

The first approach leads to a significant cancelation of systematic errors. In the second approach more precise measurement can be done due to possibility of using a set of different sub-detectors.

Even in the absence of oscillations, near and far detector neutrino spectra are different. However, in this case the difference is well understood. The near detector sees beam in a different way (relatively wide range of decay angles) than the far detector (only small range of angles). If a neutrino source would be point like and isotropic, the far-to-near ratio would be energy independent and given by the solid angle. In the real life this is not the case, the far-to-near ratio is complicated and depends on the neutrino energy. The discussion about knowledge of the far-to-near ratio is presented in chapter 5.2. The oscillation parameters can be probed by comparison of information measured in the far detector and information transformed from the near to far detector without oscillations.

This approach can be summarized as follows:

$$\Phi^{Far}(E_\nu)^{without\ oscillations} * \sigma = R\ (E_\nu)^{without\ oscillations} * \Phi^{Near}(E_\nu) * \sigma$$

where $\Phi^{Far}(E_\nu)^{without\ oscillations} * \sigma$ is an expected number of events in the far detector without oscillations (flux * cross section), and $R\ (E_\nu)^{without\ oscillations}$ is a far-to-near ratio, and $\Phi^{Near}(E_\nu) * \sigma$ is a number of events measured in the near detector;

then oscillation parameters can be found from comparison of number of events registered in the far detector and number of events expected in the far detector without oscillations: $\Phi^{Far}(E_\nu) * \sigma / \Phi^{Far}(E_\nu)^{without\ oscillations} * \sigma$

where $\Phi^{Far}(E_\nu) * \sigma$ is a number of events registered in the far detector.

This approach is valid for all oscillation analyses: disappearance and appearance approaches. From this ratio one can find information about $|\Delta m^2|$ by looking at the position of the minimum and about $\sin^2 2\theta$ by looking at the depth of the minimum (see Figure 20).

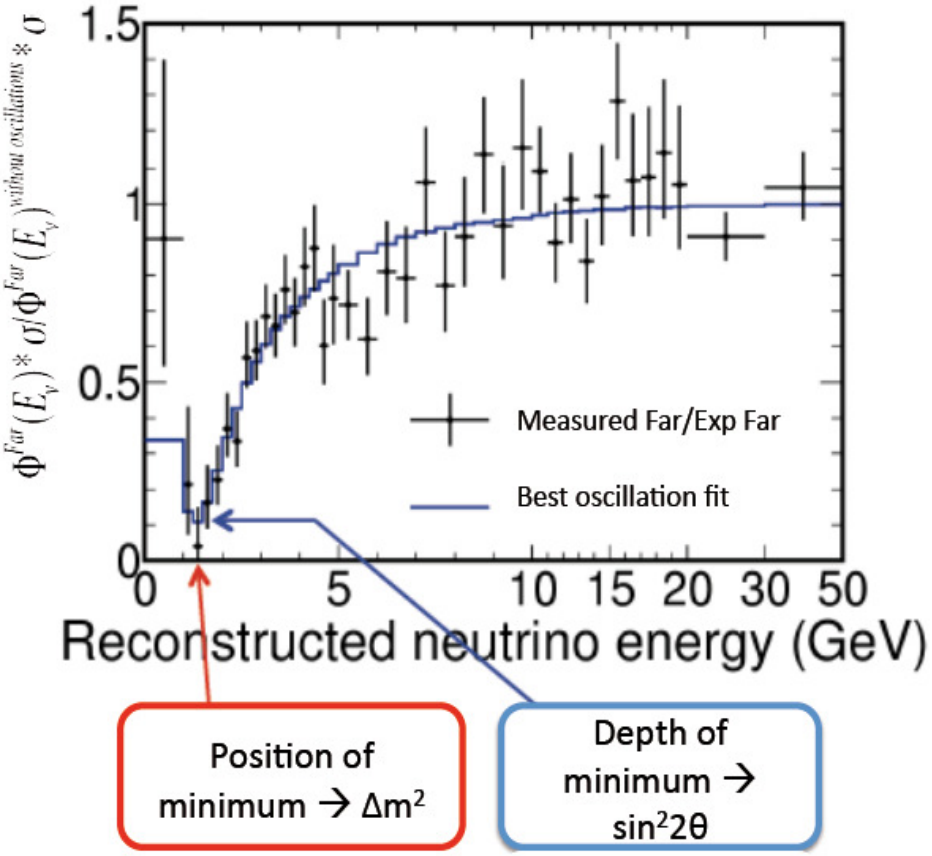

Figure 20. Possible evaluation of oscillation parameters from comparison of measured information in far detector and extrapolated information measured in near detector to far detector without oscillations. Ratio equal to one means no oscillations. Own elaboration based on the picture from [105], points and oscillation fit from the real experiment – MINOS.

Main uncertainties in the long baseline neutrino oscillation experiments come from:

- poor knowledge of hadron production in target (mainly pion and kaon multiplicities),
- cross sections modeling,
- proton beam,
- beam direction,
- target and focusing system alignment.

Near and far detector specific systematic error sources are also important but as it was mentioned, some cancelations can occur especially when near and far detectors are functionally identical. The point connected with hadron production in the target is the most important and has the largest contribution to the systematic error. This subject is discussed in chapter 5.2.

Chapter 4 Neutrino beams

In this chapter conventional neutrino beams are discussed. The future neutrino facilities like the Neutrino Factories [62] and Beta-beams [62, 172] are not the subject of this thesis and will not be discussed.

4.1 Conventional neutrino beams

Nowadays, accelerator experiments probe neutrino oscillation parameters by two types of approaches:

- Disappearance experiment – the search of muon neutrinos disappearance in muon neutrino beam.
- Appearance experiment – the search of other flavor neutrinos appearance in muon neutrino beam.

In both approaches, a precise knowledge of the muon neutrino beam is essential to minimize systematic uncertainties and obtain the assumed precision.

Conventional muon neutrino beams are produced using interactions of high energy protons on the nuclear targets. The idea of an accelerator neutrino beam was proposed independently by Schwartz [162] and Pontecorvo [153]. The first neutrino beam was used in experiment by Lederman, Schwartz, Steinberger and collaborators [86]. A schematic view of the first accelerator neutrino experiment is shown in Figure 21.

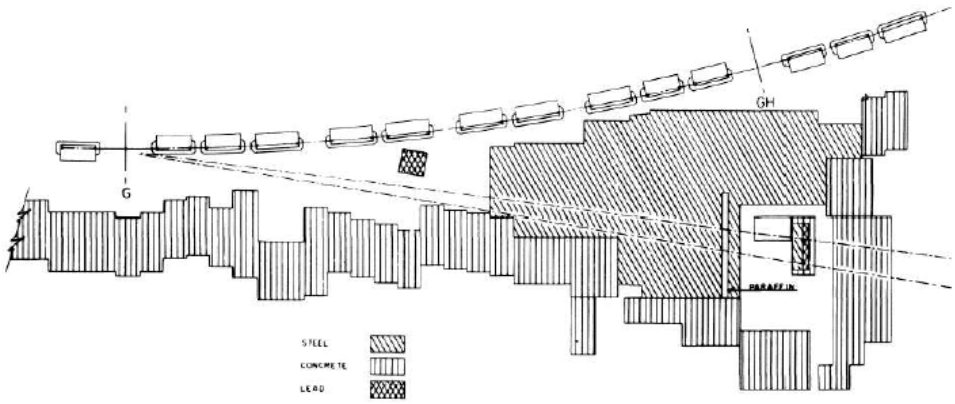

Figure 21. Schematic view of the first accelerator neutrino experiment [86].

The concept of operation of neutrino beams is based on interactions of protons with nuclear target from which secondary hadrons are produced that decay and as a consequence produce neutrinos. The decays of pions and kaons, which are listed below [110], mainly contribute to the production of conventional muon neutrino beams.

$\pi^{\pm} \rightarrow \mu^{\pm}\nu_{\mu}(\overline{\nu}_{\mu})$ with Branching Ratio (BR) = 99.9877 %
$\pi^{\pm} \rightarrow e^{\pm}\nu_{e}(\overline{\nu}_{e})$ with BR = 0.0123 %

$K^{\pm} \rightarrow \mu^{\pm}\nu_{\mu}(\overline{\nu}_{\mu})$ with BR = 63.55 %
$K^{\pm} \rightarrow \pi^{0}e^{\pm}\nu_{e}(\overline{\nu}_{e})$ with BR = 5.07 %
$K^{\pm} \rightarrow \mu^{\pm}\nu_{\mu}(\overline{\nu}_{\mu})$ with BR = 3.35 %

To achieve a huge precision in new long baseline oscillation neutrino experiments also neutral kaons and charged muons need to be taken into consideration. The leptonic decay channels of neutral kaons are listed below

$K_L^0 \to \pi^{\pm} e^{\mp} \nu_e(\bar{\nu}_e)$ with BR 40.55 %
$K_L^0 \to \pi^{\pm} \mu^{\mp} \nu_{\mu(}(\bar{\nu}_{\mu})$ with BR 27.04 %

and muon decay

$\mu^{\pm} \to e^{\pm} \nu_e(\bar{\nu}_e) \bar{\nu}_{\mu}(\nu_{\mu})$ with BR ≈ 100 %

The muon decays lead to rise of electron (anti-) neutrinos and muon (anti-) neutrinos what is rather unwanted background. The schematic view of the conventional neutrino beam production is presented in Figure 22.

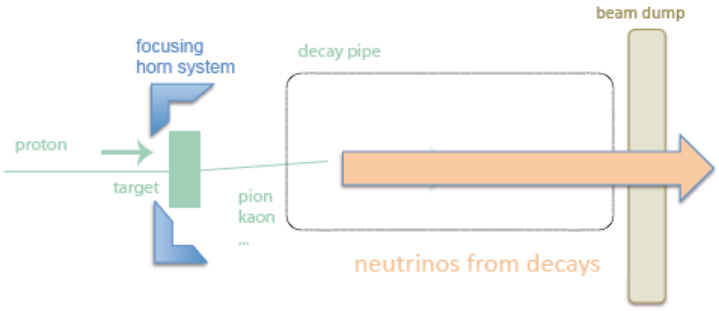

Figure 22. Schematic view of the conventional neutrino beam production. Own elaboration.

The manipulation of the secondary hadrons is in general made by magnetic horn(horns) that is(are) focusing positives (negatives) and defocusing negatives (positives). Therefore muon (anti-) neutrino flux is enhanced while muon antineutrino (neutrino) background is reduced. The first neutrino experiments were working in the "bare target beam" mode. It means that there were not any collimations of the secondaries emanating from the target. Simon van der Meer developed the idea of the "magnetic horn" in 1961 [168]. This focusing device was invented to collect the secondary pions and kaons from the target and directing them toward the downstream experiments, thereby increasing the neutrino flux. From 1961 horn systems were developed and various geometries were investigated: conical horns [169], parabolic horns [69], ellipsoidal lenses [57, 89], magnetic fingers [146]. The basis of magnetic horn lays in production of toroidal magnetic field whose $q\bar{v} \times \bar{B}$ force provides focusing force for particles of one sign and defocusing force for the other sign (see Figure 23). The toroidal magnetic field is produced between two axially symmetric conductors with a current sheet running down the inner conductor and returning on the outer conductor. The magnetic field of the horn varies inversely with radius $B = \mu_0 I/2\pi r$ (I is the horn current, r is radius). This results in a change in angle of

$$\Delta\theta = \frac{B\,x}{p} = \frac{\mu_0 I\,x}{2\pi\,r\,p}$$

, where x is the path length , I is the horn current, p is the particle momentum.

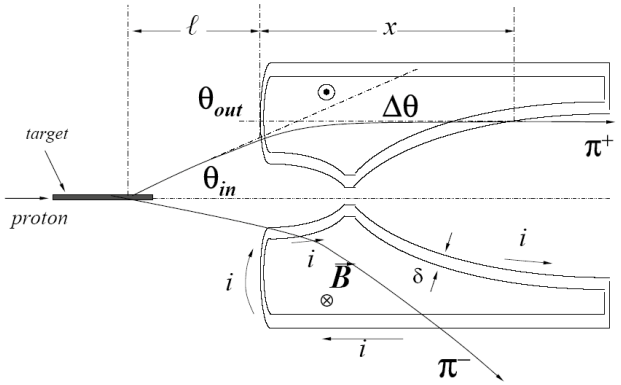

Figure 23. Focusing and defocusing of particles in magnetic horn. Toroidal magnetic field is produced between two axially-symmetric conductors with a a current sheet running down the inner conductor and returning on the outer conductor. The picture is taken from [169].

Horns must stand magnetic forces, thermal load from the pulsed current, and beam energy deposition in the horn conductors. The other possibility to focus neutrino beam is to use a so called Quadropole-focused beams which are relatively less expensive than horn systems but also less efficient. A single quadropole magnet produces an effect of focusing lens in one plane and defocusing in the other. Therefore, system of quadropoles is used (pairs or triplets). These systems focus both signs of secondaries. In experiments in which only one neutrino species is desired, sign selection of secondaries is done by dipole. Another option for focusing system is plasma lens based on the idea to place a cylindrical insulating vessel around the beam axis downstream of the target. In this device, the toroidal magnetic field is produced, similar to this produced in magnetis horn. One more option is to use DC-operated lenses like Magnetic Spokes [127] or Solenoid lens [56].

Nowadays, secondaries are focused by focusing system that is in general made from the set of two or more magnetic horns (in the T2K there is a set of three magnetic horns, the MINOS has two horns but in the MiniBoone there is only one horn). Palmer found that a set of horns allows refocusing particle trajectories improperly focused by the first focusing element [146]. First time this system was used at the CERN PS neutrino beam [47] and after that almost every Wide-Band Beam experiment has been using this type of system. Two horns focusing system is shown in Figure 24.

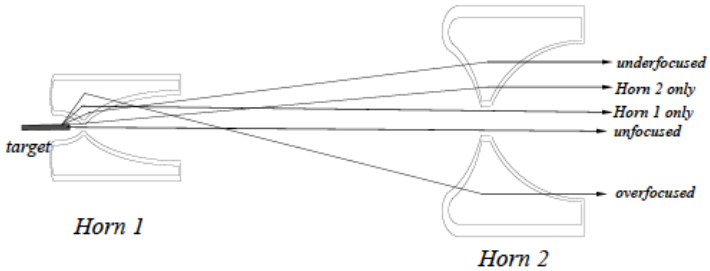

Figure 24. Two horns focusing system. Second horn, placed further from target than the first, improves the collection efficiency of particles over or unfocused by the first one [9].

The standard horn-focused beam produces a wide range of neutrino energies corresponding to a variety of particle trajectories passing through the magnetic horn (Figure 25).

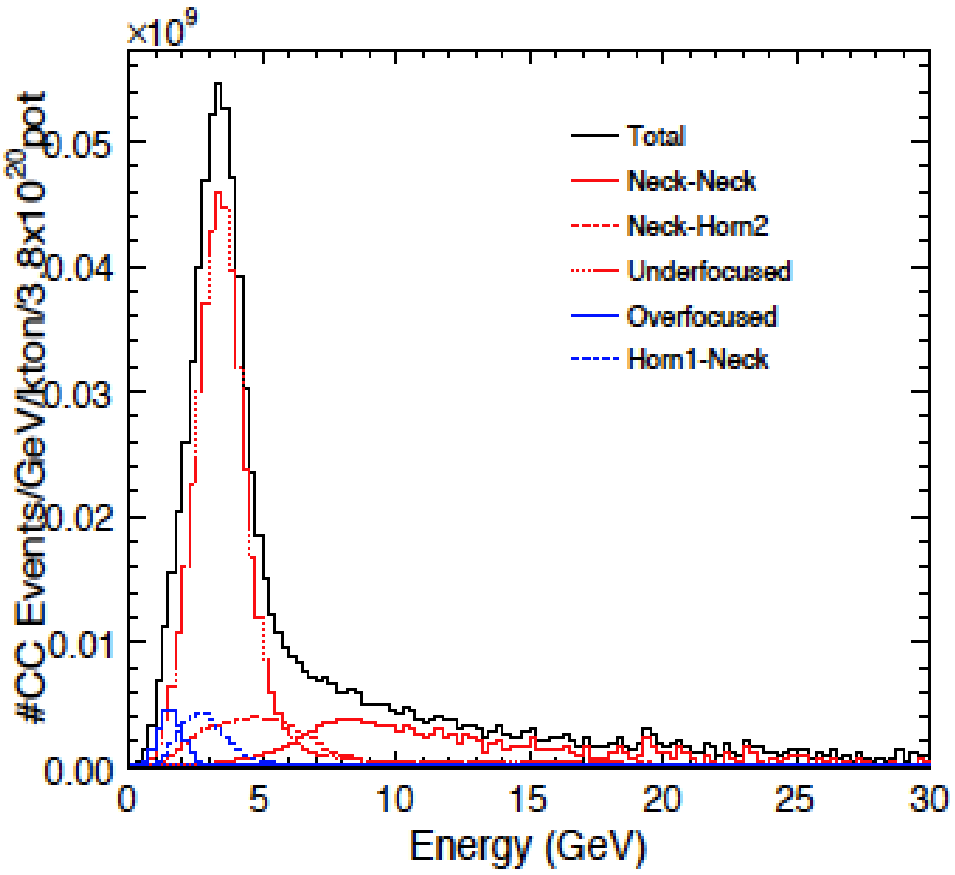

Figure 25. Neutrino spectrum from the standard two horn system beam at the NuMI at FNAL. The components of the spectrum correspond to the different particle trajectories. The possible trajectories are presented in Figure 23. The picture is taken from [149].

The focused secondaries are directed towards a decay volume (also called a decay pipe). The decay volume must be designed to minimize subsequent muon decays which implies larger unwanted νe contamination. Often, the decay volume is filled with helium gas to minimize multiple Coulomb scattering and reduce absorption. At the end of the decay pipe, a beam dump is located, which is absorbing hadrons that reached this point. In the T2K, the beam dump is made of graphite blocks cooled with water in aluminum pipes. In the MiniBoone, beam dump is made of steel. Apart from neutrinos, high energy muons can pass the beam dump. Therefore, in some cases muon monitors used to monitor the beam direction are located after the dump.

The energy of emitted neutrinos is related to the energy of secondaries which is shown in Figure 26 (for pion decay). In on-axis experiments, average neutrino energy is linearly related to the energy of secondaries. This relation is not as strong in off-axis experiments and the dependence is flatter.

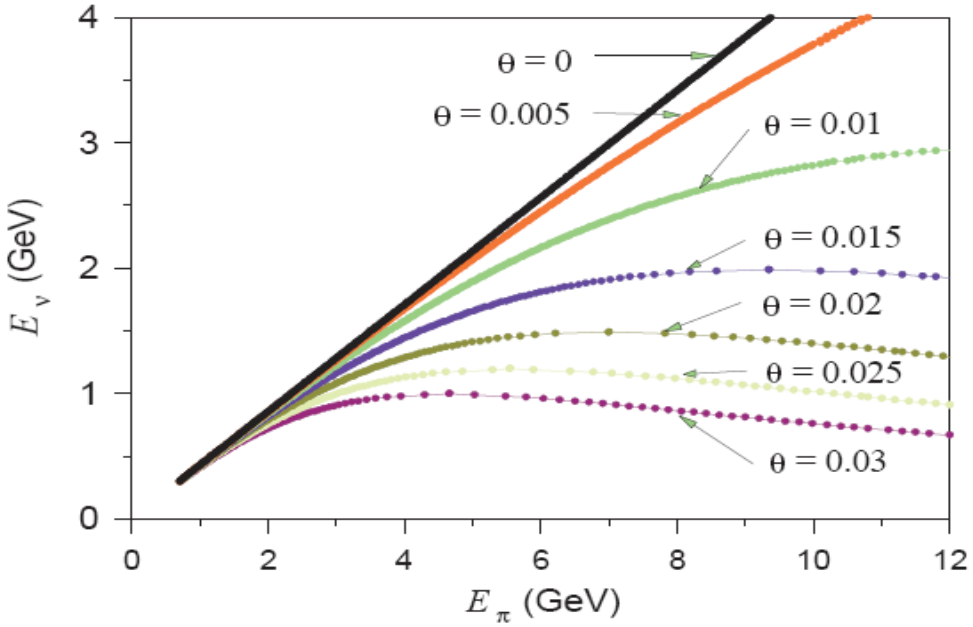

Figure 26. Neutrino energy as a function of energy of decaying pions [135]. The angle θ is an angle between pion direction and neutrino direction (in radians).

In off-axis experiments, change of the off-axis angle influences also the neutrino energy spectrum what is shown in Figure 27.

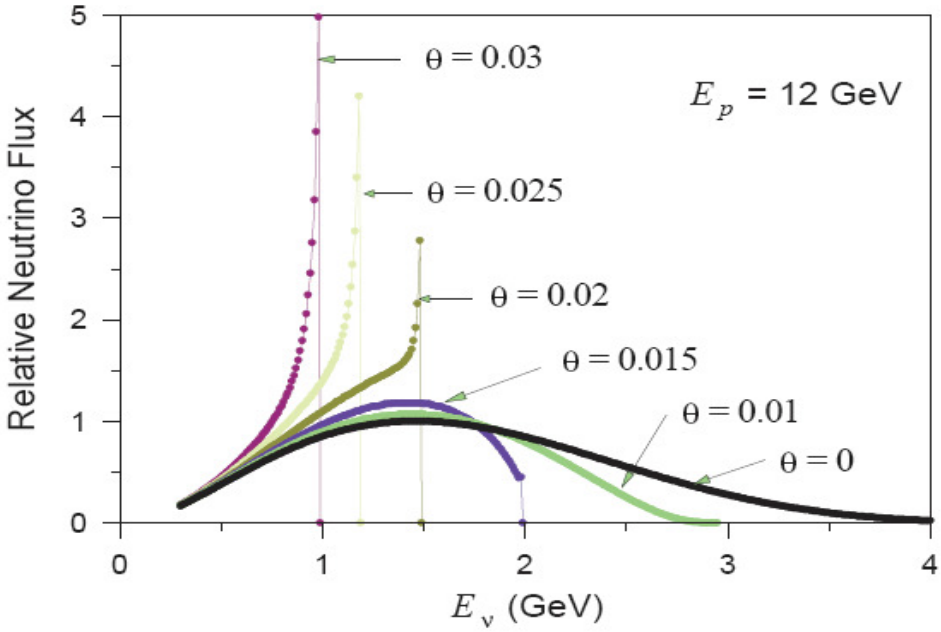

Figure 27. Neutrino fluxes integrated over all pion energies (simulations for proton energy of 12 GeV) [135]. The angle θ is an angle between pion direction and neutrino direction (in radians).

The off-axis setup allows generating a narrowband neutrino spectrum using a broadband secondary beam. This idea was first proposed by the BNL experiment E889 [58] and nowadays is used in the long baseline neutrino oscillation experiment T2K (will be used in

the N0νA as well). The farther one goes from the beam axis, the narrower neutrino beam one gets but the flux also became smaller. This two effects need to be taken into consideration when off-axis neutrino beam is designed.

Other options to produce a narrowband neutrino beam are:

- Dichromatic beam [130]

  The first beam of this type was used in the Fermilab, a schematic view is shown in Figure 28. In this approach, the dipole magnets were used to defocus wrong-sign secondaries while quadroploes were used to focus right-sign secondries as they head into the decay tunnel. The momentum of secondary beam is fixed but presence of pions and kaons leads to two possible values of the neutrino energy. Off-angle decays of pions and kaons lead to the change in neutrino energy.

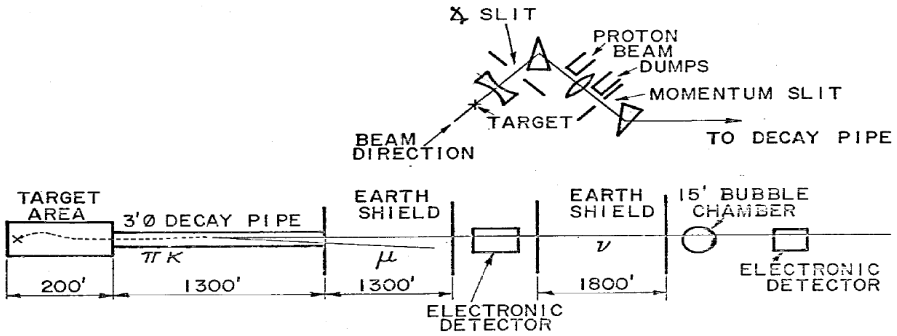

Figure 28. Schematic view of the first di-chromatic neutrino beam at Fermilab [52].

- Horn beam with plug [147]

  This approach uses a Tungsten block (beam "plug") at the end of the target to eliminate those particles, which travels, through the field free area of horns. This cuts off the largest range of neutrinos energies (different components of the neutrino spectrum are shown in Figure 25). The horn beam with plug system was developed in a series of experiments at the BNL. The system of two beam plugs and collimator was developed. Such a setup has the effect of eliminating those particles that do not cross the beam center line. As a consequence, only the smallest momenta are not cut out. The similar setup was made at the Fermilab.

- Horn beam with dipole [9]

  In this setup a dipole magnet placed between the two horns increases momentum and sign selection efficiency. In this approach, a dump for the primary beam must be placed in the target hall. This is a huge challenge for high-intensity neutrino beams.

Different sources of uncertainties for conventional neutrino beams are discussed in chapter 5.2 .

Chapter 5 Main background sources for long baseline neutrino oscillation experiments

5.1 Background sources for measurement of neutrino interaction

The detection technique used implies which background sources need to be considered. Mainly three detection techniques are considered in future neutrino oscillation experiments:

- Water Cherenkov detectors
- Liquid scintillator detectors
- Liquid Argon Time Projection Chamber (LArTPC) detection technology
- Sandwitch-like detectors (combining different types of detection technologies, e.g. MINOS)

In the T2K experiment main measurements will be done in the far detector – huge water Cherenkov Super-Kamiokande (SK) detector. Second very promising technique is detection in LArTPC, which is used in the ICARUS detector. In this chapter detection techniques and background processes for measurement of neutrino interaction in the SK and ICARUS detectors are discussed. This thesis is not covering detection technique based on the Liquid scintillator. The sandwitch-like detectors are also not discussed in this thesis.

Neutrino interactions with matter are well described by the Standard Model. Neutrinos are electrically neutral leptons therefore they interact only weakly with other particles. One can distinguish two types of interactions: charge current exchange (when $W^{\pm}$ bosons are exchanged) and neutral current exchange (when Z^0 is exchanged). Depending on the detection technique used different neutrino interactions can be explored.

5.1.1 Water Cherenkov

The basis of detection is based on the fact that the relativistic charged products of neutrino interactions produce Cherenkov light. This light can be detected by photomultipliers (PMTs).

The Super-Kamiokande is a 50 kiloton ring-imaging water Cherenkov detector located underground in the Kamioka-mine, Hida-city, Gifu, Japan. The location 1 km underground (2700 m of water equivalent) provides very good shielding from cosmic ray particles except from highest energy muons (minimum of 1.3 TeV is needed for penetration). The wall of the cave is covered by polyurethane material, which blocks radon emanating from the rock. The layout of the detector is presented in Figure 29.

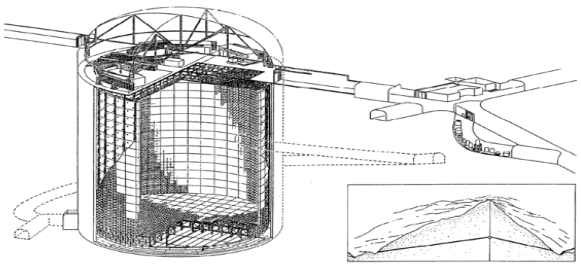

Figure 29. Schematic view of the Super-Kamiokande detector [144].

The detector is a cylindrical, vertically oriented, stainless steel tank of 39.3 m in diameter and 41.4 m in height, containing 50 kilotons of water. The water tank is made of stainless steel. It is divided into an outer part and an inner part. The 11146 20-inch photomultipliers (PMTs) in the inner detector and 1885 8-inch PMTs in the outer detector are used for the light detection. Selected parameters of the Super-Kamiokande detector are presented in Table 7.

Tank	Dimensions Volume	39.3 m in diameter 41.4 m in height 50 kton
Outer part	Thickness Volume Num. of PMT	2.6 m (7.2 Radiation Length (R.L) and 4.3 Nuclear interaction Length (N.L) on top and bottom 2.75 m (7.6 R.L. and 4.6 N.L.) on barrel 32 kton 302 (top), 308 (bottom) and 1275 (barrel)
Inner part	Dimensions Volume Num. of PMT	33.8 m in diameter 36.2 m in height 18 kton 1748 (top and bottom) and 7650 (barrel)
Fiducial area	Thickness Volume	2 m (5.5 R.L. and 3.3 N.L.) from the inner wall 22 kton

Table 7. Selected parameters of the Super-Kamiokande detector [144].

In this type of detector, muon neutrino and electron neutrino charged current interactions can be distinguished through capability of discrimination between electron and muon specific light patterns detected by the set of photomultipliers. Typical muon like and electron like rings detected by the Super-Kamiokande are presented in Figure 30. The shape of a ring identifies a particle. Two classes of particles can be recognized in the Super-Kamiokande: e-like particles – electrons and gamma rays, and μ-like particles – muons and charged pions.

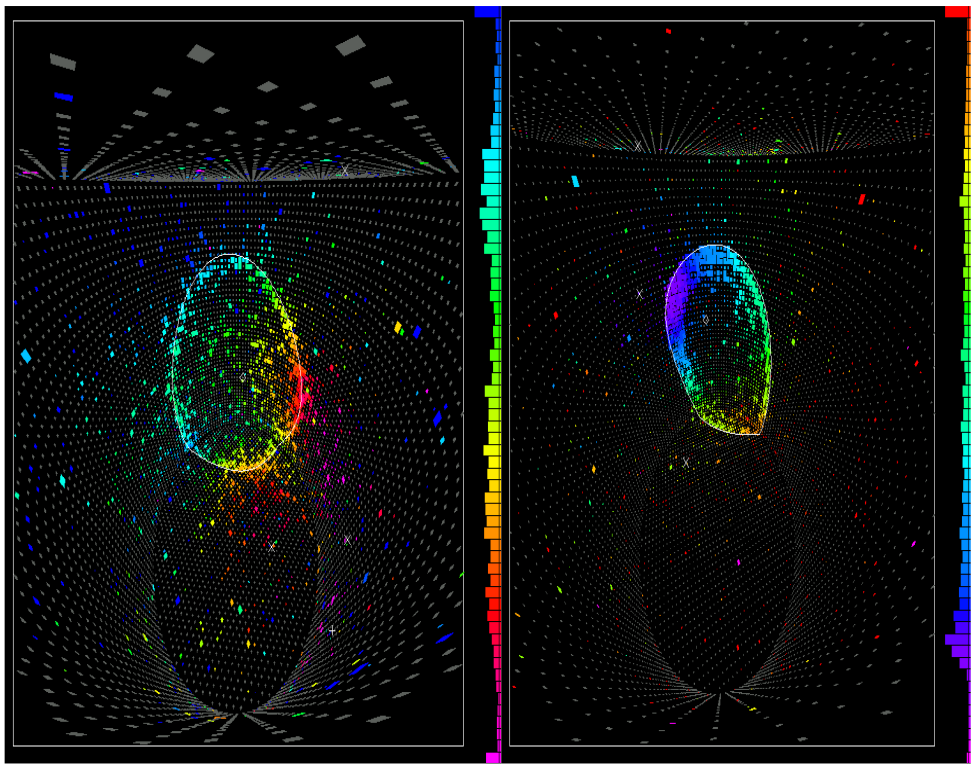

Figure 30. Typical electron like (left) and muon like (right) rings registered by the Super Kamiokande detector [48].

The neutrino elastic NC scattering (NCE) interaction, which can be written by equation:

$\nu + N \rightarrow \nu + N$

(where N is a nucleon),

is usually undetectable in water Cherenkov detectors (outgoing protons do not have a sufficient amount of momentum to be visible and neutrons are undetectable).

In case of the long baseline neutrino oscillation experiment like T2K, two processes are important, as they constitute signal in electron neutrino appearance and muon neutrino disappearance approaches.

These are:

- Electron neutrino charge current quasi-elastic interaction (CCQE) which leads to production of a single electron that tags electron neutrino interaction in Super-Kamiokande:
  $\nu_e + n \rightarrow e^- + p$
- Muon neutrino charge current quasi-elastic interaction (CCQE) which leads to production of a single muon that tags muon neutrino interaction in Super-Kamiokande:
  $\nu_\mu + n \rightarrow \mu^- + p$

For neutrino energies from 1 GeV up to a few GeV the neutrino scattering off nucleons with production of resonances (RES) becomes important:

$$NC : \nu + N \rightarrow \nu + r^* \rightarrow \nu + N' + meson(s)$$

$$CC : \nu + N \rightarrow l + r^* \rightarrow l + N' + meson(s)$$

where N is a nucleon, l a lepton and r* is a resonance.

- Coherent scattering off whole nuclei (COH) is a situation in which neutrino interacts with a target nucleus as a whole leaving the nucleus in the initial ground state. It usually results in production of a forward-going lepton and meson (most likely pion). Both RES and COH processes are important as they are a source of pions, that constitute one of the main backgrounds to oscillation signal in water Cherenkov detectors.
- Deep inelastic scattering (DIS) interactions dominates for neutrino energies higher than several GeV.

The main source of background for the electron neutrino appearance in water Cherenkov detectors is muon neutrino neutral current scattering with neutral pion production. This interaction looks like this:

$\nu_\mu + N \rightarrow \nu_\mu + N + \pi^0 + n \times \pi^\pm$

where n >= 0.

A π^0 in 98.8% of cases quickly decays into two gammas and these in turn initiate electromagnetic cascades. Similar cascade is produced when electron is passing through detector medium. When two gamma showers overlap or one is not detected this can lead to misidentification of NC π^0 production as a CCQE event. If π^0 decayed via the Dalitz decay to photon and electron-positron pair this also can lead to similar topology as for the charge current electron nutrino interaction.

The main source of background of the muon neutrino disappearance in water Cherenkov detectors is muon neutral current scattering with positive pion production. This interaction looks like:

$$\nu_\mu + p \rightarrow \nu_\mu + n + \pi^+$$

This is a specific background source for water Cherenkov detector because in this detection technique it is very hard to distinguish between muons and pions (μ-like particles).

5.1.2 Liquid Argon

The ICARUS is the only large Liquid Argon (LAr) Time Projection Chamber (TPC) detector working at present located underground in Gran Sasso, Italy. The LAr TPC concept was proposed by C. Rubia in 1977 [156]. The T600 ICARUS detector is composed of two identical modules with a common cathode placed in the middle. The electric field shaping system, LAr purity monitors, and PMTs are enclosed in each module. LAr temperature is stabilized by external thermal insulation and Liquid Nitrogen circuit. The LAr purification system is used to achieve required purity which is controlled by monitors. Dimensions of each module are 3.6 m (width), 3.9 m (height) and 19.9 m (length). Three parallel planes (two Induction and one Collection plane) of anod wires are placed along the longest sidewalls of each module. Wires are oriented at 60° with respect to each other. Total number of wires is 53248 in each module. The volume of LAr in the detector is 760 tons. The LAr TPC provides calorimetric measurement of particle energy together with three-dimensional track reconstruction from the electrons drifting along electric field lines in sufficiently pure LAr. A schematic view of working principle of detection is shown in Figure 31.

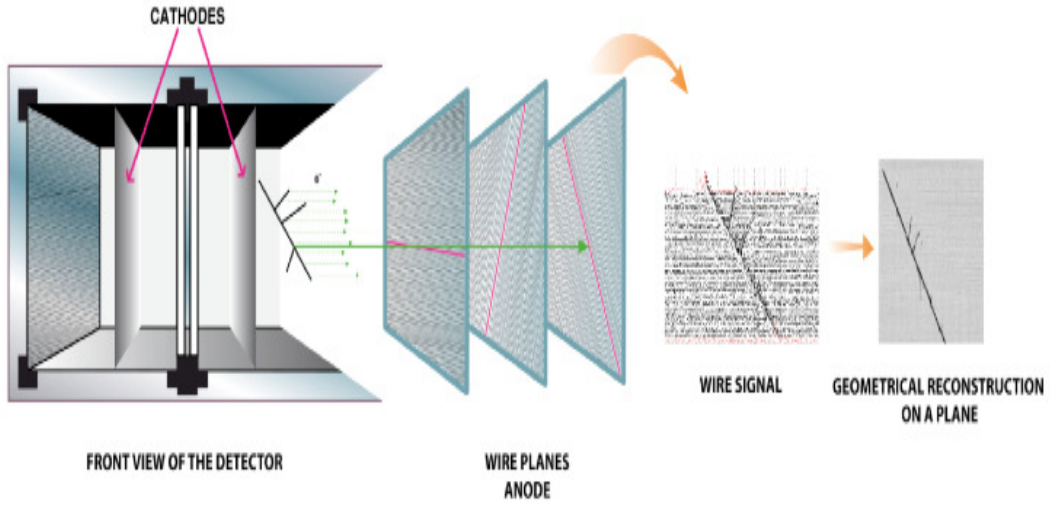

Figure 31. Principle of detection in the ICARUS T600 Lar TPC [158].

In order to distinguish ν_e charge current from the ν_μ neutral current interaction good separation between electrons and pions is needed. To check the potentiality of the LAr technique in respect to distinguish between photon-induced showers from π^0 decay and the electron showers from electron neutrino interactions simulations using the NUX-FLUKA chain were done. Apart from that, real data from the surface test run were studied. The measured distribution of the two photon invariant mass from real data is shown in Figure 32.

In case of a few pions in the event, photon pairs with minimum χ^2 of the difference between reconstructed two photon invariant mass and the real π^0 mass were chosen.

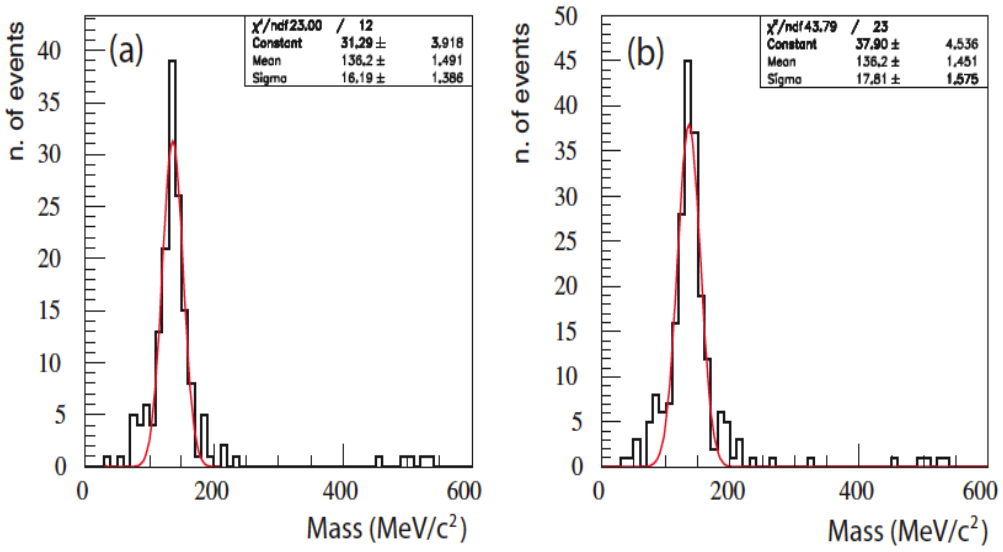

Figure 32. Two photon invariant mass spectrum from muon neutrino NC events. One pion events (left – a), all pion events (right – b). Pions from primary and secondary verteces are included. The emision of 5 η(547) mesons was found and its masses were properly reconstructed. The picture is taken from [157].

The position of the peak in reconstructed two photon invariant mass spectrum was found to be consistent with π^0 mass. The width of the peak is similar to the one obtained for the real data (measurement based on the 212 selected events from the surface test run) [157]. The tails of the invariant mass distribution come from π^0s emitted from secondary vertices (Λ or K meson decays) close to the primary one. If distance between primary and secondary vertex is smaller than 1 cm that allows distinguishing between them due to good special resolution what is not the case in water or sandwich-like detectors.

In the LAr TPC detector an NC ν_μ event with π^0 production can be misidentified with CC ν_e interaction if one from the following situations occurs:

- One of the photons has too small energy (E<20 MeV) and therefore is lost in the background. The calculation based on the decay kinematics showed that percentage of such events never exceeds 2.5%.
- The two photons overlap. Only for π^0 energy up to about 1 GeV the angle between two showers is sufficiently large to indentify two showers. However, for the more energetic pion decays it is possible to use dE/dx method to distinguish between the beginning of the electron track and beginning of the lepton pair from the conversion of photon [165].
- One photon is lost due to either Dalitz decay or photon conversion near the neutrino interaction vertex. This contribution was estimated to be at the level of one per mil.

The author made simulations, scanning, and analysis of electromagnetic showers indicated by electrons and photons (using the NUX-FLUKA) from which energy resolution of showers was obtained. The author was also involved in scanning of real events from the 2001 Pavia surface test run.

5.2 Systematic errors related to knowledge of conventional neutrino beam production.

In the analysis technique used in long baseline neutrino oscillation experiments, neutrino oscillation parameters are probed by comparing interaction rates at far detectors with predictions with and without oscillations. The extrapolation of measurements in near detectors is done by so-called far-to-near ratio, which strongly depends on the knowledge of the primary hadron production in the target. Far-to-near ratios (in ν_e and ν_μ case) predicted by JNUBEAM simulations (used in the T2K experiment) and their ratios are presented in Figure 33.

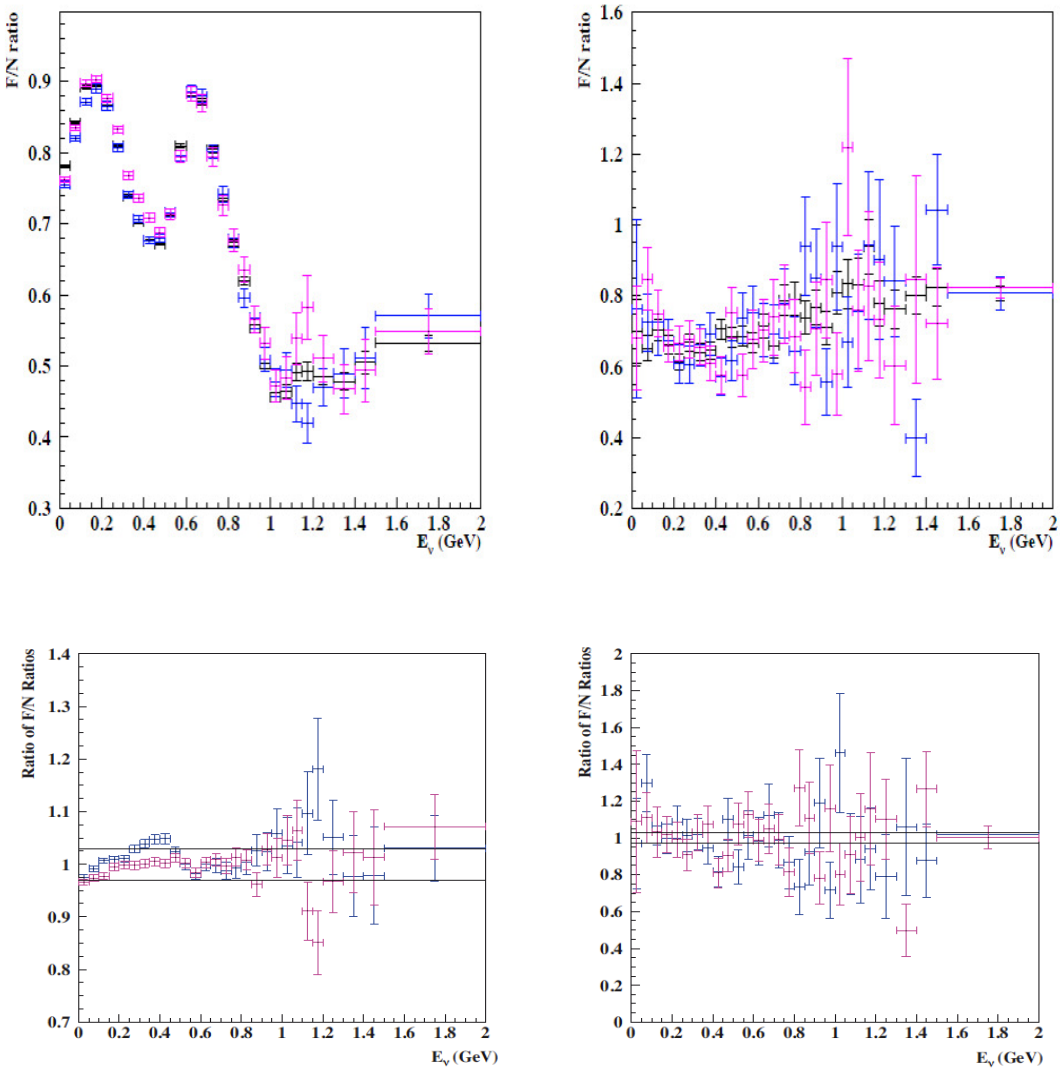

Figure 33. Top panels: Far-to-near ratios predicted by JNUBEAM simulations (GCALOR – black, GFLUKA – pink, GHEISHA – blue); Bottom panels: Ratio of far-to-near ratios predicted by GHEISHA with respect to GCALOR (blue) and GFLUKA with respect to GCALOR (purple). Left panels for νμ case. Right panel for νe case. The horizontal lines show ±3% band. The pictures are taken from [4].

The far-to-near ratios have non-trivial dependence on neutrino energy, especially in low energy region below 1GeV/c, which is very important for the T2K experiment. This feature will not be as important for the new planned NOνA experiment because it will have neutrino energy peak at 1.8 GeV/c. From the bottom panels of the Figure 33 it clearly visible that even for the NOνA experiment it will not be possible to reach precision of the far-to-near ratio knowledge at the level of a few percents without independent measurements of the pion and kaon production (which will lead to accurate far-to-near ratio estimation). For example, T2K measurements are strongly correlated with the far-to-near ratio knowledge. From the Monte Carlo studies, it was shown that the far-to-near ratio needs to be known at the level of around 3% [122] to reach the assumed precision.

The precision of far-to-near ratio estimation is the most important source of systematic uncertainty connected with knowledge of conventional neutrino beam production.

The conventional neutrino beams are produced in such a way that not only one type of neutrinos is produced. The contamination of unwanted neutrino species in produced neutrino beam is also one of the sources of the systematic error. Nowadays, very precise and stable focusing systems are used what allows minimizing unwanted background. In the T2K experiment detailed studies of neutrino parent decays were done. The $\overline{\nu}_\mu, \nu_e, and\ \overline{\nu}_e$ fluxes are 7.0%, ~1.1%, and ~0.17% of the ν_μ flux respectively.

Chapter 6 NA61/SHINE experiment

6.1 Main goals of the NA61/SHINE experiment

The NA61/SHINE (Super proton synchrotron Heavy Ion and Neutrino Experiment) experiment is a large acceptance hadron spectrometer, which was designed to study three different physics fields [39, 40, 5, 6]:

6.1.1 Study of the onset of deconfinment and search for critical point of strongly interacting matter.

Results from the CERN SPS scan program on the energy dependence of hadron production in central Pb+Pb collisions at various energies from 20A to 158A GeV show some hints for the evidence of the existence of a transition to a new form of strongly interacting matter (Quark Gluon Plasma (QGP)). At the top SPS [117, 155, 134, 60] and RHIC [44, 49, 11, 13] energies created at the early stage of central Pb+Pb (Au+Au) collisions, matter is in the state of QGP. For the central Pb+Pb (Au+Au) measurements, a few anomalies were found in distributions of energy dependence of hadron production in relation to p+p data, what is shown in Figure 34.

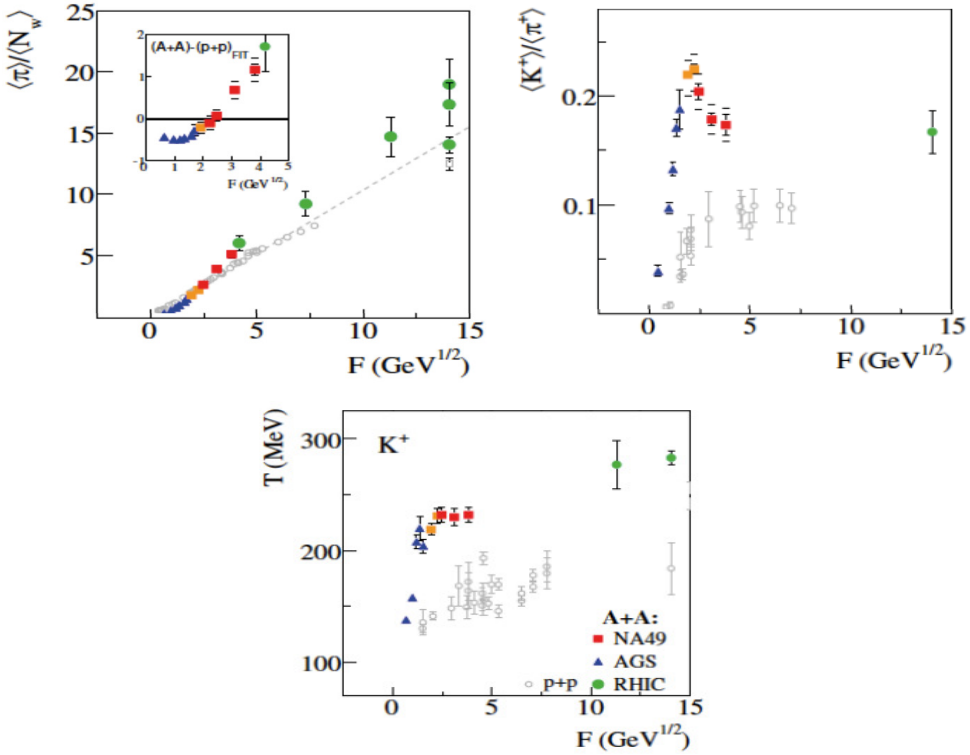

Figure 34. Energy dependence of hadron production properties in central Pb+Pb (Au+Au) collisions (closed symbols) and p+p interactions (open symbols). Mean pion multiplicity per wounded nucleon (left top panel), the relative strangeness production (bottom panel), the inverse slope parameter of m_T spectra of K^- mesons (right top panel). The pictures are taken from [39].

The models without assumed deconfinement phase transition (HGM [80], RQMD [164], UrQMD [55], and HSD [73]) failed to describe central Pb+Pb (Au+Au) data. Models reproduce anomalies when the 1st order phase transition at low SPS energies is introduced (SMES [106] and hydro [109, 107]). The results on energy dependence of hadron production from the central Pb+Pb (Au+Au) collisions are shown in Figure 35.

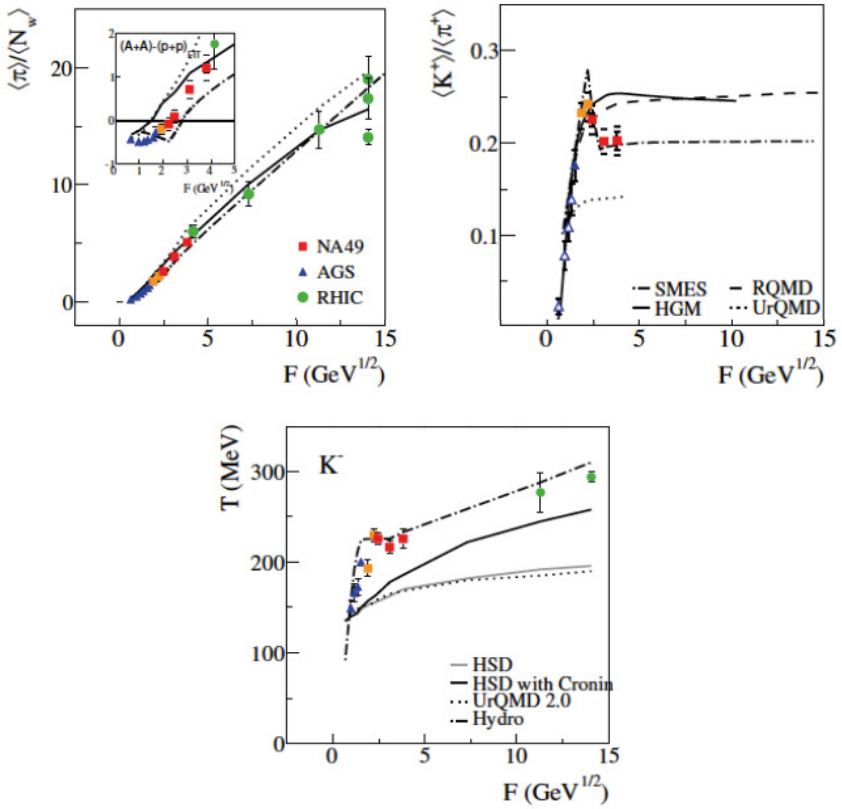

Figure 35. Energy dependence of hadron production properties in central Pb+Pb (Au+Au) collisions with model comparison. Mean pion multiplicity per wounded nucleon (top left panel), the relative strangeness production (bottom panel), the inverse slope parameter of m_T spectra of K^- mesons (top right panel). The pictures are taken from [39].

There are ongoing attempts to model-dependent extrapolation of proton-nucleus to explain nucleus-nucleus collisions [82]. The set of detailed p+A data is very important to model properly this extrapolation. In these studies one need to take into account that qualitative statements on similarities or differences between p+A and A+A collisions can be done only if all kinematic effects are taken into account. Recent string-hadronic models [164, 55, 73] considered all these effects and are able to parameterize reasonably well p+p and p+A data. Nevertheless, A+A data are not modeled properly in these models.

The existence and exact location of the critical point of strongly interacting matter can be searched by measurements of hadron production with different energies and system sizes. Critical point, if exists, should appears as a maximum of fluctuations of the scaled variance of the produced particle multiplicity distribution [39]. From the lattice QCD, which can be performed at chemical potential (μ_B) equals zero, a rapid crossover from the hadron gas to the QGP at the temperature (T) in the range between 170 – 190 MeV [124, 125] is suggested. The hypothetical phase diagram of strongly interacting matter in the (T, μ_B) plane is shown in Figure 36. In this figure, also available (NA49, STAR) and future data (NA61/SHINE) that

can be used to probe interesting region are shown. The temperature and chemical potential are not directly measurable. However, T and μ_B coordinates of the chemical freeze-out have one-to-one correspondence with energy (E) and system size (A) of the collisions [59]. This fact allows searching for critical point of strongly interacting matter via systematic E-A scan.

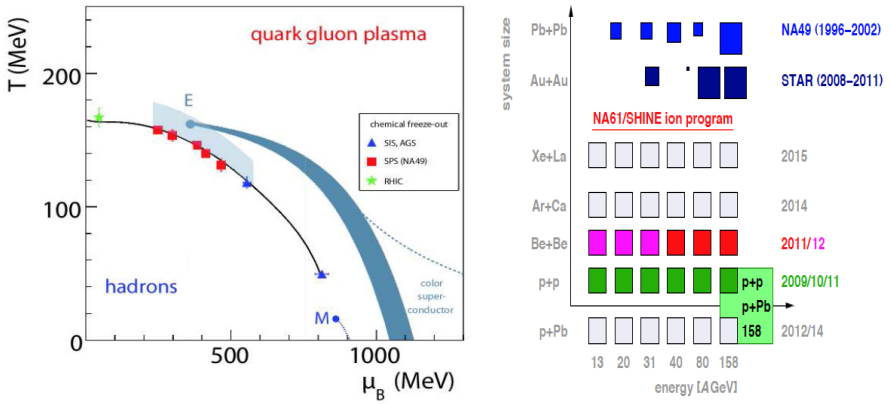

Figure 36. Hypothetical phase diagram of strongly interacting matter in the (T, μ_B) plane (left panel). Solid symbols show the chemical freeze-out points extracted from the analyses of hadron yields in central Pb+Pb (Au+Au) collisions at different energies. Gray band shows the region, which will by covered by NA61/SHINE measurements compiled with existing NA49 and STAR data. The NA61/SHINE ion program and existing data from NA49 and STAR (right panel). The area of the boxes is proportional to the number of registered central collisions, which is typically 2*10⁶ for the SHINE ion program. The pictures are taken from [15].

The measurements of hadron production in p+p, p+A, and A+A collisions are necessary to achieve further progress in understanding of physics in this field.

6.1.2 Measurements done for neutrino physics.

The main contributors to the T2K neutrino flux are pions and kaons, which through their decays produce neutrinos. Up to now, no direct measurements of pion and kaon production in proton carbon interactions at 31 GeV/c (the T2K setup) exist. The closest available data from proton Carbon interactions are from the HARP experiment at 12 GeV and from the NA49 from 158 GeV (in both cases pion yield only). The MIPP E907 also published some preliminary results from proton Carbon interactions at 60 GeV.

Several opportunities like the COMPASS at CERN, MIPP at Fermilab, and NA61/SHINE have been studied to find the most promising option to measure the pion and kaon yields for the T2K. Finally, after detailed Monte Carlo studies it was shown that upgrade of the NA49 detector has the acceptance and the particle identification capabilities needed for this measurement therefore the NA61/SHINE was chosen. Momentum versus polar angle distributions of pions and kaons that are producing neutrinos seen in far detector of the T2K are shown in Figure 37. The full pion and kaon phase space need to cover by measurements to avoid extrapolation and in consequence model dependent uncertainties.

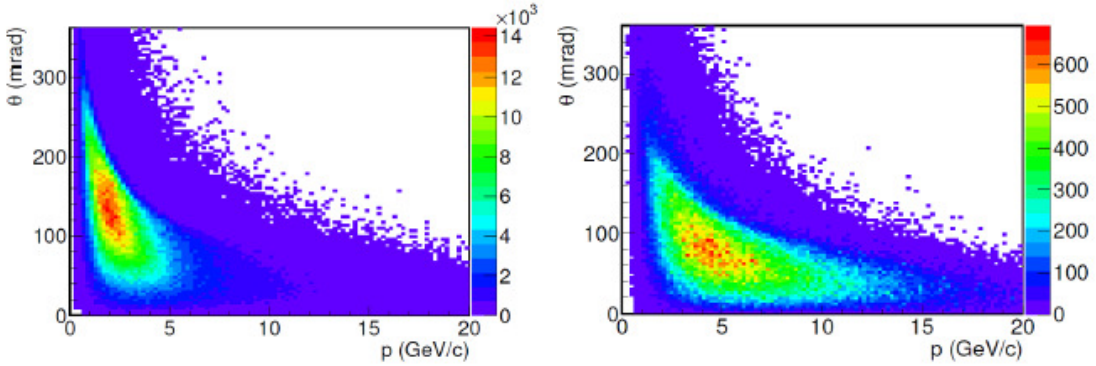

Figure 37. Momentum versus polar angle distributions of positively charged pions (left) and kaons (right) that are producing neutrinos seen in far detector of T2K. JNUBEAM simulations [8].

Without measurement of the NA61/SHINE systematic uncertainties on the neutrino flux predictions and the far-to-near ratio were estimated by comparing the results from different hadronization models (GCALOR [184], GFLUKA [68], and GHEISHA [97]). Discrepancies between different predictions are huge e.g. differences in the absolute neutrino fluxes can reach up to a factor 2. It proved that discrepancies between these models would strongly influence the precision of the neutrino cross-section measurements. This lack of knowledge also influence near-to-far ratio what was shown in Figure 33. To fulfill the T2K designated precision error on far-to-near ration cannot be larger than 3%. Precise direct measurements of pion and kaon yields from proton Carbon interactions at 31 GeV/c are crucial for the T2K. Measurements were done in two configurations: with thin (2 cm) carbon target and with T2K replica target (90 cm). First configuration is important for measuring the primary particle production without distortions due to reinteractions in the target. Neutrino parents are not only produced in the primary proton interactions in the T2K target. This indirect contribution will be studied using measurement done in second configuration. In it is shown that not only pions and kaons are important for the knowledge of neutrino flux in the T2K. It is of importance to measure as well neutral strange hadrons (K^0_S, Λ) because these particles contribute directly or via decays to the neutrino production in the T2K.

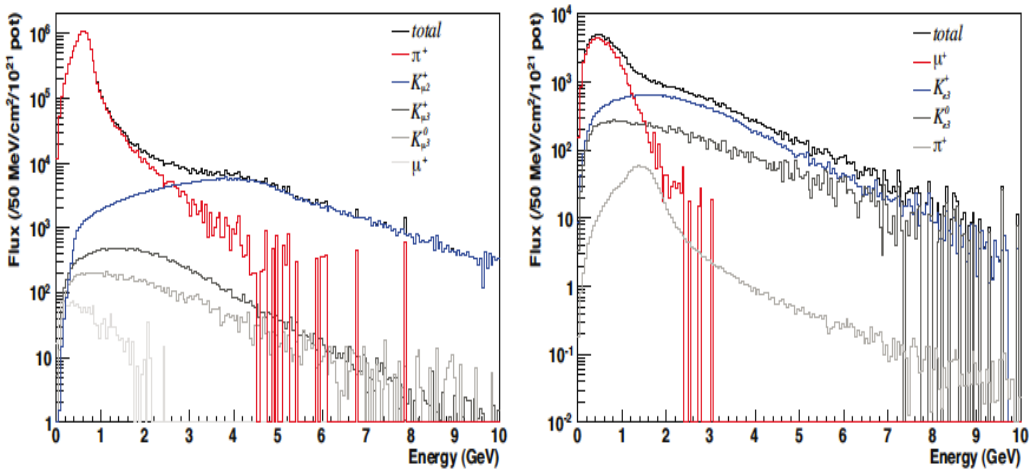

Figure 38. νμ (left) and νe (right) energy spectrum at far detector of T2K. Different contributions of parents are shown. JNUBEAM simulations [4].

6.1.3 Measurements done for cosmic ray physics.

Dedicated runs collected for the Pierre Auger and KASCADE experiments. It has been shown that not only high energy range is important for predictions of extensive air shower characteristics [39]. The hadron production in the energy range up to a few hundred GeV is also very important in particular to minimize large uncertainties connected with measurements of shower particles at large lateral distances from the shower core.

6.2 Detector description

The NA61/SHINE detector at CERN is a large acceptance hadron spectrometer for the studies described in Chapter 6.1 by collisions of various beam particles (p, π, Be, Ar, Xe, Au, Pb) with a variety of fixed targets (C, Be, Ca, La, Au, Pb). The detector is located in the North Area site at the H2 beam line of the Super Proton Synchrotron (SPS). The sketch of the CERN's accelerator complex is shown in Figure 39. The relevant part to the NA61/SHINE of the complex is shown in Figure 40.

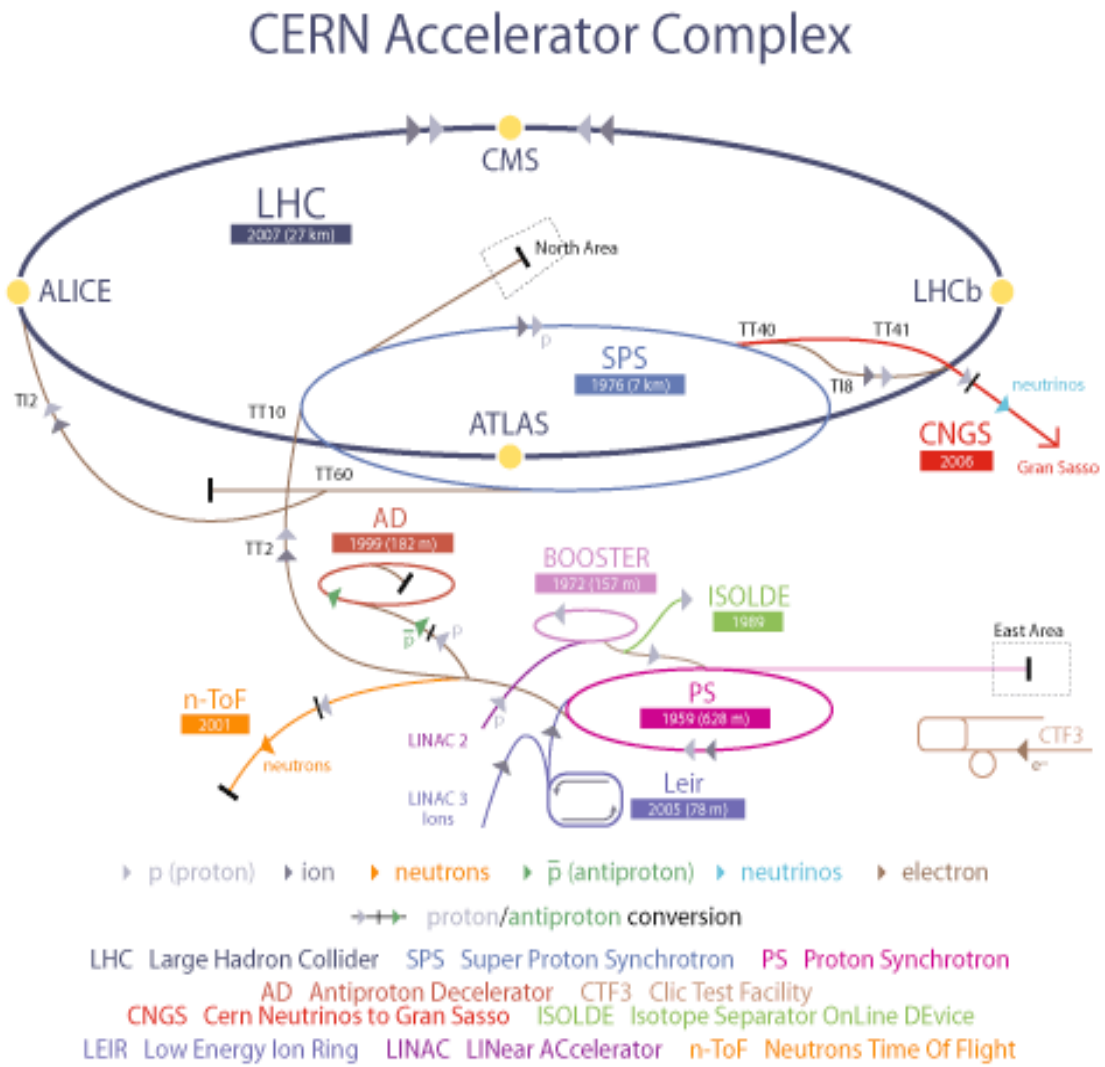

Figure 39. CERN's accelerator complex [181].

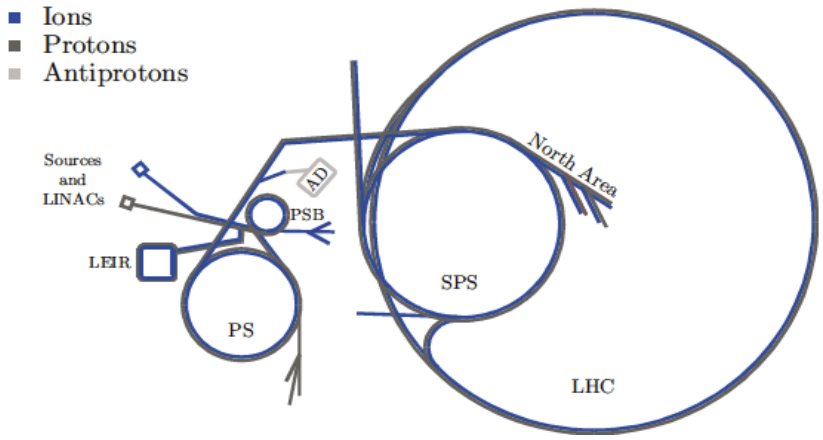

Figure 40. Relevant to the NA61/SHINE part of the CERN's accelerator complex [181].

As it was mentioned, beam particles interacting with NA61/SHINE targets are from the H2 beam line. At the beginning, protons are obtained by removing electrons from hydrogen atoms. They are accelerated in the LINAC2 and injected to the PS Booster (PSB). Then to the Proton Synchrotron (PS) where they are accelerated to 14 GeV/c and after that to the SPS where they are further accelerated to 400 GeV/c. These protons are extracted to the H2 beam line. Secondary beam particles (hadrons, electrons, muons) of energies from 10 to 360 GeV/c are produced by interactions of primary beam protons with the T2 target located at the beginning of the H2 beam line. The momentum and intensity of the secondary beam is controlled by the set of collimators. Bending magnets (BENDs), correction dipoles (TRIMs), and quadrupoles (QUADs) are used to focus the beam. Further beam detectors and counters in from of the NA61/SHINE detector are discussed in Chapter 6.3.2 Trigger).

The NA61/SHINE inherited its main detector components from the NA49 experiment. Four large Time Projection Chambers (TPCs), one small TPC for the low emission angle particles (GAP TPC), and two time-of-flight detectors (TOFs) are former NA49 detectors, which are used in the NA61/SHINE experiment. Large TPCs and new, specially designed for the T2K needs, TOF are the main components of the NA61/SHINE experiment. New to the NA49 is also Particle Spectator Detector (PSD), which is important for the centrality determination in nucleus-nucleus collisions. The detector layout is presented in Figure 41.

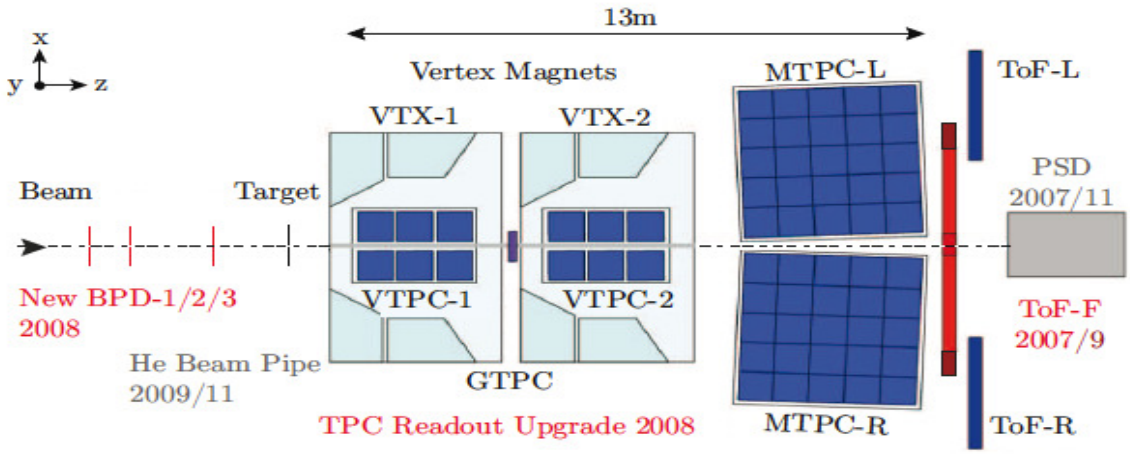

Figure 41. Layout of the NA61/SHINE detector.

6.2.1 Time Projection Chambers (TPCs)

The NA61/SHINE TPCs are multi-wire proportional chambers with the readout pads filled with gas compositions of Ar and CO_2. They allow obtaining track reconstruction in three dimensions.
TPC operation basic principles are broadly discussed in the literature [161, 129, 111]. When charged particles fly through the sensitive volume of the detector they lose kinetic energy by excitation of bound electrons and ionization. This can leads to electron-ion pair production. Free electrons, that are at the beginning located along the trajectory of the charged particle, drift in the homogeneous electric field towards the read-out chamber. The schematic view of this process is presented in Figure 42.

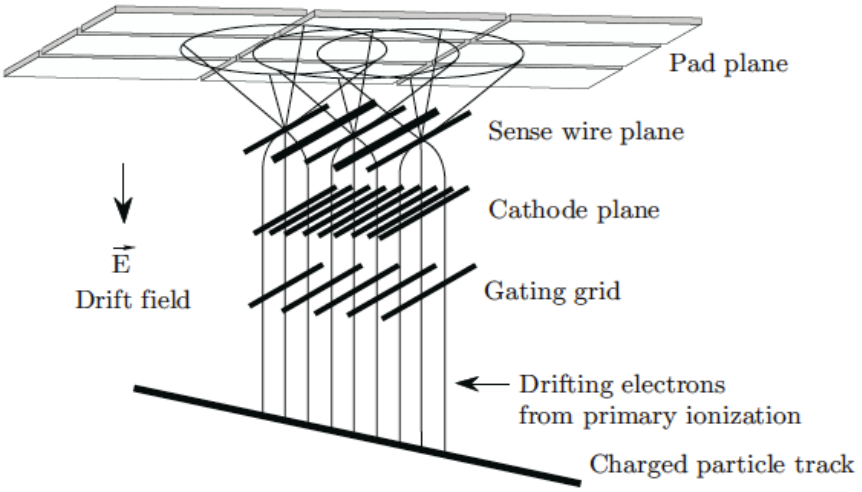

Figure 42. Layout of the Time Projection Chamber readout with schematic view of charged particle traverses through the sensitive volume of the detector [17].

First of all, electrons that are arriving at the readout plane have to pass the gating grid, which is open during the readout time. During this time gating grid is at the same potential as the drift field at that point what allows to electrons drift through. A cathode plane follows the gating grid. It is is at 0 V, thus it separates the drift volume from the amplification region. In amplification region electrons are accelerated in the electric field of the sense wire plane producing an avalanche (multiplication by a factor of 10^4). The wires absorb electrons. The much heavier charged ions crate voltage pulse on the readout pads before they drift towards the cathode plane. At that time the gating grid is closed what prevents ions from drifting in the detector volume and also prevents electrons from entering the readout chamber.
The two small TPCs (VTPC-1 and VTPC-2) are placed inside super-conducting dipole magnets what allows determining momentum using track curvature (maximum combined bending power of 9 Tm over 7 m length). The track momentum can be determine using following equation:

$$p\,[GeV/c] = 0.3 \cdot q\,[e] \cdot B\,[T] \cdot R\,[m] \cdot \frac{1}{\cos\lambda}$$

where p is particle momentum, q is particle charge, B is the magnetic field, R is the radius of curvature of the track, and λ is the angle between the track and the bending plane. Depending on the phase space region a resolution of $\sigma(p)/p^2 \approx (0.3\text{-}7.0) * 10^{-4}$ $(GeV/c)^{-1}$ is reached. The maximum possible magnetic field is 1.5 T in the VTX1 and 1.1 T in the VTX2 magnet. The two large TPCs (MTPC-L and MTPC-R) are used only for the ionization energy loss

measurements. Information from the smallest TPC (GTPC) placed between VTPCs along the beam line was not used in analyses performed on the 2007 pilot run data. GTPC detector was used to extend geometrical acceptance of particles emitted at small polar angles. Information from this detector will be used in analyses of the 2009 data.
The dimensions and gas compositions of the NA61/SHINE TPCs are presented in Table 8.

	VTPC-1/2	MTPC-L/R	GTPC
Width [m]	2	3.9	0.384
Length [m]	2.5	3.9	0.196
Height [m]	0.98	1.8	0.590
Gas	Ar/CO_2 (90/10)	Ar/CO_2 (95/5)	Ar/CO_2 (90/10)
Drift Voltage [kV]	13	19	11
Drift Velocity [cm/μm]	1.4	2.3	~1.2
Number of Pads	27648	63360	672
Pad dimensions [mm]	3.5 *16/28	3.6/5.5 *40	4*28

Table 8. Technical parameters of the NA61/SHINE TPCs.

Each pad in the TPC readout:

- corresponds to x-z coordinate pair,
- has assigned a sector number, pad-row number, and pad number.

VTPC-1/2 and MTPCs readout pads are assembled respectively in 6 and 25 sectors each. There are 62 sectors in total as shown in Figure 43.

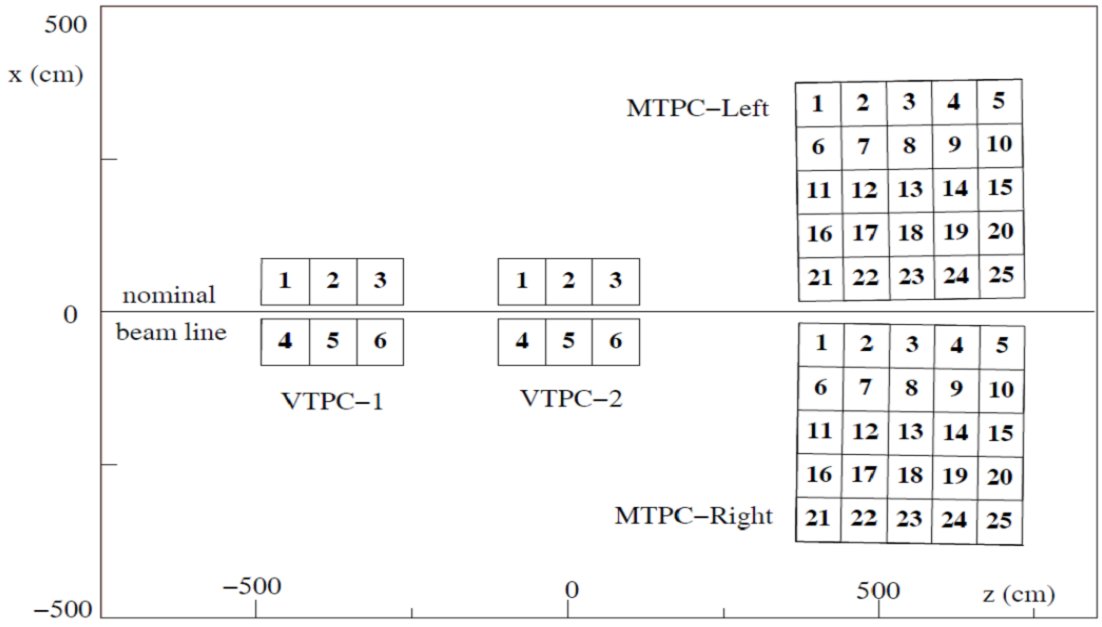

Figure 43. Sectors of the NA61/SHINE TPCs [171].

Ssector rows near the beam line in MTPCs (21-25 for MTPC-L, and 1-5 for MTPC-R) are the sectors where pads being narrower – high resolution sectors. The other sectors in MTPCs have standard resolution. Pads locations were optimize to maximize track reconstruction. Each pad is tilted with respect to the beam line to agree with the average track angles at the given x-z position.

6.2.2 Time Of Flight detectors (TOFs)

In the NA61/SHINE experiment TPCs are complemented by the setup of Time Of Flight detectors (TOFs). The TOF operation principle is very simple. The time of flight of the particle is reproduced from the start signal that is given by the one of the trigger detectors (S1 scintillator counter, detectors used in trigger logic are discussed in chapter 6.3.2 Trigger) and from the stop signal that comes from the readout of the TOF after the particle hits scintillator bar. The TOF-F is made of 64 scintillator bars with photomultipliers (PMTs) readout at both ends. The TOF-F has a time measurement resolution of ~115 ps (while TOF-L and TOF-R have resolution of 60 ps). This detector was installed in 2007 in order to extend the particle identification acceptance to low momenta (p<4 GeV/c). The measurement of the time is done as follows:

$$t = t_{S1} - \frac{t_{up} + t_{down}}{2} + t_0$$

where t_{S1} is the start signal from S1 counter, t_{up} and t_{down} are the signals from the top and bottom of the scintillator bar, t_0 is a calibration constant individual for each channel.

6.2.3 Particle Spectator Detector (PSD)

The whole NA61/SHINE detector is completed with the Particle Spectator Detector (PSD) that is a new type of the zero degree calorimeter. The PSD will be used for the centrality determination in nucleus-nucleus collisions. Information from this detector was not used in analyses of data from 2007 pilot run. More information about the PSD can be found in [159].

6.3 Trigger and data acquisition

6.3.1 Beam Position Detectors (BPDs)

Three two-plane multiwire proportional chambers, which are called the Beam Position Detectors (BPDs), were used to measure the trajectory of the beam particles. These counters were providing a resolution of about 200 μm in two orthogonal directions. The beam spot and divergence obtained from the BPD measurements are presented in Figure 44.

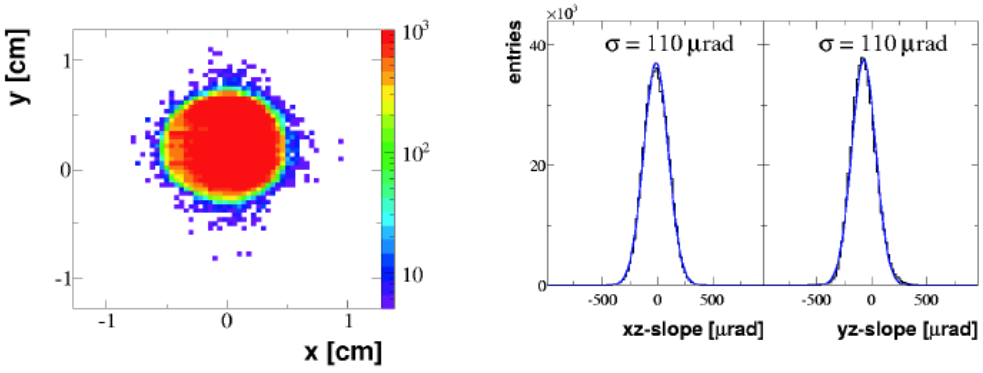

Figure 44. Left: The beam spot as measured by BPD-3 after the $\overline{V1}$ cut described in the text. Right: The beam divergence in x and y. The pictures are taken from [7].

6.3.2 Trigger

The trigger and beam detectors used in the NA61/SHINE experiment during 2007 pilot run are presented in Figure 45.

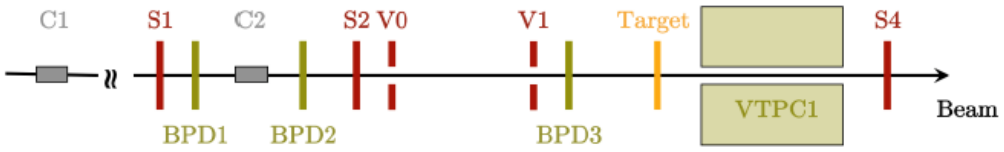

Figure 45. Trigger and beam detectors used in the NA61/SHINE experiment during 2007 pilot run [166]. C - Cherenkov detectros, S – Scintilator detectors, V – Veto counters.

Two Cherenkov counters, CEDAR (C1) and threshold counter (C2), identify protons from the secondary hadron beam. C1 was used to identify protons (pressure was set to 3.3 bar) and C2 operated at the pressure lower than proton threshold (1.65 bar). C2 worked in anti-coincident mode in trigger logic. The fraction of protons in the secondary hadron beam was about 14%. Two scintillator (S1, S2) and two veto (V0, V1) counters provide the beam definition and timing. The S1 counter was also used to provide the start signal for the TOF detectors. The purity of identification of beam protons based on the selection made by Cherenkov counters was of about 99%. Purity studies were done by bending the beam into the TPCs with the full magnetic field and using dE/dx identification method.
During 2007 pilot run beam protons were selected by the coincidence $S1 \cdot S2 \cdot \overline{V0} \cdot \overline{V1} \cdot C1 \cdot \overline{C2}$. The beam momentum, presented in Figure 46, was measured in dedicated run by bending the incoming particles into TPCs with the full magnetic field.

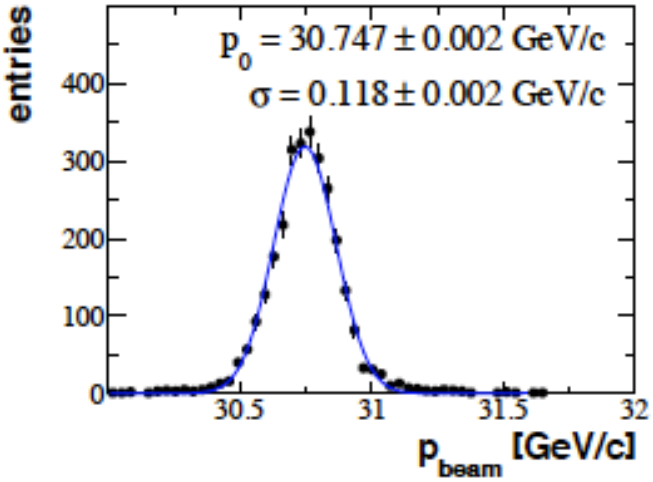

Figure 46. Beam momentum distribution measured by the reconstruction of beam particles in the TPCs with the full magnetic field. Only statistical errors are shown. The picture is taken from [7].

The mean value of 30.75 GeV/c was obtained. This agrees with the set value of 30.92 GeV/c within the available precision of setting the magnet currents in the H2 beam line.

Interactions in the target were selected by anti-coincidence of the incoming beam protons with S4 scintillator counter placed on the beam trajectory between VTPC-1 and VTPC-2. Therefore, the interaction trigger is a minimum bias trigger based on the

disappearance of the incident proton.

During 2007 pilot run 667 k events were recorded with the thin carbon target, 46 k events with the thin carbon target removed, 80 k events for calibration purposes, and 230 k events with the T2K replica target.

6.4 Normalization of particle yields.

The main motivation and goal of the analysis of the data collected during 2007 pilot run is to present results in terms of mean multiplicities and inclusive particle cross sections in proton Carbon interactions. In this chapter two approaches of the normalization procedure developed by the NA49 Collaboration are discussed. First approach, further called the NA61 normalization, was used to normalize h- results to π^- production cross sections and to meant π^- multiplicity in all production p+C interactions. The second approach, further called the NA49 normalization, was used to normalize K^0_S and Λ results. It was shown that these two normalization approaches lead to the same results [16].

6.4.1 NA61 normalization

This approach has been used for the determination of the inclusive production of charged pions in proton proton and proton Carbon collisions at 158 GeV/c beam momentum registered by NA49 [17]. In this approach the particle cross sections are evaluated from the data. Then, additional corrections are applied to correct for all experimental biases. The differential inclusive cross section for a particle type α is calculated as:

$$\frac{d\sigma_\alpha}{dp} = \frac{\sigma_{trig}}{1-\varepsilon}\left(\frac{1}{N^I}\frac{\Delta n^I_\alpha}{\Delta p} - \frac{\varepsilon}{N^R}\frac{\Delta n^R_\alpha}{\Delta p}\right)$$

where:

- p is momentum of a α particle at the proton Carbon interaction point (Δp is momentum bin width).
- N^I and N^R are the number of events after event and cuts for the target in and target out configurations, respectively.
- Δn^I_α and Δn^R_α are numbers of corrected α particles in given cell for the target in and target out configurations, respectively.
- $\sigma_{trig} = 298.1 \pm 1.9 \pm 7.3$ mb is the trigger cross section.
- $\varepsilon = 0.118 \pm 0.001$ is the ratio of the interaction probabilities for removed and inserted target operation.

This normalization was used in h- analysis to obtain negatively charged pion results ($\alpha = \pi^-$). In this procedure normalization factors are evaluated from the analyses of the trigger data.

The normalization to mean α particle multiplicity in production interactions is calculated using this formula:

$$\frac{dn^\alpha}{dp} = \frac{1}{\sigma_{prod}}\frac{d\sigma_{prod}}{dp}$$

where $\sigma_{prod} = 229.3 \pm 1.9 \pm 9.0$ mb is the production cross section which is determined from the inelastic cross section (by subtracting the cross section of quasi-elastic p+C interactions at 31 GeV/c which was calculated accordingly to the Glauber model). The inelastic cross section was evaluated from the trigger cross section using Geant4 simulations (two corrections were applied – subtraction of part connected with coherent elastic scattering and addition of the lost inelastic events due to fake signals in S4 by charged particles produced in interaction).

The same approach was used in other variables sets. Details on the normalization procedure can be found in [7].

6.4.2 NA49 normalization

This approach is based on the event cuts, for example cut on the vertex z position, which are performed in such a way that in consequence the elastic events are rejected. However, performing of that kind of cuts rejects as well a small fraction of inelastic events. This is taken into account by the Monte Carlo correction. In this approach, vertex z distributions are used to normalize target out data. The normalization factor is obtained by the comparison of vertex distributions far from the target where we are certain that all of them are non-target interactions. From the ration of events in this region normalization factor was estimated.
The normalization to mean α particle multiplicity in production interactions is calculated as:

$$\frac{dn^{\alpha}}{dp} = \frac{1}{N_{inel}\Delta p}(\Delta n_{\alpha}^{I} - c\Delta n_{\alpha}^{R})$$

where:

- p is momentum of a α particle at the proton Carbon interaction point (Δp is momentum bin width).
- Δn^{I}_{α} and Δn^{R}_{α} are numbers of corrected α particles in given cell for the target in and target out configurations, respectively.
- c is a target out normalization factor.
- N_{inel} is number of inelastic events after event cuts. This number is evaluated from the number of events accepted after event cuts by addition of contribution of rejected inelastic events which was calculated from the Monte Carlo studies.

The normalization to the differential inclusive cross section for a particle type α is calculated as:

$$\frac{d\sigma_{\alpha}}{dp} = \sigma_{prod}\frac{dn^{\alpha}}{dp}$$

where $\sigma_{prod} = 229.3 \pm 1.9 \pm 9.0$ mb is the production cross section.

This approach was used in the normalization of K^{0}_{S} and Λ results.

6.5 Reconstruction chain

The track reconstruction procedure of the NA61/SHINE is based on the approach developed by the NA49 experiment [17]. The track reconstruction chain is schematically presented in Figure 47. The reconstruction process starts from the MINICLIENTS that:

- extract scaler data from the beam counters,
- reconstruct beam track using BPD information,
- calculate velocities in TPCs, and reconstruct charge clusters

After that, the cluster reconstruction in TPCs is done. Then, whole chain of tracking is performed to find out tracks in a particular detectors (local). After that, local tracks are matched and global tracks are formed. The momentum of the global track is calculated from the curvature in the magnetic field by the momentum-reconstruction module.

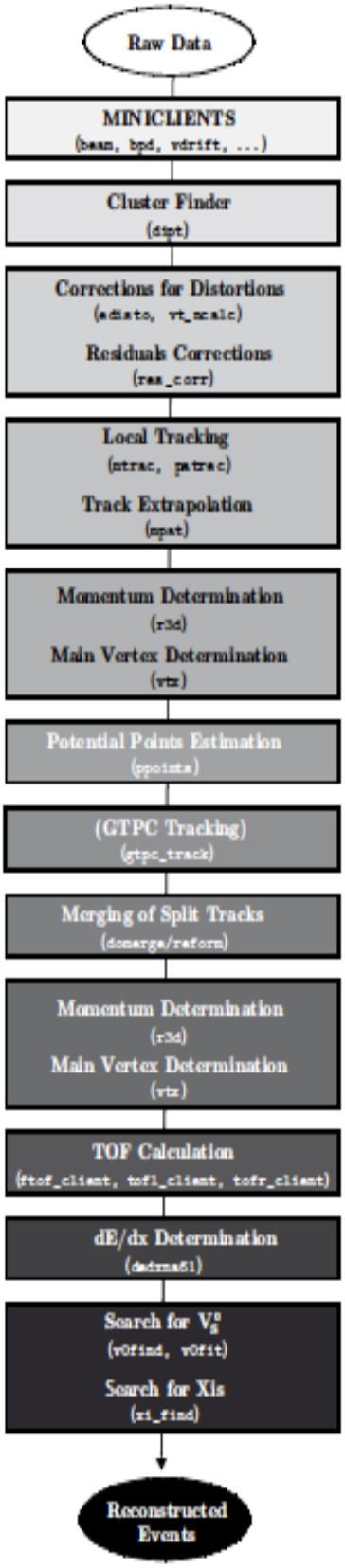

Figure 47. Schematic view of the reconstruction chain used in NA61/SHINE experiment. The picture is taken from [166].

6.5.1 Track reconstruction in Thin target case

In the thin target (2C) case, the main vertex is evaluated. During 2007 pilot run the 2C target was installed at z=-580 cm. The BPD vertex had a fixed z position equals to the nominal target position. x and y positions were obtained from the extrapolation of the beam track to the z-position of the target. Fitted Vertex was evaluated using x and y positions of the BPD vertex and information from the fit on the closest approach of all global tracks. In 2007 reconstruction chain Main Vertex was corresponding to the BPD vertex. In case BPD vertex was not found fitted vertex was used. If non of vertices were found nominal (x,y,z) position of the target was used. The tracking of the global track is done using extrapolation of local tracks to the target plane. Straight tracks are reconstructed in MTPCs. MTPC tracks are extrapolated to VTPCs. Track found in VTPCs which were not extrapolated from MTPCs are matched and fitted. After that, for the refitted global tracks momentum is determined. Track segments are matched using one of the merging clients (DOMERGE, REFORM). Information from the tracking procedure is stored in two data structures: rtrack (in which information without the assumption about primary vertex is stored), track (information obtained with assumption that track comes from the primary vertex).

6.5.2 Track reconstruction in T2K replica target case

In the 90 cm long T2K target replica case, it is almost impossible to evaluate main vertex of the interaction. In this case analyses are made on rtracks that are obtained at the local tracking level. The problem of the main vertex determination is not important because these data were collected to study not only primary vertex interactions but all the possible parents of the neutrinos emitted from the target. That is why backward propagated tracks to the target surface are reconstructed.

6.5.3 Reconstruction of V^0 candidates

At the end of the reconstruction chain search for V^0 candidates is done. V^0s are pairs of charged tracks originated from the same point that can be interpreted as daughters of the weakly decaying particles. The reconstruction is done by two clients: v0find and v0fit. First one loops over all positively charge tracks and looks for the negatively charged tracks that match. These two tracks need to fulfill certain conditions:

- Tracks need to have sufficient number of points inside TPCs (≥10 for VTPC-1 and ≥20 for VTPC-2) .
- Distance of closest approach (DCA) between those tracks need to be sufficiently small (DCA-x and DCA-y ≤ 1 cm).
- Separation of the tracks at the target plane in x and a y direction is demanded (≤ 0.75 cm).
- V^0 candidate needs to be close enough to the target (in x and y ≤ 25 cm)
- Angle between the normal to the decay plane and the vector that is perpendicular to the V^0 particle's momentum has to be in certain range([0.2, 2.9] rad).

After that, the second client using nine parameter Levenburgh-Marquardt procedure fits V^0 candidates. Those parameters are coordinates of the decay vertex and momenta components of the daughter particles. At the information about decay vertex,V^0s momentum, and tracks is stored.

6.6 Modelling of the detector response

The Monte Carlo chain used for the modeling of the detector response was based on the simulation chain developed by the NA49 Collaboration. As primary event generator VENUS 4.12 model was used. The GEANT 3.21 was used for the propagation of particles through the detector. Simulation of the detector response was made using dedicated packages. Then Monte Carlo events were reconstructed using exactly the same reconstruction chain as used for the real data. At the end simulated particles were matched with reconstructed tracks. Validation of the Monte Carlo chain used was based on the comparison of distribution of several reconstructed variables with the measured ones in the real data. The comparison was done using three sample of tracks: all, tracks with $q*p_x>0$ so called Right Side Tracks (RST), and tracks with $q*p_x<0$ so called Wrong Side Tracks (WST). RST and WST are separate subsamples of the all tracks sample. An example of negatively charged RST and WST is shown in Figure 48 and Figure 49, respectively.

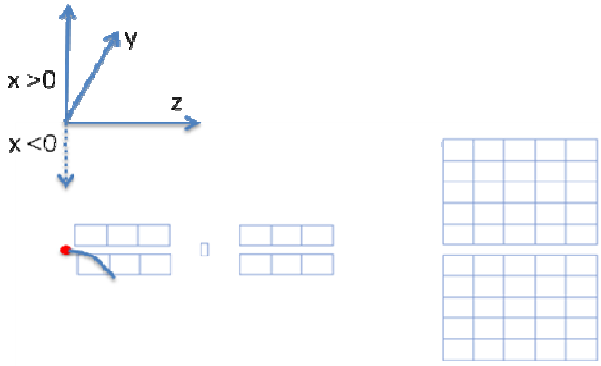

Figure 48. Example of negatively charged RST (px<0 and q<0). Main vertex is shown by red dot. Top view (x, z plane).

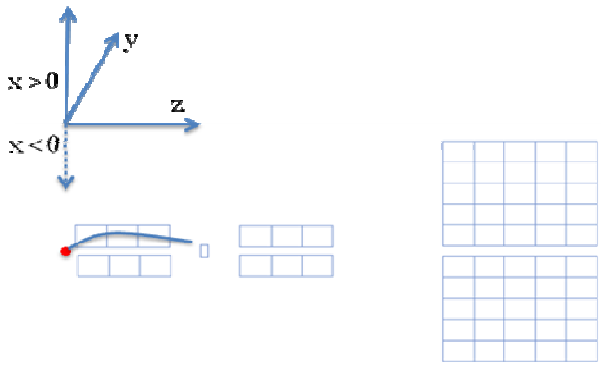

Figure 49. Example of negatively charged WST (px>0 and q<0). Main vertex is shown by red dot. Top view (x, z plane).

The data and MC distributions were compared for the following variables:

- Momentum and polar angle with respect to the beam direction
- Number of measured points in all TPCs (NPoint)
- Number of measured points in VTPCs
- Number of potential points in all TPCs (NMaxPoint)
- Ratio of measured to potential points
- Impact parameters

  - The distance in x and y directions between extrapolation of the track to the target plane and position of the main vertex (Bx and By, respectively)
- Azimuthal angle
- Feynman x (xf = 2 $p_L/\sqrt{s}$, where p_L and $\sqrt{s}$ are given in the nucleon-nucleon c.m.s)
- Transverse momentum p_T
- Rapidity of the particles assuming pion mass in the c.m.s (y*(π))

The studies of the negatively charged RSTs and WSTs were performed in order to validate possibility to use both samples in the analyses in order to minimize statistical errors. WSTs were not used before in the NA49 analyses because detector was designed to maximize RSTs reconstruction. The minimization of the statistical error was therefore the key issue.

The studies of the positively charged tracks reconstructed to primary vertex were performed to assess the full picture.

The momentum distributions for different types of negatively charged tracks are shown in Figure 50.

Negatively charged tracks

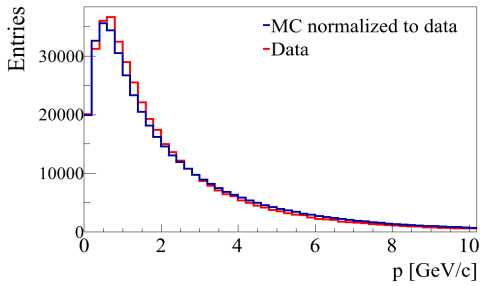

Negatively charged RST

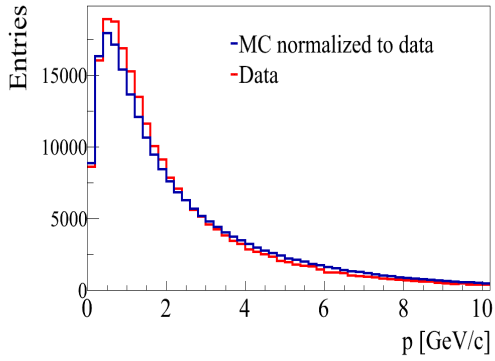

Negatively charged WST

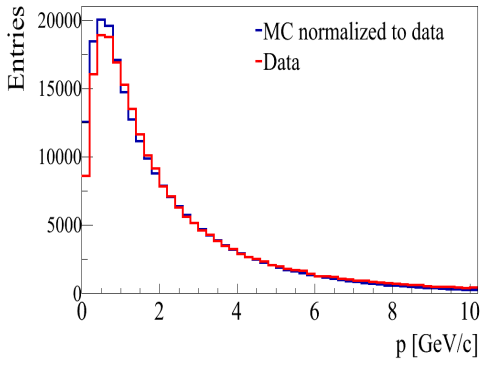

Figure 50. Momentum distributions for different types of negatively charged reconstructed tracks. The MC normalized to data.

The Monte Carlo distributions are normalized to data. Very good agreement between data and MC was found. The shapes of MC distributions differ insignificantly.

The polar angle distributions for different types of negatively charged tracks are shown in Figure 51. The full set of studied distributions is shown in appendix.

Negatively charged tracks

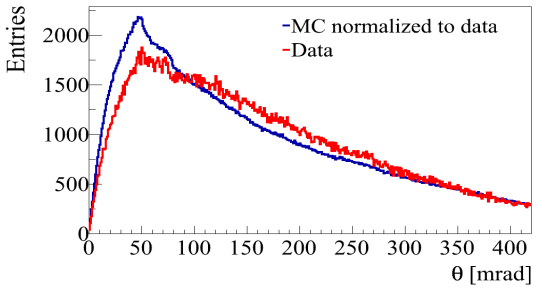

Negatively charged RST

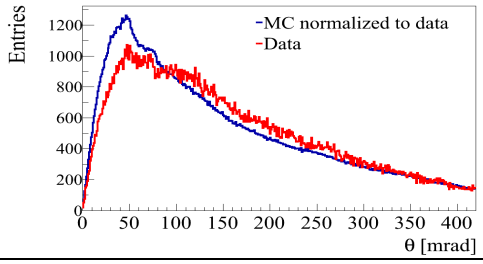

Negatively charged WST

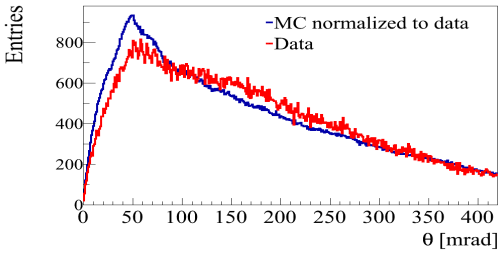

Figure 51. Polar angle distributions for different types of negatively charged reconstructed tracks. The MC normalized to data.

Larger discrepancies (than for momentum distributions) between data and MC predictions of polar angle distributions were observed. Shapes of data distributions are steeper. These differences do not disqualify the use of the MC predictions in the analyses. In analyses made in momentum and polar angle variables to avoid model dependent corrections incorporating differences in shapes of those distributions small bin size is used. A similar approach is used in the analyses made in different sets of variables (xf, p_T or y, p_T).

The two-dimensional distributions of polar angle versus momentum of real data and Monte Carlo (not normalized) for different types of negatively charged tracks are shown in Figure 52 and in Figure 53, respectively.

Negatively charged tracks

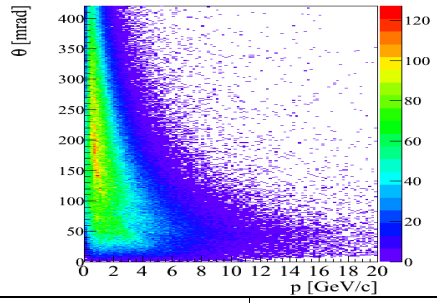

Negatively charged RST	Negatively charged WST
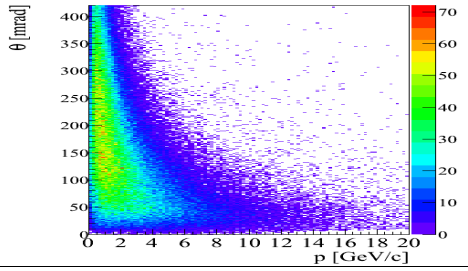	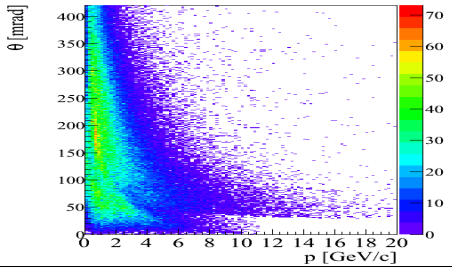

Figure 52. Two-dimensional distributions of polar angle versus momentum for different types of negatively charged tracks. Real data – reconstructed tracks.

Negatively charged tracks

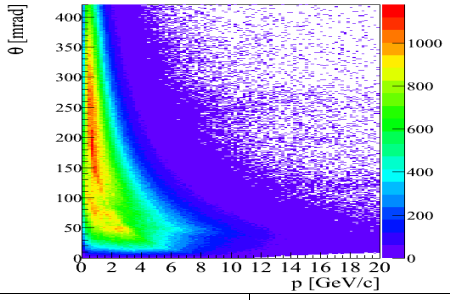

Negatively charged RST	Negatively charged WST
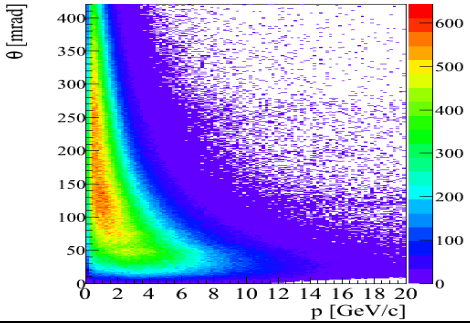	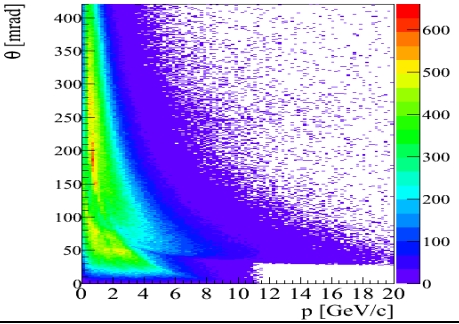

Figure 53. Two-dimensional distributions of polar angle versus momentum for different types of negatively charged tracks. Monte Carlo – reconstructed tracks.

The good agreement between data and MC was observed (for all sets of distributions – for additional information see appendix). In addition from these distributions one can find other information:

- Slightly different phase space regions are covered by negatively and positively charged tracks.
  - Positively charged tracks cover larger region in momentum, mainly due to larger contribution of Kaons and protons than in negatively charged particles case (only small contribution of K- and anti protons).
  - RSTs and WSTs also are covering not exactly the same phase space regions. This fact is important when making comparisons of these subsamples.

The distributions of number of measured points in all TPCs for different types of negatively charged tracks are presented in Figure 54.

Negatively charged tracks

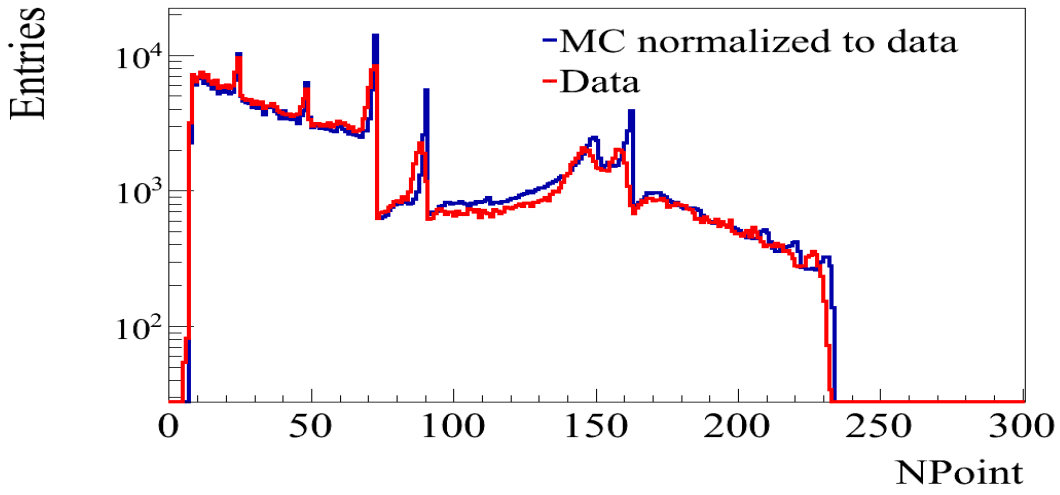

Negatively charged RST

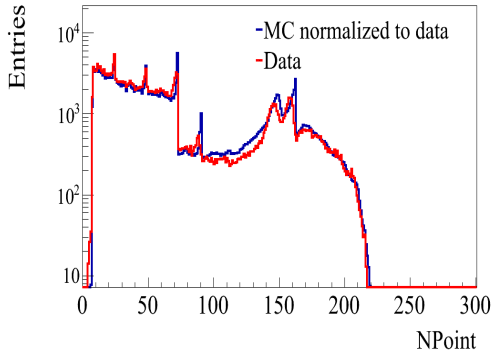

Negatively charged WST

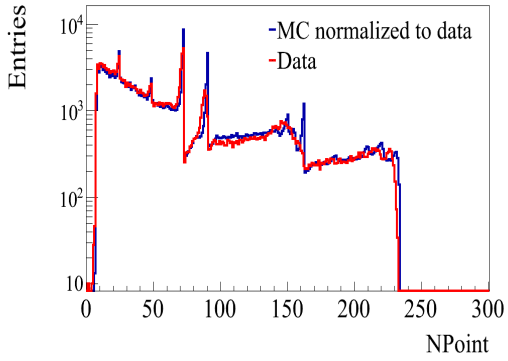

Figure 54. Number of measured points in all TPCs for different types of negatively charged reconstructed tracks. The MC normalized to data.

In the MC, distribution are narrower at the places of the edges of TPCs. Apart from the region of the VTPC2 and part of the MTPC (NPoint larger than 72 and smaller than ~140), where small discrepancies were observed, good agreement between data and MC was found.

Dedicated studies of number of measured points in sum of VTPCs were performed to establish requirement on this variable needed for the good determination of the momentum

from the curvature of the tracks. These studies will not be discussed in details in this thesis. As an outcome, we found that at least 12 measure points is needed for a precise momentum determination. On the other hand minimum number of measured points for the momentum determination is 5 in one of VTPCs .

The distributions of number of potential points (NMaxPoint) in all TPCs for different types of negatively charged tracks are presented in Figure 55.

Negatively charged tracks

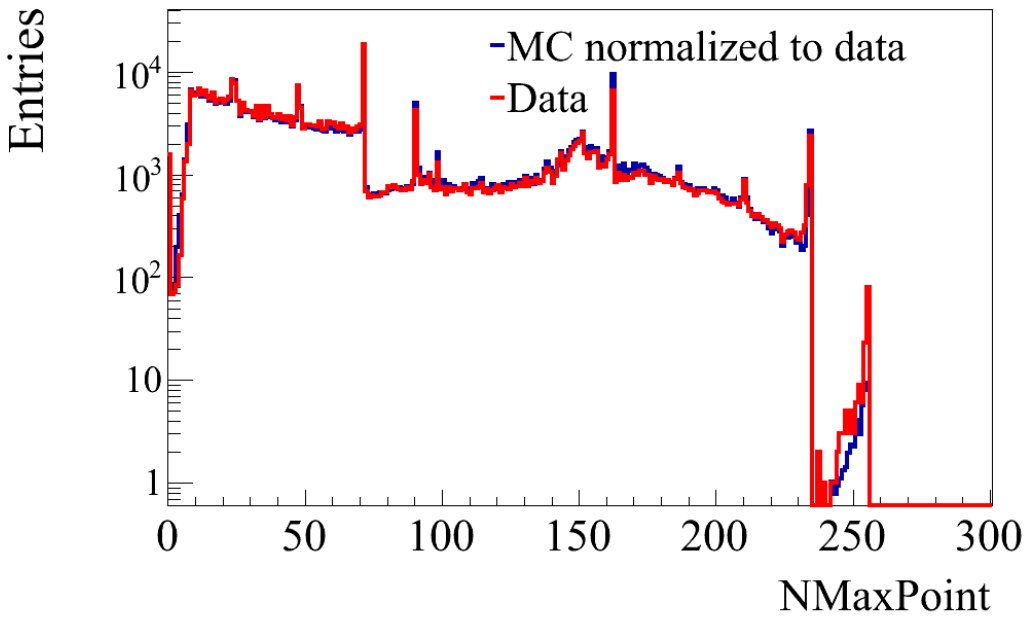

Negatively charged RST

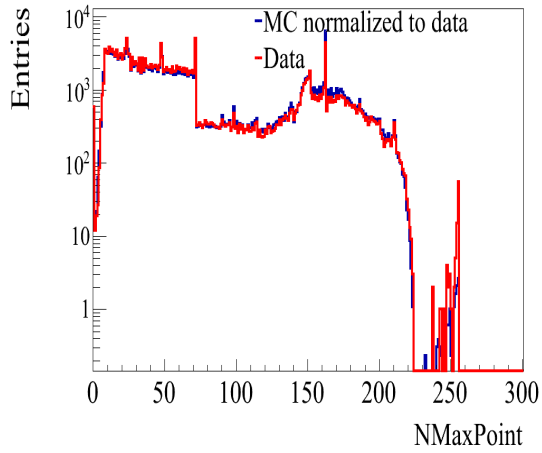

Negatively charged WST

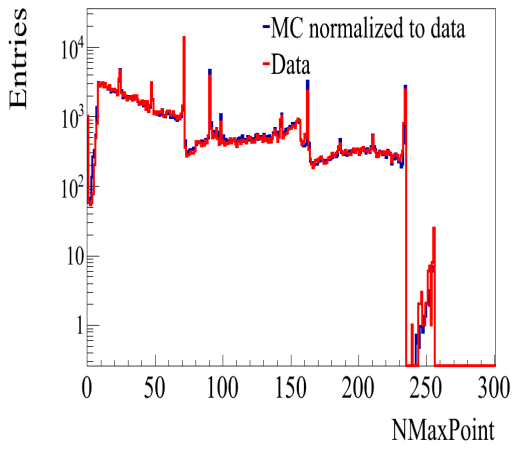

Figure 55. Number of potential points in all TPCs for different types of negatively charged reconstructed tracks. The MC normalized to data.

The distributions of number of measured to potential points ratios in all TPCs for different types of tracks are presented in appendix. For these distributions reasonable agreement between real data and MC predictions was found. This information was used in analyses to

reject double counting of split tracks. If the number of measured points is consistent with the number of potential points there is no anxiety that the track was divided into parts and only one part has been reconstructed.

The distributions of the bx impact parameter for different types of negatively charged tracks are presented in Figure 56.

Negatively charged tracks

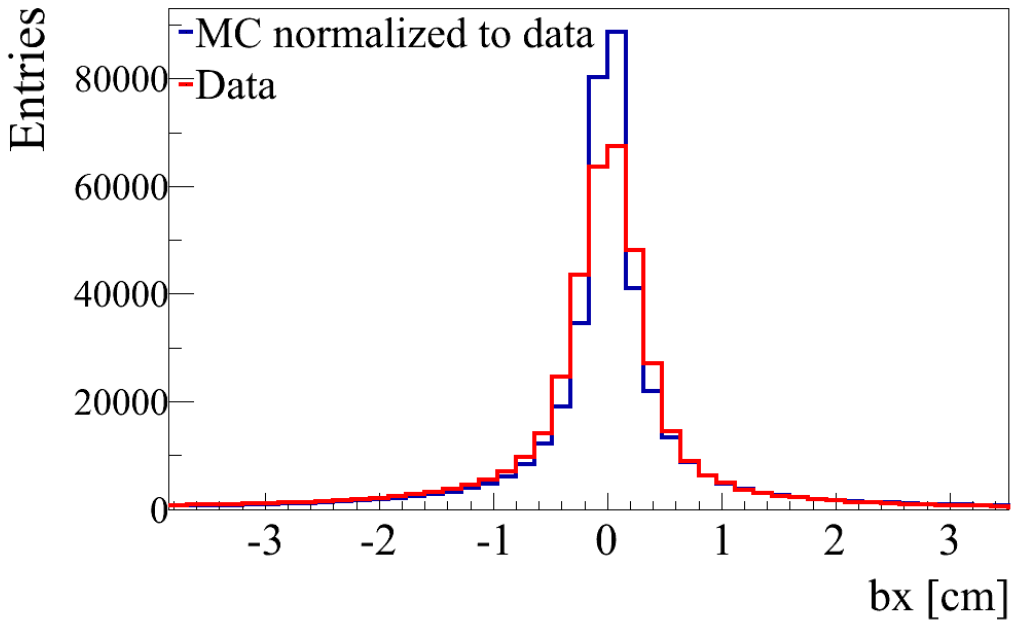

Negatively charged RST

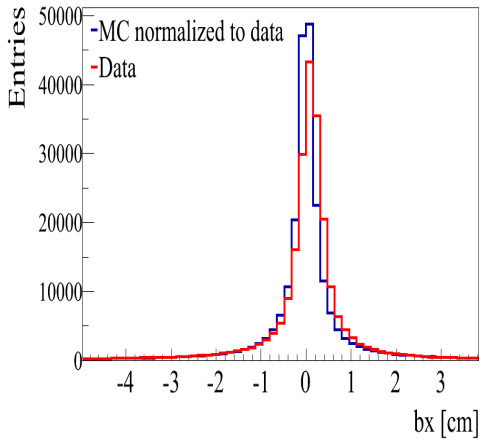

Negatively charged WST

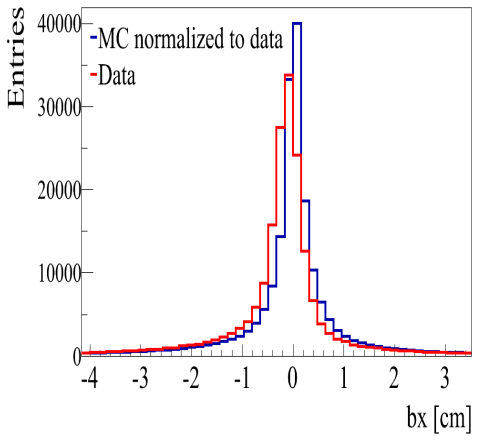

Figure 56. bx impact parameter distributions for different types of negatively charged reconstructed tracks. The MC normalized to data.

Impact parameters distributions should be centered around zero. Small shift with respect to the center position (zero) of the peaks in data and MC was observed. MC did not reflect the same tendency of the shift. In addition, MC distributions were narrower than distributions of real data. This lead us to the use of very lose cuts on these variables in the analyses based on the primary tracks sample. Such approach leads to the larger contribution of the non primary

tracks and influence systematic error connected with this fact. Studies of the impact parameters were performed. Among others we studied behavior of these distribution in different polar angle intervals. As an example distributions of bx impact parameter versus polar angle for different types of negatively charged tracks are shown in Figure 57 and in Figure 58 for real data and MC, respectively

Negatively charged tracks

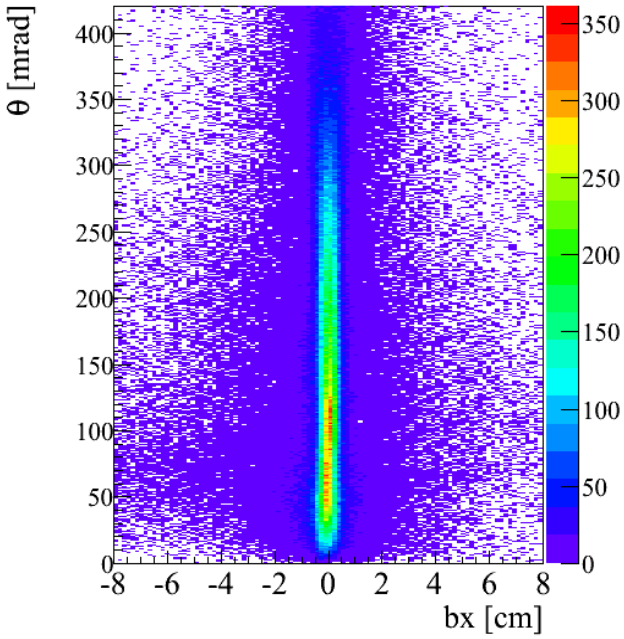

Negatively charged RST

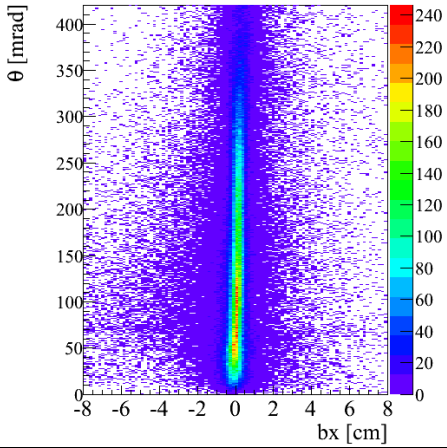

Negatively charged WST

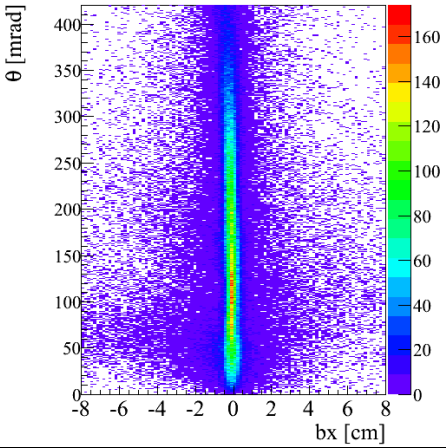

Figure 57. Two-dimensional distributions of bx impact parameter versus polar angle for different types of negatively charged tracks. Real data – reconstructed tracks.

Negatively charged tracks

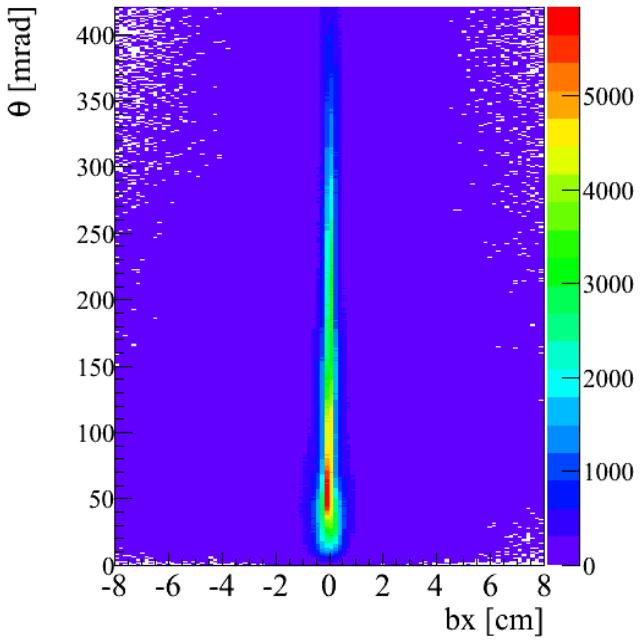

Negatively charged RST

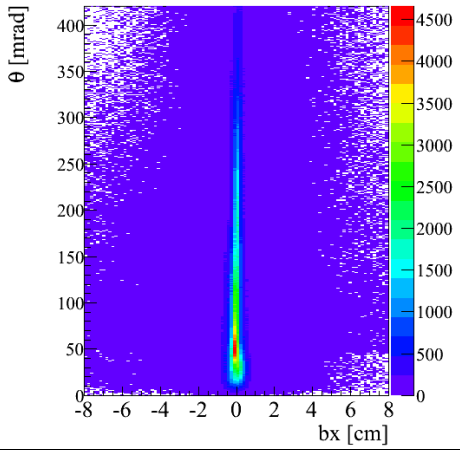

Negatively charged WST

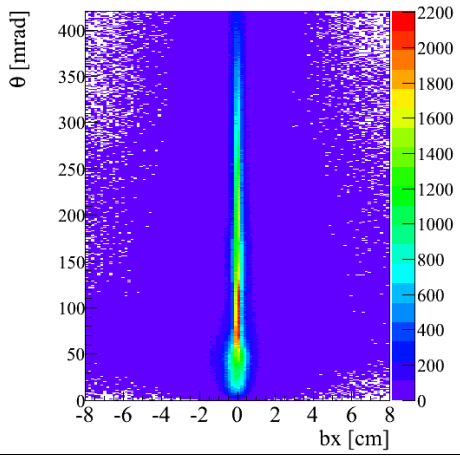

Figure 58. Two-dimensional distributions of bx impact parameter versus polar angle for different types of negatively charged tracks. Monte Carlo – reconstructed tracks.

The reasonable agreement between by impact parameter in polar angle slices for real data and MC predictions was observed. However, small shifts, which were in different directions, of the positions of the peaks were found. Not all details of bx impact parameter distributions were reproduced by Monte Carlo predictions. In particular, in the region below 100 mrad disagreement was larger.

The azimuthal angle distributions for the different types of negatively charged tracks are presented in Figure 59.

Negatively charged tracks

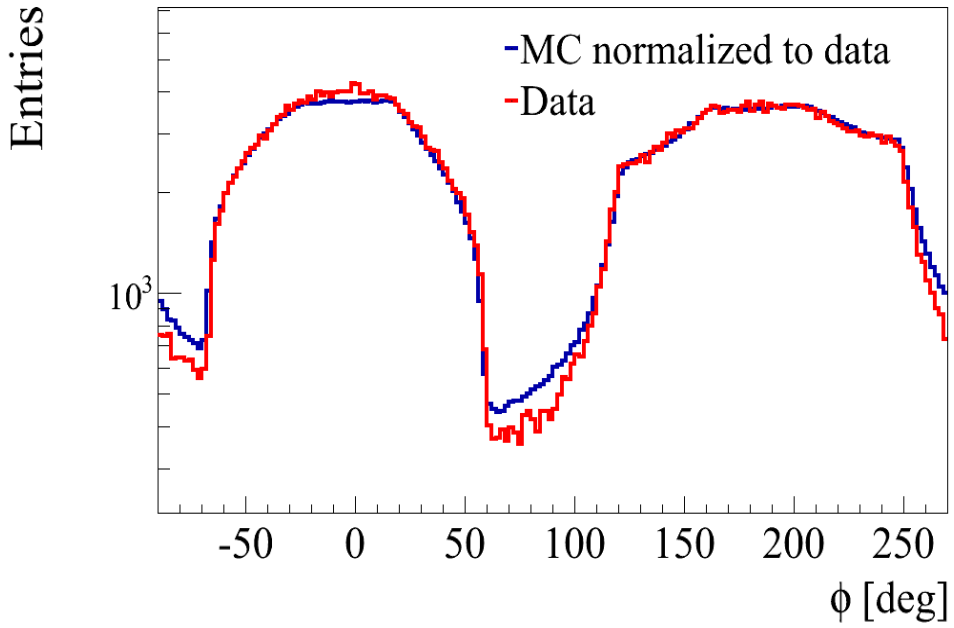

Negatively charged WST [-90, 90] deg	Negatively charged RST [90, 270] deg

Figure 59. Azimuthal angle distributions for the different types of negatively charged reconstructed tracks. The MC normalized to data.

Apart from the regions populated by tracks from the edges of the TPCs, reasonable agreement between real data and MC predictions was observed (notice vertical axis log scale). In our detector possibility of observing tracks in different azimuthal angles for different polar angle slices is different. For a large polar angle values, available region of azimuthal angle in geometrical acceptance is getting smaller what is shown in two-dimensional plots of polar angle versus azimuthal angle for different types of negatively charged tracks - see Figure 60 for real data and Figure 61 for MC (not normalized)).

Negatively charged tracks

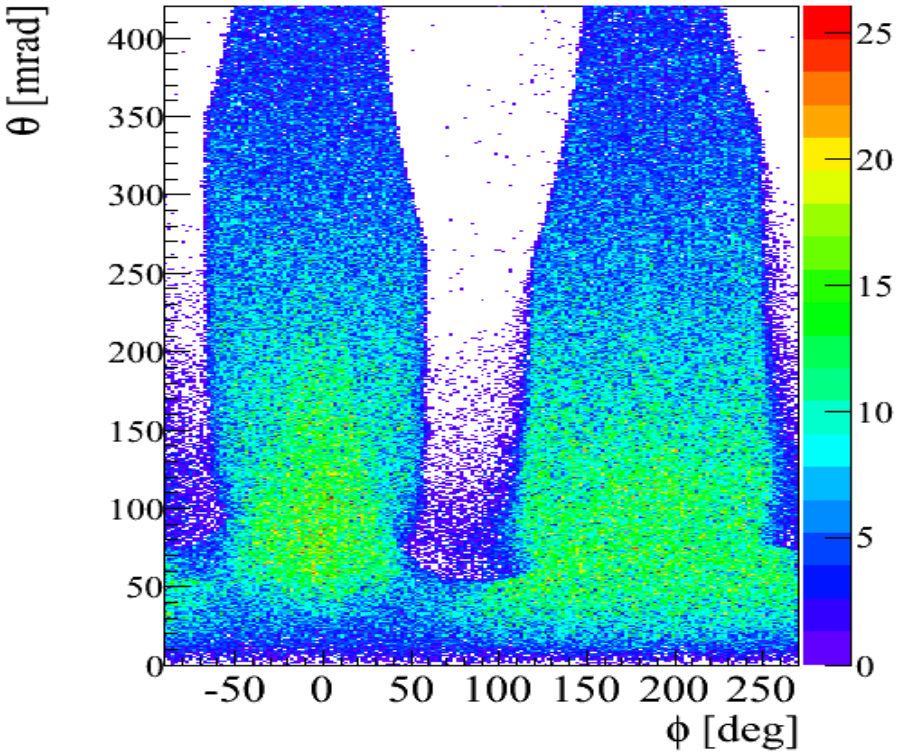

Negatively charged RST

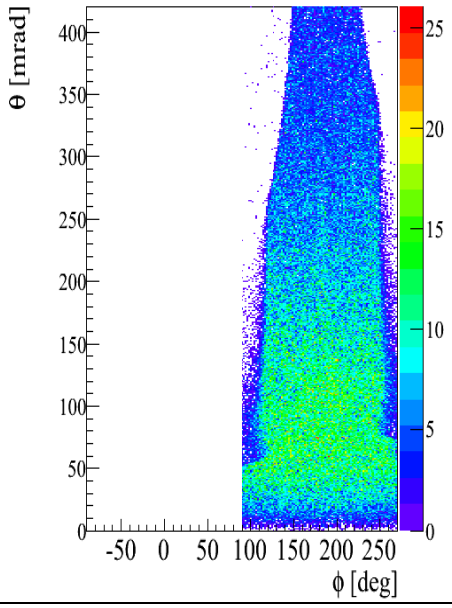

Negatively charged WST

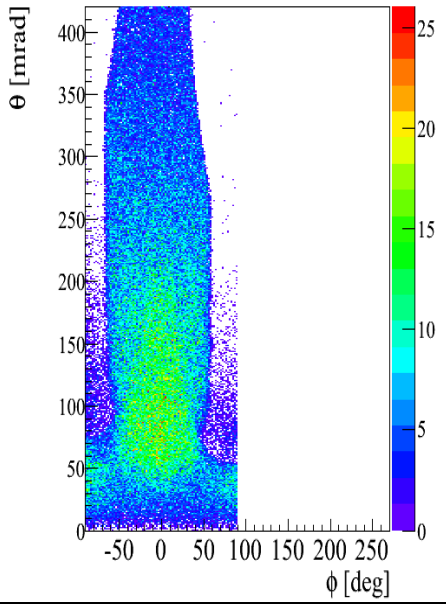

Figure 60. Two-dimensional plots of polar angle versus azimuthal angle for different types of negatively charged tracks. Real data – reconstructed tracks.

Negatively charged tracks

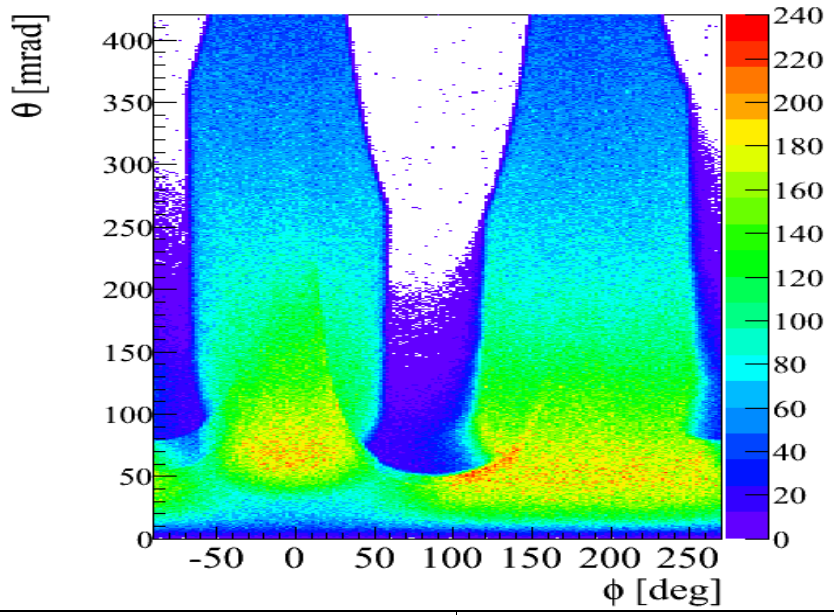

Negatively charged RST

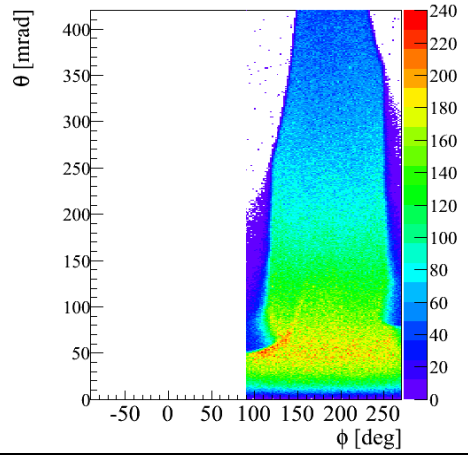

Negatively charged WST

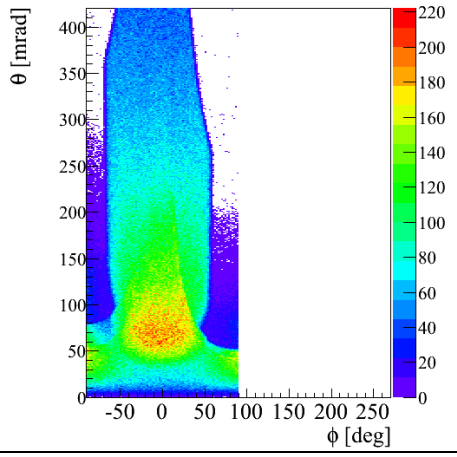

Figure 61. Two-dimensional plots of polar angle versus azimuthal angle for different types of negatively charged tracks. Monte Carlo – reconstructed tracks.

These studies shown that in analyses different azimuthal angle cuts need to be done in different polar angle slices. In h- analysis, which is based on the negatively charged tracks sample, only regions connected with the edges of the TPCs were rejected by azimuthal angle cuts because besides these regions very good agreement between data and MC was found. Azimuthal angle distributions for the polar angles smaller than 60 mrad were free from differences, therefore, cuts in this region were not used.

The transverse momentum, Feynman x, and two-dimensional pictures of transverse momentum versus Feynman x are presented in Appendix I. The good agreement between data and Monte Carlo prediction in those variables was observed.

Presented studies laid the groundwork for the designation of cuts used in the analyses. Author of this thesis and two other PhD students [154, 141] played the crucial role in determination

of the list of basic cuts approved by the NA61 Collaboration as a official cuts for the 2007 data analyses. In these studies we checked influence of different cuts made on the presented above variables. Also the order of appearance of cuts was studied in details.

In addition, presented studies showed that analyses can be conducted using all tracks while appropriate cleaning cuts are applied. It was very important because of the need to maximize the available data statistics to obtain results with high precision. Therefore, all presented analyses in this thesis were made on the whole sample of tracks.

6.7 Reconstruction efficiency and geometrical acceptance of the detector

6.7.1 Geometrical acceptance

Geometrical acceptance studies were performed on the flat phase space simulations. The primary generator was switched off. Particles were generated evenly in each cell in which analyses were performed by simple root macros. Then, such files were passed to the geant3.21, which did propagation of the particles through the detector. Analyses were performed in the three sets of variables: (polar angle, momentum), (rapidity, transverse momentum), and (Feynman x, transverse momentum). The Geant3.21 as a input requires text file which is in the format shown below:

Number_of_tracks Event_Number
Particle_Id px py pz

Therefore, after generation of the flat phase space information in variables used in the analyses one had to convert that information to the geant input format. These conversions were done using formulas listed below:

- In momentum and polar angle variables:
  - px = p sinθ cosφ
  - py = p sinθ sinφ
  - pz = p cosθ
- In rapidity and transverse momentum variables:
  - px = p_T cosφ
  - py = p_T sinφ
  - pz = $\sqrt{m^2 + p_T^2}\sinh y$
    - where m is a mass of the particle
- In Feynman x and transverse momentum variables:
  - px = p_T cosφ
  - py = p_T sinφ
  - pz = $\gamma\,(p_{ZCMS} + \beta\sqrt{p_{ZCMS}^2 + p_T^2 + m^2})$
    - where $p_{ZCMS} = x_f \frac{\sqrt{s}}{2}$

In geant3.21 only energy loss of particles was switched on. Other physics cards were switched off. The physics cards used in these studies are listed in appendix.

In this chapter geometrical acceptance of the NA61/SHIEN detector in respect to the TPCs track analyses is presented. The studies were performed in all sets of variables, however, we will discuss here only momentum and polar angle set.

The two-dimensional plot of the geometrical acceptance in momentum and polar angle variables in respect to the h- analysis (based on the TPCs tracks) is shown in Figure 62.

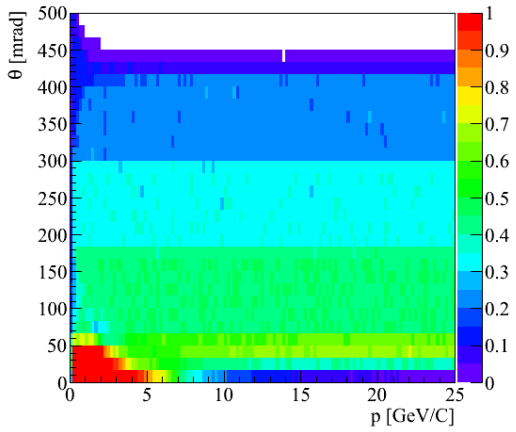

Figure 62. Geometrical acceptance plot in momentum and polar angle variables in respect to the h- analysis.

The decreasing of the acceptance for the larger polar angle values is connected with the geometry of the detector and azimuthal angle cuts used in h- analysis. The azimuthal angle cuts in this approach were only rejecting edges of the distributions. Therefore, presented picture can be treated as approximation of the geometrical acceptance of the TPCs. In this picture, azimuthal angle cuts affects only sharpness of the transitions between different regions of acceptance. At low polar angle values and larger momenta drop of acceptance was observed which is connected with the gap between TPCs. In future analyses based on the 2009 data this region will be covered because from 2009 small TPC called GAP-TPC was used and information from it was reconstructed in the reconstruction chain. In 2007 data information from GAP-TPC was not available.

However, from the T2K point of view, the most important phase space region is fully covered by the TPCs geometrical acceptance. The geometrical acceptance of the tracks reaching TOF detectors is significantly smaller what can be seen in the two-dimensional distributions of polar angle versus momentum of TPCs+TOFs tracks reconstructed to the primary vertex for real data (for positively charged tracks see Figure 63, for different types of tracks see appendix). The TOF information is needed for the positively charged pion identification.

Positively charged tracks

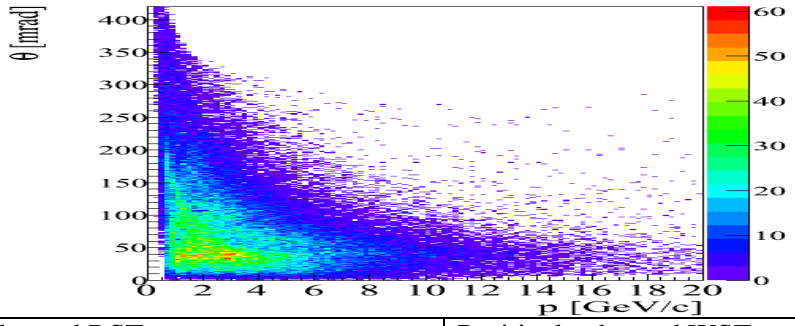

Positively charged RST

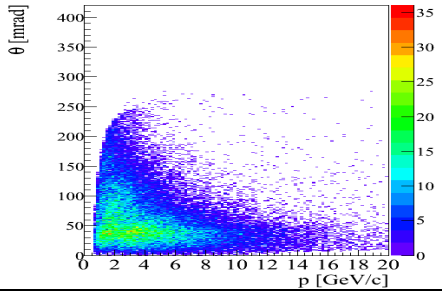

Positively charged WST

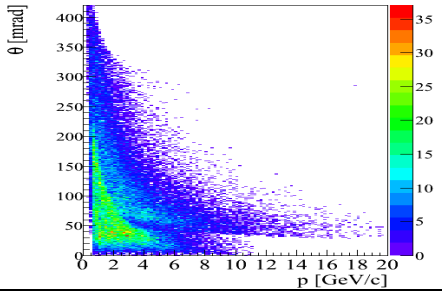

Figure 63. Two-dimensional distributions of polar angle versus momentum of TPCs+TOFs positively charged tracks reconstructed to the primary vertex. Real data.

For the polar angles larger than 250, only the WSTs are registered. The presented two-dimensional momentum versus polar angle plots show advantage of the global correction analysis, which is not using TOF detectors. In this case results can be obtained in larger phase region.

6.7.2 Reconstruction efficiency

The reconstruction efficiency was studied for different types of track topologies (All, RSTs, WSTs), tracks with different charge (positively and negatively charged tracks separately), tracks registered in different TPCs (only VTPC1, VTPC1+VTPC2, All TPCs). In addition, we studies reconstruction efficiency for different types of particles: primary π^+s, π^-s, protons, secondary e^+s, e^-s.

- Different track topologies.
  - The studies of the reconstruction efficiency of all tracks reconstructed to the primary vertex, and subsamples of those tracks - RSTs, and WSTs shown that different track topologies are reconstructed in the same way with the same efficiency. The efficiencies were at the level of ~98-99% in a wide range of phase space besides small momentum region (below 400 MeV/c)
  - The efficiencies for these types of tracks are at the same level as for the negatively charged tracks samples and/or positively charged track samples which will be discussed in details in this chapter.

- Tracks registered in different TPCs.
    - We found that efficiencies for different detectors are almost at the same level and consistent with efficiencies computed for different track topologies. The small drop (less than 3%) of the efficiency of tracks registered in VTPC1+VTPC2 at a few GeV/c momentum region compared to VTPC1 and all TPCs efficiencies was found.
- Tracks with different charge
    - The maps of reconstruction efficiencies in momentum and polar angle variables were computed for positively and negatively charged tracks reconstructed to the primary vertex (see Figure 64, Figure 65)

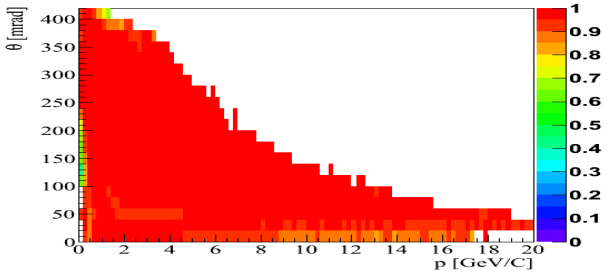

Figure 64. Reconstruction efficiency as a function of momentum and polar angle of the negatively charged tracks reconstructed to the primary vertex.

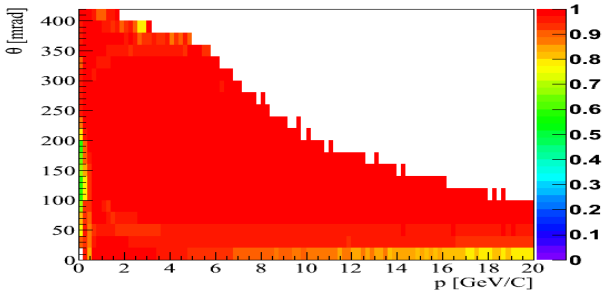

Figure 65. Reconstruction efficiency of the positively charged tracks reconstructed to the primary vertex.

The drop of the reconstruction efficiencies at the low polar angle values and larger momenta is connected with the gap in the acceptance. These regions are not fully covered by the detector, therefore, there were rejected in the analyses. In the [0, 20] mrad polar angle interval, the full geometrical acceptance of NA61/SHINE detector is up to 7.2 GeV/c. Apart from these regions, reconstruction efficiency for both negatively and positively charged tracks is flat in a whole momentum and polar angle phase space. It amount to ~98-99% besides very low momentum region where we found drop to ~60% at ~100MeV/c. Therefore, the analyses start at the 200MeV/c in momentum because below this value momentum determination of the tracks at our detector is almost impossible.

The one-dimensional pictures of the reconstruction efficiencies versus momentum of negatively and positively charged tracks are presented in Figure 66.

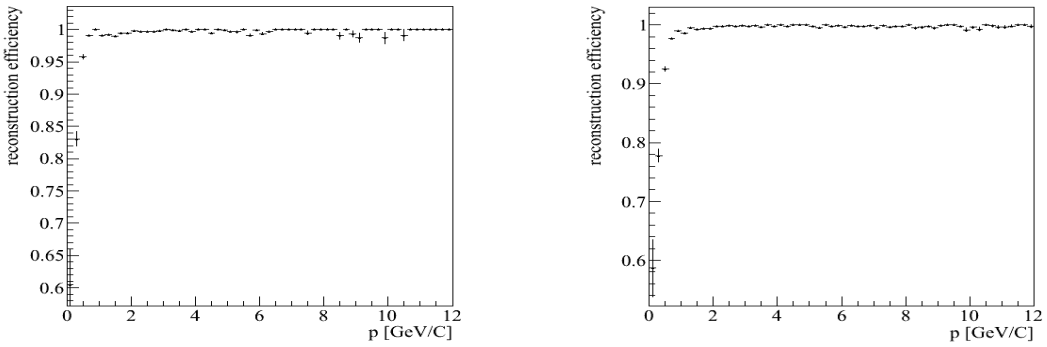

Figure 66. Reconstruction efficiencies versus momentum of negatively (left) and positively (right) charged tracks.

- Reconstruction efficiencies of different types of particles:
  - primary π^+s, π^-s, and protons,
  - secondary e^+s and e^-s (also from the decays of the short live particles eg. π^0 decays).

- The maps of reconstruction efficiencies for different types of particles computed in momentum and polar angle variables are shown in Figure 67.

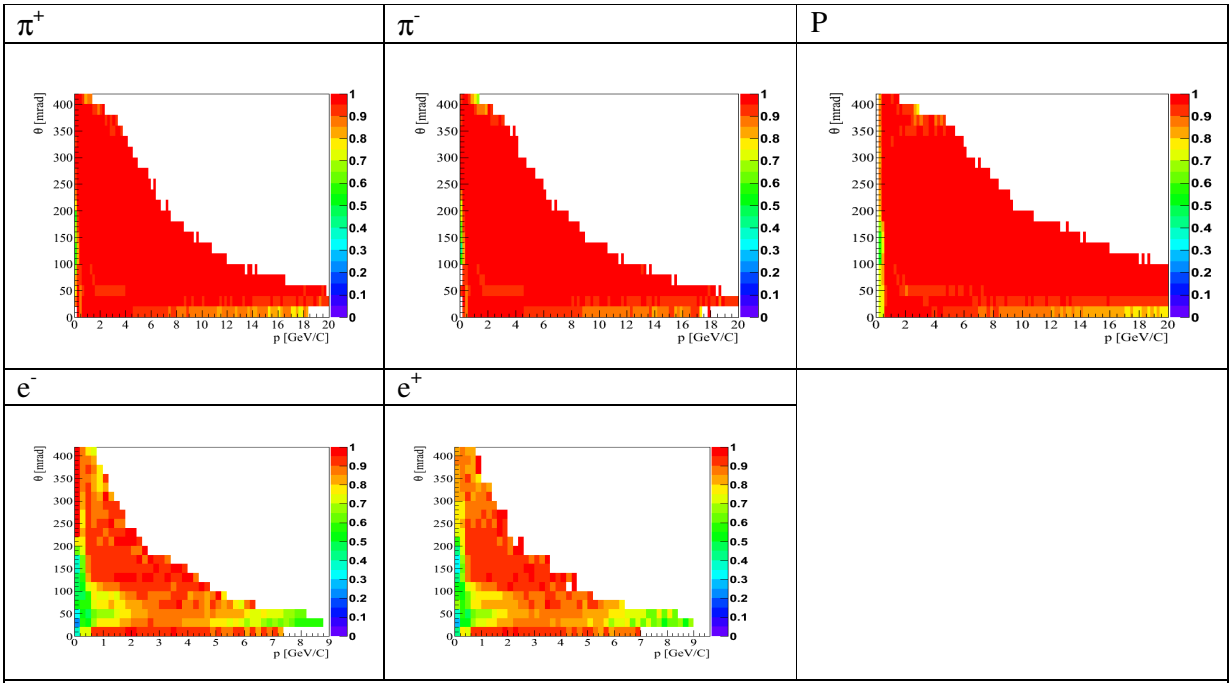

Figure 67. Two dimensional maps of reconstruction efficiencies in polar angle and momentum variables for different types of particles.

The primary tracks have the same reconstruction efficiencies which are at the level of ~98-99% besides very low momentum region. No differences between negatively charged pions, positively charged pions, and protons were found.

The tested secondary particles i.e. electrons and positrons have the same reconstruction efficiencies (~92-95%) which are, however, at a lower level than the efficiencies of the primary particles (~98-99). The one-dimensional pictures of the reconstruction efficiencies versus momentum of secondary electrons and positrons are presented in Figure 68.

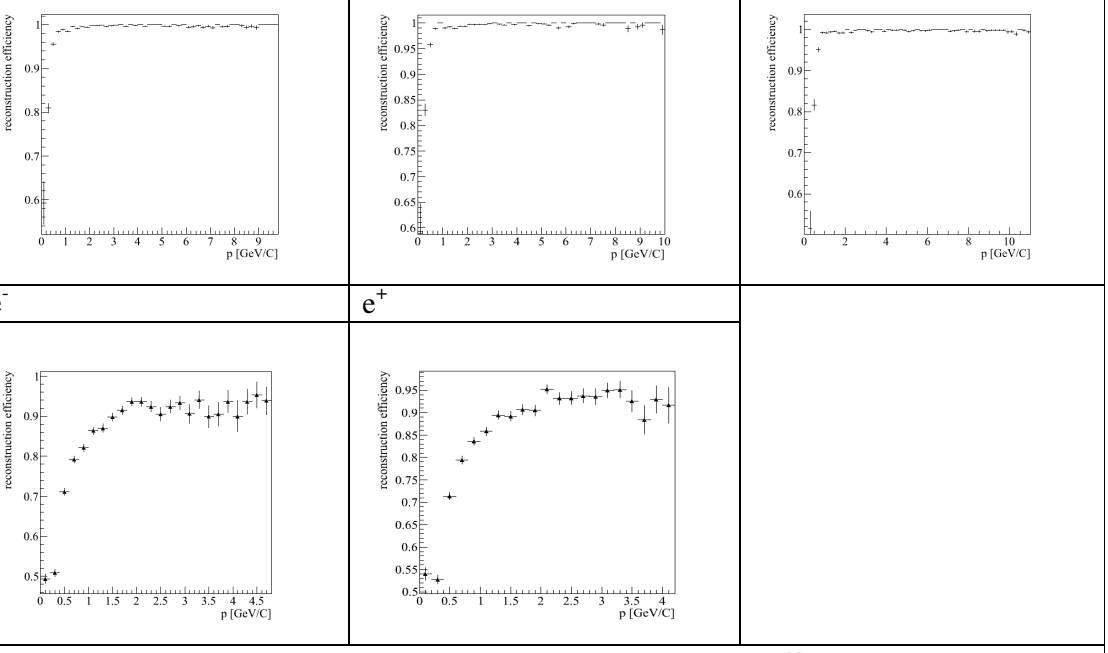

Figure 68. One-dimensional pictures of the reconstruction efficiencies versus momentum of primary positively charged pions, negatively charged pions, protons, secondary electrons, and positrons.

These drops in efficiencies can be explained by the fact that along the electron and positron track due to Bremsstrahlung phenomenon photons are produced what affects the smoothness of the track. Additional track cuts, which are used in primary vertex analysis, slightly improve reconstruction efficiencies of electrons and positrons (to the level of 94-98%) mainly for the fact that longer tracks are selected and the larger emphasis is put to reconstruct whole trace of the track.

These studies lead to the conclusion that the track reconstruction efficiency does not strongly depend on the tracks topologies, and charge of the particles. It is flat in the momentum and polar angle variables and in a wide phase space region is equal to ~98-99% for primary vertex tracks and ~92-95% for secondary vertex tracks which could be badly reconstructed as primary.

The reconstruction efficiency studies were also made in different types of variables: rapidity and transverse momentum, and Feynman x and transverse momentum. These studies had similar outcome and will not be discussed in this thesis.

Chapter 7 Study of negatively charged hadron production from the primary vertex (h- method)

7.1 Analysis method

The analysis of negatively charged pions is based on theoretical and experimental premises stating that the production of negative particles at low energies results mainly in negative pion mesons with small admixture of electrons, negative kaons, and almost negligible fraction of antiprotons (see Figure 69).

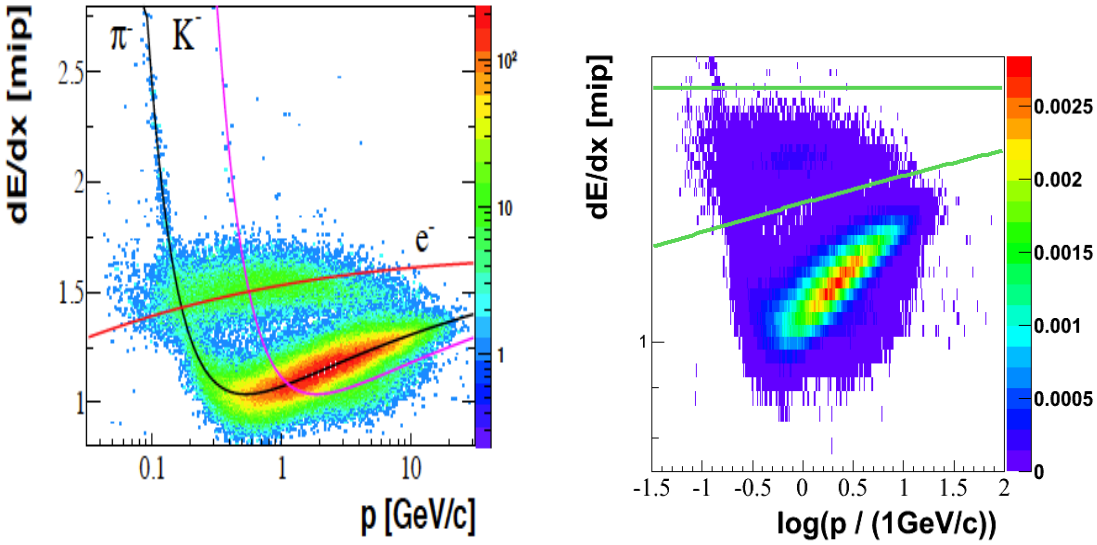

Figure 69. Measured dE/dx as a function of momentum for negatively charged particles reconstructed to the primary vertex with Bethe-Bloch curves superimposed (left). Zoomed region, distribution normalized by the number of tracks (right). The green lines show basic cuts used to estimate number of electrons (right). The thin Carbon target.

The number of e- and e+ of momenta larger than 200 MeV is almost the same in our data [150]. It confirms the origin of electrons from the dilepton pairs - either from internal (meson Dalitz decays) or the external conversion. The main role is played by $\pi^0 \to \gamma\gamma$ decay (BR = 98.823 ± 0.034 %) and subsequently γ conversions. From the basic calculations, if we took into account that the mean free path for photons is equal to the 9/7 of Xo for electrons because the photons loose their energy only via pair production, we can estimate relative number of electrons produced from this process. The radiation length of graphite is equal to 42.7 g/cm^2, density of the graphite thin target is equal to 1.84 g/cm^3. Therefore, the mean free path λ is equal to 29,8 cm. The probability of the e^+ e^- pair production in $\pi^0 \to \gamma\gamma$ decay for 1 cm distance can be expressed by this formula: $P = 2\,(1 - \exp(-1/\lambda))$
where 2 comes from the fact that two photons can convert. In conclusion, the e^+ e^- pair production occurs for 6.8% of π^0s. The next sources of the electrons are π^0 Dalitz decays ($\pi^0 \to e^+e^-\gamma$), η decays, and ρ decays. The branching ratio of the π^0 Dalitz decay is equal to 1.174 ± 0.035 %.
The contribution from η and ρ decays is small relatively to the sources discussed above because at our energy production of these mesons is rare. If we neglect this admixture, the e^+ e^- pair production occurs for 8% of π^0s. The number of π^0 can be estimated from the equation:

1/2 (< π^+> + <π^->) motivated by isospin symmetry. In VENUS simulation the mean number of π^+ is ~1.2 times mean number of π^-. Consequently, the number e- should be equal to about 8.8% of the number of negatively charged pions.

The basic dE/dx cuts (see Figure 69) allow estimating number of electrons in the real data. The used procedure as an outcome gives not the exact number of electrons because in this approach in the region where electron and pion's Bethe Bloch curves crosses all particles are counted as electrons. From this procedure number of e- candidates was estimated to be about 10% of the other negatively charged particles. This result is consistent with the analytical estimation and with Monte Carlo predictions.

If we took into account admixture of electrons, negative kaons, antiprotons, and decay products the preliminary information on the differential cross sections for the pions production from the proton Carbon interactions can be obtained even before the detailed identification studies. This approach is valid in the wide phase space region. The negatively charged pion analysis in the thin target case is based on selection of negatively charged tracks fitted to the primary vertex. In the T2K replica target case analysis is based on selection of backward propagated tracks (in NA61/SHINE nomenclature so called rtracks) to surface of the target. The electron contribution in this case is larger (see Figure 70). Therefore, this method will have larger model dependent uncertainty in the low momentum region.

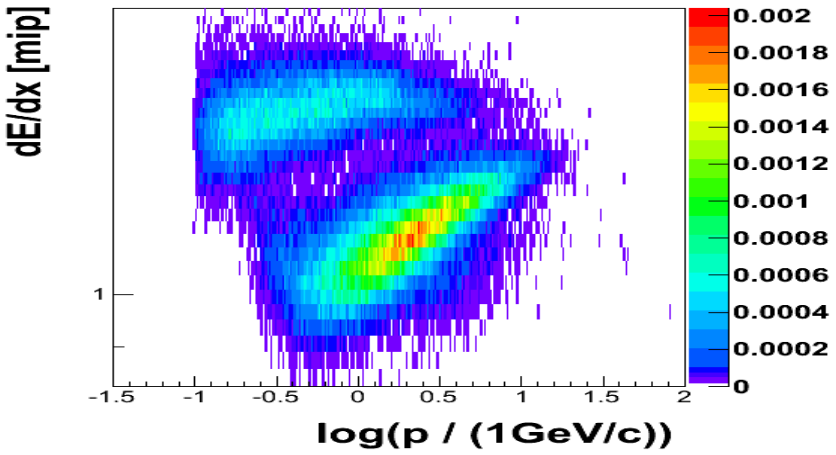

Figure 70. Measured dE/dx as a function of momentum for negatively charged particles reconstructed to the primary vertex. Normalized by the number of tracks. The T2K replica target.

In the MC case we are able to recognize the true origin of the track (primary or secondary) and its true momentum (p), emission angle (θ). We are also able to calculate for each particle its Feynman x (xf), rapidity (y), transverse momentum (p_T). It permits to find the ratio between initial number of primary particles of a given type and the number of tracks reconstructed as a "primary" in a given (p, θ), (xf, p_T), (y, p_T) cells. It also permits to find the ratio between number of backward propagated pions and the number of all backward propagated tracks what is important in the T2K replica target case. Monte Carlo chain (VENUS, Gheisha, Geant3) is used to find information on geometric acceptance and reconstruction efficiency, measurement smearing, decays, and non-pion admixture. In 2C target case it is also used to predict correction for decays. Using MC correction factor corrected negative pions spectrum is obtained. The method applied does not use the information on particle identification. With the use of dE/dx analysis and TOF information, it

is possible to verify the achieved results. Thus, it is possible to put corrections into MC models and then verify achieved results and in this iterative manner, to gain a better understanding of the physics of investigated process. Monte Carlo simulations are used to correct the acquired data both for physical and detector effects. In pion analyses detector effects are dominant. In pion analysis case physics effects do not play crucial role (in a wide range of phase space correction for the physics effects is at the level of a few percents).

7.1.1 The thin carbon target analysis

The analysis in thin carbon target case is carried out as follows:

1. Negatively charged tracks reconstructed to the primary vertex are selected from data and then quality cuts are applied.
2. Monte Carlo method is used to model the proton carbon interaction and then simulated tracks are led through the detector using Geant3 code.
3. Correction factors can be estimated for example in (p, θ) variables (the same approach can be done in (xf, p_T) and (y, p_T)):

$C(p; \theta)pion = Nsp(p; \theta)/Nr(p; \theta)$

where: Nsp - simulated negative primary pion tracks,
and Nr - all negative tracks after quality cuts (the same as used for real data) reconstructed to the primary vertex.
Correction factor error calculation is done taking into account correlated part of correction nominator and denominator, in this case binomial distribution is used, and uncorrelated part, when standard error calculation is used. Split into these two parts must be done because in the reconstructed to the primary vertex tracks sample we have not only primary tracks - we have also non-primary tracks badly reconstructed to the main vertex (mainly electrons).

4. Finally, the correction factor estimated with MC is used to acquire corrected spectra of negative pions.

Overall, in this method, the correction factor is estimated by analysis of MC events reconstructed in the same manner as the real data. As a result of such analysis, one factor correcting for all effects is obtained. Different corrections were studied separately and inaccuracies connected with them were taken into account in the systematic error studies.

7.1.2 The T2K replica target analysis

In the T2K replica target data case analysis is carried out as follows:

1. tracks backward propagated to the replica target are selected from data and then quality cuts are applied.
2. Correction factors for pion analysis is estimated (in p θ case):

$C(p; \theta)pion = Nsp/Nr$

where: Nsp - simulated negative pion tracks which are coming out from the replica target (p, θ),
and Nr - all negative tracks backward extrapolated to the replica target (p, θ)

3. This approach can not be used in some phase space regions where contribution of the other negative particles is large. In the T2K replica target especially contribution of electrons at low momentum region is huge. Such a phase space regions are determined using dE/dx information and was not taken into account for further analysis.
4. Using correction factor corrected spectra of backward propagated pions are obtained.

Such an approach can be done for different parts of the target separately. Six different slices of the target were selected (five slices in z and upstream face of the target) based on the

mc simulation studies made by T2K Collaboration.
In this case correction factors are calculated using this equation:
C(p; θ; z)pion = Nspz/Nrz
where: Nspz - simulated negative pion tracks which are coming out from the replica target (p, θ, z), and Nrz - all negative rtracks backward extrapolated to the replica target (p, θ, z).

In the T2K replica case only analysis in (p, θ, z) variables was performed.

7.2 Selection of events and tracks

7.2.1 Event cuts

Analysis is done on the data collected in 2007 run. For an event selection, cut based on Beam Position Detector (BPD) information was used which was cleaning BPD outliers and ensured a well-defined beam track. Information from BPD detectors before and after event cuts for thin target data is presented in Figure 71. BPD cuts are based on the selection of events with signals in each plane of all three BPD detectors together with correctly reconstructed beam tracks that have measured points on both planes of BPD-3.

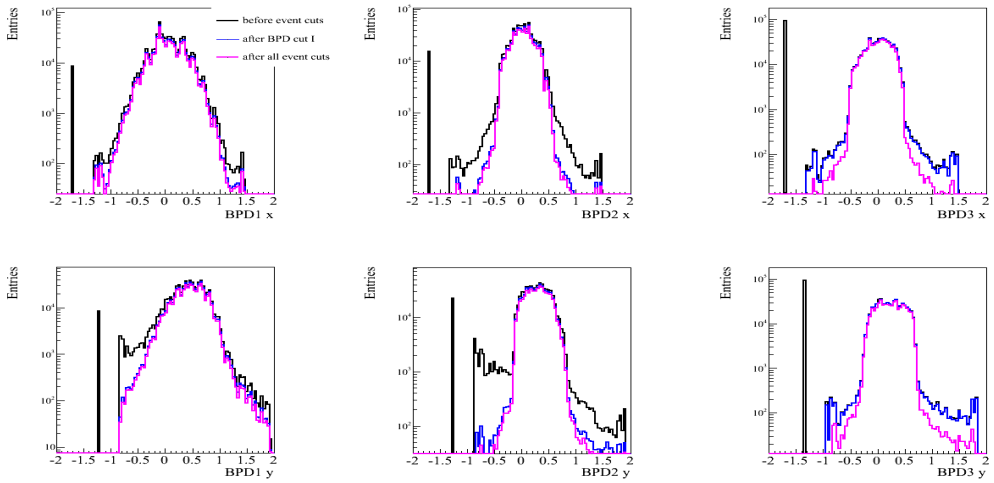

Figure 71. BPD Information before and after event cuts. Black line - All collected events. Blue line - events after BPD Cut I. Pink line - after all event cuts (BPD Cuts I+II).

7.2.2 Track cuts

In thin carbon target data analysis after event cuts based on the information from BPDs, to select clean sample of tracks the following track cuts were applied:

First of all, we selected negatively charged tracks from the main vertex.
In standard cuts case five additional cuts were applied to obtain clean tracks sample:

First, cut for the number of points measured in time projection chambers VTPC1 and VTPC2 was applied to ensure appropriate measurement of momentum, which is estimated in those detectors based on the analysis of the curvature of tracks (NPoint VTPC1+VTPC2>= 12). It means that at least twelve measured points in sum of vertex time projection chambers are needed. No constrains are put on number of points in separate VTPCs. It means that we can have for example at least 12 points in VTPC1 or at least 12 points in VTPC2 and such a track will fulfill this cut.

Another cut involved the number of measured points in a track, which was set as higher than 30. This cut was used for selection of well-defined tracks placed mostly within the geometric acceptance of the detector.

Very loose cut for impact parameter was also applied (|bx| and |by| <= 4.0).

Fourth, cut on the ratio between number of fitted points and number of potential points was applied (point ratio> 0:5). This cut was used to exclude double matching of parts of the tracks.

Last, cuts on azimuthal angle (phi) in polar angle slices (θ) were used. In case of h- analyses in (x_F, p_T) and (y, p_T) the same cuts were applied. It was checked that after phi cuts in θ slices phi distributions in p_T slices are reproduced well by Monte Carlo. In this case there was no need to change phi cuts in (x_F, p_T) and (y, p_T) h- analyses. Standard h- phi in θ slices cuts are based on the comparison of data and Monte Carlo. Very good agreement was found for θ smaller than 60 mrad. In this region no phi cuts were applied. In θ region between [60, 180], [180, 300], and [300, 420] mrad respectively 40, 30, and 20 degree phi cut were applied. Such a cuts were chosen after detailed Monte Carlo studies. Impact of change of values of cuts was studied and implemented in systematic error studies.

7.2.3 Effects of the quality cuts on the number of events and tracks

Analyses were made on two samples of events, which were differently reconstructed. Two reconstruction chains were used: one based on the REFORM client, second one based on the DOMERGE client. Data reconstructed with reform are tagged as 07N production and data reconstructed with DOMERGE are tagged as 07M production. Analyses on two productions were done to estimate systematic error connected with reconstruction chain used.

The effects of the quality cuts on the number of events and tracks are summarized in Table 9 and in Table 10.

Event Cuts	Number of events 07N production	Number of events 07M production
Before cuts	671824	671917
BPD Cut I	565576 (~84% of events)	565662 (~84% of events)
BPD Cut I+II	521238 (~78% of events)	521315 (~78% of events)

Table 9. Effects of the quality cuts on the number of events. Thin carbon data.

In Monte Carlo chain BPDs are not included. Simulations are done in this way that they lead to properly generated events – primary protons always interact with the nuclear target.

	Number of tracks data 07N production	Number of tracks MC 07N production	Number of tracks data 07M production	Number of tracks MC 07M production
Number of tracks after event cuts	1204556	15803501	1224970	16064440
Number of negatively charged tracks after event cuts	437688 ~36% of all	5583682 ~35% of all	446282 ~36% of all	5684842 ~35% of all
Number of track with minimum	380051 ~31% of all	4884612 ~31% of all	388021 ~32% of all	4972927 ~31% of all

number of the found points in the VTPC1+2 of 12	~87% of neg	~87% of neg	~87% of neg	~87% of neg
Number of tracks with number of measured points larger than 30:	279254 ~23% of all ~64% of neg	3667069 ~23% of all ~66% of neg	282373 ~23 of all ~63% of neg	3685214 ~23% of all ~65% of neg
Number of tracks after cut on impact parameter $\|Bx\| \leq 4.0$ and $\|By\| \leq 4.0$	269208 ~22% of all ~61% of neg	3573108 ~23% of all ~64% of neg	270803 ~22% of all ~61% of neg	3582881 ~22% of all ~63% of neg
Number of tracks after cut on the point ratio	268191 ~22% of all ~61% of neg	3573103 ~23% of all ~64% of all	258173 ~21% of all ~58% of neg	3450036 ~21% of all ~61% of neg
Number of tracks after phi cuts in θ slices	198568 ~16% of all ~45% of neg	2513868 ~19% of all ~45% of neg	189556 ~15% of all ~42% of neg	2760210 ~17% of all ~48% of neg

Table 10. Effects of the quality cuts on the number of tracks. The thin carbon data and MC.

The T2K replica target analysis was based on the provisionally reconstructed data. Therefore this analysis should be treated as an example that such approach has the ability to obtain negatively charged pion yields. In this case no systematic error studies were done. To select clean sample of events besides BPD Cut additional wave form analyzer cut was used. The effects of the event cuts on the number of events are summarized in Table 11.

	Number of events	% of all events
Wave form analyzer cut	131677	~ 56
BPD Cut 1	108901	~ 46
BPD Cut 2	109402	~ 46

Table 11. Effects of the quality cuts on the number of events. The T2K replica target data.

Track selection in T2K replica target case was different than in thin carbon target case. Only basic cuts were done: cut on number of point registered in VTPC1 plus VTPC2 and number of measured points in all TPCs. Programs developed by author of this thesis were passed to ETH Zurich group and will be further expand within NA61 and T2K collaborations. The effects of track cuts on the number of tracks are summarized in Table 12.

	Number of tracks	% of all tracks
Negatively charged tracks	115813	~ 40
Measured points in VTPC1+VTPC2 cut	110487	~ 38
Measured points in TPCs cut	81830	~ 28

Table 12. Effects of the quality cuts on the number of tracks. The T2K replica target data.

7.3 Data after event and track cuts

Studies of available statistics of uncorrected thin carbon data allowed to determine bin sizes in different variables in such a way that:

- T2K needs were fulfill (momentum and polar angle variables)
  - Full T2K phase space region should be covered
  - Momentum region between 0.5-2.5 GeV/c is most important
  - Small polar angle values (0-60 mrad) should be precisely scanned
- Forward-backward asymmetry of pC interaction was precisely sampled (Feynman x and transverse momentum variables and rapidity and transverse momentum variables)
  - In sampling of negative xf values main limitation is detector acceptance

For the T2K replica target, bining was chosen to obtain reasonable statistics in not to large bins.

7.3.1 Thin carbon data

7.3.1.1 Uncorrected data in momentum and polar angle variables

The uncorrected data after event and track cuts (presented in chapter 7.2) in momentum and polar angle variables are presented in Figure 72. In addition two-dimensional map of selected bining with information about statistical errors is shown.

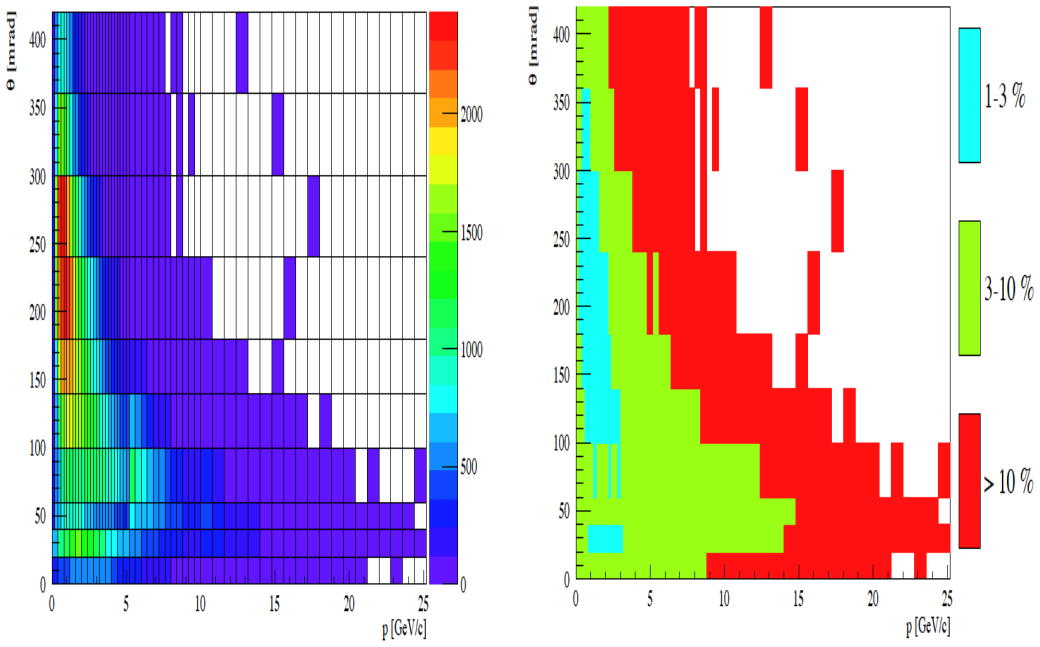

Figure 72. Uncorrected negatively charged tracks reconstructed to the primary vertex in momentum and polar angle variables after event and track cuts used in h- analysis (left). The relative statistical error in selected binning (right).

7.3.1.2 Uncorrected data in Feynman x and transverse momentum variables

The uncorrected data after event and track cuts (presented in chapter 7.2) in Feynman x and transverse momentum variables are presented in Figure 73. In addition two-dimensional map of selected bining with information about statistical errors is shown.

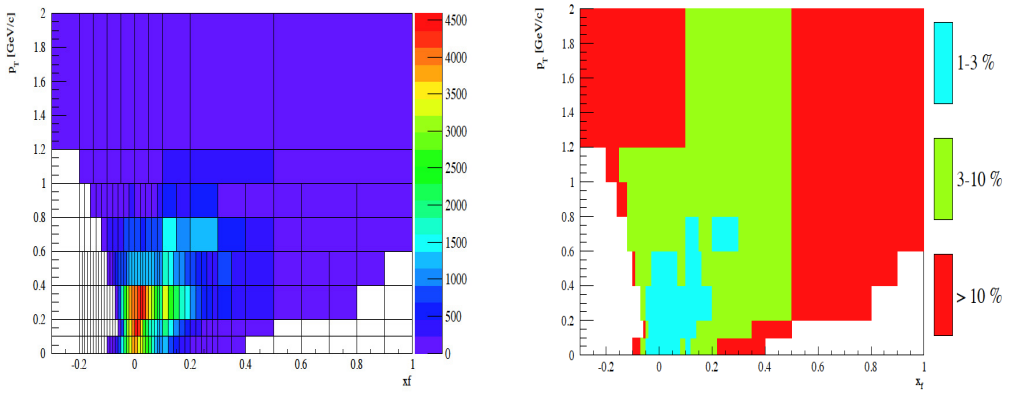

Figure 73. Uncorrected negatively charged tracks reconstructed to the primary vertex in Feynman x and transverse momentum variables after event and track cuts used in h- analysis (left). The relative statistical error in selected binning (right).

7.3.1.3 Uncorrected data in rapidity and transverse momentum variables

The uncorrected data after event and track cuts (presented in chapter 7.2) in rapidity in c.m.s assuming pion mass and transverse momentum variables are presented in Figure 74. In addition two-dimensional map of selected bining with information about statistical errors is shown.

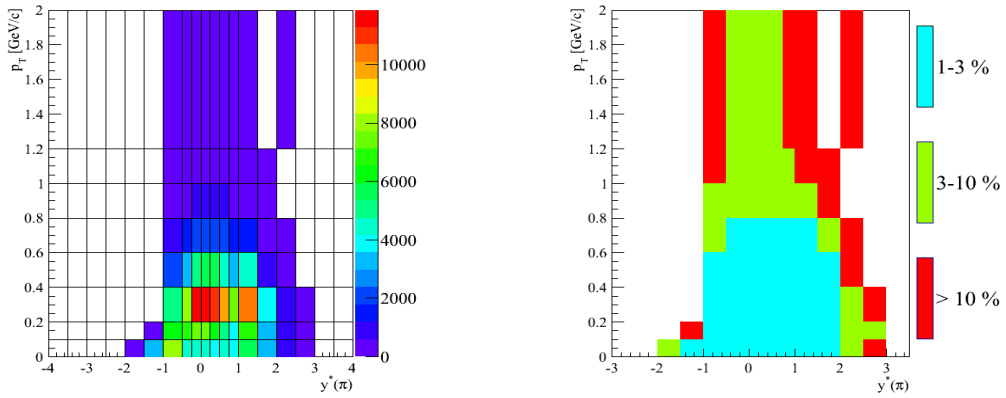

Figure 74. Uncorrected negatively charged tracks reconstructed to the primary vertex in rapidity and transverse momentum variables after event and track cuts used in h- analysis (left). The relative statistical error in selected binning (right).

7.3.2 T2K replica target

The uncorrected data after event and track cuts (presented in chapter 7.2) in momentum and polar angle variables for different parts of T2K replica target are presented in Figure 75. Studies were performed in the six parts of the target along the z axis. As a last part upstream face of the target was selected. The selection of these target parts has been imposed by the T2K collaborations, preceded by detailed Monte Carlo simulations.

Slice 1
Z [-625.7, -634.7]

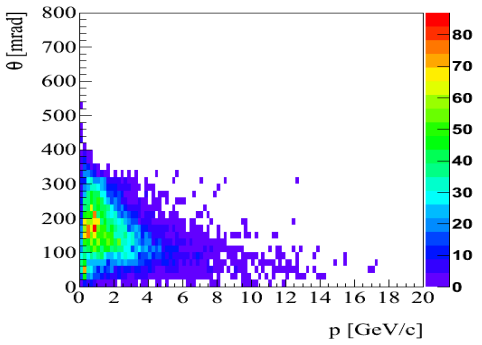

Slice 2
Z [-643.7, -616.7]

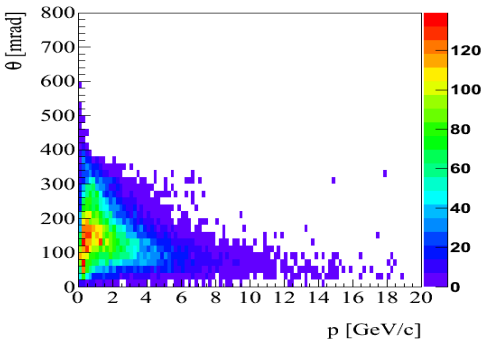

Slice 3
Z [-616.7, -598.7]

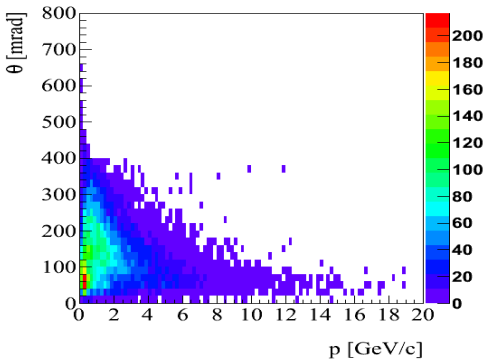

Slice 4
Z [-598.7, -580.7]

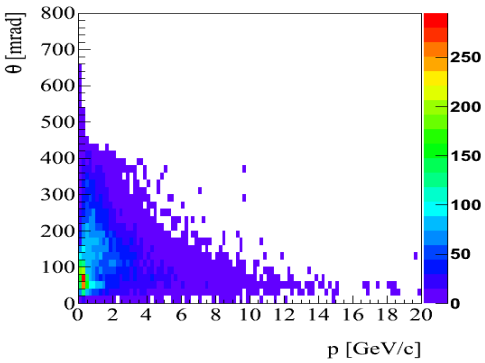

Slice 5
Z [-580.7, -562.7]

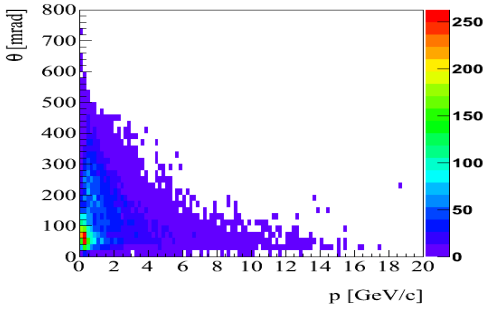

Slice 6 (upstream face of the target)
Z >= -562.7
Vertex $x^2+y^2 < 1.3$

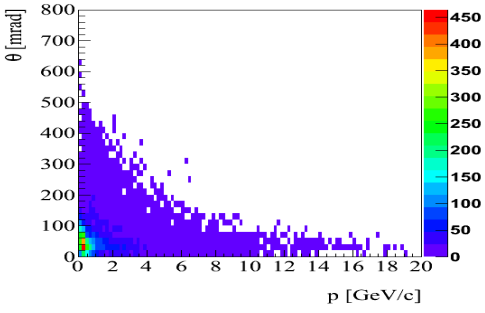

Figure 75. Two-dimensional momentum versus polar angle plots of uncorrected backward propagated tracks to the taget surface for different parts of T2K replica target after all cuts.

7.4 Correction factors and corrected data

The correction factors were calculated accordingly to the formulas presented in chapter 7.1. The corrected data presented in this chapter are not normalized. Detector effects (like geometrical acceptance, reconstruction efficiency) and model corrections (i.e. in the thin carbon target case electron contamination, pion decays, and correction for other primary particles) were included. In thin carbon case as a outcome we have information about primary pions produced in proton Carbon interactions. In T2K replica target case, corrections lead to information about all pions (primary and secondary) leaving the target.

7.4.1 Thin carbon data

7.4.1.1 Correction factors in momentum and polar angle variables

The two-dimensional efficiency (c^{-1}) plot in momentum and polar angle variables is shown in Figure 76.

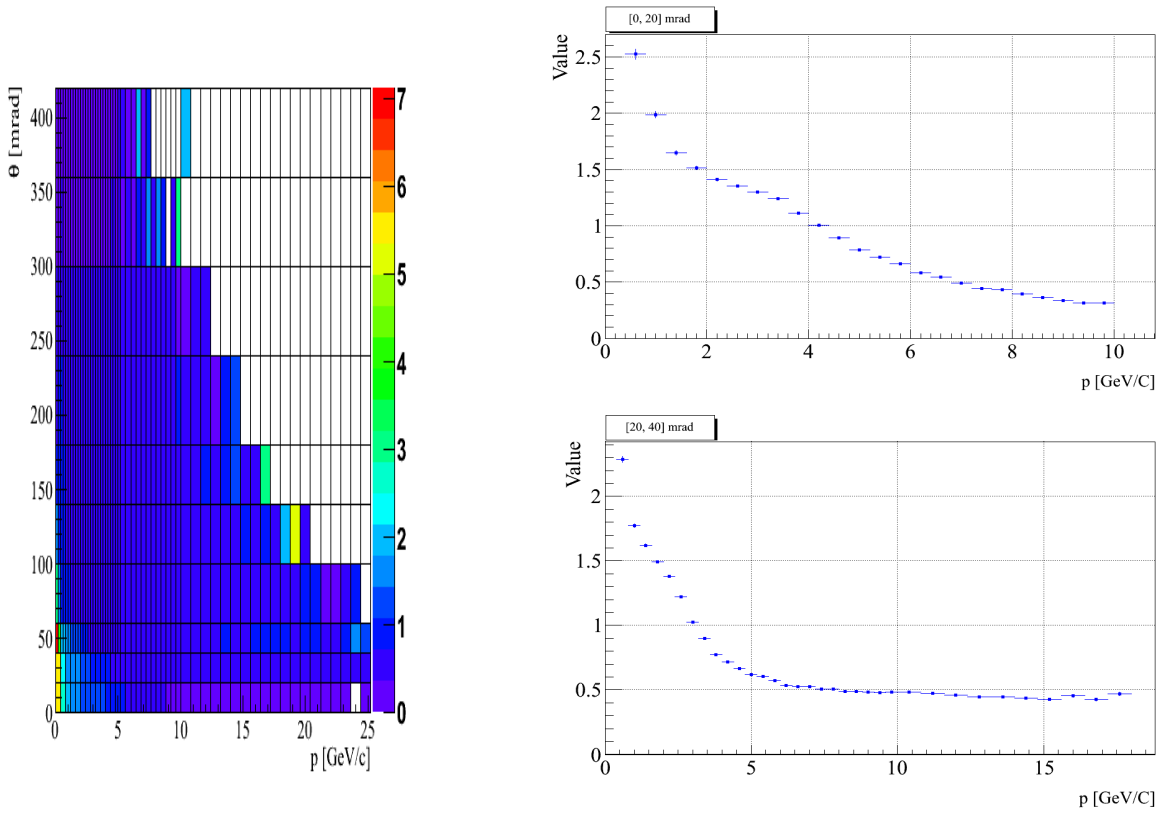

Figure 76. Two-dimensional efficiency (c^{-1}) plot in momentum and polar angle variables (left). Projections in two first polar angle slices - [0,20] and [20, 40] mrad (right). Bins where corrections were larger than three are not shown and also were rejected from tha analysis.

Apart from the low momentum and polar angle region, corrections are smaller than one in almost whole phase space region. The large correction region is connected with the electron contamination. Bins were this contribution was too large (correction>3) were rejected from further analysis. Different parts of correction were studied separately. The main contribution

to the total correction apart from the electron contamination (which is only important at low momenta) came from geometrical acceptance of the detector (an example is shown in Figure 77).

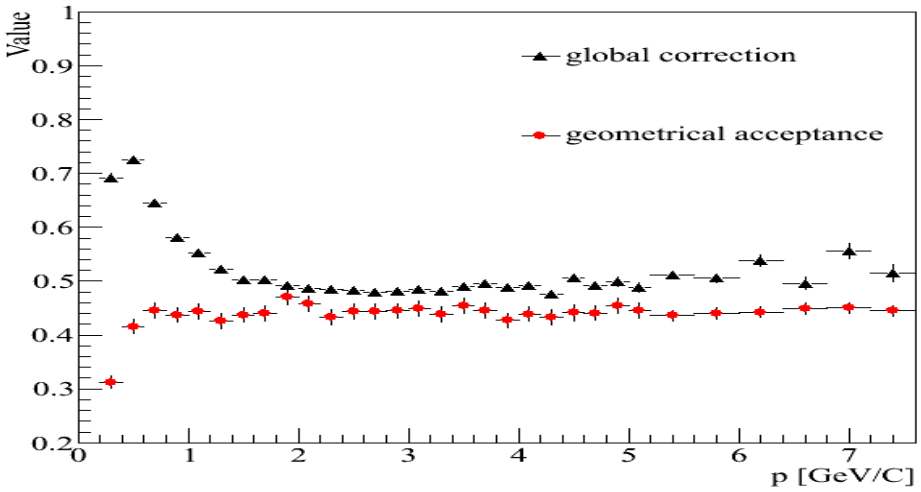

Figure 77. Efficiency factor in [140, 180] mrad polar angle interval. Part of the correction connected with the geometrical acceptance is shown by red dots.

7.4.1.2 Corrected data in momentum and polar angle variables

The two-dimensional picture of corrected data without normalization in momentum and polar angle variables is shown in Figure 79.

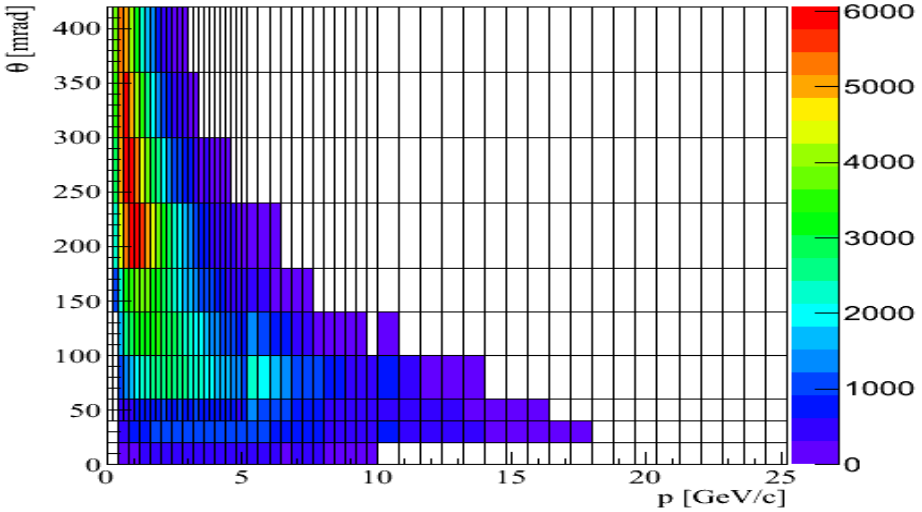

Figure 78. Two-dimensional picture of corrected data (without normalization) in momentum and polar angle variables.

Regions were statistical error was larger than 20% were rejected from the further analysis.

7.4.1.3 Correction factors in Feynman x and transverse momentum variables

The two-dimensional efficiency (c^{-1}) plot in Feynman x and transverse momentum variables is shown in Figure 79.

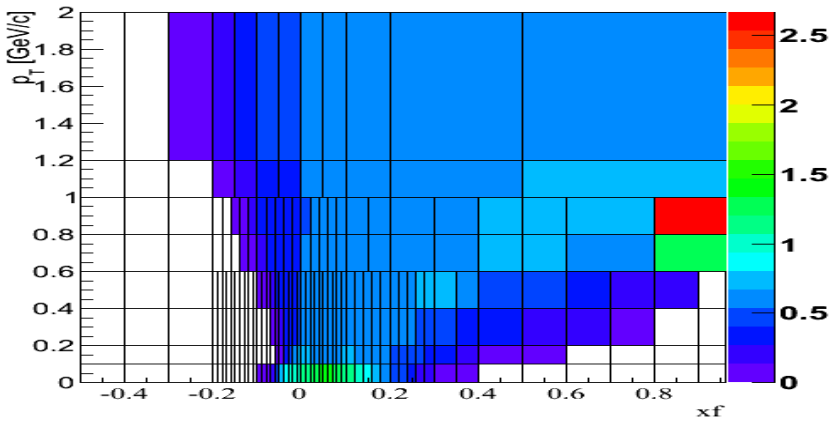

Figure 79. Two-dimensional efficiency (c^{-1}) plot in Feynman x and transverse momentum variables.

7.4.1.4 Corrected data in Feynman x and transverse momentum variables

The two-dimensional picture of corrected data without normalization in Feynman x and transverse momentum variables is shown in Figure 80.

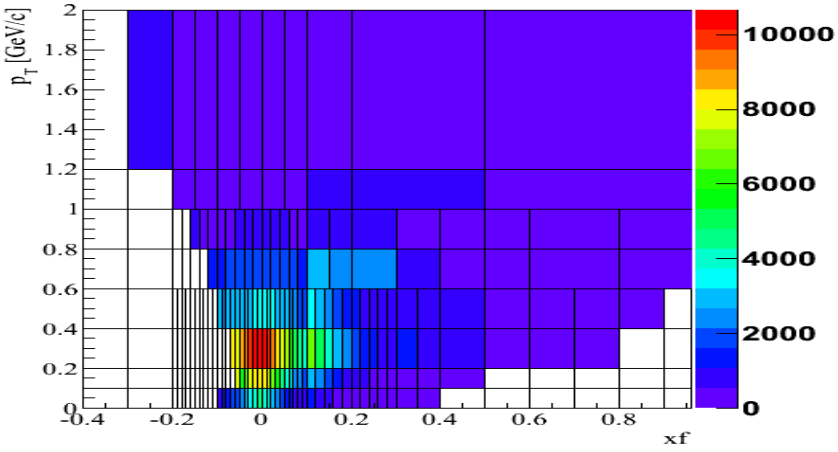

Figure 80. Two-dimensional picture of corrected data (without normalization) in Feynman x and transverse momentum variables.

Using available 2007 statistics we were able to obtain results up to 0.6 xf. The region of small values of Feynman x and transverse momentum has been extensively studied. The region of large transverse momentum values (>1.2 GeV/c) is very weakly populated and hence large statistical errors in this region appear. Regions were statistical error was larger than 20% were rejected from the further analysis.

7.4.1.5 Correction factors in rapidity and transverse momentum variables

The two-dimensional efficiency (c^{-1}) plot in rapidity and transverse momentum variables is shown in Figure 81.

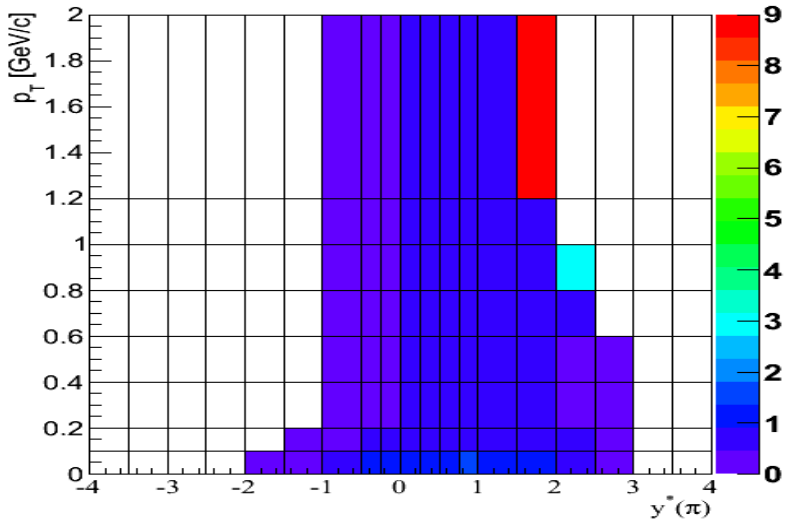

Figure 81. Two-dimensional efficiency (c^{-1}) plot in rapidity in c.m.s assuming pion mass and transverse momentum variables.

Regions were correction factor was larger than three were rejected from further analysis.

7.4.1.6 Corrected data in rapidity and transverse momentum variables

The two-dimensional picture of corrected data without normalization in rapidity in c.m.s assuming pion mass and transverse momentum variables is shown in Figure 82.

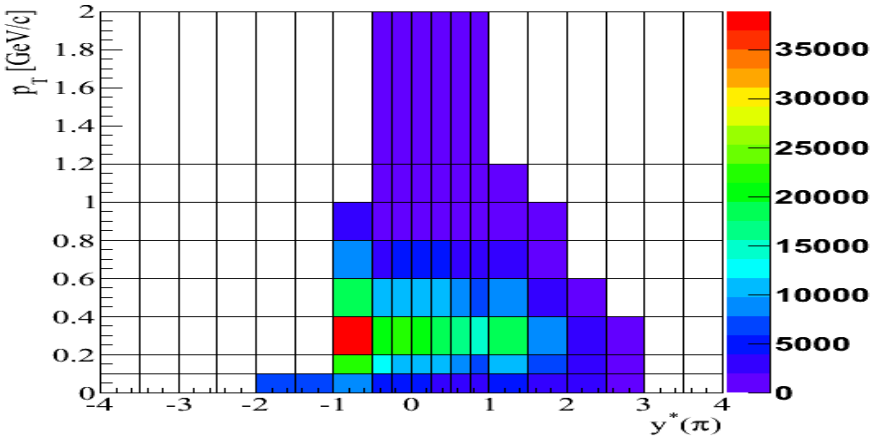

Figure 82. Two-dimensional picture of corrected data (without normalization) in rapidity in c.m.s assuming pion mass and transverse momentum variables.

7.4.2 T2K replica target

7.4.2.1 Correction factors

The efficiencies (c^{-1}) for each part of the T2K replica target are presented in Figure 83.

Slice 1
Z [-625.7, -634.7]

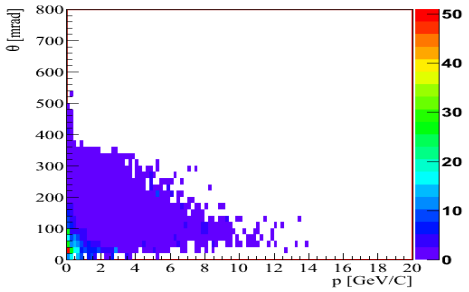

Slice 2
Z [-643.7, -616.7]

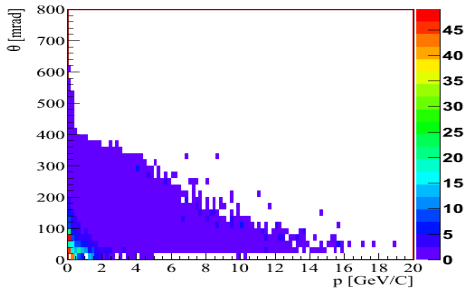

Slice 3
Z [-616.7, -598.7]

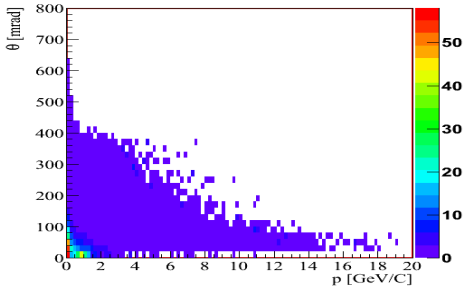

Slice 4
Z [-598.7, -580.7]

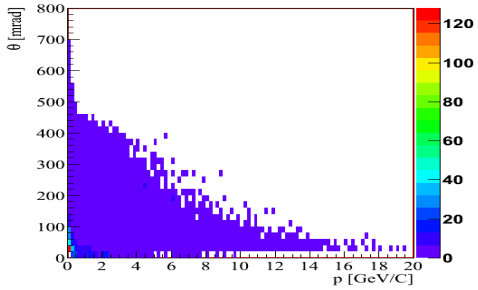

Slice 5
Z [-580.7, -562.7]

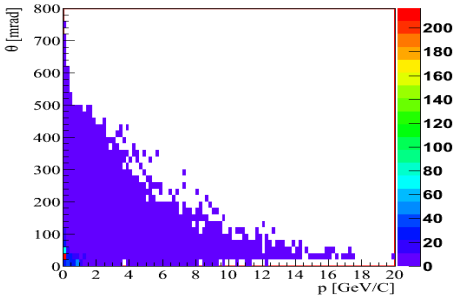

Slice 6 (upstream face of the target)
Z >= -562.7
Vertex $x^2+y^2 < 1.3$

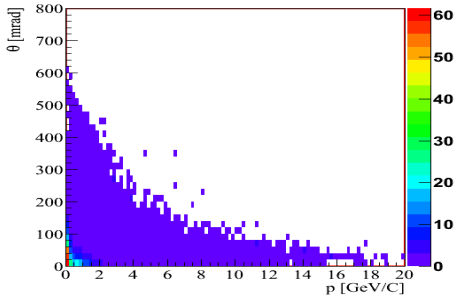

Figure 83. Two-dimensional momentum versus polar angle plots of efficiency (c^{-1}) for different parts of the T2K replica target.

For the T2K replica target, contribution of electrons and non-primary hadrons is very large (as compared with thin carbon target) especially at the low momentum and polar angle region. This leads to strongly model dependent corrections. Therefore, this part is excluded from the analysis. In future this can be cured by use of the combined method of h- with dEdx which allows to reject electron contamination by energy loss studies.

7.4.2.2 Corrected data

The corrected data plots for each part of the T2K replica target are presented in Figure 84

Slice 1
Z [-625.7, -634.7]

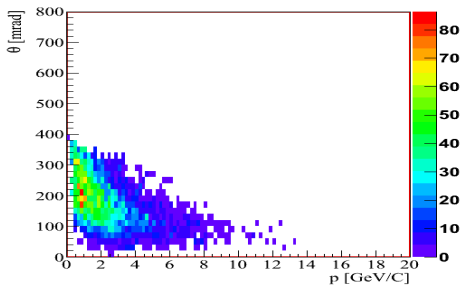

Slice 2
Z [-643.7, -616.7]

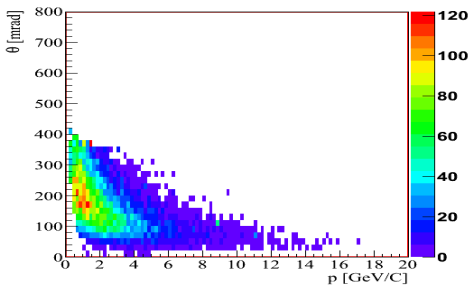

Slice 3
Z [-616.7, -598.7]

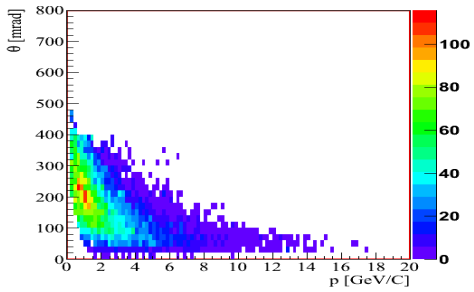

Slice 4
Z [-598.7, -580.7]

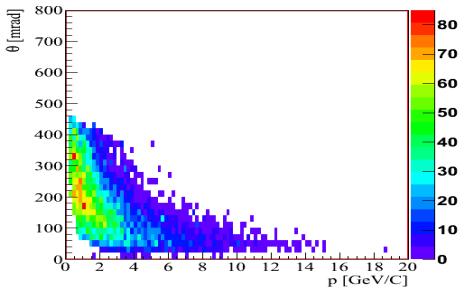

Slice 5
Z [-580.7, -562.7]

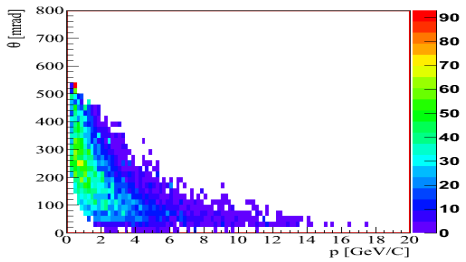

Slice 6 (upstream face of the target)
Z >= -562.7
Vertex $x^2+y^2 < 1.3$

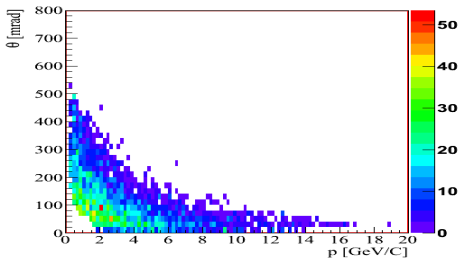

Figure 84. Two-dimensional momentum versus polar angle plots of corrected data for different parts of the T2K replica target.

Studies of the T2K replica target have shown that the h- method has the ability to be used for the particle yields extraction in this case. However, at the low momentum and polar angle region due to a large electron contamination this method should be combined with dEdx studies to get rid of strongly model dependent corrections. Developed programs were transferred to the NA61/SHINE Collaboration. Results from presented studies have been shown at the closed SPSC meeting. They constituted a major contribution to show that the NA61/SHINE collaboration developed methods of particle yields extraction from the T2K replica target what had a significant impact to obtain the approval of next data taking periods for this purpose.

7.5 Estimation of systematic errors

The studies of the systematic errors on the negatively charged pion spectra included among others contributions from the:

- Checks of the stability of the result while varying the track cuts
    - following track selection criteria were varied:
        - minimum number of points measured on the track,
        - azimuthal angle cuts
        - impact parameter cuts.

- Checks of the stability of the results based on the different track topologies (RST and WST subsamples)
- Checks of the stability of the results obtained with the different reconstruction chains
    - Different clients which were merging tracks were used (DOMERGE and REFORM)
- Uncertainty connected with reconstruction efficiency
    - This part is included in the comparison of the RST and WST subsamples. Dedicated studies have shown that this uncertainty is small (less than ~2 %). Therefore, in final systematic error this part was not separated from the uncertainty connected with different track topologies.
- Uncertainty connected with geometrical acceptance
    - This part is included as well in the uncertainty connected with the different track topologies. Furthermore, uncertainty connected with geometrical acceptance is the main contribution to this uncertainty.
- Uncertainty connected with the model dependent correction for the secondary interactions contribution.
    - We assigned an uncertainty of 30% of the correction.
- Uncertainty connected with the model dependent correction for the weak decays of the strange particles.
    - The systematic error due to the admixture of pions from the decays of strange particles reconstructed to the primary vertex depends on the knowledge of the production of strange particles. The estimate of this error was based on:
    - comparison of the number of V^0 decays reconstructed in the data and in the NA61/SHINE Official Monte Carlo
    - comparison of the strange particles yields in differen Monte Carlo generators
        - for example the K^-/π^- ratio in p+C interactions at 31 GeV/c from Fluka2009, Urqmd1.3.1 and GiBUU1.3.0 is 3.73%, 3.67% and 3.35%, respectively; these values can be compared with 4.06% from the Venus generator which was used in the NA61/SHINE official MC.
    - We assigned an uncertainty of 30% of the correction.
- Uncertainty connected with the model dependent correction for the electrons reconstructed to the primary vertex
    - We assigned an uncertainty of 20% of the correction.

The relative contribution of accepted primary K^- and anti protons to accepted primary negatively charged pions is presented in Figure 85, Figure 86, and Figure 87 for momentum and polar angle, Feynman x and transverse momentum, and rapidity and transverse momentum, respectively.

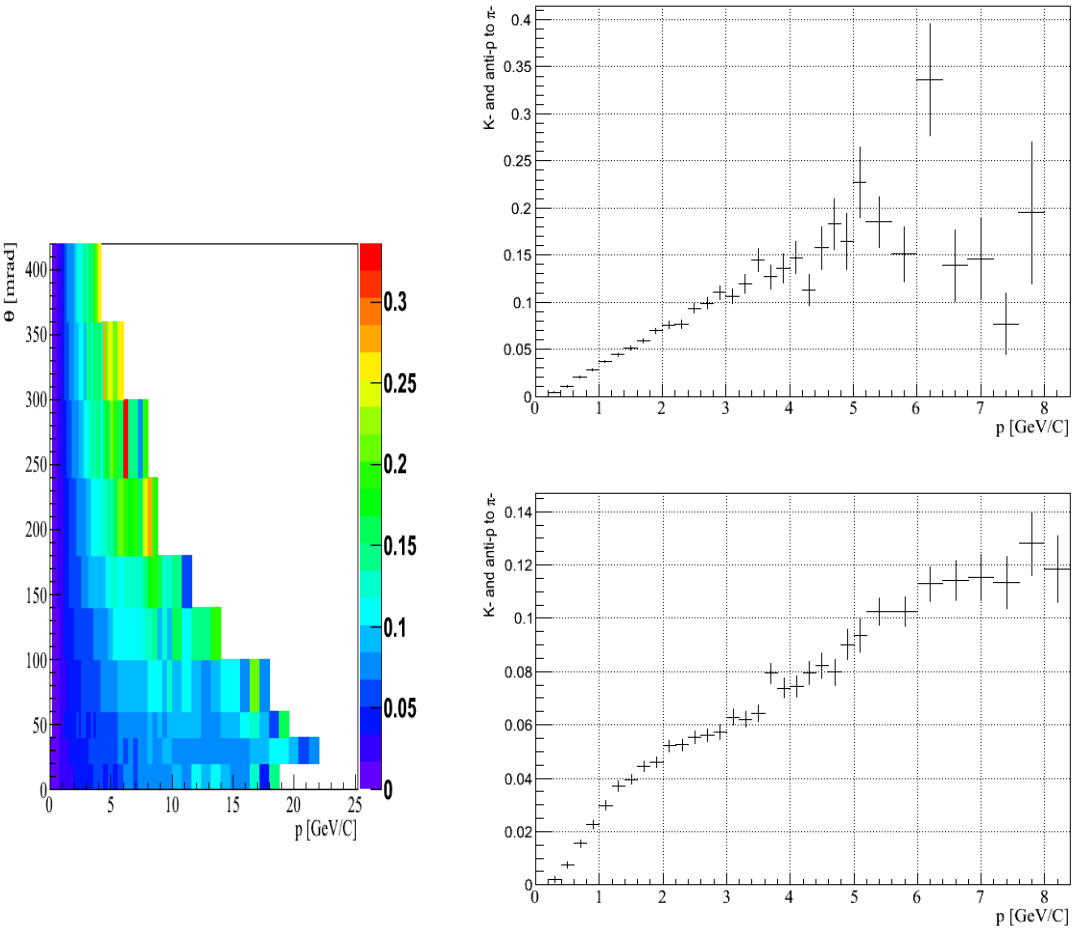

Figure 85. Relative contribution of accepted primary K^- and anti protons to accepted primary negatively charged pions in momentum and polar angle variables (left). Projections in [240, 300] mrad region (upper right), and in [100, 140] mrad region (bottom right).

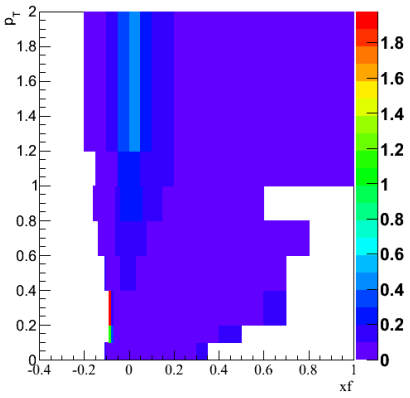

Figure 86. Relative contribution of accepted primary K^- and anti protons to accepted primary negatively charged pions in Feynman x and transverse momentum variables.

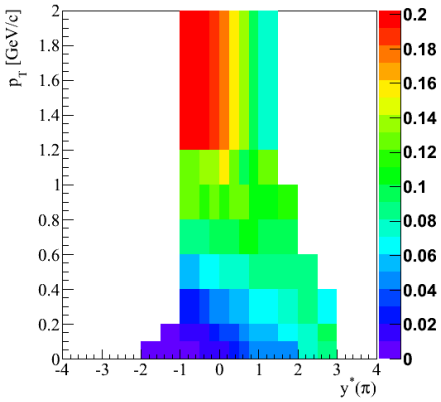

Figure 87. Relative contribution of accepted primary K^- and anti protons to accepted primary negatively charged pions in rapidity and transverse momentum variables.

The negatively charged Kaons and anti-protons are just a small admixture for negatively charged pions. In momentum and polar angle variables these admixture contributes mainly in larger momenta and larger polar angles. Apart form this region it is at the level of a few percents (< 5-10%).

After transformation to Feynman x and transverse momentum variables, mainly region of large transverse momentum is populated. We also observed two bins with large contribution at smaller transverse momentum for negative values of Feynman x. In these two bins number of negatively charged Kaons and anti-protons is larger than number of negatively charge pions. This appeared because two-dimensional plot for Kaons and anti protons in these variables is much wider than for pions what is shown in Figure 88. Apart from the discussed regions, the contribution of negatively charged Kaons is at the level of a few percents (<4-7%).

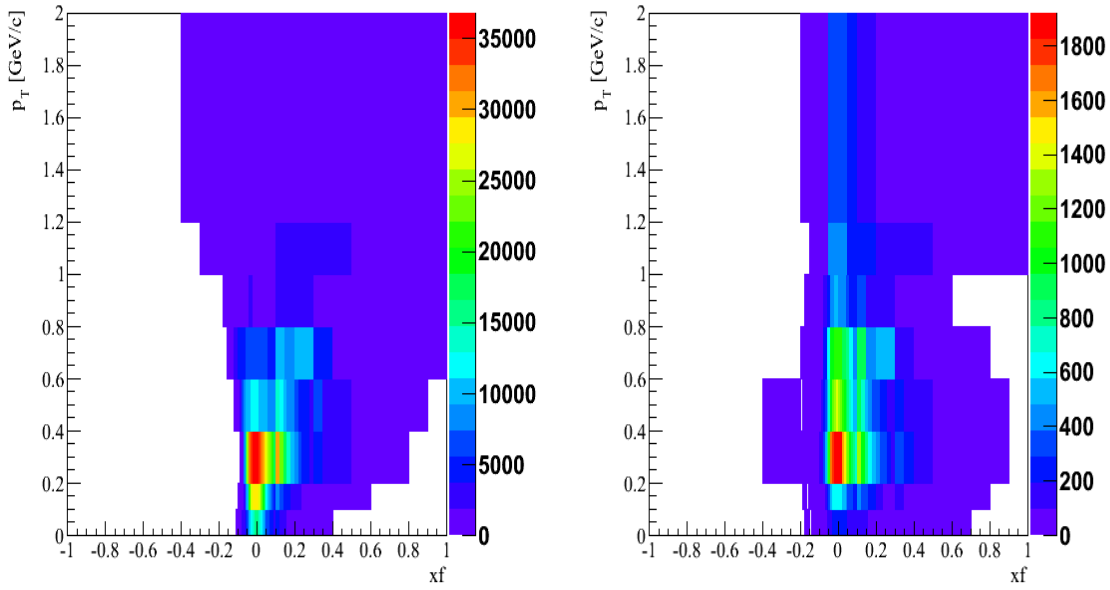

Figure 88. Feynman x versus transverse momentum distributions for simulated negatively charged pions (left) and negatively charged Kaons and anti-protons (right).

After transmission to rapidity and transverse momentum variables, besides very high transverse momentum region (>1.2 GeV/c), the contribution of negatively charged Kaons and anti-protons is at the level of a few percents (<5-10 %).

The relative contribution of accepted electrons and non-primary negatively charged hadrons to accepted primary negatively charged pions (based on the official NA61/SHINE MC) is presented in Figure 89, Figure 90, Figure 91 for momentum and polar angle, Feynman x and transverse momentum, and rapidity and transverse momentum, respectively.

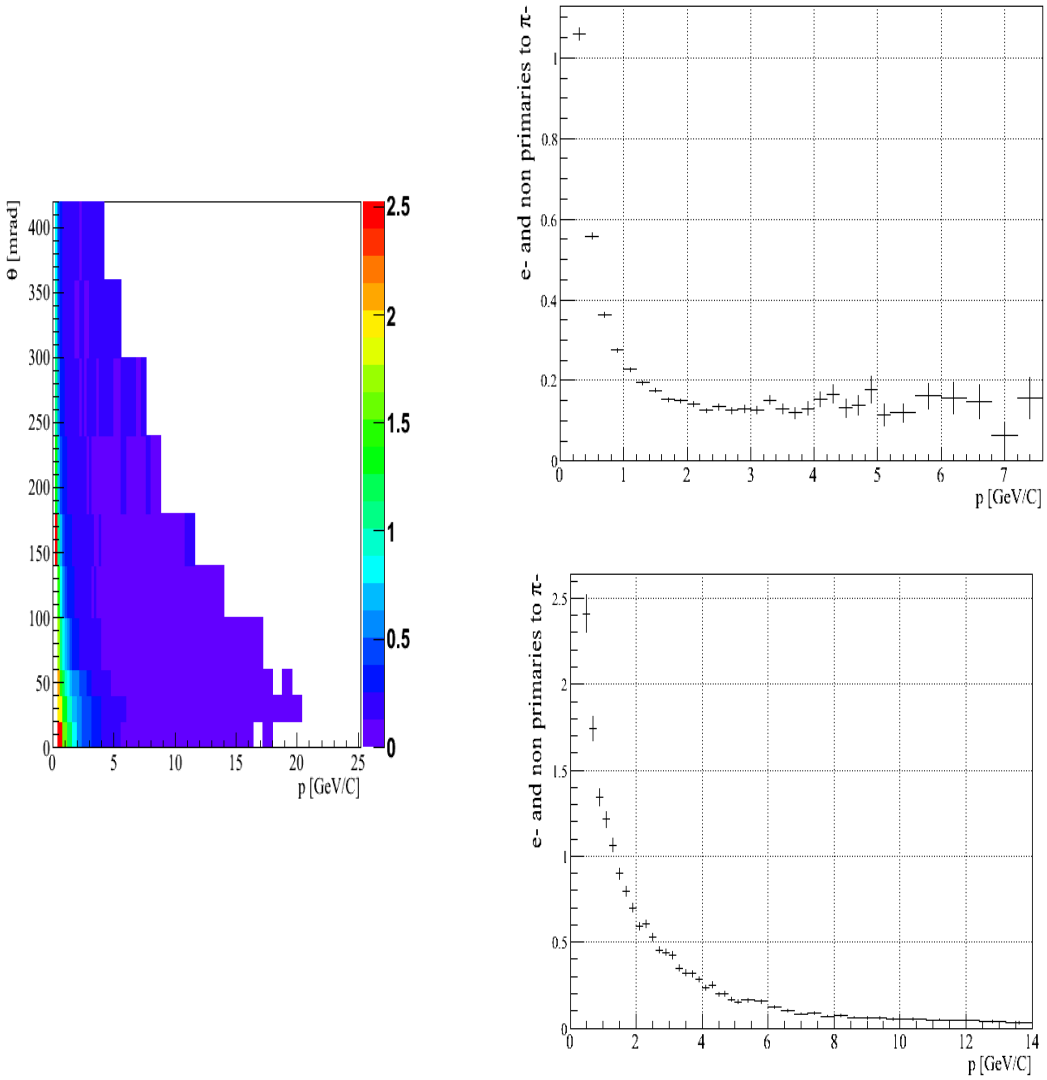

Figure 89. Relative contribution of accepted electrons and non-primary negatively charged hadrons to accepted primary negatively charged pions in momentum and polar angle variables.). Projections in [240, 300] mrad region (upper right), and in [100, 140] mrad region (bottom right).

Except for low momentum region (<2 GeV/c) the contribution from electrons and non-primary negatively charged hadrons is small and dose not depend on the polar angle and momentum. Hill which starts from 2GeV/c and goes down to the smallest values of momentum is connected with electron contamination. In the h- analysis, non-primary tracks are corrected via model correction. Therefore, we excluded region where relative contribution of electrons and non-primary hadrons affects significantly value of systematic error connected with this part (>20%). Typical value of non-primary relative contribution outside the low momentum region is at the level of 5-10%.

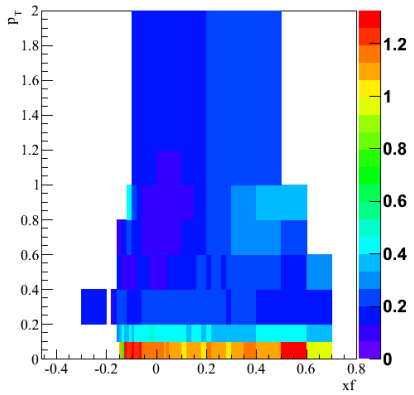

Figure 90. Relative contribution of accepted electrons and non-primary negatively charged hadrons to accepted primary negatively charged pions in Feynman x and transverse momentum variables.

After transformation to the Feynman x and transverse momentum variables. The contribution from electrons and non-primary negatively charged hadrons was found to be larger at low transverse momentum values. In this set of variables, this contribution is spread more evenly in the phase space. Excluding the low transverse momentum region, the relative contribution is at the level of 5 – 10%.

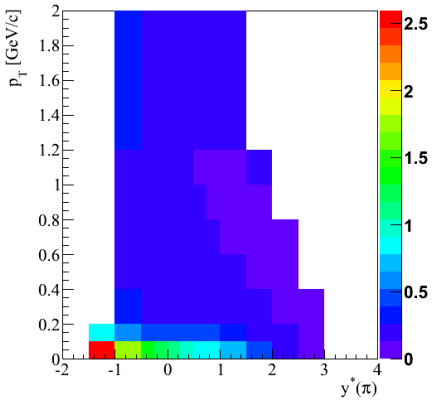

Figure 91. Relative contribution of accepted electrons and non-primary negatively charged hadrons to accepted primary negatively charged pions in rapidity and transverse momentum variables.

In rapidity and transverse momentum variables, we have mainly low transverse momentum region planted by the electrons and non-primary negatively charged hadrons. Outside this region the typical value of the relative contribution is at the level of 5-10 %.

The systematic error studies were performed in all sets of variables. As an example obtained systematic errors in momentum and polar angle are presented in chapter 7.5.1. The systematic error in other variables will not be discussed in details in this thesis.

7.5.1 Systematic errors in momentum and polar angle variables

The systematic errors connected with the main contributions from the ones described in the beginning of the chapter 7.5 for different polar angle slices are presented in Figure 92.

[0, 20] mrad

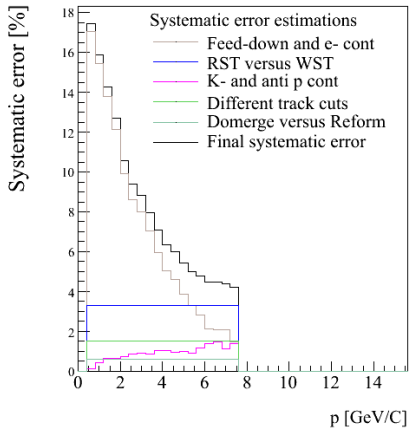

[20, 40] mrad

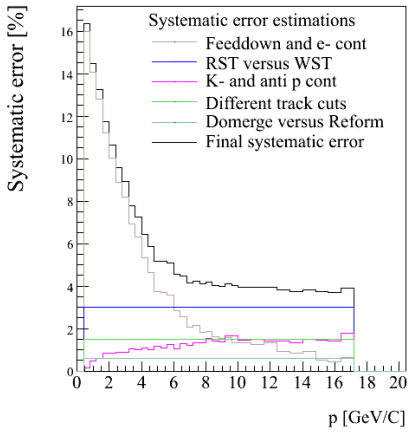

[40, 60] mrad

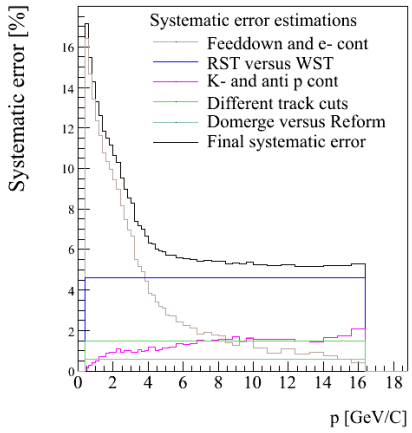

[60, 100] mrad

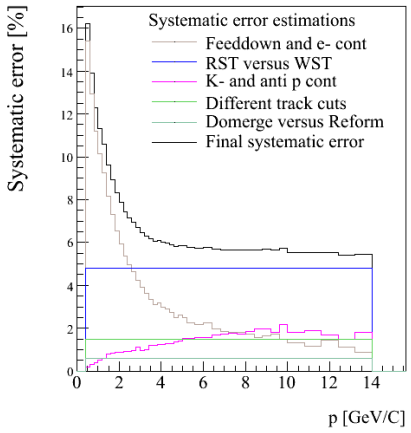

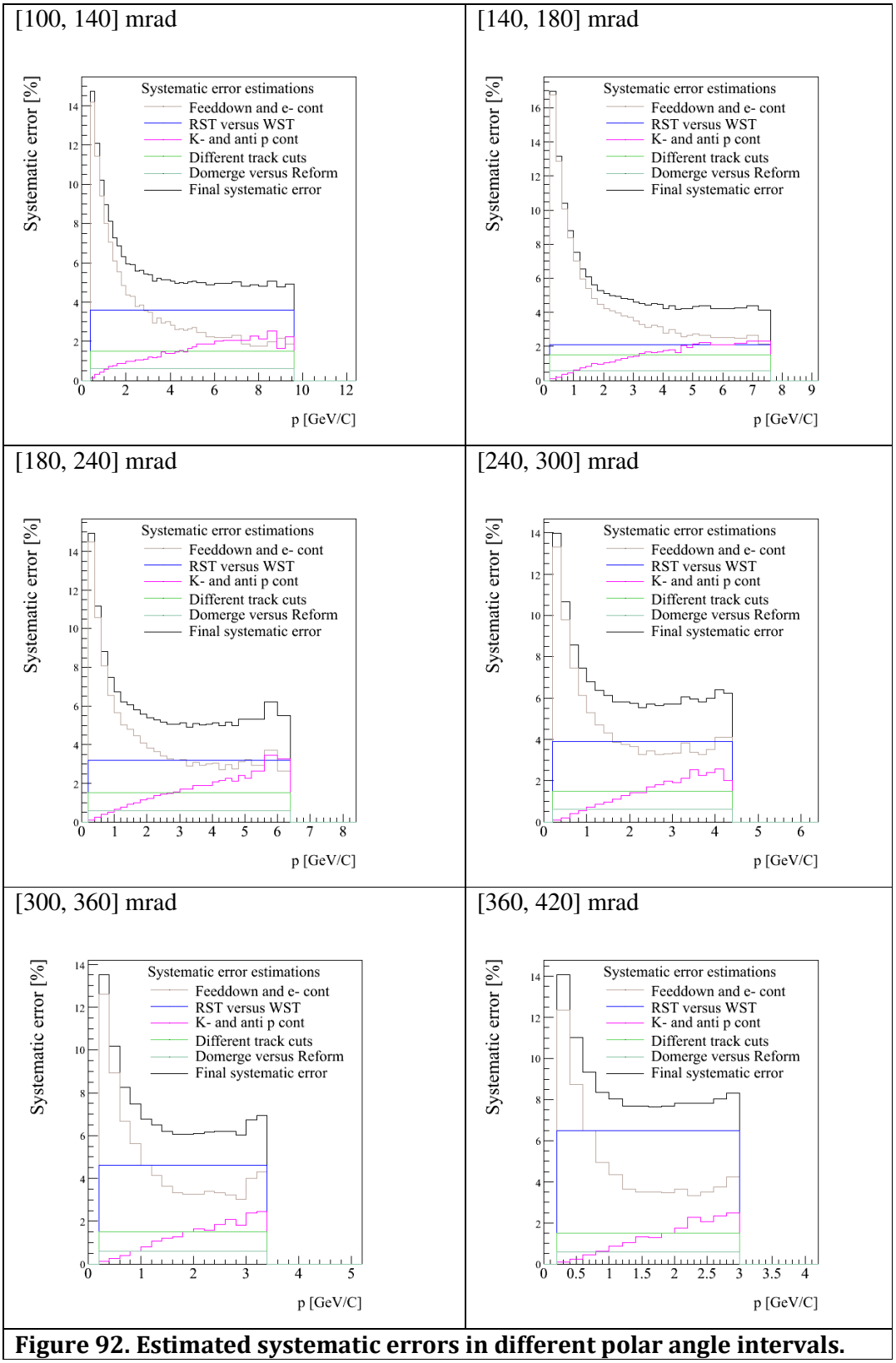

Figure 92. Estimated systematic errors in different polar angle intervals.

The main contributor to the systematic error is uncertainty connected with the strange particle decays and electron contamination (Feeddown and e- cont). The analyses of the neutral strange particle production (K^0_S and Λ which are discussed in this thesis) will allow reducing uncertainty connected with the first part. Uncertainty connected with electron contamination can be strongly reduced by the carry out analysis within electron cutoff based on the dEdx information. In future, after additional upgrades and corrections of the Monte Carlo chain, and work on the better understanding of some track topologies (dedicated studies of WSTs), and use of the information from the GAP-TPC most likely it will be possible to reduce systematic errors to the level of 3-4%. At this moment, our results have also large statistical errors but these will be reduced at least by factor of ~3 while recently collected data will be used.

7.6 Final results

The statistical errors on the negatively charged pion spectra include contributions from the finite statistics of data and from the Monte Carlo statistics (used for the correction factor evaluation), which was about 10 times larger than the data statistics. The total statistical errors are dominated by the statistical uncertainty of the data. It does not include the overall uncertainty due to the normalization procedure, namely 2.5% and 2.3% for the normalization to the inclusive cross section and mean pion multiplicity in production events, respectively.

The systematic errors on the negatively charged pion spectra were estimated by varying track cuts, by checking of the consistency of the results based on the different track topologies and results obtained with the different reconstruction chains. The dominant contribution to the systematic error came from the uncertainty in the correction for the secondary interactions and for weak decays of the strange particles.

In this chapter final results on the negatively charged pion production from the p+C (thin target) at 31 GeV/c normalized to differential production cross sections are presented. The final results normalized to mean mulplicity in production processes are compared to Monte Carlo models in chapter 9. The normalization was done accordingly to chapter 6.4.1.

7.6.1 Final results in momentum and polar angle variables

7.6.1.1 Results in momentum and polar angle variables

The differential cross section for negatively charged pion production in proton Carbon interactions at 31GeV/c in different polar angle slices are presented in Figure 93. The final results in tabularized form are presented in appendix.

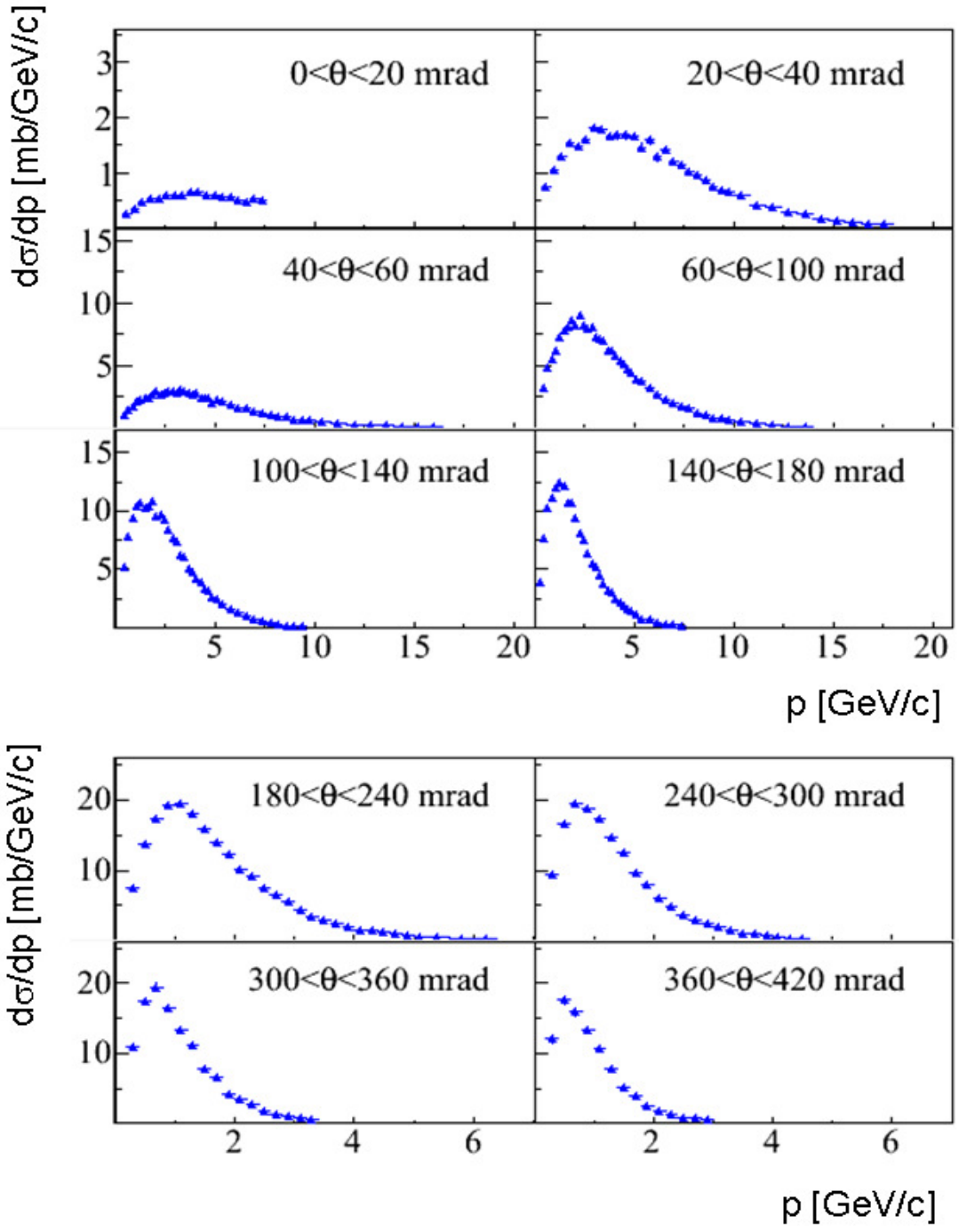

Figure 93. Differential cross section for negatively charged pion production in proton Carbon interactions at 31GeV/c in different polar angle slices. Only statistical errors are shown. Error connected with normalization is not shown (2.5%).

7.6.1.2 Comparison of results obtained in different approaches (h- versus dEdx approach and dEdx combined with TOF approach)

The final results were compared to the results obtained by the dEdx method [154] (in low momentum region <2 GeV/c) and results obtained by the combined dEdx+TOF method [141]. The reasonable agreement between different results was found. Apart from the beginning of the distributions (<0.2 GeV/c), the dEdx and h- results are within the statistical errors. The number of tracks reaching the TOF detector is significantly smaller than number of tracks in the h- analysis, especially in the low momentum region (below 5 GeV/c). In this region, some deviations between the dEdx+TOF and h- results were found.

As an example, ratios between different results in two randomly selected polar angle intervals are presented in Figure 94, Figure 95.

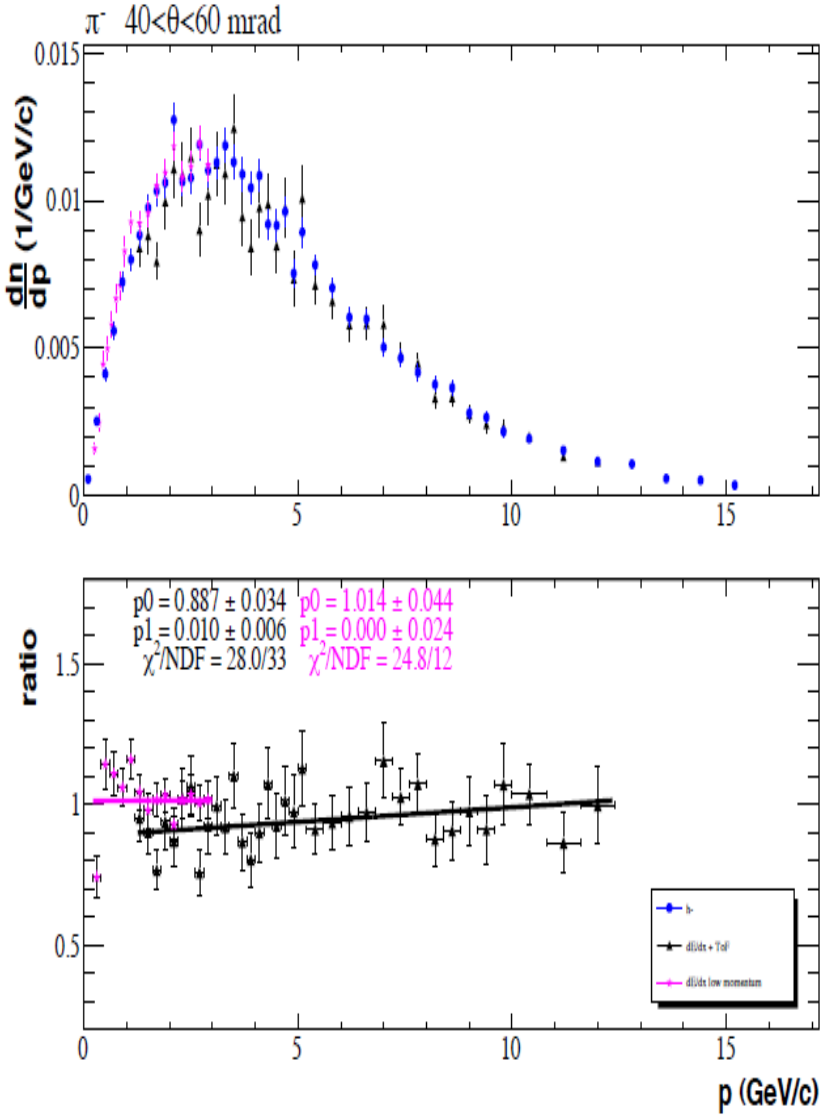

Figure 94. Comparison of h- results with dE/dx and dE/dx + TOF results in [40, 60] mrad polar angle interval. (top) All results imposed. (bottom) Ratios of dE/dx to h- (pink points) and dE/dx+TOF to h- (black points). Lines – linear fits.

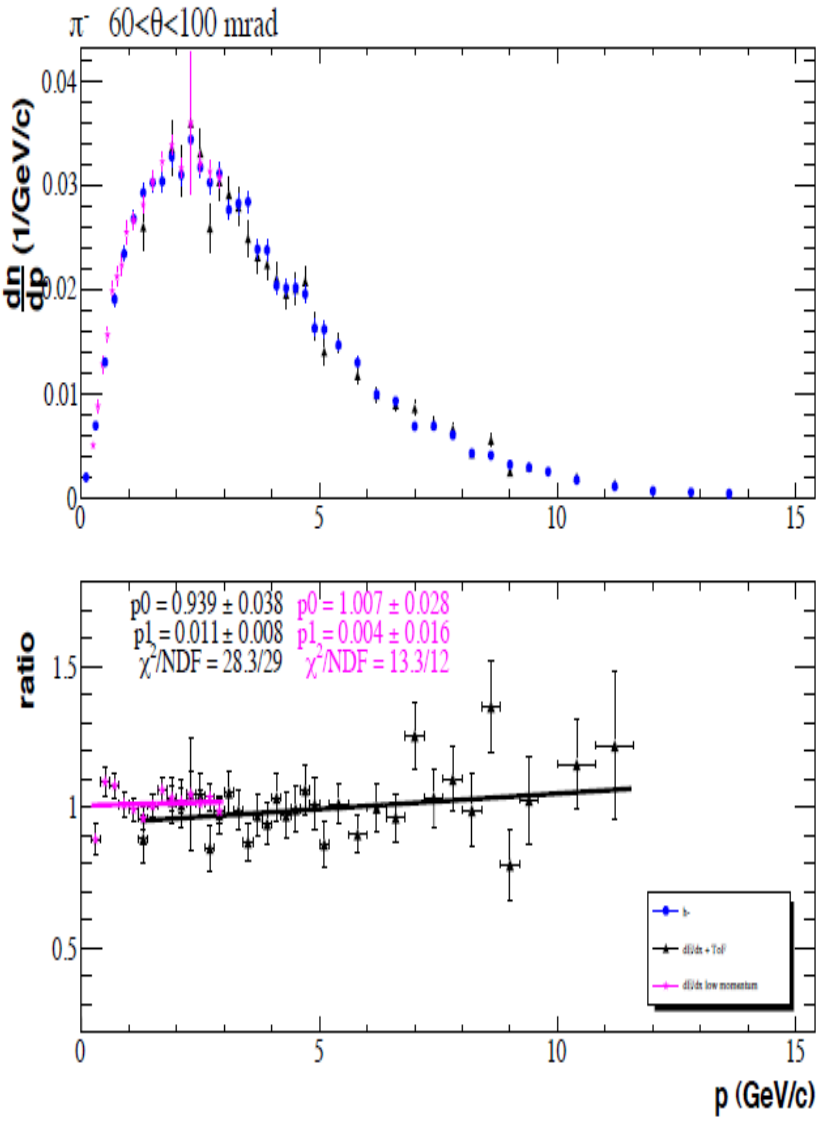

Figure 95. Comparison of h- results with dE/dx and dE/dx + TOF results in [60, 100] mrad polar angle interval. (top) All results imposed. (bottom) Ratios of dE/dx to h- (pink points) and dE/dx+TOF to h- (black points). Lines – linear fits.

7.6.1.3 Comparison of final results with the Sanford-Wang parameterization.

The final π- results (combined results from all methods) were compared with Sanford-Wang parameterization (SW), which was discussed in chapter 2.4. Figure 96 shows final results with SW parameterization, with three different sets of parameters, superimposed. One of them is parameterization obtained from the fits to the compilation of p Be data at 6.4, 12.3, 17.5 GeV/c [78]. The second set of curves shows HARP SW parameterization obtained from the fits to π- results from p C interactions at 12 GeV/c [76]. The last set of curves shows our SW parameterization fit to final π- results. Our fitting is done separately in each polar angle interval.

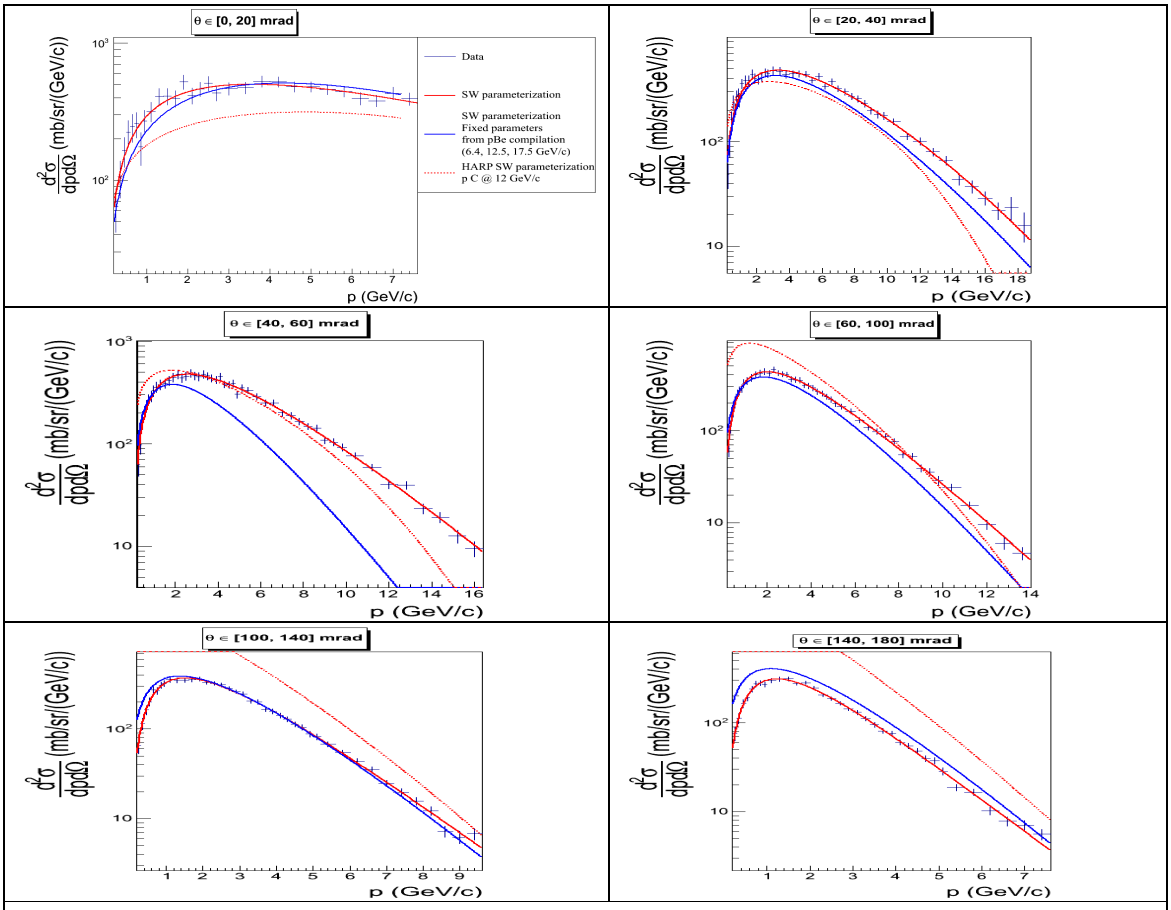

Figure 96. Final π- results (combined results from all methods) compared with Sanford-Wang parameterization. Data errors show sum of statistical and systematical errors in quadrature. The red curve shows SW parameterization fitted to our results. The blue curve shows SW parameterization obtained from the fits to the compilation of p Be data at 6.4, 12.3, 17.5 GeV/c. The red dashed lines show HARP SW parametrization.

The SW HARP parameterization and parameterization obtained from the fits to the compilation of the p Be data do not reproduce our results. Parameters of these SW parameterizations were obtained for the lower energy of incoming proton. The simple momentum scaling is not working correctly in this case. In addition in parameterization based on the p Be data no nuclear scaling was applied. However, the shape of distributions can be very well reproduced by the SW parameterization (see red solid curves) but using different set of parameters.

7.6.2 Final results in Feynman x and transverse momentum variables

The double differential production cross sections for negatively charged pion production in proton Carbon interactions at 31 GeV/c for different values of Feynman x are shown in Figure 97.

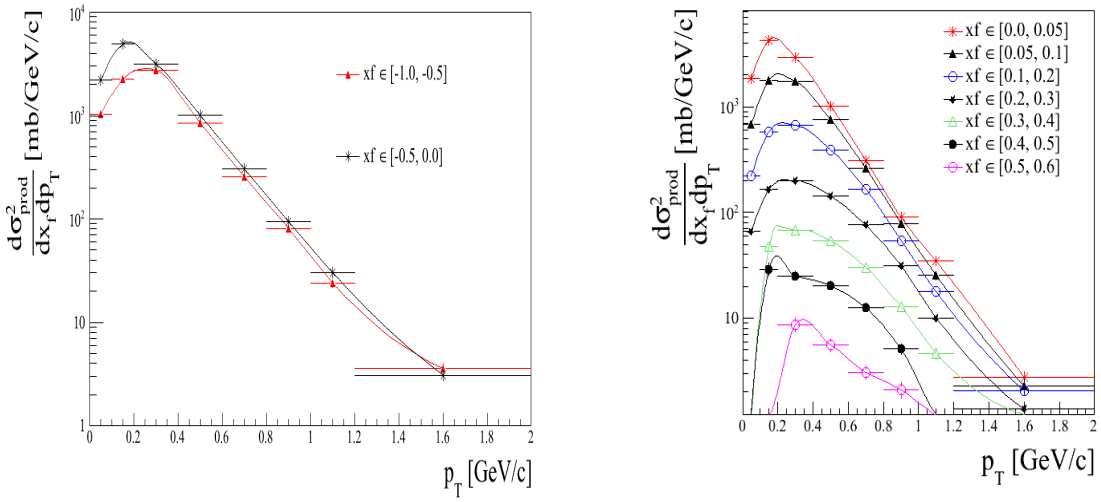

Figure 97. Double differential production cross sections for negativaely charged pion production in proton Carbon interactions at 31 GeV/c for different values of Feynman x. The curves are shown to guide the eye.

The double differential production cross sections for negatively charged pion production in the proton Carbon interaction at 31 GeV/c for different values of transverse momentum are shown in Figure 98.

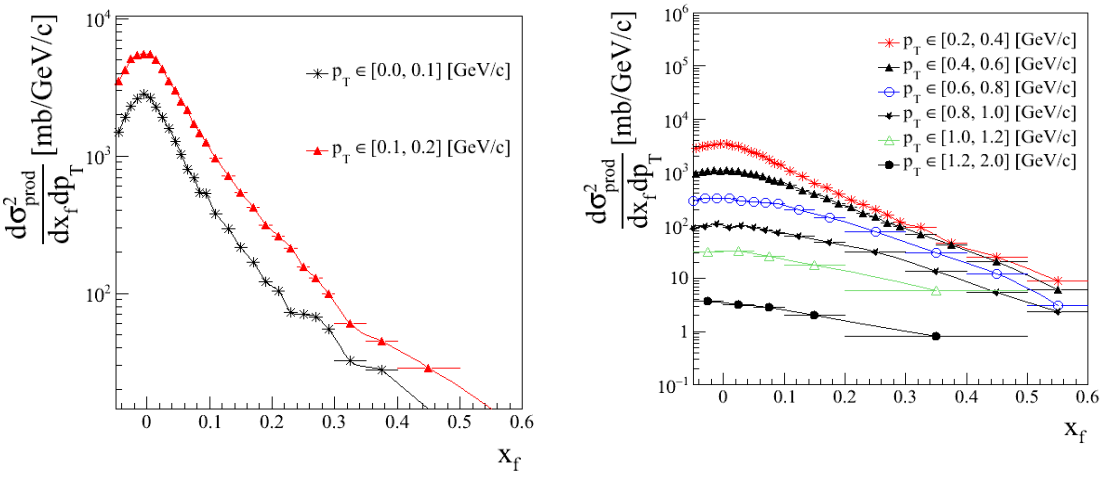

Figure 98. Double differential production cross sections for negatively charged pion production in the proton Carbon interaction at 31 GeV/c for different values of transverse momentum. Only statistical errors are shown. The curves are shown to guide the eye.

7.6.3 Final results in rapidity and transverse momentum variables

7.6.3.1 Results in rapidity and transverse momentum

The double differential production cross sections for negatively charged pion production in the proton Carbon interaction at 31 GeV/c for different values of transverse momentum are shown in Figure 99.

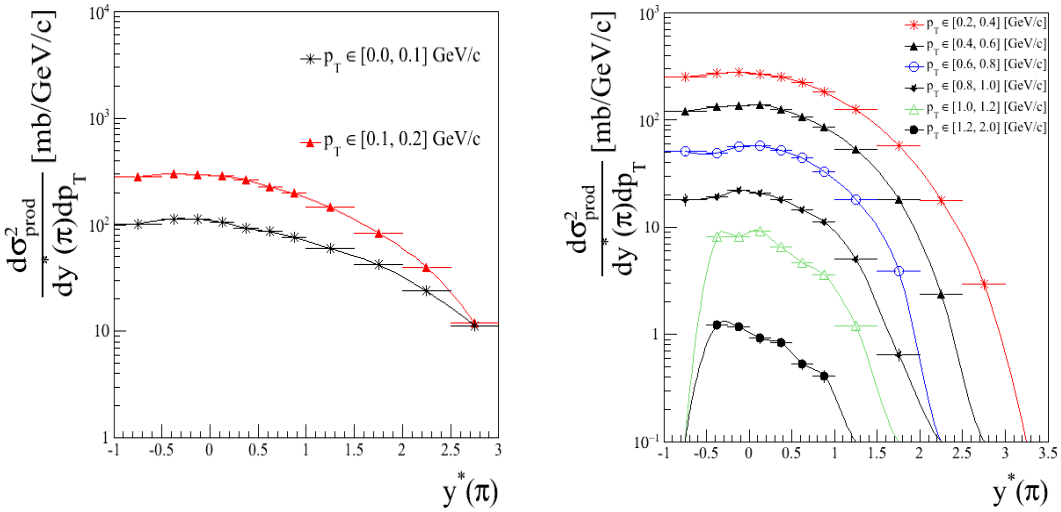

Figure 99. Double differential production cross sections for negatively charged pion production in the proton Carbon interaction at 31 GeV/c for different values of transverse momentum. The curves are shown to guide the eye.

The differential cross section dσ/dy is shown in Figure 100.

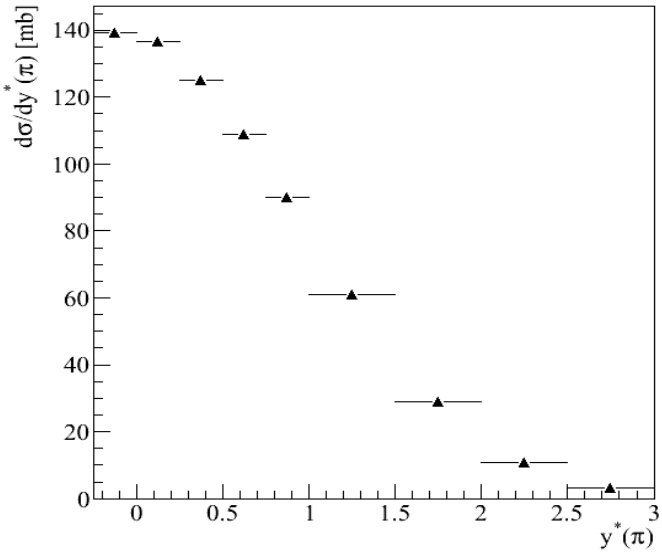

Figure 100. Differential cross section dσ/dy in full acceptance region (0 < p_T < 1 GeV/c).

7.6.3.2 Comparison of obtained result with different analysis as a cross check of the analysis chain.

The rapidity spectra of π- for $0 < p_T < 1$ GeV/c are shown in Figure 101.

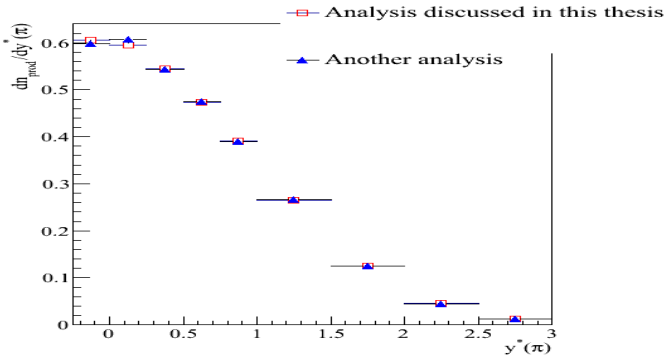

Figure 101. Rapidity spectra of π- for 0 < pT < 1 GeV/c. Red squares – Results obtained by Author of this thesis, Blue triangles – Results from another independent analysis [14].

The reasonable agreement between results obtained in two different analysis' approaches was found. Another analysis was carried out using different event and track cuts and only on the RST sample. In this approach, quality cuts were selected to maximize reconstruction efficiency of the RSTs. Therefore, small differences between these two results are perfectly understandable. Moreover, these differences can be used as a one of the possible measure of systematic bias.

The rapidity spectra from p+C interactions at 31 GeV and central Pb+Pb collisions at 30AGeV are compared in Figure 102.

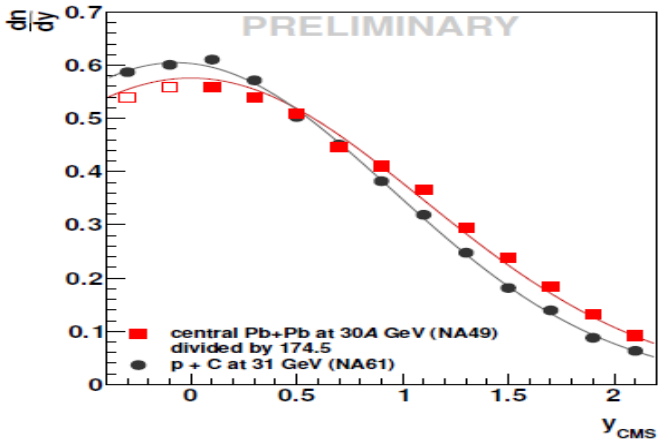

Figure 102. Rapidity spectra from p+C interactions at 31 GeV and central Pb+Pb collisions at 30AGeV. The Pb+Pb results normalized with number of wounded nucleons. Picture is taken from [15].

Due to the projectile-target asymmetry of the initial state the p+C rapidity spectrum is shifted towards target rapidity with respect to Pb+Pb. The mean pion multiplicity in the forward hemisphere was found to be proportional to the mean number of wounded nucleons of the projectile nucleus.

Chapter 8 Study of neutral hadron production

8.1 Introduction

In this chapter analyses of K^0_S and Λ particles produced in proton Carbon interaction at 31 GeV/c are presented. Data from 2007 pilot run, reconstructed using reconstruction chain with REFORM client and without GTPC, are used. K^0 production is important for accurate calculation of the ν_e and $\bar{\nu}_e$ flux from $K_L \rightarrow \pi\ e\ \nu_e$ decays. While not focused, the K_L do contaminate most beam lines. Kaon production is also important because koan decays lead to secondary pion production. Therefore, K^0 production plays important role in the neutrino beam simulations.

Following equations can approximate the Kaon production:

- $N(K^0_S) = N(K^0_L) = (NK^+ + NK^-)/2$
- $N(K^0_S) = N(K^0_L) = 1/4\ (NK^+ + 3\ NK^-)$

The first one motivated by the isospin symmetry. The second one is motivated by the quark-counting arguments, valid only for the pp interactions in the fragmentation region. Provided that the precise K^- results were available, the estimation of K^+ would be possible with the use of those formulas and measured K^0_S data. This would create a possibility to cross-check results on positively charged Kaon production. Moreover, very precise measurements of K^+, K^-, and K^0_S would deliver information needed to validate and distinguish between presented formulas.

8.1.1 K^0 properties and decay modes

K^0 is a meson that consists of d and $\bar{s}$ quarks. $\bar{K}^0$ consists of $\bar{d}$ and s quarks. Neutral Kaon has two weak eigenstates – short live K^0_S and long live K^0_L:

$$\left|K^0_S\right\rangle = \frac{1}{\sqrt{2}}\left(\left|K^0\right\rangle + \left|\bar{K}^0\right\rangle\right)$$

$$\left|K^0_L\right\rangle = \frac{1}{\sqrt{2}}\left(\left|K^0\right\rangle - \left|\bar{K}^0\right\rangle\right)$$

Neutral Kaon mass is equal to 497.614 ± 0.024 MeV/c^2. K^0_S decay modes are presented in Table 13.

Decay modes	Fraction Γ_i / Γ
Hadronic modes	
$\pi^+ \pi^-$	**(69.20 ± 0.05) %**
$\pi^0 \pi^0$	(30.69 ± 0.05) %
$\pi^+ \pi^- \pi^0$	$(3.5^{+1.1}_{-0.9}) \cdot 10^{-7}$
Modes with photons or $l\bar{l}$ pairs	
$\pi^+ \pi^- \gamma$	$(1.79 \pm 0.05) \cdot 10^{-3}$
$\pi^+ \pi^- e^+ e^-$	$(4.69 \pm 0.3) \cdot 10^{-5}$
$\pi^0 \gamma \gamma$	$(4.9 \pm 1.8) \cdot 10^{-8}$
$\gamma \gamma$	$(2.63 \pm 0.17) \cdot 10^{-6}$
Semileptonic modes	
$\pi^\pm e^m \nu_e$	$(7.04 \pm 0.08) \cdot 10^{-4}$
CP violating (CP) and ΔS = 1 weak neutral current (S1) modes	

$3\,\pi^0$	CP $<1.2 \cdot 10^{-7}$ CL=90%
$\mu^+\,\mu^-$	S1 $<3.2 \cdot 10^{-7}$ CL=90%
E^+ e-	S1 $<9 \cdot 10^{-9}$ CL=90%
$\pi^0\,e^+$ e-	S1 $(3.0^{+1.5}_{-1.2}) \cdot 10^{-9}$
$\pi^0\,\mu^+\,\mu^-$	S1 $(2.9^{+1.5}_{-1.2}) \cdot 10^{-9}$

Table 13. K^0_S decay modes [110].

The most often appearing decay of K^0_S leads to production of two charged pions with opposite signs (π^+ and π^-).

The most important K^0_L decay modes in terms of neutrino beam production are presented in Table 14. Hadronic modes, including CPV modes, and semileptonic modes with photons, modes with photons or lepton anti lepton pairs are not presented. Information about all decay modes can be found in [110].

Decay modes	Fraction Γ_i / Γ
Semileptonic modes	
$\pi^{\pm} e^{\mp} \nu_e$ called K^0_{e3}	(40.55 ± 0.12) %
$\pi^{\pm} \mu^{\mp} \nu_\mu$ called $K^0_{\mu 3}$	(27.04 ± 0.07) %
($\pi\,\mu$atom) ν	$(1.05 \pm 0.11) \cdot 10^{-7}$
$\pi^0 \pi^{\pm} e^{\mp} \nu$	$(5.20 \pm 0.11) \cdot 10^{-5}$
$\pi^{\pm} e^{\mp} \nu\, e^+ e^-$	$(1.26 \pm 0.04) \cdot 10^{-5}$

Table 14. K^0_L semileptonic decay modes [110].

8.1.2 Λ properties and decay modes

Λ is a hiperon that consists of u, d, and s quarks. It has mass equal to 1115.683 ± 0.006 MeV/c^2. Λ decay modes are presented in Table 15.

Decay modes	Fraction Γ_i / Γ
P π^-	**(63.9 ± 0.5) %**
N π^0	(35.8 ± 0.5) %
N γ	$(1.75 \pm 0.15) \cdot 10^{-3}$
P $\pi^-\,\gamma$	$(8.4 \pm 1.4) \cdot 10^{-4}$
P $e^-\,\overline{\nu_e}$	$(8.32 \pm 0.14) \cdot 10^{-4}$
P $\mu^-\,\overline{\nu_\mu}$	$(1.57 \pm 0.35) \cdot 10^{-4}$

Table 15. Λ decay modes. Information in table is taken from [110].

The most often appearing decay of Λ leads to production of negatively charged pion and proton.

8.2 Analysis method

The most frequent decay of K^0_S leads to the production of two charged pions (see Table 13). The most probable decay of Λ leads to the proton and positively charged pion production. These channels can be easily studied in TPC detectors placed in magnetic field or other detectors that allow particle identification. Even without particle identification, it is possible

to obtain information about K^0_S and Λ if a detector allows determining charge of tracks and their momenta. In such analyses, no detailed particle identification is needed. Information about K^0_S and Λ is obtained from the studies of invariant mass distributions under K^0_S or Λ hypothesis. The invariant mass of the decaying particle is described by this equation:

$$m_{inv} = \frac{1}{c^2}\sqrt{\left(\sum_i E_i\right)^2 - \left|\sum_i \overline{p}_i\right|^2 c^2}$$

where E_i are decay products' energies and $\overline{p}$ are their momentum vectors. If K^0_s hypothesis is studied, positively charged track is assumed to be a π^+ and negative one to be a π^-. In Λ hypothesis, positive one is assumed to be a proton and negative one to be a π^-. To reduce background, set of event and track cuts is done, which is described in chapter 8.3. After that, information about number of K^0_s or Λs is found from the fitting procedure, which fits sum of Lorentzian function (assumption: shape of the signal is reproduced by this function) and polynomial function. In the standard approach, 4th order polynomial is used. Influence of the different shape of the background function was studied. Lorentzian function is described by this formula:

$$Lorentzian\ \ function(x) = A\frac{\frac{1}{2}F}{(x-x_0)^2 + \left(\frac{1}{2}F\right)^2}$$

where parameter A controls peak's height, F is a full width at half maximum (FWHM), x_0 is a mean value (in this case, expected K^0_S or Λ mass).

Information about number of K^0_S or Λs in selected invariant mass region is obtained from the integral from the signal function (background is subtracted using fitted background function). Integral is calculated in a region from x-(3/2)*F to x+(3/2)*F. Those K^0_S' or Λs that are outside of this region are not counted. The same approach is used for real data and for reconstructed Monte Carlo tracks. This leads to a small model dependent correction because it is assumed that the same percent of signal is lost in real data and Monte Carlo while integral is calculated. This effect was estimated to be negligible as compared to systematic errors from different sources that are discussed in chapter 8.6. After estimation of number of K^0_S or Λs, Monte Carlo correction is calculated. It takes into account correction for branching ratio for studied type of decay, geometrical acceptance, and reconstruction efficiency. In respect to Λ hyperon, it also includes corrections for Σ^0, which decays into $\Lambda\ \gamma$ (BR≈100%). This correction is small because Σ^0 is only a small admixture (~2%) to the Λ production. The MC correction is calculated using the following formula (in each cell of studied variables):

$$C = \frac{N_{K^0_S(or\,\Lambda)}reconstructed}{N_{K^0_S(or\,\Lambda)}simulated}$$

where N reconstructed is a number of reconstructed particles (K^0_S or Λ) from exactly the same fitting procedure as for real data and N simulated is a number of generated primary particles (K^0_S or Λ). The error of correction was calculated using binomial distribution:

$$C_{error} = \sqrt{\frac{C(1-C)}{N_{K^0_S(or\,\Lambda)}simulated}}$$

At the end, corrected data are normalized using the NA49 normalization approach to production cross-sections or to mean multiplicity in all production proton Carbon interactions. The normalization procedure is described in chapter 6.4.2

8.3 Selection of events and tracks

Apart from event cuts presented in chapter 7.2, a set of additional event cuts was used. Three cuts listed below were applied:

- Fitted vertex existence cut. In some cases interaction point is not determined by reconstruction software.
- Fitted vertex iflag cut. There is a small contribution of events with determined interaction point but with feeble fit (Chi square/NDF is significantly larger or smaller than 1.0).
- Fitted vertex z coordinate cut. Interactions which took place outside the target (z coordinate outside region between -575 and -585) are rejected

The effects of the additional event cuts on the number of events are summarized in Table 16.

Event Cuts	DATA 07N Number of events (V0 candidates)	MC 07N Number of events (V0 candidates)
Before additional cuts (For Data case = after BPD Cut I & II and wrong run cut, For MC)	521238 (156084)	4981232 (1843262)
After fitted vertex & fitted vertex iflag cuts	309121 (151787)	4321644 (1822898)
After all cuts	276481 (148467)	4026511 (1782264)

Table 16. V^0 event cuts.

To purify the sample additional track cuts were applied:

- Invariant mass window cut. The analysis is made in the specific invariant mass window cut. The selected window should be the nearest possible to the peak but also should have some information outside the peak for the background fit procedure. The selection of the invariant mass window can influence the final results because description of the background is not precisely known. Therefore, fitting of the background function in a very narrow window can differ from the fit in wide window. This effect was checked and added to the systematic error studies.

K^0_S:

- For standard cuts wide window was used – [0.3, 0.7] GeV/c^2 (see Figure 103).

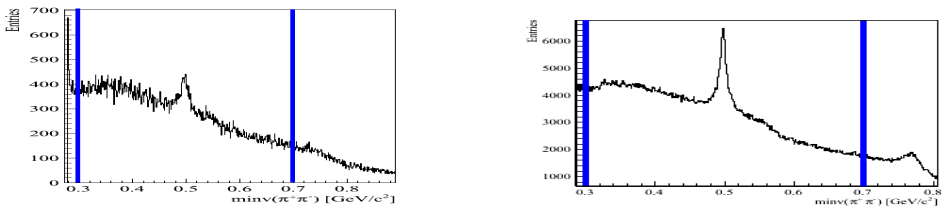

Figure 103. π+ π- invariant mass distribution of K^0_S candidates after event cuts. Invariant mass window cut is shown by blue lines. Real data (left). MC (right).

Λ:

- For standard cuts, wide window was used - [1.09, 1.16] GeV/c^2 (see Figure 104).

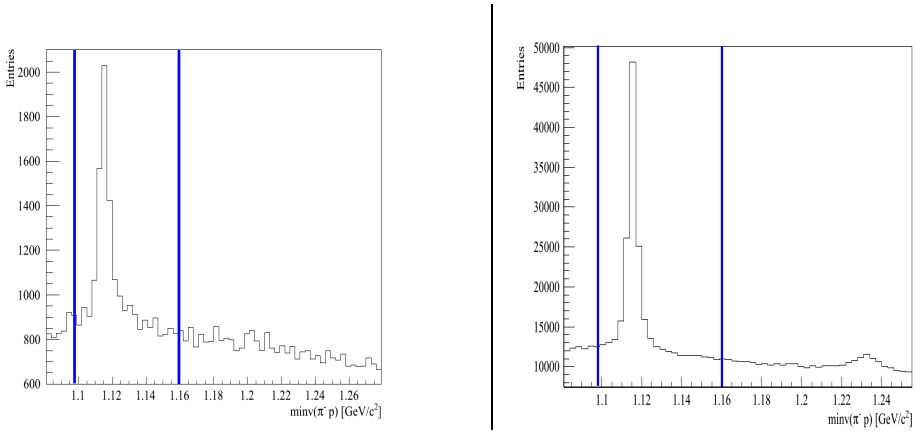

Figure 104. π- p invariant mass distribution for Λ candidates after event cuts. Blue lines show invariant mass window cut. Real data (left). MC (right).

- Cut on the angle between V^0 candidate and its decays products' momenta in the c.m.s. The distribution of this angle, further called ε, must be isotropic in the rest frame. According to the foregoing, distribution of cosine of this angle should be flat. A bad reconstruction can influence this distribution. Therefore cut is applied to cut off regions where cosine of ε is not within flat region.
  - K^0_S:
    - For standard cuts, cut for cosine of ε is used that selects region between – [-0.95, 0.8] (see Figure 105).

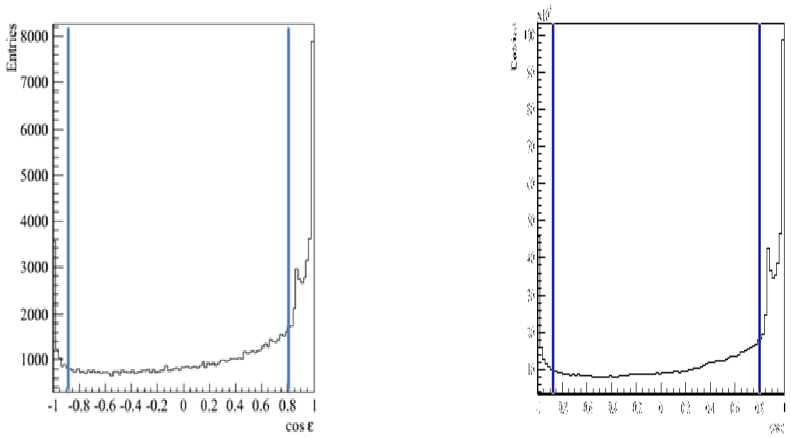

Figure 105. Cosine of ε angle for the K^0_S case. Blue lines represent cut edges. Real data (left). MC (right).

- Λ:
  - cosine of ε in region between [-0.8, 0.8] was selected (see Figure 106)

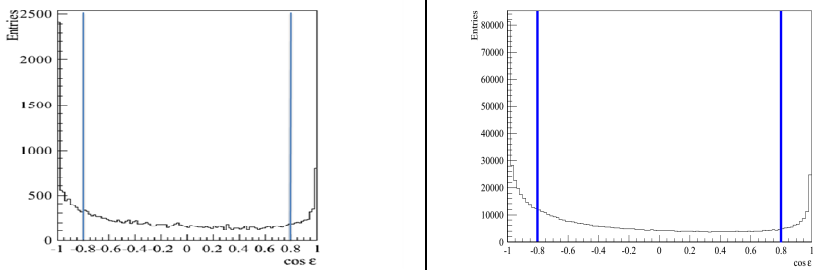

Figure 106. Cosine of ε angle for the Λ case. Blue lines represent cut edges. Real data (left). MC (right).

- Cut on the distance between the fitted vertex z coordinate and V^0 vertex z coordinate (dz). This cut is used to reject possible situation where primary vertex tracks were wrongly reconstructed as a V^0 tracks. Distance of 3 cm is used as a standard value in K^0_S and in Λ case as well. Distance distribution in K^0_S case is shown in Figure 107.

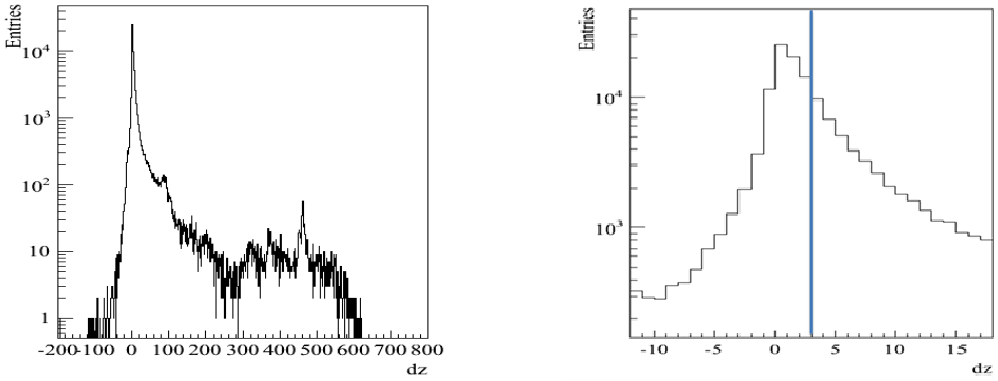

Figure 107. Distance between the fitted vertex z coordinate and V^0 vertex z coordinate in K^0_S case (left). Zoomed region of small dz values, blue line shows cut value (right).

- Cut on the Armenteros-Podolanski plot. Using two-dimensional plot of the Armenteros transverse momentum p_T^{ARM} and longitudinal momentum asymmetry α of V^0 decay products is possible to distinguish between different types of V^0 particles what is shown in theoretical Figure 108.

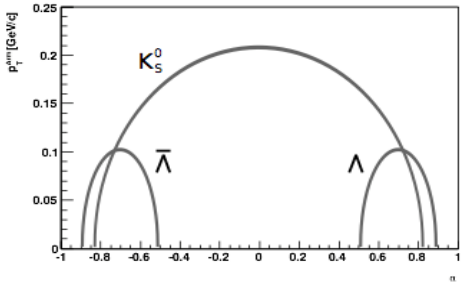

Figure 108. Theoretical picture of two-dimensional plot of the Armenteros transverse momentum p_T^{ARM} and longitudinal momentum asymmetry α of V^0 decay products. The picture is taken from [151].

The Armenteros transverse momentum is defined as:

$$p_T^{ARM} = p^{+,-} \sin \varphi^{+,-}$$

It is a absolute value of one daughter particle's momentum component transverse to the direction of motion of the V^0. The longitudinal momentum asymmetry is defined as follows:

$$\alpha = \frac{p_L^+ - p_L^-}{p_L^+ + p_L^-}$$

The graphical interpretation of the Armenteros transverse momentum, p^+_L, and p^-_L is shown in the Figure 109.

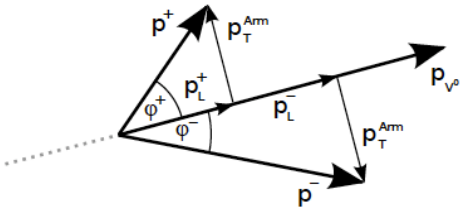

Figure 109. Graphical interpretation of the Armenteros transverse momentum, p+L, and p-L. The picture is taken from [151].

o K^0_S:

The Armenteros-Podolanski plots before and after all cuts are presented in Figure 110.

The standard cut is defined as follows:

Exclude regions: 1) $p_T^{ARM} < 0.05$

2) $p_T^{ARM} < 0.12$ && $\alpha > 0.5$

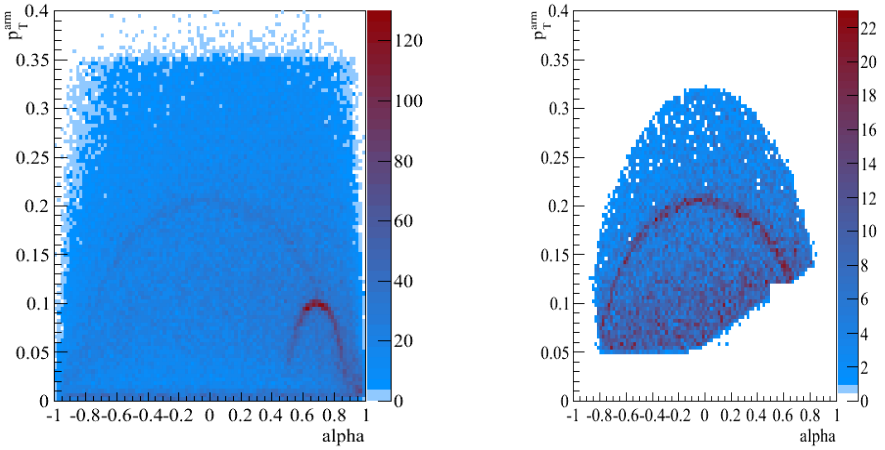

Figure 110. Armenteros-Podolanski plots before and after all cuts for K^0_S case.

o Λ:

The Armenterose-Podolanski plots after all cuts is presented in Figure 111.

The standard cut is defined as follows:

Excluded regions: 1) $p_T^{ARM} < 0.03 \parallel p_T^{ARM} > 0.11$

2) $\alpha < 0.45$

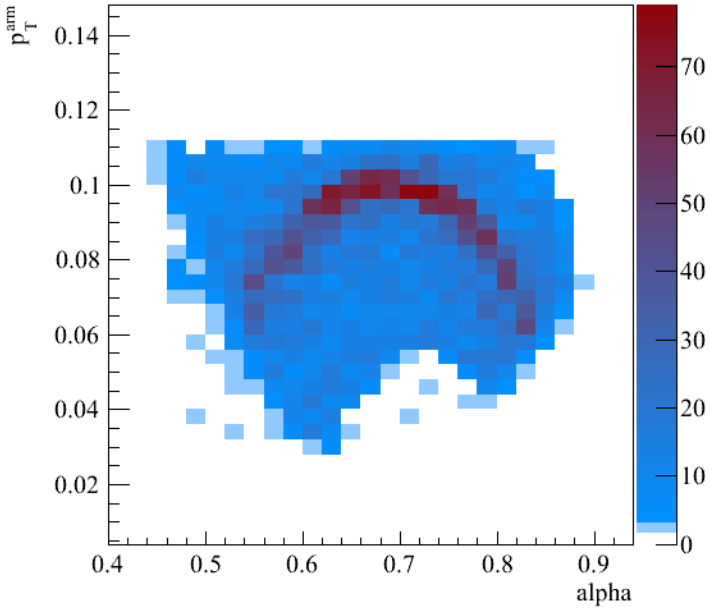

Figure 111. Armenteros-Podolanski plot after all cuts for Λ case.

8.4 Binning and uncorrected data

Studies of available statistics of uncorrected thin carbon data allowed to determine bin sizes in different variables in such a way that:

- For K^0_S and Λ, in momentum and polar angle variables
  - To be able to compare with results on the positively charged kaon production.
  - the same polar angle intervals were chosen
  - As small momentum bins as possible were chosen to be less model dependent and to be able to compare in details shapes of obtained distributions with MC predictions.
  - Variable bin size was used.
- For K^0_S in rapidity and transverse momentum variables
  - To be able to have a direct comparison with results obtained in [85].

8.4.1 K^0_S binning

The K^0_S candidate's momentum and polar angle distribution with imposed binning is shown in Figure 112. Bins colored in black were similar to the bins used in positively charged kaon studies. Larger bins colored in red were used only in total production cross-section studies. These bins were more exposed to the model dependent corrections because in that cases shapes of Monte Carlo distributions used for the correction calculations could affect final results.

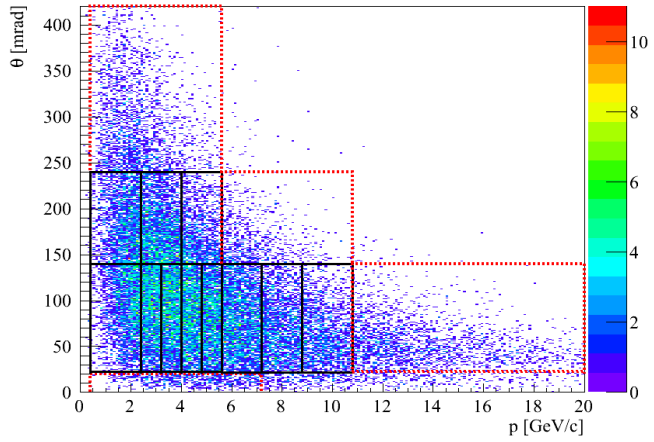

Figure 112. K^0_S candidate's momentum and polar angle distribution with superimposed binning.

The π+ π- invariant mass distributions in selected p, θ bins are presented in Figure 113.

[240, 420] mrad	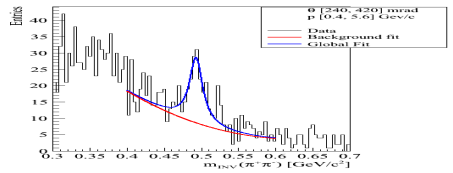 Chi^2/ndf 1.17263 K^0_S mass 0.49754					
[140,240] mrad	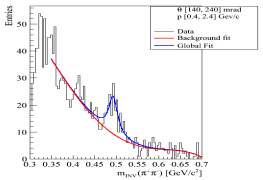 Chi^2/ndf 0.97686 K^0_S mass 0.49811	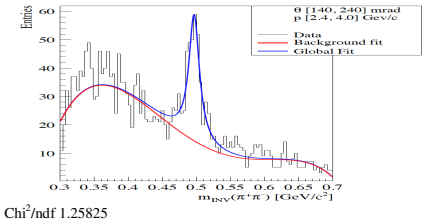 Chi^2/ndf 1.25825 K^0_S mass 0.49653	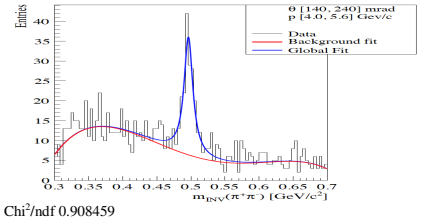 Chi^2/ndf 0.908459 K^0_S mass 0.496259			
[20, 140] mrad	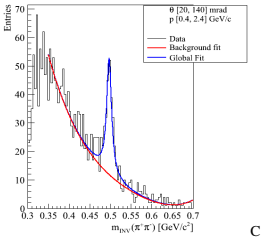 hi^2/ndf 1.30076 K^0_S mass 0.497706 C	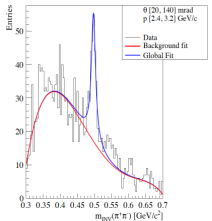 Chi^2/ndf 1.23891 K^0_S mass 0.49706	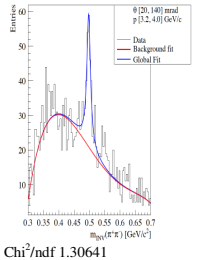 Chi^2/ndf 1.30641 K^0_S mass 0.497303	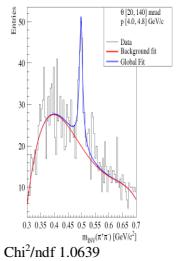 Chi^2/ndf 1.0639 K^0_S mass 0.497584	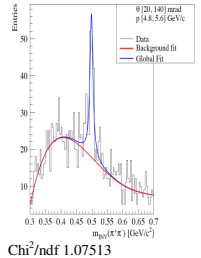 Chi^2/ndf 1.07513 K^0_S mass 0.498449	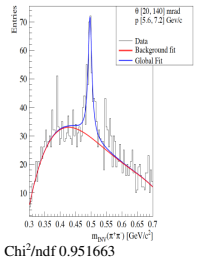 Chi^2/ndf 0.951663 K^0_S mass 0.49645	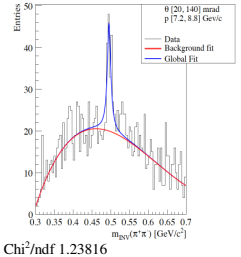 Chi^2/ndf 1.23816 K^0_S mass 0.495075
[0, 20] mrad	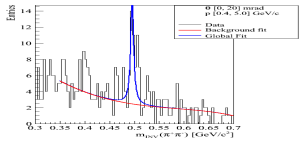 Chi^2/ndf 1.17263 K^0_S mass 0.49736					

Figure 113. π+π- invariant mass distributions for K^0_S candidates in selected p, θ bins.

The number of Kaons found in selected momentum and polar angle cells are presented in Table 17.

θ_{low} θ_{high} [mrad]	p_{low} p_{high} [GeV/c]	Nrec	ΔNrec
0 20	0.4 7.2	51	7
20 140	0.4 2.4	183	13
	2.4 3.2	186	13
	3.2 4.0	181	13
	4.0 4.8	137	12
	4.8 5.6	142	12
	5.6 7.2	182	13
	7.2 8.8	75	9
	8.8 10.8	108	10
	10.8 20.0	130	11
140 240	0.4 2.4	112	10
	2.4 4.0	262	16
	4.0 5.6	138	12
	5.6 10.8	78	9
240 420	0.4 5.6	132	11

Table 17. Number of Kaons found from the fitting procedure in selected momentum and polar angle cells.

8.4.2 Λ binning

The Λ candidate's momentum and polar angle distribution with imposed binning is shown in Figure 114.

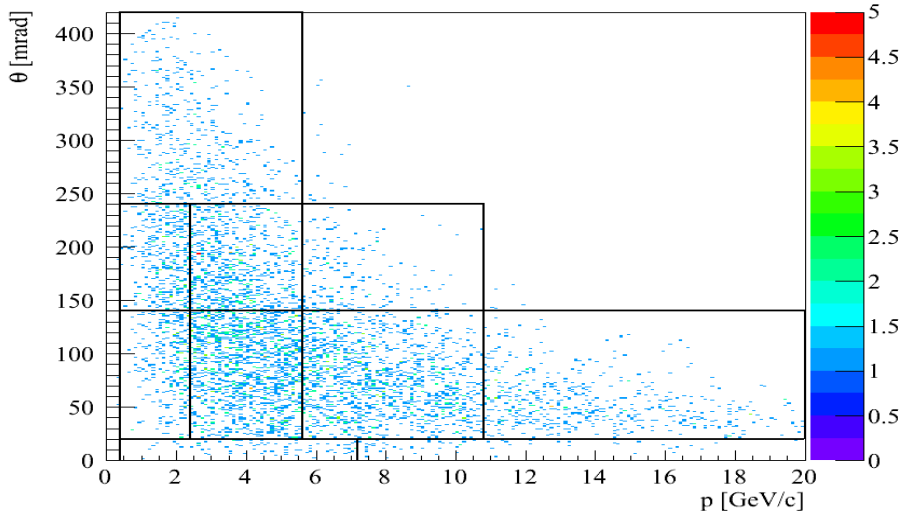

Figure 114. Λ candidate's momentum and polar angle distribution with superimposed binning .

The π- p invariant mass distributions in selected p, θ bins are presented in Figure 115.

The number of Λ found in selected momentum and polar angle cells are presented in Table 18.

θ_{low} θ_{high} [mrad]	p_{low} p_{high} [GeV/c]	Nrec	ΔNrec
20 140	0.4 2.4 2.4 5.6 5.6 7.2 7.2 10.8 10.8 20.0	53 562 248 468 347	8 26 16 22 19
140 240	0.4 2.4 2.4 5.6 5.6 10.8	51 400 85	10 21 10
240 420	0.4 5.6	224	17

Table 18. Number of Λ found from the fitting procedure in selected momentum and polar angle cells.

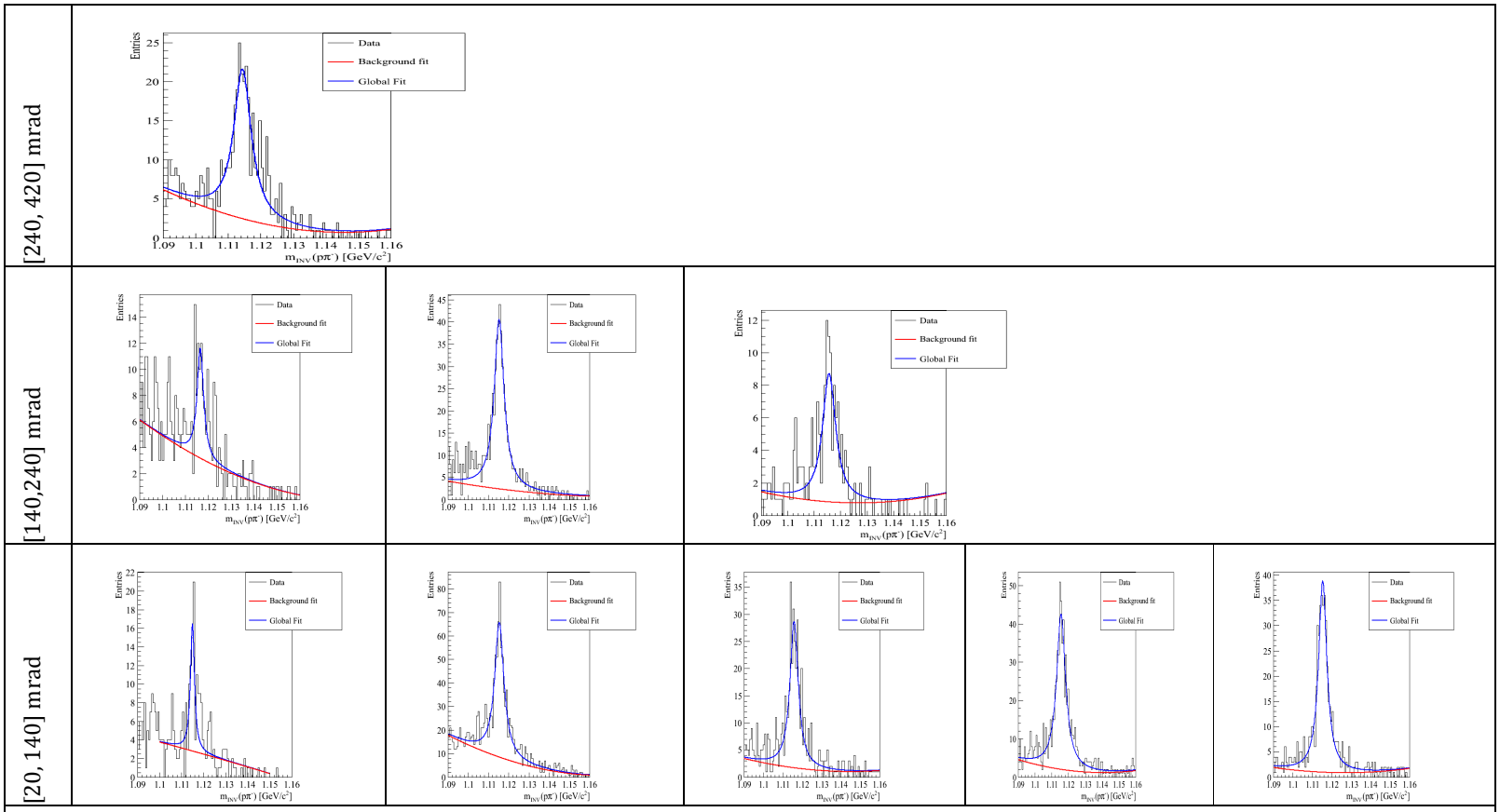

Figure 115. π- p invariant mass distributions in selected p, θ bins.

8.5 Correction factors

In this chapter correction factors calculated are presented. To calculate correction, information about reconstructed particles (K^0_S or Λ) and information about simulated particles of each type are needed. Information about reconstructed particles is obtained in the same way as for the real data. The momentum versus polar angle distribution of simulated K^0 is presented in Figure 116.

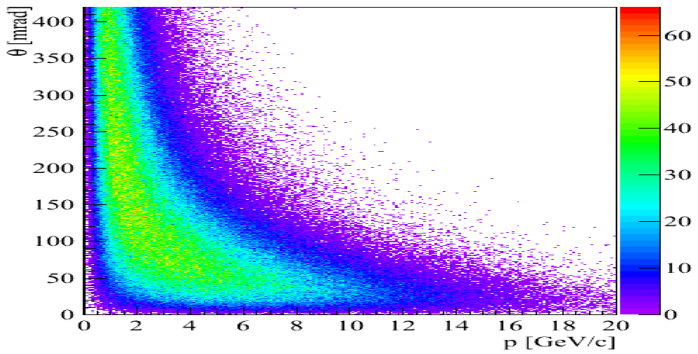

Figure 116. Momentum versus polar angle distribution of simulated K0. Information from the VENUS generator.

The momentum versus polar angle distribution of simulated Λ is presented in Figure 117.

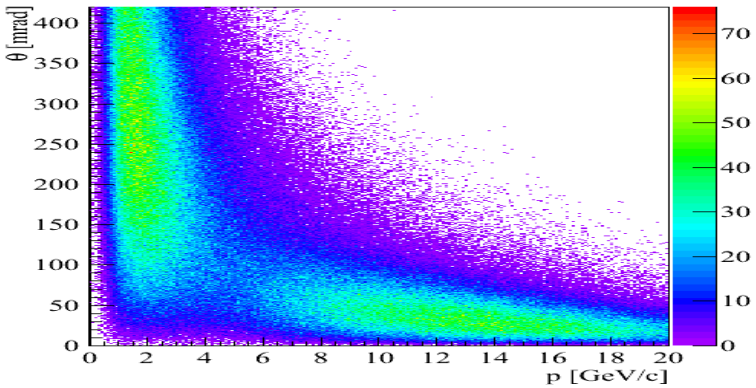

Figure 117. Momentum versus polar angle distribution of simulated Λ. Information from the VENUS generator.

The $\pi+$ $\pi-$ invariant mass distributions in selected p, θ bins from reconstructed Monte Carlo data are presented in Figure 118.

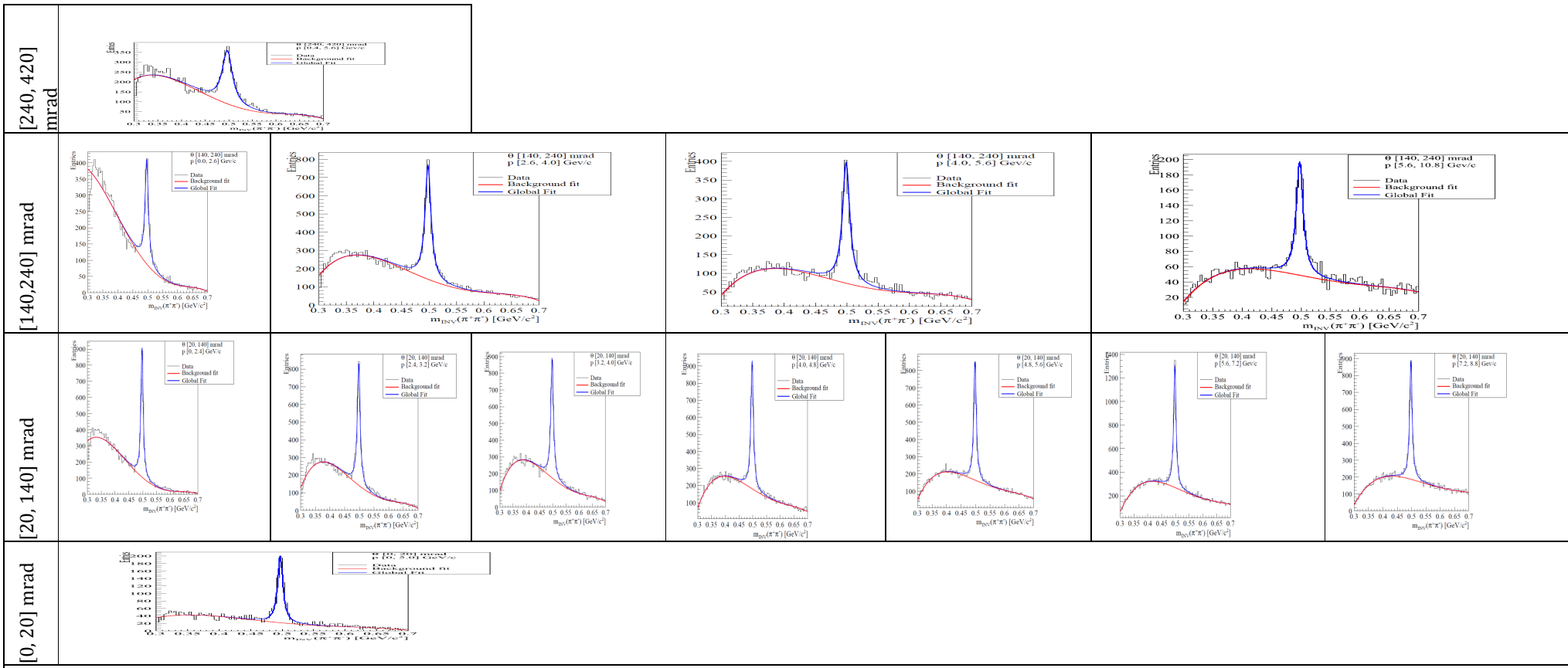

Figure 118. π+ π- invariant mass distributions in selected p, θ bins. Reconstructed Monte Carlo data.

The Kaon corrections evaluated from the Monte Carlo in momentum and polar angle variables are presented in Table 19.

θ_{low} θ_{high} [mrad]	p_{low} p_{high} [GeV/c]	Nsim	ΔNsim	Nrec	ΔNrec	MC correction	MC correction error
0 20	0.4 7.2	10908	104	1067	33	0.0979	0.0028
20 140	0.4 2.4	58087	241	2417	49	0.0416	0.0008
	2.4 3.2	32905	181	2472	50	0.0751	0.0014
	3.2 4.0	31544	178	2624	51	0.0831	0.0015
	4.0 4.8	28274	168	2574	50	0.0910	0.0017
	4.8 5.6	24330	156	2241	47	0.0921	0.0018
	5.6 7.2	36936	192	3345	58	0.0905	0.0014
	7.2 8.8	24172	155	2325	48	0.0962	0.0018
	8.8 10.8	18054	134	1726	41	0.0956	0.0021
	10.8 20.0	16742	129	1521	39	0.0909	0.0022
140 240	0.4 2.4	69280	263	1359	37	0.0196	0.0005
	2.4 4.0	31443	177	2548	50	0.0810	0.0015
	4.0 5.6	10373	102	1417	38	0.1366	0.0033
	5.6 10.8	4250	65	661	26	0.1557	0.0056
240 420	0.4 5.6	119075	345	2209	57	0.0185	0.0004

Table 19. Kaon correction factors evaluated from the Monte Carlo in momentum and polar angle variables.

The π^- p invariant mass distributions in selected p, θ bins for reconstructed Monte Carlo data are presented in Figure 119.

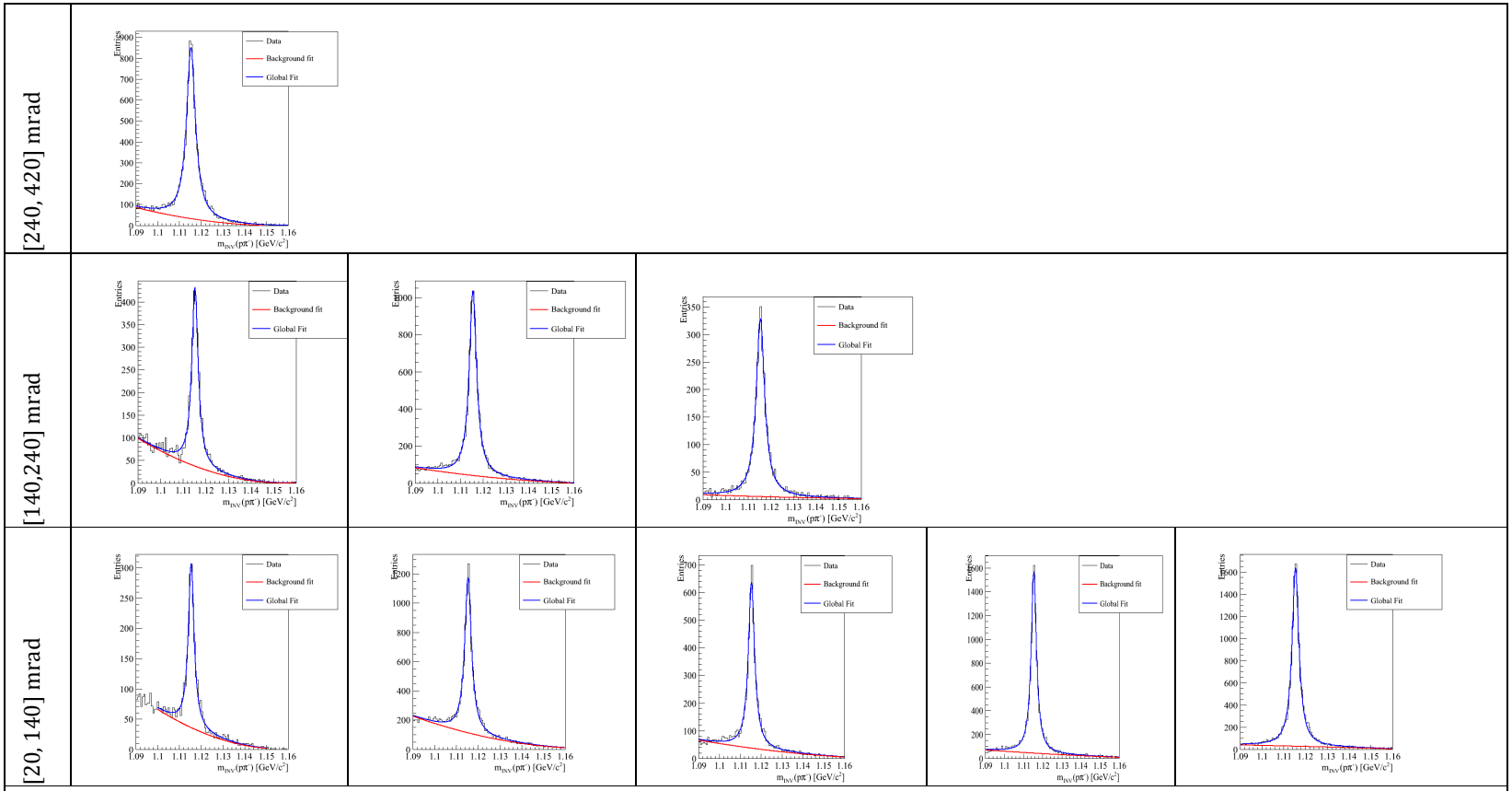

Figure 119. The π- p invariant mass distributions in selected p, θ bins. Reconstructed Monte Carlo information.

The Λ corrections evaluated from the Monte Carlo in momentum and polar angle variables are presented in Table 20.

θ_{low} θ_{high} [mrad]	p_{low} p_{high} [GeV/c]	Nsim	ΔNsim	Nrec	ΔNrec	MC correction	MC correction error
20 140	0.4 2.4	38316	196	1557	43	0.041	0.001
	2.4 5.6	62777	250	7081	90	0.113	0.001
	5.6 7.2	30357	174	3896	64	0.128	0.002
	7.2 10.8	79015	281	9122	95	0.115	0.001
	10.8 20.0	121755	349	10883	102	0.089	0.001
140 240	0.4 2.4	61866	249	2377	52	0.038	0.001
	2.4 5.6	58957	243	6929	84	0.117	0.001
	5.6 10.8	15894	126	2595	51	0.163	0.003
240 420	0.4 5.6	173157	416	7216	85	0.0417	0.0004

Table 20. Λ correction factors evaluated from the Monte Carlo in momentum and polar angle variables.

8.6 Estimation of systematic errors

Presented below, possible sources of systematic errors were studied:

- uncertainty connected with track cuts
- uncertainty connected with background fit function used in fitting procedure of invariant mass spectra.
    - Besides standard 4th order polynomial three different functions were used:
        - 3rd order polynomial
        - 6th order chebyshev polynomial
        - argus function, which is described:
            - $$Argus(x) = x\left(1-\left(\frac{x}{m}\right)^2\right)^p \exp\left(c\left(1-\left(\frac{x}{m}\right)^2\right)\right)$$

              where m, p, c are parameters of the function.

Influence of different background function was checked on the all versions of cuts. The examples of different two background fits for K^0_S all candidates after standard cuts are presented in Figure 120. For the final systematic errors, studies were performed in each cell of momentum and polar angle.

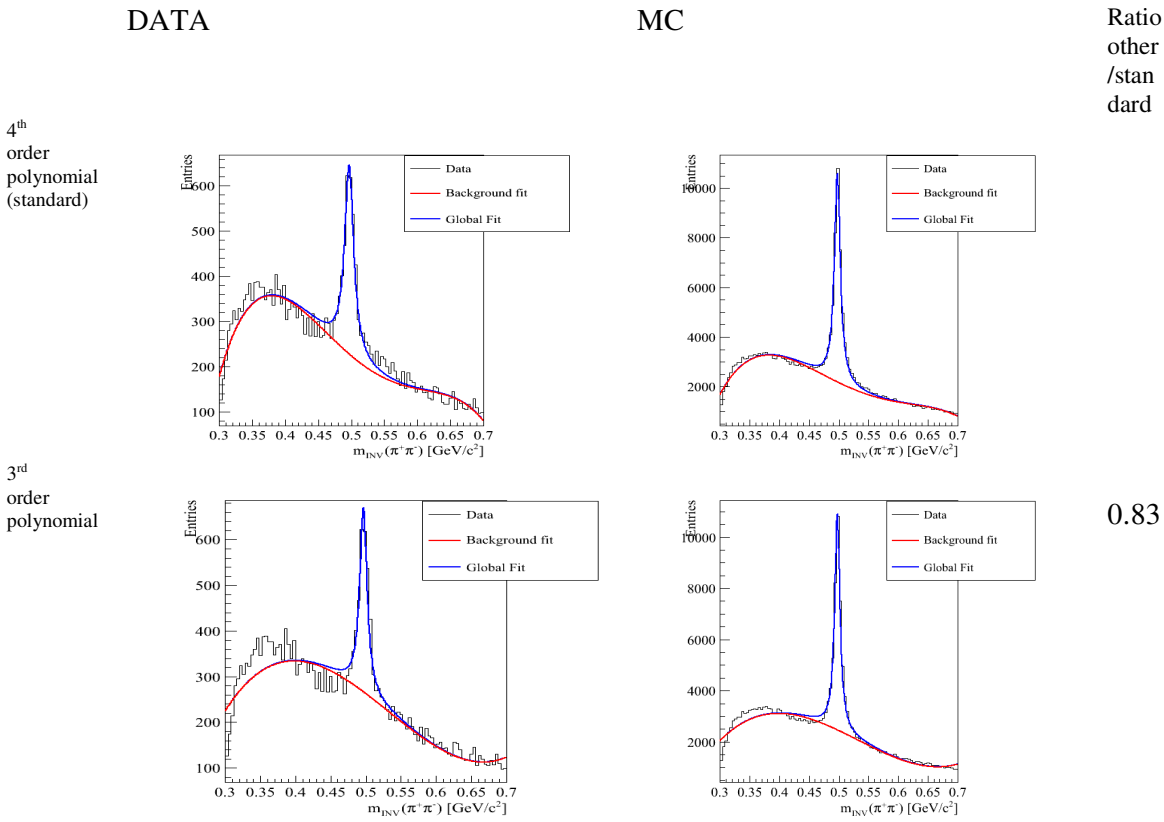

Figure 120. Examples of different background fit for K0S case and standard cuts.

In K^0_S case, Argus function and 3rd order polynomial have problems with reproduction of low values invariant mass distribution behavior (<0.4 GeV/c^2). While narrower window is used ([0.4, 0.6]) all fitting procedures lead to the similar results (differ from standard result less than ~5%). Region of small values of invariant mass is not important in these studies. However, the 6th order chebyshev polynomial very well reflects behavior in this region.

- uncertainty connected with geometrical acceptance, reconstruction efficiency, different reconstruction algorithms of track merging.

Systematic error connected with those sources was evaluated from the systematic errors calculated for the h- analysis. In this approach, assumption that V^0 tracks have the same reconstruction efficiency and geometrical acceptance as π^- is done. Furthermore, assumption that there is no difference between π^-, π^+, and proton tracks is made. In h- analysis, geometrical acceptance studies were done on the flat phase space simulation.
Estimated errors are presented in Table 21.

Polar angle interval	Systematic error [%]
[0, 20] mrad	~ 3.6
[20, 140] mrad	~ 4.3
[140, 240] mrad	~ 3.1
[240, 420] mrad	~ 4.5

Table 21. Systematic error connected with geometrical acceptance, reconstruction efficiency, and different reconstruction algorithms of track merging in V^0 analyses.

In inclusive cross section for K^0_S production additional systematic error needs to be estimated because in this approach partially model dependent correction is used in regions where gaps in geometrical acceptance appear. These errors weas estimated using information from different Monte Carlo models.
First of all numbers of simulated K^0_S in the region where acceptance gap appears (<300 MeV/c and below 10 mrad && >7.6 GeV/c and for polar angle > 420 mrad) was calculated for different MC models. These numbers differed up to 30%. In VENUS this number was equal to ~29% of all K^0_S.
At the end, final result was calculated using to corrections number of simulated particles from VENUS in acceptance plus number of simulated particles outside the acceptance and plus/minus 30% of these particles. These results were compared and model dependent systematic error was estimated.

8.7 Final results

Normalization was done accordingly to procedure described in chapter 6.4.2. Empty target subtraction had a very small influence in case of V^0 analyses. Number of events, accepted after cuts, is presented in Table 22.

Event Cuts	Target IN	Target OUT
All	671824	23933
Wrong run cut	671303	23933
BPD Cut I	565510	10436
BPD Cut II	521238	9239
Fitted vertex existence and iflag cut	309121	1882
Fitted vertex z position cut	276481	27

Table 22. Number of events after event cuts in Target IN and Target OUT case.

After all track cuts, there is no V^0 candidates left in K^0_S and Λ analyses. In this case, empty target subtraction changed only number of events taken to the normalization procedure.
Number of events accepted after all cuts was equal to Ntarget IN – c * Ntarget Out = 276481 – c * 27 = 276481 – 2.198*27 = 276421. In to Out ratio factor was obtained from the comparison of the vertex z distributions of in and out target setups. It was equal to 2.198 +- 0.027. Correction for inelastic events cut off was calculated using Monte Carlo simulations. The numbers of Monte Carlo events before and after event cuts are presented in Table 16. The correction for inelastic events was equal to 0.808. At the end, number of events taken to

normalization was equal to 276421/0.808 = 342105. The cross section for production processes is equal to σ_{prod}= 229.3 ±1.9 ± 9.0 mb.

The overall normalization uncertainty (~3%) is not propagated in the analyses.

The mean multiplicity in production processes and inclusive cross section for K^0_S production were obtained. These result were evaluated from the results obtained in momentum and polar angle variables. Regions outside the geometrical acceptance were corrected accordingly to VENUS simulations. Therefore, additional systematic error was quoted.

The final results with systematic errors are presented below:

- The K^0_S mean multiplicity in production processes is equal to:
  - **$<NK^0_S>$ = 0.125 ± 0.007 (stat) ± 0.007 (sys)**
- The inclusive cross section for K^0_S production is equal to:
  - **σK^0_S = 28.58 ± 1.85 (stat) ± 1.72 (sys) [mb]**

The K^0_S mean multiplicity in production processes from proton Carbon interactions was compared with compilation of total integrated K^0_S yields from proton proton interaction experiments [38]. To be able to compare these results, our result was scaled by the mean number of collisions (<ν>) in proton Carbon interactions. We assumed that <ν> is equlat to 1.6 ± 0.8. In different models these number differs from ~1.5 to ~1.7 (see Figure 121).

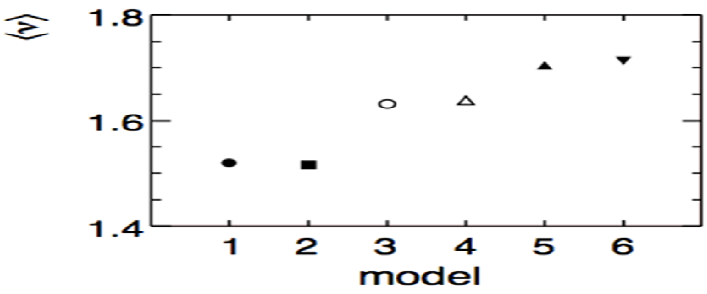

Figure 121. Mean number of collisions for different nuclear density parametrizations (1-Woods-Saxon, 2 – Gaussian, 3 – Fourier-Bessel, 4 – Sum of Gaussians, 5 – Fourier-Bessel unfolded, 6 – Sum of Gaussians unfolded). Picture is taken from [53].

The comparison of our data with compilation of existing results is shown in Figure 122.

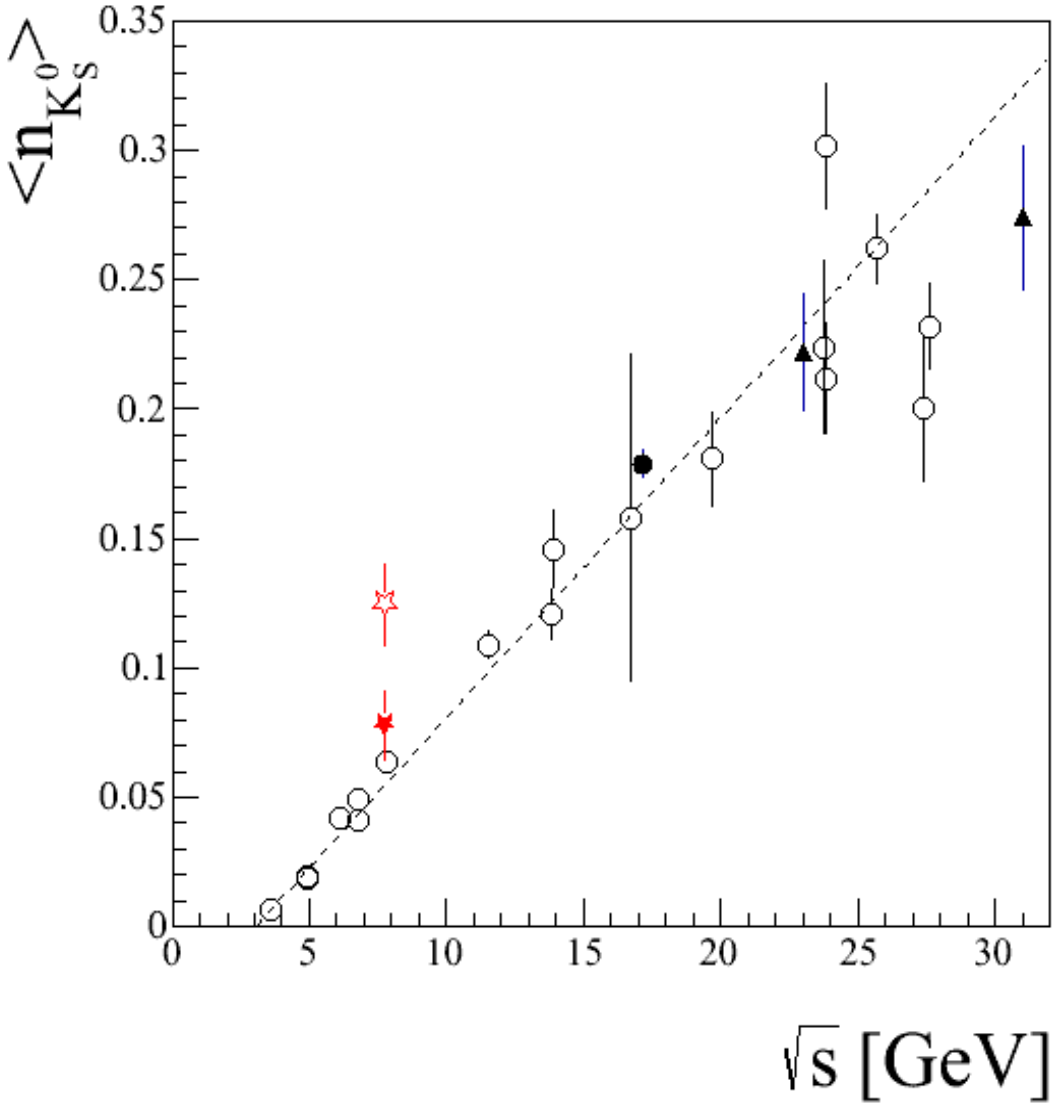

Figure 122. Total integrated K^0_S yields as a function of $\sqrt{s}$. Open black points taken from [38]. The $(K^+ + K^-)/2$ from NA49 - full circle. The $(K^+ + K^-)/2$ from ISR extr./UA5 – triangles. Result from this thesis not scaled by mean number of collisions - red open star. Result from this thesis after scaling by mean number of collisions equal to 1.6 – red full star. The dashed line is shown to guide the eye.

The reasonable agreement between obtained result and other results was found. The systematic error connected with a possible change of the mean number of collisions value is not shown in this figure.

The K^0_S production cross sections and mean multiplicity distributions from production interactions were obtained. The production cross sections in polar angle slices are shown in Figure 123.

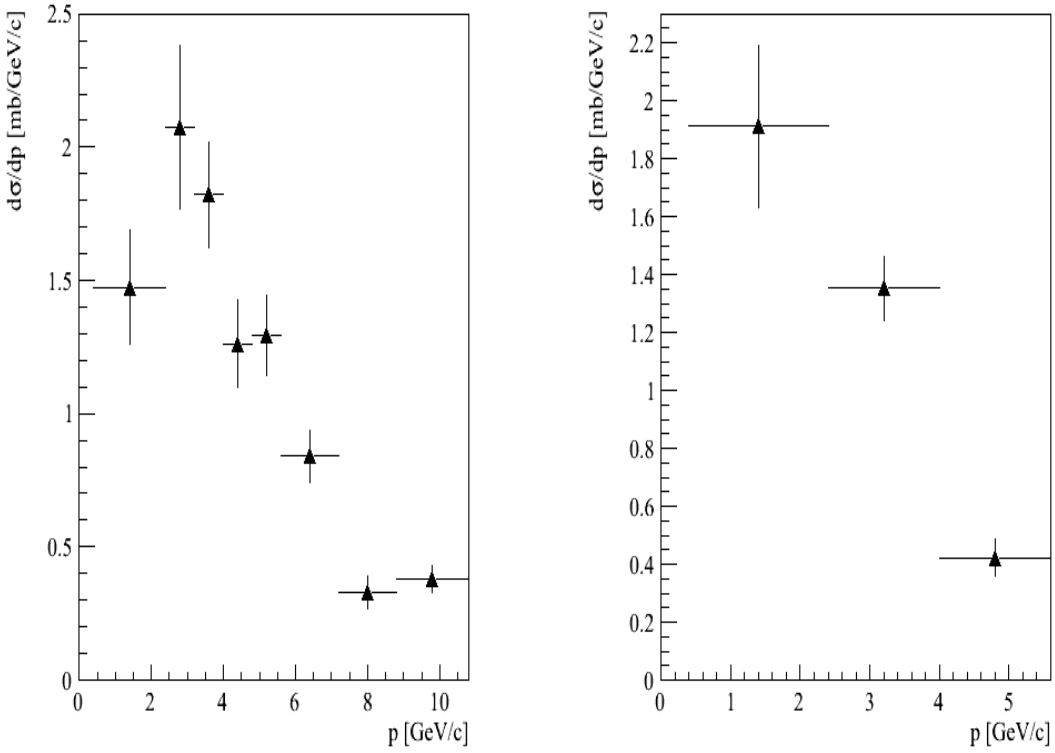

Figure 123. K^0_S production cross sections in two polar angle intervals: [20, 140] mrad (left) and [140, 240] mrad (right). Only statistical errors are shown. Error connected with normalization was not propagated.

The final K^0_S results with systematic errors are presented in Appendix.

The Λ production cross sections and mean multiplicity distributions from production interactions were also obtained. The production cross sections in polar angle slices are shown in Figure 124.

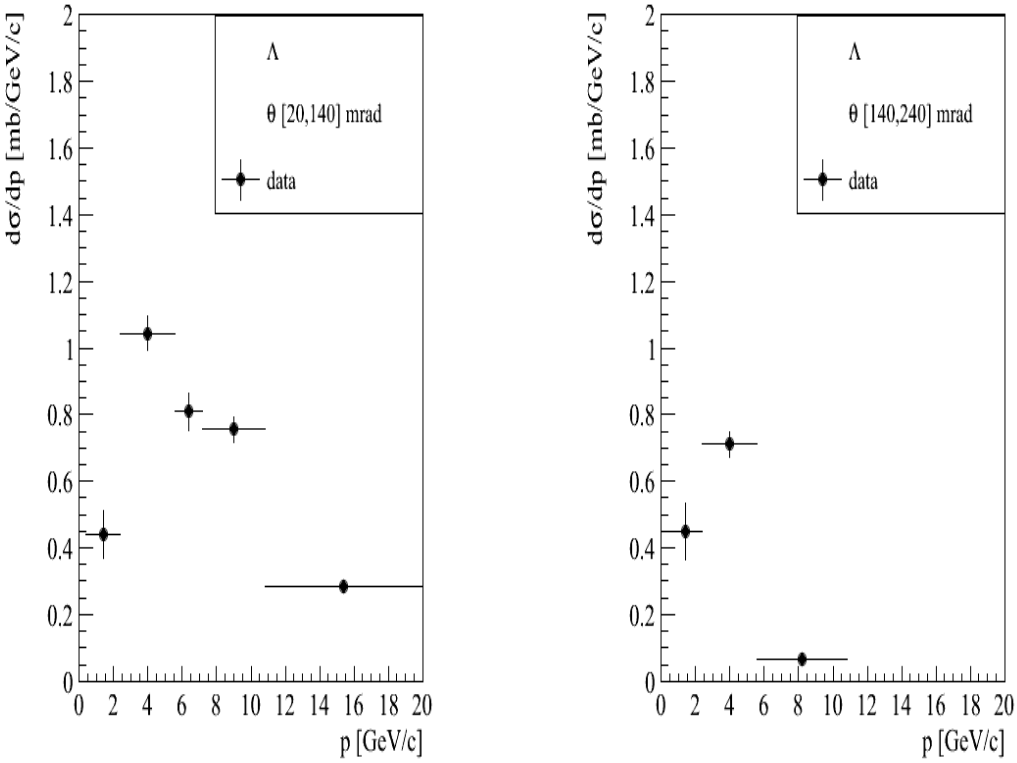

Figure 124. Λ production cross sections in two polar angle intervals: [20, 140] mrad (left), [140, 240] mrad (right). Only statistical errors are shown. Error connected with normalization was not propagated.

Chapter 9 Comparison of results with Monte Carlo models

9.1 Monte Carlo models used for comparison

9.1.1 VENUS

The VENUS (Very ENergetic NUclear Scattering) is used in the official NA61/SHINE Monte Carlo chain as a particles generator. The VENUS generator is based on the Gribbov-Regge theory. In this theory the concept of Reggeon or Pomeron exchange is used which can be linked to special Quantum Chromo Dynamics diagrams [10].

9.1.2 UrQMD

The UrQMD (Ultra-relativistic Quantum Molecular Dynamics) is a model based on the phase space description of the interaction with the transport theory [10]. In this model full relativistic calculation of the reaction is performed in four dimensions. The excitation, coalescence, and resonance decay or string fragmentation are used to parametrized particle production. The propagation of particles is calculated numerically. Cross sections are interpreted geometrically – interaction appears if two particles come close enough to each other. Cross sections are given as an input in tabulated or parameterized form from experimental measurements. As an input also two-body potentials and decay widths are given.

9.1.3 FLUKA

The Fluka is also microscopic model [175]. It is based on the resonance production and decay below a few GeV, and on the DPM model above in case of hadron-nucleon interactions. In hadron-nucleus interaction also two models are used: the PEANUT package (based on the Intra-Nuclear Cascade and preequilibrium stage) at low moment 3-5 GeV/c and the Gribov-Glauber multiple collision mechanism at high energies. After that, equilibrium, evaporation, fission, Fermi break-up, and gamma deescitation are taken into account.

9.2 Predictions for negatively charged pion production in proton Carbon interactions

9.2.1 π^- results in momentum and polar angle

The final π^- results (results from h- combined with results from dE/dx analysis) in momentum and polar angle variables normalized to mean particle multiplicity in production processes are shown in Figure 125 with predictions from Monte Carlo models.

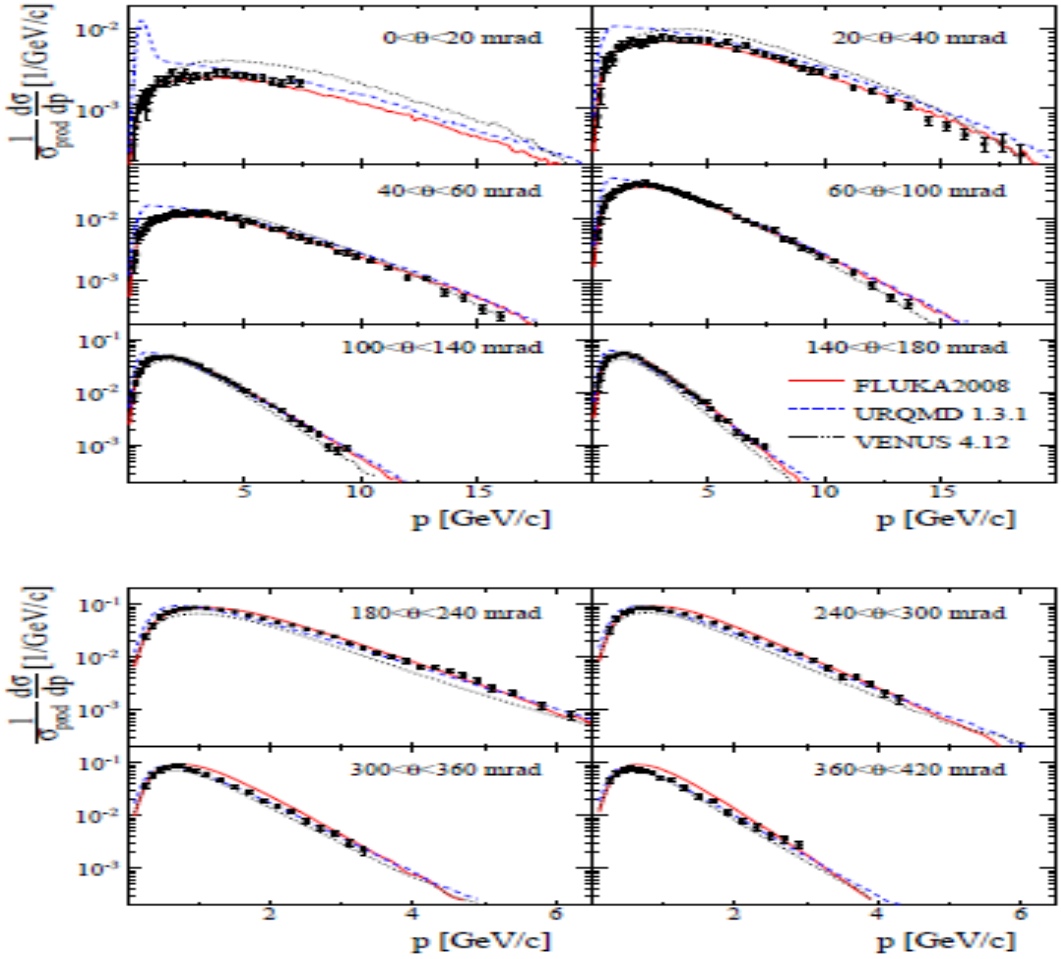

Figure 125. Final π^- results (results from h- combined with results from dE/dx analysis) in momentum and polar angle variables normalized to mean particle multiplicity in production processes. Monte Carlo model predictions are superimposed. Only statistical errors are shown. Error connected with normalization (2.5%) is not shown.

The discrepancies between data and UrQMD prediction at low polar angle intervals were observed. This was reported to the authors of the UrQMD. As a result, new patched version of the UrQMD was released in which these problematic regions were corrected. The best agreement with Fluka 2008 predictions was found. Nonetheless, the Fluka authors also used these results to tune their model.

9.2.2 π^- results in Feynman x and transverse momentum

In this subchapter the final π^- results in Feynman x and transverse momentum variables normalized to mean particle multiplicity in production processes are shown with predictions from Monte Carlo models.
The $d^2n/dx_f dp_T$ versus x_f distributions for different p_T intervals are shown in Figure 126. The Fluka 2008, Venus, and UrQMD predictions are superimposed.

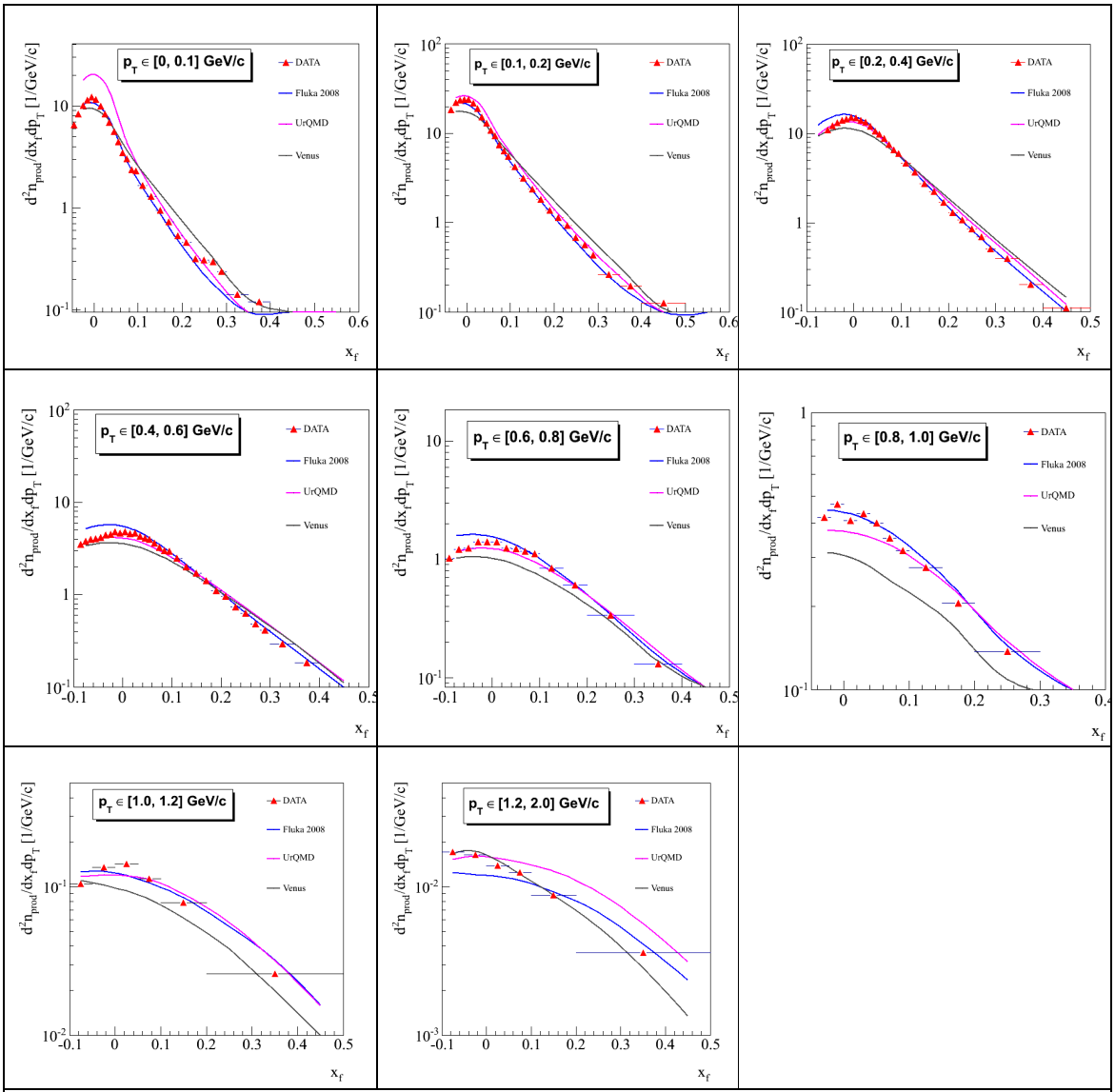

Figure 126. $d^2n/dx_f dp_T$ versus x_f distributions for different p_T intervals. The Fluka 2008 (blue), UrQMD (pink), and Venus (black) predictions are superimposed.

The best agreement with Fluka 2008 predictions was found. Mainly in the region of negative values of Feynman x some discrepancies are visible. In this region, UrQMD predictions reflect the data well. However, in the first p_T interval UrQMD predictions are inconsistent with the data at small values of x_f. In other p_T intervals, UrQMD predictions are almost always above the data for larger values of x_f.
The $d^2n/dx_f dp_T$ versus p_T distributions for different x_F intervals are shown in Figure 127.

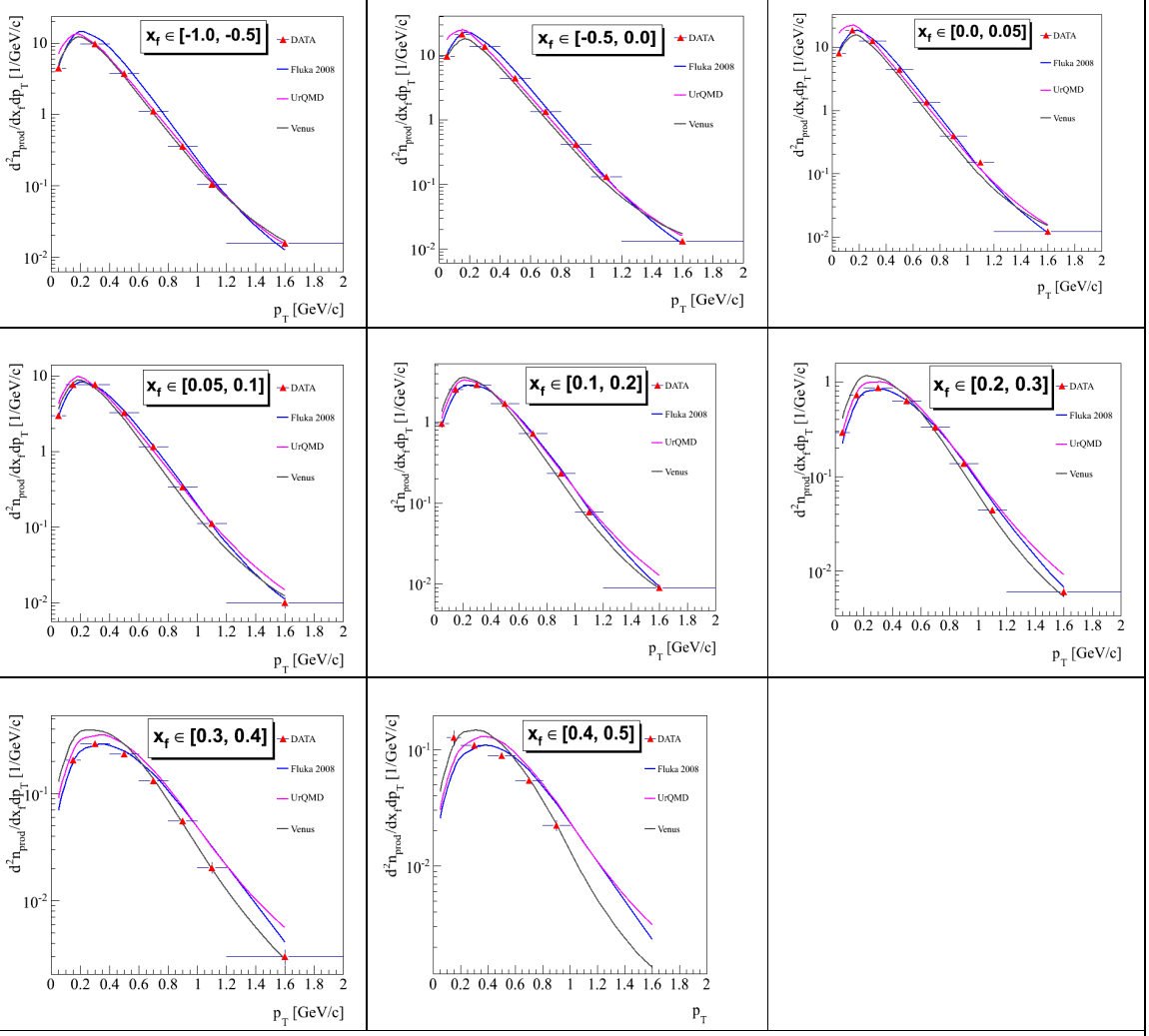

Figure 127. $d^2n/dx_f dp_T$ versus p_T distributions for different X_F intervals. The Fluka 2008 (blue), UrQMD (pink), and Venus (black) predictions are superimposed.

The reasonable agreement with Venus predictions was found.

For the larger values of xf (>0.2):

- in the low p_T region (<0.6 GeV/c) VENUS predictions are always above the data,
- in the high p_T region (>0.6 GeV/c) the Fluka 2008 and UrQMD predictions are above the data.

The models reflect the behavior of the data for $d^2n/dx_f dp_T$ versus x_f and $d^2n/dx_f dp_T$ versus p_T distributions. The shapes of the distribution are similar. However, observed differences in some specific region are larger than 30%. This shows that our results are important to understand and tune Monte Carlo predictions.

9.3 Predictions for neutral strange hadron production in proton Carbon interactions

9.3.1 K^0_S in momentum and polar angle variables

The K^0_S results in momentum and polar angle variables normalized to mean particle multiplicity in production processes are shown in Figure 128 with predictions from Monte Carlo models.

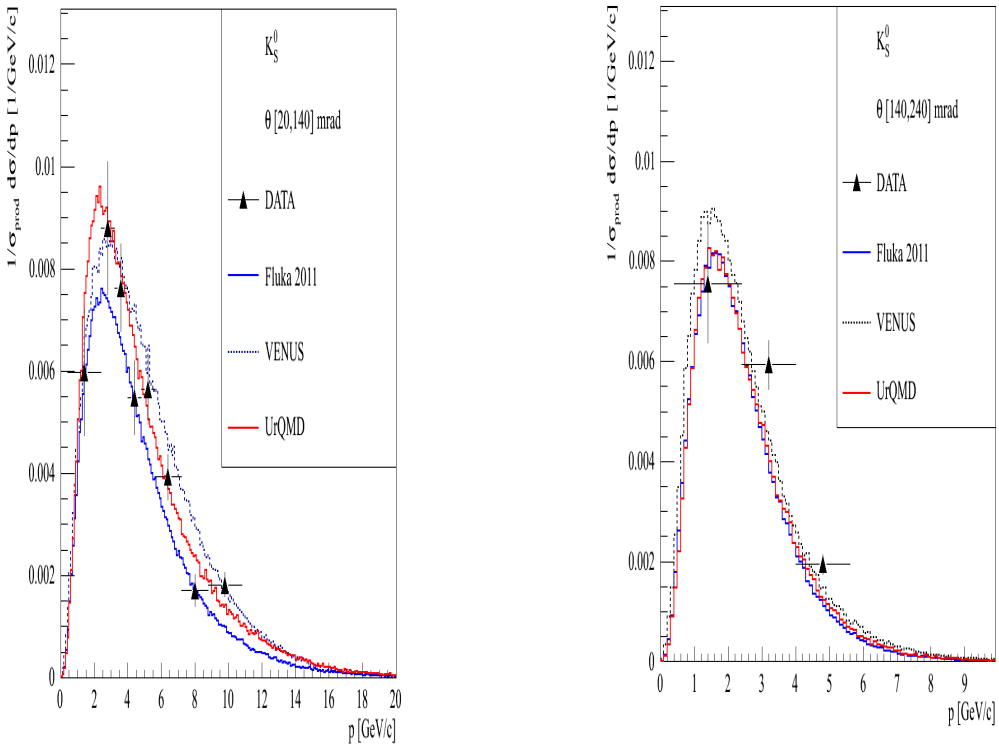

Figure 128. K^0_S mean particle multiplicity in production processes in polar angle intervals: [20, 140] mrad (left), [140, 240] mrad (right). Monte Carlo model predictions are superimposed. Only statistical errors are shown.

The reasonable agreement between data and Monte Carlo predictions was observed. However, the experimental points are mostly above FLUKA predictions.

9.3.2 K^0 / π^- ratios versus momentum in selected polar angle intervals

In the production point the number of K^0_S is the same as the number of K^0_L .Thereofre, the K^0_S results could be easily transformed to the K^0 results.
The K^0 / π^- ratios versus momentum in selected polar angle intervals are show in Figure 129.

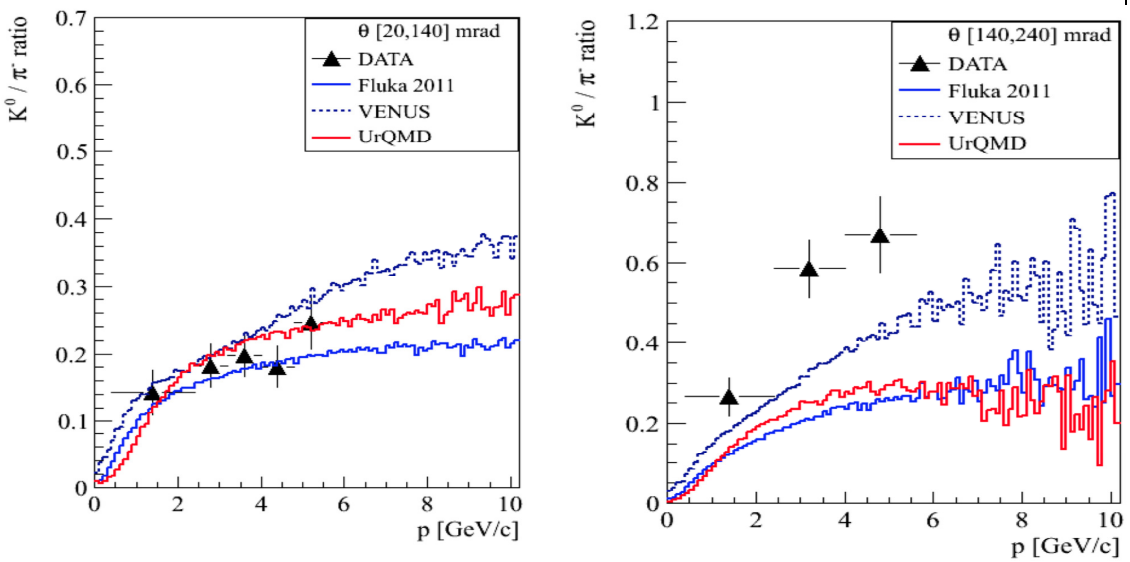

Figure 129. K^0/π^- ratios versus momentum in two polar angle intervals. Left [20, 140] mrad, right [140, 240] mrad. The vertical error bars on the data points show the total (stat. and syst.) uncertainty. Monte Carlo models are superimposed.

The ratio of K0's to pion's provides information on strangeness suppression factor since it is a ratio of $d\bar{s}$ to $d\ \bar{u}$ quark system.

9.3.3 K^0_S / K^+ ratios versus momentum in selected polar angle intervals

The K^0_S / K^+ ratios in selected polar angle intervals are shown in Figure 130. For the ratios calculations the K+ results obtained by NA61/SHINE using dE/dx+TOF analyses were used.

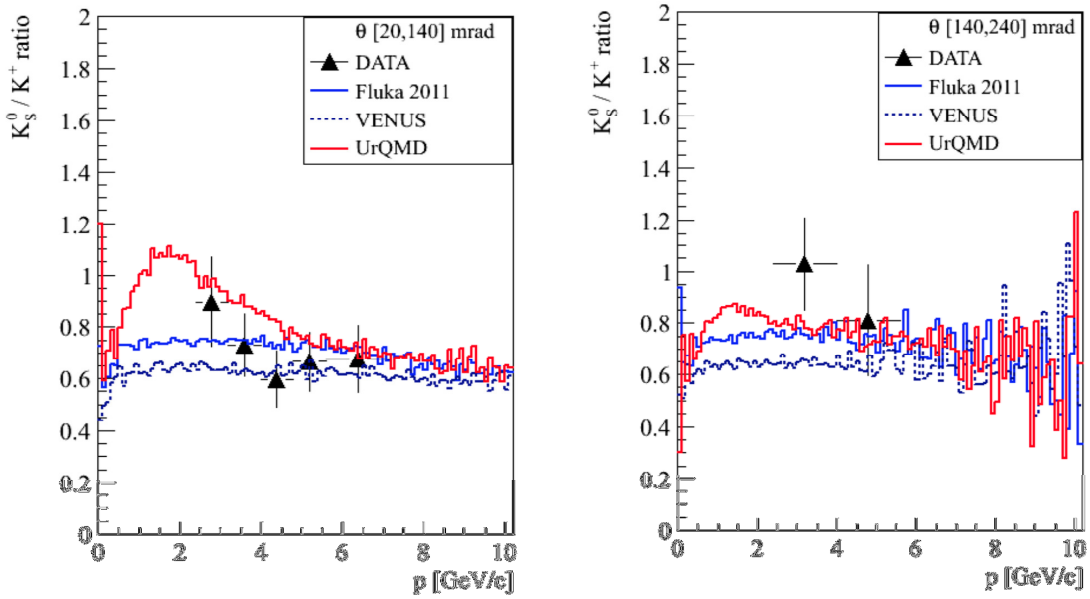

Figure 130. K^0_S / K^+ ratios in two polar angle intervals. Left [20, 140] mrad, right [140, 240] mrad. The vertical error bars on the data points show the total (stat. and syst.) uncertainty. Monte Carlo model predictions are superimposed.

The reasonable agreement between ratios and Monte Carlo predictions was observed. Lack of the dEd/dx+TOF data in the low momentum region unables to distinguish between UrQMD and other Models.

9.3.4 Λ results in momentum and polar angle variables

The Λ results in momentum and polar angle variables normalized to mean particle multiplicity in production processes are shown in Figure 131 with prediction from Monte Carlo models.

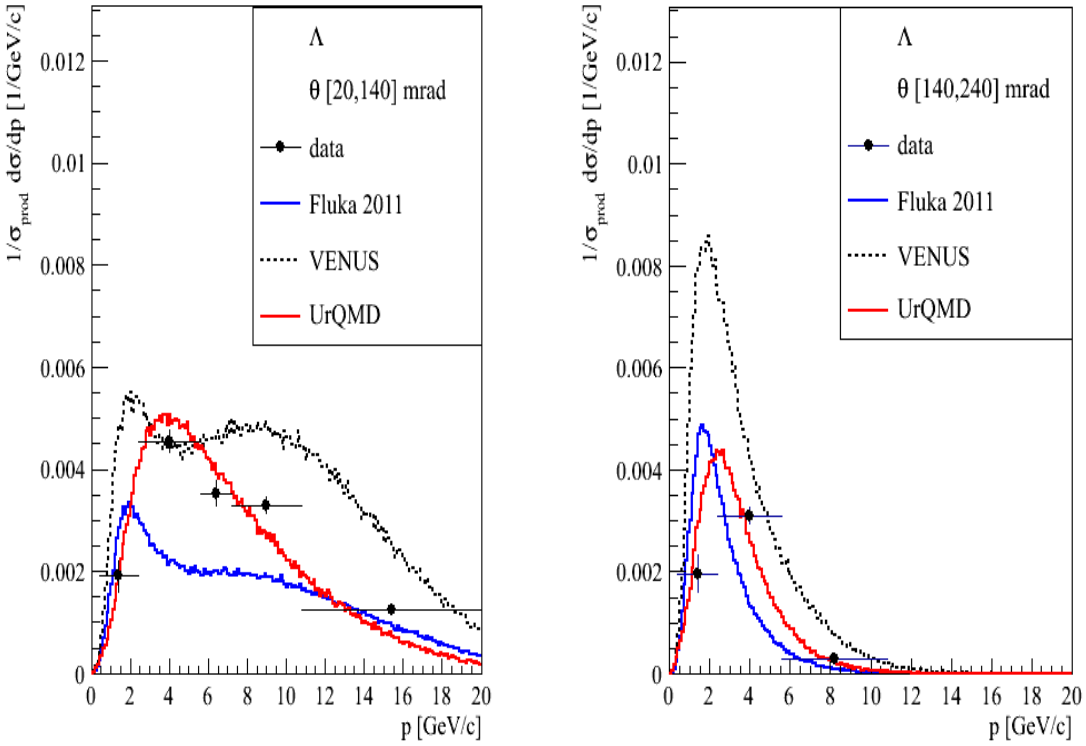

Figure 131. Λ mean particle multiplicity in production processes in polar angle intervals: [20, 140] mrad (left), [140, 240] mrad (right). Monte Carlo model predictions are superimposed. Only statistical errors are shown. Error connected with normalization (~3%) is not shown.

The Fluka and VENUS models do not reproduce our results. The reasonable agreement in case of UrQMD predictions was found.

Chapter 10 Summary and conclusions

The thesis presents differential cross sections important for the neutrino beam flux predictions in T2K experiment. Moreover, presented results are of high importance for the cosmic ray simulations and for hadronic interaction simulations. The developed methods are valid for ongoing and future hadron production experiments.

The main results are differential production cross sections and mean multiplicities in production processes for negatively charged pions, neutral Kaons, and Lambdas obtained in p+C interactions at 31 GeV/c measured within NA61/SHINE experiment. In addition, the inclusive cross section for Kaon production corrected to the whole phase space region was obtained.

The negatively charged pion analysis was based on the global correction method (h- method), which allows obtaining results in a wide phase space region. The final results were compared to dE/dx results at low momenta and dE/dx+TOF results in a wider range.

The K^0_S and Λ analyses were based on the invariant mass distribution studies.

The presented π- from (thin carbon target), K^0_S, and Λ results were fully corrected for the detector and other model dependent effects. The different sources of the systematic uncertainties were studied. The obtained K^0_S will allow minimizing one of the main systematic errors of the h- method – uncertainty connected with the neutral strange particle decays.

The negatively charged pion yields extraction method for the T2K replica target was developed and preliminary results were obtained, and presented at the closed SPCS meeting.

The presented results were used by T2K Collaboration to minimize systematic error connected with a poor knowledge of the neutrino beam. The UrQMD and Fluka authors also used these results to tune their models. The obtained K^0_S and π^- results give a hint about strangeness suppression factor (λ). The π^- results in Feynman x and rapidity variables are important for the future analyses of the onset of deconfinement and search for critical point of strongly interacting matter.

All developed computer codes were transferred to the NA61/SHINE Collaboration.

Bibliography

[1] J. N. Abdurashitov (et al.). Measurement of the solar neutrino capture rate with gallium metal. *Phys. Rev. C*, 60.055801, 1999.
[2] J. N. Abdurashitov (et al.). Measurement of the solar neutrino capture rate by the russian-american gallium solar neutrino experiment during one half of the 22-year cycle of solar activity. *J. Exp. Theor. Phys.*, 95:181–193, 2002.
[3] J. N. Abdurashitov (et al.). Measurement of the solar neutrino capture rate with gallium metal. iii: Results for the 2002–2007 data-taking period. *Phys. Rev. C*, 80, 2009.
[4] B. Levy J. M. Abgrall, N. Popov. Predictions of neutrino fluxes for t2k: Na61 analysis and data taking strategy. *NA61/T2K Internal note 2009-01 draft 2.1*, 2010.
[5] N. Abgrall (et al.). Further information requested in the proposal review process. *CERN-SPSC-2007-019*, 2007.
[6] N. Abgrall (et al.). Calibration and analysis of the 2007 data. *CERN-SPSC-2008-018*, 2008.
[7] N. Abgrall (et al.). Measurements of cross sections and charged pion spectra in proton-carbon interactions at 31 gev/c. *Phys. Rev. C (arXiv:1102.0983)*, 84, 2011.
[8] N. Abgrall (et al.). Neutrino flux predictions. *T2K-TN-038*, 2011.
[9] A. G. Abramov (et al.). Beam optics and target conceptual design for the numi project. *Nucl. Instr. Meth. A*, 485, 2002.
[10] K. Ackerstaff (et al.). A hadron–nucleus collision event generator for simulations at intermediate energies. *Nucl. Instr. and Meth. A*, 491:492–506, 2002.
[11] J. Adams (et al.). Experimental and theoretical challenges in the search for the quark gluon plasma: The star collaboration's critical assessment of the evidence from rhic collisions. *arXiv:nucl-ex/0501009v3*, 2005.
[12] P. Adamson (et al.). Measurement of neutrino oscillations with the minos detectors in the numi beam. *Phys. Rev. Lett.*, 101, 2008.
[13] K Adcox (et al.). Formation of dense partonic matter in relativistic nucleus-nucleus collisions at rhic: Experimental evaluation by the phenix collaboration. *arXiv:nucl-ex/0410003v3*, 2005.
[14] A. Aduszkiewicz. *Ph.D. Thesis in preparation*. PhD thesis, University of Warsaw.
[15] A. Aduszkiewicz. Na61/shine at the cern sps: plans, status and first results. *Acta Phys. Pol. B (APPB Proccedings Supplement)*, 2011.
[16] A. Aduszkiewicz. Normalisation using the fitted vertex z, April 2011.
[17] S. Afanasev (et al.). The na49 large acceptance hadron detector. *Nucl. Instrum. Meth. A*, 430:210, 1999.
[18] N. Agafonova (et al.). Observation of a first vt candidate in the opera experiment in the cngs beam. *Phys. Lett. B*, 691, 2010.
[19] M. Aglietta (et al.). Experimental study of atmospheric neutrino flux in the nusex experiment. *Europhys. Lett.*, 8:611, 1989.
[20] A. A. Aguilar-Arevalo (et al.). The miniboone detector. *Nucl. Instrum. Meth. A*, 599, 2009.
[21] B. Aharmim (et al.). Electron energy spectra, fluxes, and day-night asymmetries of 8b solar neutrinos from the 391-day salt phase sno data set. *Phys. Rev. C*, 72, 2005.
[22] B. Aharmim (et al.). Low-energy-threshold analysis of the phase i and phase ii data sets of the sudbury neutrino observatory. *Phys. Rev. C*, 81, 2010.
[23] B. Aharmim (et al.). Combined analysis of all three phases of solar neutrino data from the sudbury neutrino observatory. *arXiv:nucl-ex/1109.0763v1*, 2011.

[24] Q. R. Ahmad (et al.). Measurement of the rate of nue+d->p+p+e- interactions produced by 8b solar neutrinos at the sudbury neutrino observatory. *Phys. Rev. Lett.*, 87.71301, 2001.
[25] J. K. Ahn (et al.). Reno: An experiment for neutrino oscillation parameter theta13 using reactor neutrinos at yonggwang. *arXiv:hep-ex/1003.1391v1*, 2010.
[26] M. H. Ahn (et al.). Measurement of neutrino oscillation by the k2k experiment. *Phys. Rev. D*, 74, 2006.
[27] U. Akgun (et al.). Proposal to upgrade the mipp experiment. *arXiv:hep-ex/0609057v1*, 2006.
[28] M. Altmann (et al.). Gno solar neutrino observations: Results for gnoi. *Phys. Lett. B*, 490:16–26, 2000.
[29] M. Altmann (et al.). Complete results for five years of gno solar neutrino observations. *Phys. Lett. B*, 616:174, 2005.
[30] I. Ambats (et al). Nova proposal to build a 30-kiloton off-axis detector to study neutrino oscillations in the fermilab numi beamline. *arXiv:hep-ex/0503053*, 2005.
[31] G. Ambrosini (et al.). Measurement of charged particle production from 450 gev/c protons on beryllium. *Eur. Phys. J. C*, 10, 1999.
[32] M. Ambrosio (et al.). Matter effects in upward-going muons and sterile neutrino oscillations. *Phys. Lett. B*, 517:59–66, 2001.
[33] M. Ambrosio (et al.). Atmospheric neutrino oscillations from upward through going muon multiple scattering in macro. *Phys. Lett. B*, 566:35, 2003.
[34] L. A. Anchordoqui. Ultrahigh energy cosmic rays: Facts, myths, and legends. *arXiv:hep-ph/1104.0509v1*, 2011.
[35] G. Holgersson I. Mansson O. Andersson, B. Gustafson. A model for the reaction mechanism and the baryon fragmentation distributions in low p perpendicular hadronic interactions. *Nucl. Phys. B*, 178:242–262, 1981.
[36] G. Nilsson-Almqvist B. Andersson, B. Gustafson. A model for low-pt hadronic reactions with generalizations to hadron-nucleus and nucleus-nucleus collisions. *Nucl. Phys. B*, 281:289–309, 1987.
[37] R. E. Ansorge (et al.). Charged particle multiplicity distributions at 200-gev and 900-gev center-of-mass energy. *CERN-EP-88-172*, 1988.
[38] T. Anticic (et al.). Inclusive production of charged kaons in p+p collisions at 158 gev/c beam momentum and a new evaluation of the energy dependence of kaon production up to collider energies. *CERN-PH-EP/2009-029*, 2009.
[39] N. Antoniou (et al.). Study of hadron production in collisions of protons and nuclei at the cern sps. *CERN-SPSC-2006-034*, 2006.
[40] N. Antoniou (et al.). Additional information requested in the proposal review process. *CERN-SPSC-2007-004*, 2007.
[41] M. Apollonio (et al.). Limits on neutrino oscillations from the chooz experiment. *Phys. Lett. B*, 466:415–430, 1999.
[42] F. Ardellier (et al.). Double chooz: A search for the neutrino mixing angle theta13. *arXiv:hep-ex/0606025*, 2006.
[43] C. Arpesella (et al.). Direct measurements of the 7be solar neutrino flux with 192 days of borexino data. *Phys. Rev. Lett.*, 101, 2008.
[44] I. Arsene (et al.). Quark gluon plasma an color glass condensate at rhic? the perspective from the brahms experiment. *arXiv:nucl-ex/0410020v1*, 2004.
[45] D. Aschman (et al.). Production of pi0 pi0 and pi0 n in photon-photon-collisions. *Phys. Lett. B*, 107:310–327, 1981.
[46] Y. Ashie (et al.). Evidence for an oscillatory signature in atmospheric neutrino oscillation. *Phys. Rev. Lett.*, 93, 2004.
[47] Ch. Asner, A. Iselin. Layout of the new cern neutrino beam. *CERN-66-24*, 1966.

[48] Super Kamiokande Group at University of California.
http://www.ps.uci.edu/ tomba/sk/tscan/pictures.html.
[49] B. B. Back (et al.). The phobos perspective on discoveries at rhic. *arXiv:nucl-ex/0410022v2*, 2005.
[50] K. A. Baker, M. Ter-Martirosyan. Gribov's reggeon calculus: Its physical basis and implications. *Phys. Rep.*, 28:1–143, 1976.
[51] V. D. Barger (et al.). Neutrino decay and atmospheric neutrinos. *Phys. Lett.*, 82, 1999.
[52] B. C. Barish (et al.). Recent results on total neutrino and antineutrino cross sections by the cfrr collaboration. *Fermilab-81/80-EXP*, 1981.
[53] G. Barr (et al.). Charged pion production in p+c collisions at 158 gev/c beam momentum: Discussion. *Eur. Phys. J. C*, 49:919–945, 2007.
[54] D. S. Barton (et al.). Experimental study of the a dependence of inclusive hadron fragmentation. *Phys. Rev. D*, 27, 1983.
[55] S. A. Bass (et al.). Microscopic models for ultrarelativistic heavy ion collisions. *arXiv:nucl-th/9803035v2*, 1998.
[56] A. A. Batalov (et al.). A focusing device for neutrino sources at meson factories. *Nucl. Instr. Meth. A*, 251, 1986.
[57] B. F. Bayanov (et al.). Wide-angle optics with strong magnetic fields for efficient generation of secondary-particle beams. *Proc. 10th Int. Conf. High Energy Accel., Protvino*, 2:109–109, 1984.
[58] D. Beavis (et al.). P889: Long baseline neutrino oscillation experiment at the ags. *Report No. BNL-52459*, 1995.
[59] J. Gazdzicki M. Becattini, F. Manninen. Energy and system size dependence of chemical freeze-out in relativistic nuclear collisions. *Phys. Rev. C (arXiv:hep-ph/0511092v3)*, 73, 2006.
[60] L. Piccinini F. Polosa A. D. Riquer V. Becattini, F. Maiani. Correlating strangeness enhancement and j/psi suppression in heavy ion collisions at sqrt(s)_nn = 17.2 gev. *arXiv:hep-ph/0508188v2*, 2005.
[61] A. Bellerive. Review of solar neutrino experiments. *Int. J. Mod. Phys. A*, 19:1167–1179, 2004.
[62] J. Bernabeu (et al.). Euronu wp6 2009 yearly report: Update of the physics potential of nufact, superbeams and betabeams. *arXiv:hep-ph/1005.3146v1*, 2010.
[63] P. Bertini, H. W. Gurthri. Results from medium-energy intra-nuclear-cascade calculation. *Nucl. Phys. A*, 169, 1971.
[64] H. W. Bertini (et al.). Intra-nuclear-cascade calcula- tion of the secondary nucleon spectra from nucleon-nucleus interactions in the energy range 340 to 2900 mev and comparisons with experiment. *Phys. Rev.*, 188, 1969.
[65] A. Bialas. Particle production in hadron nucleus collisions at high-energies. *13th International Symposium on Multiparticle Dynamics - proceedings*, pages 328–358, 1982.
[66] B. Bilenky, S. M. Pontecorvo. The lepton-quark analogy and muonic charge. *Sov. J. Nucl. Phys.*, 24:316–319, 1976.
[67] A. Pietropaolo F. Tabarelli de Fatis T. Bonesini, M. Marchionni. On particle production for high energy neutrino beams. *Eur. Phys. J. C*, 20:13–27, 2001.
[68] F. Brun, R. Carminati. Geant detector description and simulation tool. *CERN Program Library Long Writeup W5013*, 1993.
[69] L. Bruno. The cngs target. *3rd International Workshop on Neutrino Beams and Instrumentation, CERN*, http://proj-cngs.web.cern.ch/proj-cngs/2002 workshop/announce 1.html, 2003.
[70] A. Capella. Hadronic interactions at low pt. *Acta Physica Polonica*, B14:359–373, 1983.
[71] A. Capella. Dual parton model. *Surveys in High Energy Physics*, 16:3–4, 2001.

[72] U. Tan C. I. Tran Thanh Van J. Capella, A. Sukhatme. Jets in small-pt hadronic collisions, universality of quark fragmentation, and rising rapidity plateaus. *Phys. Lett. B*, 81:68–74, 1979.
[73] E. L. Juchem S. Cassing, W. Bratkovskaya. Excitation functions of hadronic observables from sis to rhic energies. *arXiv:nucl-th/0001024v1*, 2000.
[74] M. G. Catanesi (et al.). Proposal to study hadron production for the neutrino factory and for the atmospheric neutrino flux. *CERN-SPSC-99-35, CERN-SPSC-P-315*, 1999.
[75] M. G. Catanesi (et al.). The harp detector at the cern ps. *Nucl. Instrum. Meth. Phys. Res.*, A 571:527–561, 2007.
[76] M. G. Catanesi (et al.). Measurement of the production cross-sections of pi± in p-c and pi±-c interactions at 12 gev/cmeasurement of the production cross-sections of pi± in p-c and pi±-c interactions at 12 gev/c. *Astro. Phys.*, 2008.
[77] M. G. Catanesi (et al.). Measurement of the production crosssections of pi± in p–c and pi±–c interactions at 12 gev/c. *Astropart. Phys.*, 29, 2008.
[78] I. Chemakin (et al.). Pion production by protons on a thin beryllium target at 6.4, 12.3, and 17.5 gev/c incident proton momenta. *Phys. Rev. C*, 77, 2008.
[79] B. T. Cleveland (et al.). Measurement of the solar electron neutrino flux with the homestake chlorine detector. *Ap. J.*, 496:505–526, 1998.
[80] K. Cleymans, J. Redlich. Chemical and thermal freeze-out parameters from 1 to 200 a.gev. *arXiv:nucl-th/9903063v2*, 1999.
[81] L. Perkins D. H. Cocconi, G. Koester. Lbl report no. ucrl 10022. 1961.
[82] B. A. Cole (et al.). Strangeness enhancement in p-a collisions: Consequences for the interpretation of strangeness production in a-a collisions. *Phys. Lett. B (arXiv:nucl-ex/0503009v1)*, 639:210–213, 2006.
[83] P. D. B. Collins. An introduction to regge theory & high energy physics. *Cambridge University Press*, 1977.
[84] D. A. Cottingham, W. Greenwood. An introduction to the standard model of particle physics. *Cambridge University Press*, ISBN 0-521-58832-4., 1998.
[85] T. Czopowicz. Study of k0s meson production in na61 experiment at the cern sps. Master's thesis, Warsaw University of Technology, 2010.
[86] G. Danby (et al.). Observation of high-energy neutrino reactions and the existence of two kinds of neutrinos. *Phys. Rev. Lett.*, 9, 1962.
[87] K. Daum (et al.). Determination of the atmospheric neutrino spectra with the frejus detector. *Z. Phys. C*, 1995:417, 66.
[88] Y. Declaise (et al.). Search for neutrino oscillations at 15, 40 and 95 meters from a nuclear power reactor at bugey. *Nucl. Phys. B*, 434:503–532, 1995.
[89] V. Dohm (et al.). Linear focusing of neutrino parents. *Nucl. Instr. Meth.*, 124, 1975.
[90] Z Friedlander G. Dostrovsk, I. Fraenkel. Monte carlo calculations of nuclear evaporation processes. iii. applications to low-energy reactions. *Phys. Rev.*, 116:683–702, 1959.
[91] Z Friedlander G. Dostrovsk, I. Fraenkel. Monte carlo calculations of nuclear evaporation processes. iv. spectra of neutrons and charged particles from nuclear reactions. *Phys. Rev.*, 118:781–791, 1960.
[92] K. Eguchi (et al.). First results from kamland: Evidence for reactor anti-neutrino disappearance. *Phys. Rev. Lett.*, 90, 2003.
[93] K. Eguchi (et al.). Precision measurement of neutrino oscillation parameters with kamland. *Phys. Rev. Lett.*, 100, 2008.
[94] T. Eichten (et al.). Particle production in proton interactions in nuclei at 24 gev/c. *Nucl. Phys. B*, pages 33–343, 1972.
[95] O. Elgaroy (et al.). A new limit on the total neutrino mass from the 2df galaxy redshift survey. *Phys. Rev. Lett.*, 89.061301, 2002.

[96] E. Fermi. Versuch einer theorie der beta-strahlen. *Zeitschrift für Physik*, 88 (3-4):161–177, 1934.
[97] H. Fesefeldt. The simulation of hadronic showers: Physics and applications. *PITHA-85-02*, 1985.
[98] V. N. Wellisch J. P. Folger, G. Ivanchenko. The binary cascade nucleon nuclear reactions. *The Europ. Phys. Jour. A*, 21:407–417, 2003.
[99] S. Fukuda (et al.). Tau neutrinos favored over sterile neutrinos in atmospheric muon-neutrino oscillations. *Phys. Rev. Lett.*, 85:3999–4003, 2000.
[100] S. Fukuda (et al.). Determination of solar neutrino oscillation parameters using 1496 days of super-kamiokande i data. *Phys. Lett. B*, 539, 2002.
[101] Y. Fukuda (et al.). Solar neutrino data covering solar cycle 22. *Phys.Rev.Lett. 77*, 77:1683–1686, 1996.
[102] Y. Fukuda (et al.). Evidence for oscillation of atmospheric neutrinos. *Phys. Rev. Lett.*, 81, 1998.
[103] T. K. Gaisser. Atmospheric neutrinos. *AIP Conf. Proc.*, 944:140–142, 2007.
[104] W. Gajewski (et al.). A search for oscillation of atmospheric neutrinos with the imb detector. *Nucl. Phys. Proc. Suppl.*, 28A:161, 1992.
[105] H. Gallagher (et al.). New results from the minos experiment. *Nucl. Phys. B*, 434:503–532, 1995.
[106] M. I. Gazdzicki, M. Gorenstein. On the early stage of nucleus–nucleus collisions. *Acta Phys.Polon. B (arXiv:hep-ph/9803462v3)*, 30, 1999.
[107] M. I. Grassi F. Hama Y. Socolowski O. Gazdzicki, M. Gorenstein. Incident-energy dependence of the effective temperature in heavy-ion collisions. *Braz. J. Phys. (arXiv:hep-ph/0309192v1)*, 34:322–325, 2004.
[108] C. W. Giunti, G. Kim. *Fundamentals of Neutrino Physics and Astrophysics*. Oxford University Press, 2007.
[109] M. Bugaev K. Gorenstein, M. I. Gazdzicki. Transverse activity of kaons and the deconfinement phase transition in nucleus–nucleus collisions. *Phys.Lett. B (arXiv:hep-ph/0303041v1)*, 567:175–178, 2003.
[110] Particle Data Group. http://pdg.lbl.gov/.
[111] B. Grupen, C. Schwartz. *Particle Detectors*. Cambridge University Press, 2008.
[112] Yusuf Oguzhan Gunaydin. *Cross section measurements in the Main Injector Particle Production (FNAL-E907) experiment at 58 GeV Energy*. PhD thesis, University of Iowa, 2009.
[113] J. F. Gunion. Quarks and gluons in low pt physics. *SLAC-PUB-2607*, 1980.
[114] X. Guo (et al.). A precision measurement of the neutrino mixing angle theta13 using reactor antineutrinos at daya bay. *arXiv:hep-ex/0701029*, 2007.
[115] W. Hampel (et al.). Gallex solar neutrino observations: results for gallex iv. *Phys. Lett. B*, 447:127–133, 1999.
[116] J. Hanssgen, K. Ranft. The monte carlo code nucrin to simulate inelastic hadron-nucleus interactions at laboratory energies below 5 gev. *Comp. Phys. Commun.*, 39, 1986.
[117] M. Heinz, U. W. Jacob. Evidence for a new state of matter: An assessment of the results from the cern lead beam programme. *arXiv:nucl-th/0002042*, 2000.
[118] K. S. Hirata (et al.). Experimental study of the atmospheric neutrino flux. *Phys. Lett. B*, 205:416, 1988.
[119] Y. Okamura N. Takeuchi T. Honda, M. Kao. A simple parameterization of matter effects on neutrino oscillations. *arXiv:hep-ph/0602115*, 2006.
[120] J. Hosaka (et al.). Solar neutrino measurements in super-kamiokande-i. *Phys. Rev. D*, 73, 2006.
[121] R. C. Hwa. Recent developments in the valon model. *13th International Symposium on Multiparticle Dynamics - proceedings*, pages 779–798, 1982.

[122] Y. Itow (et al.). The jhf-kamioka neutrino project. *Nucl. Phys. Proc. Suppl.*, 111:146, 2001.
[123] K. A. Kaidalov, A. B. Ter-Martirosyan. Pomeron as quark-gluon strings and multiple hadron production at sps-collider energies. *Phys. L*, 117:247–251, 1982.
[124] F. Karsch. Thermodynamic properties of strongly interacting matter at non-zero baryon number density. *J. Phys. G (arXiv:hep-lat/0412038v1)*, 31, 2005.
[125] S. D. Katz. Equation of state from lattice qcd. *Nucl. Phys. A (arXiv:hep-ph/0511166v1)*, 774:159–168, 2006.
[126] J. Shabelski Yu. M. Kobrinsky, M. N Nyiri. *Quark Model and High Energy Collisions*. World Scientific, 2004.
[127] D. D. Koetke (et al.). A direct-current pion focusing magnet for low-energy in-flight muon neutrino beams. *Nucl. Instr. Meth. A*, 378, 1996.
[128] S. Kopp. Accelerator neutrino beams. *Phys. Rept.*, 439:101, 2007.
[129] W. R. Leo. *Techniques for Nuclear and Particle Physics Experiments*. Springer, 2008.
[130] P. Limon (et al.). A sign-selected di-chromatic neutrino beam. *Nucl. Instr. Meth.*, 116, 1974.
[131] A. Montanino D. Lisi, E. Marrone. Probing possible decoherence effects in atmospheric neutrino oscillations. *Phys. Rev. Lett.*, 85, 2000.
[132] F. E. Low. Model of the bare pomeron. *Phys. Rev. D*, 12:163–173, 1975.
[133] A. J. Malensek. Empirical formula for thick target particle production. *Fermilab-FN-341*, 1981.
[134] H. Matsui, T. Satz. J/psi suppression by quark-gluon plasma formation. *Phys.Lett. B*, 178:416, 1986.
[135] K. McDonald. An off-axis neutrino beam. *arXiv:hep-ex/0111033v1*, 2001.
[136] J. Engel R. Haungs A. Roth M. Meurer, C. Blumer. Muon production in extensive air showers and its relation to hadronic interactions. *Czech. J. Phys.*, 56, 2006.
[137] J. Engel R. Haungs A. Roth M. Meurer, C. Blumer. New p+c data in fixed target experiments and the muon component in extensive air showers. *Nucl. Phys. B. Proc. of ISVHECRI2006*, 2006.
[138] D. G. Michael (et al.). Observation of muon neutrino disappearance with the minos detectors and the numi neutrino beam. *Phys. Rev. Lett.*, 97, 2006.
[139] A. Y. Mikheev, S. P. Smirnov. Resonance enhancement of oscillations in matter and solar neutrino spectroscopy. *Sov. J. Nucl. Phys.*, 42, 1985.
[140] N. Moggi. *Soft Multiparticle Production in p antip Interactions at 1800 and 630 GeV*. PhD thesis, Universita degli studia di pavia, 1999.
[141] S. Murphy. *Measurement of charged Pion and Kaon production cross sections with NA61/SHINE for T2K*. PhD thesis, University of Geneva, 2012.
[142] E. Nilsson-Almqvist, B. Stenlund. Interactions between hadrons and nuclei: The lund monte carlo - fritiof version 1.6. *Comp. Phys. Commun.*, 43:387–397, 1987.
[143] S. Nussinov. Colored-quark version of some hadronic puzzles. *Phys. Rev. Lett.*, 34:1286–1289, 1975.
[144] Super Kamiokande official web page. http://www-sk.icrr.u-tokyo.ac.jp/sk/index-e.html.
[145] J. Paley (et al.). First results from mipp. *AIP Conf. Proc.*, 981:154–156, 2008.
[146] R. B. Palmer. Magnetic fingers. *CERN Informal Workshop on Neutrino Physics, CERN-65-32*, pages 141–146, 1965.
[147] J. M. Pattison. The cern neutrino beam. *CERN Informal Workshop on Neutrino Physics, CERN-69-28*, pages 13–32, 1969.
[148] W. Pauli. Letter to the attendees of a physics conference in tübingen.
[149] Z. Pavlovic. *Studies of the Neutrino Flux for the NuMI Beam at FNAL*. PhD thesis, University of Texas at Austin, 2008.

[150] D. H. Perkins. *High Energy Physics*. Cambridge University Press, 2003.
[151] R. Podolanski, J. Armenteros. Analysis of v-events. *Phil. Mag.*, 45, 1954.
[152] B. Pontecorvo. Mesonium and anti-mesonium. *Zh. Eksp. Teor. Fiz*, 33:549–551, 1957. reproduced and translated in Sov. Phys. JETP 6: 429. 1957.
[153] B. Pontecorvo. Electron and muon neutrinos. *J. Exp. Theor. Phys.*, 37, 1959.
[154] M. Z. Posiadala. *Measurements of Hadronic Cross Section for Precise Determination of Neutrino Beam Properties in T2K Oscillation Experiment*. PhD thesis, University of Warsaw, 2012.
[155] B. Rafelski, J. Muller. Strangeness production in the quark-gluon plasma. *Phys. Rev. Lett.*, 48:1066–1069, 1982.
[156] C. Rubbia. The liquid-argon time projection chamber:a new concept for neutrino detector. *CERN-EP/77-08*, 1977.
[157] C. Rubbia (et al.). Energy reconstruction of electromagnetic showers from pi0 decays with the icarus t600 liquid argon tpc. *Acta Phys. Polon. B*, 41:103–125, 2010.
[158] C. Rubbia (et al.). Underground operation of the icarus t600 lar-tpc: first results. *JINST*, 6, 2011.
[159] A. Sadovsky. Physics motivation and development of the projectile spectator detector (psd) for the cpod program of na61/shine experiment at the cern sps. *CPOD 2010, JINR Dubna*, 2010.
[160] M. C. Sanchez (et al.). Measurement of the l/e distributions of atmospheric neutrinos in soudan 2 and their interpretation as neutrino oscillations. *Phys. Rev. D.*, 68, 2003.
[161] F. Sauli. Principles of operation of multiwire proportional and drift chambers. *CERN report 77-09*, 1977.
[162] M. Schwartz. Feasibility of using high-energy neutrinos to study the weak interactions. *Phys. Rev. Lett.*, 4:306–307, 1960.
[163] R. Serber. Nuclear reactions at high energies. *Phys. Rev.*, 72, 1948.
[164] H. Greiner W. Sorge, H. Stocker. Poincare invariant hamiltonian dynamics: Modelling multi-hadronic interactions in a phase space approach. *Annals of Physics*, 192:266–306, 1989.
[165] T. Stefan, D. Wachala. Application of neural networks to simulated data for liquid argon tpc's. *Acta Phys.Polon. B37 (2006) 2187-2195*, 37:2187–2195, 2006.
[166] C. Strabel. *Evaluation of Particle Yields in 30 GeV Proton–Carbon Inelastic Interactions for Estimating the T2K Neutrino Flux*. PhD thesis, ETH Zurich, 2011.
[167] V. Uzhinsky. Tuning of the geant4 fritiof (ftf) model using na61/shine experimental data. *arXiv:hep-ph/1109.6768v1*, 2011.
[168] S. van der Meer. A directive device for charged particles and its use in an enhanced neutrino beam. *CERN-61-07*, 1961.
[169] S. van der Meer. Neutrino flux calculations. *CERN Informal Workshop on Neutrino Physics CERN-63-37*, 1963.
[170] G. Veneziano. Regge intercepts and unitarity in planar dual models. *Nucl. Phys. B*, 74:365–377, 1974.
[171] G. I. Veres. *Baryon Momentum Transfer in Hadronic and Nuclear Colisions at the CERN NA49 Experiment*. PhD thesis, Eotvos Lorand University, 2001.
[172] C. Volpe. Topical review on beta-beams. *J. Phys. G*, 34, 2007.
[173] C. L. Wang. Pion, kaon, and antiproton production between 10 and 70 bev. *Phys. Rev. Lett.*, 25:1068, 1970.
[174] C. L. Wang. Pion production in high-energy collisions. *Phys. Rev. D*, 10, 1974.
[175] Fluka web page. http://www.fluka.org.
[176] Geant3 web page. http://wwwasd.web.cern.ch/wwwasd/geant/.
[177] Geant4 web page.
http://geant4.cern.ch/g4usersdocuments/usersguides/physicsreferencemanual/html/node131.html.

[178] Geant4 web page.
http://geant4.cern.ch/support/proc_mod_catalog/models/hadronic/bertinicascade.html.
[179] Geant4 web page. http://geant4.web.cern.ch/geant4/.
[180] MARS web page. http://www-ap.fnal.gov/mars/.
[181] Official CERN's web page. http://public.web.cern.ch/public/.
[182] V. Weisskopf. Statistics and nuclear reactions. *Phys. Rev.*, 52:295–303, 1937.
[183] H. Yukawa. On the interaction of elementary particles. *Proc. Phys. Math. Soc. Jap*, 17:48, 1935.
[184] T. A. Zeitnitz, C. Gabriel. The geant-calor interface and benchmark calculations of zeus test calorimeters. *Nucl. Instr. Meth. A*, 349, 1994.

Appendix

Appendix I

The physics cards used in geometrical acceptance studies were as follows (in brackets additional information about cards is added):

`DCAY 0` (Decay in flight, 0 – off, 1- on with generation of secondaries, 2 – on without generation of secondaries)

`ANNI 0` (Positron annihilation, 0 – off, 1 – on with generation of photons, 2 – on without generation of photons)

`BREM 0` (Bremsstrahlung, 0 – off, 1 – on with generation of photon, 2 – on without generation of photon)

`COMP 0` (Compton scattering, 0 – off, 1- on with generation of e-, 2 – on without generation of e-)

`HADR 0` (Hadronic interactions, 0 – off, 1 – on with generation of secondaries, 2 – on without generation of secondaries)

`MUNU 0` (Muon-nucleus interactions, 0 – off, 1- on with generation of secondaries, 2 – on without generation of secondaries)

`PAIR 0` (Pair production, 0 – off, 1 – on with generation of e+/e-, 2 – on without generation of e+/e-)

`PFIS 0` (Nuclear fission induced by a photon, 0 – off, 1 – on with generation of secondaries, 2 – on without generation of secondaries)

`PHOT 0` (Photoelectric effect, 0 – off, 1 – on with generation of the electron, 2 – on without generation of the electron)

`RAYL 0` (Rayleigh effect, 0 – off, 1 – on)

`LOSS 1` (Continuous energy loss, 0 – off, 1 – on with generation of δ-rays above cut and restricted Landau fluctuations below cut, 2 – on without generation of δ-rays and with full Landau fluctuations, 3 – same as 1, 4 – on without fluctuations, values from the table are used)

`DRAY 0` (δ-ray production, 0 – off, 1 – on with generation of e-, 2 – on without generation of e-)

`MULS 0` (Multiple scattering, 0 – off, 1 – on based on the Moliere theory, 2 – same as 1, 3 – on based on the Rossi formula)

`CUTE -1. -1. -1.` (sets standard values for the cuts)

Appendix II

The final π- and π+ differential cross sections in polar angle intervals with systematic errors. The presented results were obtained by combining results from all three methods (h-, dE/dx, and dE/dx+TOF).

Table I: The NA61/SHINE results for the differential π^+ and π^- production cross section in the laboratory system, $d\sigma^{\pi}/dp$, for p+C interactions at 31 GeV/c. Each row refers to a different ($p_{low} \leq p < p_{up}$, $\theta_{low} \leq \theta < \theta_{up}$) bin, where p and θ are the pion momentum and polar angle in the laboratory frame, respectively. The central value as well as the statistical (Δ_{stat}) and systematic (Δ_{stat}) errors are given. The overall uncertainty (2.5%) due to the normalization procedure is not included.

θ_{low}	θ_{up}	p_{low}	p_{up}	$\frac{d\sigma^{\pi^+}}{dp}$	Δ_{stat}	Δ_{sys}	p_{low}	p_{up}	$\frac{d\sigma^{\pi^-}}{dp}$	Δ_{stat}	Δ_{sys}
(mrad)		(GeV/c)		(mb/(GeV/c))			(GeV/c)		(mb/(GeV/c))		
0	20	0.2	0.3	0.067	0.025	0.012	0.2	0.3	0.081	0.023	0.017
		0.3	0.4	0.151	0.037	0.020	0.3	0.4	0.133	0.033	0.023
		0.4	0.5	0.179	0.044	0.021	0.4	0.5	0.207	0.042	0.028
		0.5	0.6	0.228	0.057	0.025	0.5	0.6	0.282	0.050	0.034
		0.6	0.7	0.419	0.066	0.044	0.6	0.7	0.309	0.062	0.036
		0.7	0.8	0.454	0.069	0.046	0.7	0.8	0.324	0.058	0.036
		0.8	0.9	0.456	0.079	0.046	0.8	0.9	0.220	0.054	0.024
		0.9	1.0	0.537	0.088	0.058	0.9	1.0	0.338	0.054	0.039
							1.0	1.2	0.399	0.045	0.047
		1.2	1.6	0.636	0.057	0.045	1.2	1.4	0.512	0.049	0.053
		1.6	2.0	0.816	0.069	0.053	1.4	1.6	0.516	0.048	0.054
		2.0	2.4	0.752	0.060	0.049	1.6	1.8	0.495	0.047	0.049
		2.4	2.8	0.826	0.070	0.052	1.8	2.0	0.655	0.048	0.061
		2.8	3.2	0.825	0.069	0.050	2.0	2.2	0.519	0.049	0.049
		3.2	3.6	0.900	0.073	0.056	2.2	2.4	0.581	0.048	0.052
		3.6	4.0	0.715	0.085	0.048	2.4	2.6	0.639	0.053	0.055
		4.0	4.4	0.80	0.10	0.05	2.6	2.8	0.543	0.051	0.047
		4.4	4.8	0.763	0.079	0.045	2.8	3.2	0.584	0.032	0.052
		4.8	5.2	0.975	0.093	0.057	3.2	3.6	0.593	0.034	0.047
		5.2	5.6	1.16	0.10	0.07	3.6	4.0	0.662	0.038	0.047
		5.6	6.0	0.862	0.091	0.049	4.0	4.4	0.655	0.038	0.041
		6.0	6.4	1.05	0.10	0.06	4.4	4.8	0.604	0.039	0.036
		6.4	6.8	0.817	0.096	0.047	4.8	5.2	0.604	0.040	0.033
		6.8	7.2	1.159	0.099	0.065	5.2	5.6	0.577	0.042	0.029
		7.2	7.6	1.08	0.15	0.06	5.6	6.0	0.558	0.044	0.027
							6.0	6.4	0.498	0.047	0.022
							6.4	6.8	0.477	0.040	0.021
							6.8	7.2	0.541	0.051	0.024
							7.2	7.6	0.492	0.046	0.021
20	40	0.2	0.3	0.210	0.041	0.027	0.2	0.3	0.183	0.034	0.036
		0.3	0.4	0.427	0.059	0.041	0.3	0.4	0.337	0.051	0.051
		0.4	0.5	0.674	0.082	0.054	0.4	0.5	0.621	0.072	0.080
		0.5	0.6	0.967	0.096	0.069	0.5	0.6	0.901	0.089	0.098
		0.6	0.7	1.12	0.11	0.08	0.6	0.7	0.761	0.085	0.080
		0.7	0.8	1.14	0.11	0.07	0.7	0.8	1.02	0.09	0.10
		0.8	0.9	1.32	0.12	0.08	0.8	0.9	1.07	0.09	0.10
		0.9	1.0	1.34	0.13	0.08	0.9	1.0	0.936	0.092	0.089
							1.0	1.2	1.35	0.07	0.13
		1.2	1.6	1.97	0.09	0.15	1.2	1.4	1.45	0.08	0.14
		1.6	2.0	2.10	0.10	0.14	1.4	1.6	1.45	0.08	0.14
		2.0	2.4	2.19	0.11	0.14	1.6	1.8	1.67	0.08	0.15
		2.4	2.8	2.22	0.15	0.14	1.8	2.0	1.53	0.08	0.13
		2.8	3.2	2.52	0.15	0.16	2.0	2.2	1.48	0.08	0.13
		3.2	3.6	2.60	0.15	0.16	2.2	2.4	1.55	0.08	0.13
		3.6	4.0	2.81	0.15	0.17	2.4	2.6	1.72	0.08	0.14
		4.0	4.4	2.66	0.15	0.16	2.6	2.8	1.69	0.08	0.13
		4.4	4.8	2.86	0.16	0.17	2.8	3.2	1.80	0.06	0.16
		4.8	5.2	2.77	0.16	0.16	3.2	3.6	1.78	0.06	0.14

Continued on next page

θ_{low}	θ_{up}	p_{low}	p_{up}	$\frac{d\sigma}{dp}^{\pi^+}$	Δ_{stat}	Δ_{sys}	p_{low}	p_{up}	$\frac{d\sigma}{dp}^{\pi^-}$	Δ_{stat}	Δ_{sys}
(mrad)		(GeV/c)		(mb/(GeV/c))			(GeV/c)		(mb/(GeV/c))		
		5.2	5.6	2.94	0.15	0.18	3.6	4.0	1.65	0.06	0.12
		5.6	6.0	2.45	0.14	0.12	4.0	4.4	1.68	0.07	0.11
		6.0	6.4	2.70	0.15	0.13	4.4	4.8	1.683	0.071	0.099
		6.4	6.8	2.27	0.14	0.11	4.8	5.2	1.667	0.068	0.086
		6.8	7.2	2.48	0.15	0.12	5.2	5.6	1.463	0.067	0.076
		7.2	7.6	2.06	0.13	0.10	5.6	6.0	1.587	0.070	0.081
		7.6	8.0	1.90	0.13	0.09	6.0	6.4	1.284	0.067	0.059
		8.0	8.4	1.70	0.12	0.08	6.4	6.8	1.423	0.068	0.063
		8.4	8.8	1.56	0.11	0.07	6.8	7.2	1.209	0.063	0.050
		8.8	9.2	1.51	0.11	0.07	7.2	7.6	1.132	0.064	0.048
		9.2	9.6	1.34	0.11	0.07	7.6	8.0	1.027	0.060	0.042
		9.6	10.0	1.04	0.12	0.05	8.0	8.4	0.967	0.059	0.040
		10.0	10.8	1.055	0.072	0.051	8.4	8.8	0.872	0.056	0.035
		10.8	11.6	0.959	0.063	0.047	8.8	9.2	0.749	0.052	0.030
		11.6	12.4	0.756	0.055	0.037	9.2	9.6	0.688	0.050	0.028
		12.4	13.2	0.632	0.053	0.031	9.6	10.0	0.667	0.049	0.027
		13.2	14.0	0.588	0.050	0.030	10.0	10.8	0.586	0.032	0.023
		14.0	14.8	0.384	0.043	0.019	10.8	11.6	0.427	0.029	0.017
		14.8	15.6	0.295	0.036	0.015	11.6	12.4	0.380	0.027	0.015
		15.6	16.4	0.275	0.035	0.014	12.4	13.2	0.301	0.025	0.011
		16.4	17.2	0.217	0.032	0.011	13.2	14.0	0.248	0.023	0.009
		17.2	18.0	0.159	0.028	0.008	14.0	14.8	0.164	0.019	0.006
		18.0	18.8	0.191	0.036	0.010	14.8	15.6	0.140	0.018	0.005
		18.8	19.6	0.168	0.034	0.009	15.6	16.4	0.109	0.016	0.004
							16.4	17.2	0.083	0.015	0.003
							17.2	18.0	0.088	0.023	0.005
							18.0	18.8	0.060	0.018	0.003
40	60	0.2	0.3	0.344	0.056	0.040	0.2	0.3	0.391	0.051	0.074
		0.3	0.4	0.763	0.087	0.062	0.3	0.4	0.616	0.073	0.091
		0.4	0.5	1.22	0.13	0.08	0.4	0.5	1.12	0.11	0.14
		0.5	0.6	1.58	0.13	0.08	0.5	0.6	1.28	0.10	0.14
		0.6	0.7	1.85	0.13	0.09	0.6	0.7	1.47	0.11	0.16
		0.7	0.8	2.22	0.16	0.11	0.7	0.8	1.69	0.12	0.17
		0.8	0.9	2.22	0.15	0.10	0.8	0.9	1.83	0.12	0.18
		0.9	1.0	2.60	0.18	0.12	0.9	1.0	2.07	0.13	0.21
							1.0	1.2	2.24	0.09	0.24
		1.2	1.4	2.98	0.33	0.24	1.2	1.4	2.37	0.10	0.24
		1.4	1.6	3.18	0.23	0.23	1.4	1.6	2.43	0.10	0.24
		1.6	1.8	3.94	0.26	0.30	1.6	1.8	2.59	0.11	0.25
		1.8	2.0	3.97	0.34	0.28	1.8	2.0	2.79	0.11	0.26
		2.0	2.2	3.85	0.34	0.25	2.0	2.2	2.98	0.13	0.27
		2.2	2.4	3.84	0.34	0.25	2.2	2.4	2.75	0.12	0.23
		2.4	2.6	3.69	0.34	0.24	2.4	2.6	2.86	0.13	0.24
		2.6	2.8	3.78	0.34	0.24	2.6	2.8	3.06	0.14	0.24
		2.8	3.0	4.18	0.35	0.27	2.8	3.0	2.88	0.13	0.21
		3.0	3.2	4.91	0.37	0.31	3.0	3.2	2.83	0.13	0.24
		3.2	3.4	4.28	0.35	0.27	3.2	3.4	2.99	0.13	0.22
		3.4	3.6	4.09	0.34	0.26	3.4	3.6	2.87	0.13	0.21
		3.6	3.8	4.65	0.36	0.29	3.6	3.8	2.73	0.13	0.19
		3.8	4.0	3.95	0.33	0.25	3.8	4.0	2.64	0.13	0.18
		4.0	4.2	3.92	0.34	0.25	4.0	4.2	2.84	0.13	0.18
		4.2	4.4	3.96	0.34	0.21	4.2	4.4	2.39	0.12	0.15
		4.4	4.6	4.16	0.35	0.22	4.4	4.6	2.36	0.12	0.14
		4.6	4.8	3.35	0.31	0.17	4.6	4.8	2.43	0.12	0.14
		4.8	5.0	3.84	0.33	0.20	4.8	5.0	1.91	0.10	0.11
		5.0	5.2	3.83	0.33	0.20	5.0	5.2	2.20	0.11	0.13
		5.2	5.6	3.63	0.22	0.19	5.2	5.6	2.08	0.08	0.12
		5.6	6.0	2.64	0.21	0.14	5.6	6.0	1.80	0.07	0.10
		6.0	6.4	3.04	0.21	0.16	6.0	6.4	1.568	0.066	0.087
		6.4	6.8	2.36	0.20	0.13	6.4	6.8	1.576	0.064	0.087

Continued on next page

θ_{low}	θ_{up}	p_{low}	p_{up}	$\frac{d\sigma}{dp}^{\pi^+}$	Δ_{stat}	Δ_{sys}	p_{low}	p_{up}	$\frac{d\sigma}{dp}^{\pi^-}$	Δ_{stat}	Δ_{sys}
(mrad)		(GeV/c)		(mb/(GeV/c))			(GeV/c)		(mb/(GeV/c))		
		6.8	7.2	2.27	0.13	0.12	6.8	7.2	1.264	0.058	0.069
		7.2	7.6	2.18	0.13	0.12	7.2	7.6	1.180	0.055	0.064
		7.6	8.0	1.74	0.11	0.09	7.6	8.0	1.038	0.053	0.056
		8.0	8.4	1.54	0.11	0.08	8.0	8.4	0.928	0.049	0.050
		8.4	8.8	1.48	0.11	0.08	8.4	8.8	0.894	0.048	0.047
		8.8	9.2	1.34	0.10	0.07	8.8	9.2	0.681	0.042	0.036
		9.2	9.6	1.189	0.097	0.065	9.2	9.6	0.654	0.041	0.035
		9.6	10.0	0.995	0.090	0.055	9.6	10.0	0.579	0.038	0.031
		10.0	10.8	0.870	0.057	0.048	10.0	10.8	0.481	0.024	0.025
		10.8	11.6	0.657	0.052	0.036	10.8	11.6	0.368	0.022	0.019
		11.6	12.4	0.562	0.046	0.031	11.6	12.4	0.253	0.019	0.013
		12.4	13.2	0.414	0.038	0.023	12.4	13.2	0.248	0.018	0.013
		13.2	14.0	0.260	0.032	0.015	13.2	14.0	0.147	0.014	0.008
		14.0	14.8	0.230	0.031	0.013	14.0	14.8	0.120	0.013	0.006
		14.8	15.6	0.168	0.027	0.009	14.8	15.6	0.079	0.011	0.004
		15.6	16.4	0.123	0.024	0.007	15.6	16.4	0.0598	0.0093	0.0032
		16.4	17.2	0.090	0.039	0.005					
60	100	0.2	0.3	1.25	0.11	0.13	0.2	0.3	1.28	0.10	0.22
		0.3	0.4	2.58	0.18	0.20	0.3	0.4	2.23	0.15	0.31
		0.4	0.5	3.98	0.23	0.26	0.4	0.5	3.23	0.20	0.38
		0.5	0.6	4.48	0.23	0.27	0.5	0.6	3.99	0.20	0.43
		0.6	0.7	5.86	0.26	0.34	0.6	0.7	5.02	0.23	0.50
		0.7	0.8	6.29	0.28	0.36	0.7	0.8	5.45	0.23	0.52
		0.8	0.9	7.81	0.32	0.47	0.8	0.9	5.74	0.24	0.52
		0.9	1.0	8.68	0.34	0.52	0.9	1.0	6.49	0.29	0.59
							1.0	1.2	6.90	0.21	0.58
		1.2	1.4	9.42	0.91	0.91	1.2	1.4	7.50	0.22	0.62
		1.4	1.6	11.6	1.1	1.5	1.4	1.6	8.09	0.25	0.63
		1.6	1.8	12.6	1.1	1.8	1.6	1.8	8.40	0.26	0.61
		1.8	2.0	12.41	0.79	0.85	1.8	2.0	8.78	0.26	0.61
		2.0	2.2	10.68	0.75	0.73	2.0	2.2	8.40	0.24	0.55
		2.2	2.4	12.96	0.81	0.96	2.2	2.4	9.24	0.25	0.58
		2.4	2.6	11.76	0.58	0.85	2.4	2.6	8.41	0.24	0.51
		2.6	2.8	10.25	0.73	0.62	2.6	2.8	8.24	0.24	0.49
		2.8	3.0	10.43	0.57	0.61	2.8	3.0	8.05	0.23	0.47
		3.0	3.2	10.88	0.56	0.61	3.0	3.2	7.21	0.23	0.47
		3.2	3.4	10.51	0.55	0.59	3.2	3.4	7.12	0.23	0.45
		3.4	3.6	9.34	0.48	0.51	3.4	3.6	7.03	0.23	0.44
		3.6	3.8	9.82	0.52	0.54	3.6	3.8	6.23	0.21	0.38
		3.8	4.0	8.66	0.48	0.47	3.8	4.0	6.11	0.21	0.37
		4.0	4.2	8.01	0.45	0.44	4.0	4.2	5.80	0.20	0.35
		4.2	4.4	7.90	0.46	0.43	4.2	4.4	5.32	0.20	0.32
		4.4	4.6	8.52	0.48	0.47	4.4	4.6	5.06	0.19	0.30
		4.6	4.8	6.37	0.42	0.35	4.6	4.8	4.68	0.18	0.27
		4.8	5.0	6.64	0.43	0.37	4.8	5.0	4.35	0.18	0.26
		5.0	5.2	5.60	0.39	0.31	5.0	5.2	3.92	0.17	0.23
		5.2	5.6	5.53	0.29	0.31	5.2	5.6	3.67	0.11	0.21
		5.6	6.0	5.14	0.27	0.29	5.6	6.0	3.24	0.11	0.19
		6.0	6.4	4.17	0.24	0.23	6.0	6.4	2.61	0.10	0.15
		6.4	6.8	4.00	0.24	0.22	6.4	6.8	2.18	0.09	0.12
		6.8	7.2	3.09	0.21	0.17	6.8	7.2	1.96	0.08	0.11
		7.2	7.6	3.09	0.21	0.17	7.2	7.6	1.735	0.078	0.098
		7.6	8.0	2.46	0.16	0.14	7.6	8.0	1.531	0.074	0.086
		8.0	8.4	2.06	0.17	0.12	8.0	8.4	1.100	0.063	0.062
		8.4	8.8	1.55	0.15	0.09	8.4	8.8	1.052	0.062	0.059
		8.8	9.2	1.28	0.14	0.07	8.8	9.2	0.785	0.054	0.045
		9.2	9.6	0.98	0.12	0.06	9.2	9.6	0.716	0.051	0.040
		9.6	10.0	1.04	0.12	0.06	9.6	10.0	0.584	0.047	0.033
		10.0	10.8	0.878	0.081	0.052	10.0	10.8	0.490	0.030	0.027
		10.8	11.6	0.505	0.063	0.030	10.8	11.6	0.312	0.024	0.017

Continued on next page

θ_{low} θ_{up} (mrad)	p_{low} (GeV/c)	p_{up}	$\frac{d\sigma}{dp}^{\pi^+}$ (mb/(GeV/c))	Δ_{stat}	Δ_{sys}	p_{low} (GeV/c)	p_{up}	$\frac{d\sigma}{dp}^{\pi^-}$ (mb/(GeV/c))	Δ_{stat}	Δ_{sys}
	11.6	12.4	0.270	0.054	0.016	11.6	12.4	0.194	0.020	0.011
	12.4	13.2	0.271	0.048	0.016	12.4	13.2	0.121	0.016	0.007
						13.2	14.0	0.095	0.014	0.005
100 140	0.2	0.3	2.27	0.28	0.22	0.2	0.3	1.96	0.21	0.29
	0.3	0.4	3.72	0.34	0.25	0.3	0.4	3.47	0.26	0.44
	0.4	0.5	5.95	0.37	0.35	0.4	0.5	4.92	0.29	0.50
	0.5	0.6	7.18	0.38	0.40	0.5	0.6	6.04	0.30	0.56
	0.6	0.7	8.99	0.41	0.48	0.6	0.7	8.18	0.34	0.68
	0.7	0.8	10.02	0.45	0.54	0.7	0.8	8.00	0.34	0.61
	0.8	0.9	10.96	0.49	0.63	0.8	0.9	9.28	0.37	0.67
	0.9	1.0	11.73	0.47	0.68	0.9	1.0	9.67	0.38	0.67
	1.0	1.2	13.2	0.9	1.1	1.0	1.2	10.68	0.27	0.68
	1.2	1.4	13.0	0.9	1.0	1.2	1.4	10.50	0.26	0.69
	1.4	1.6	14.4	1.0	1.1	1.4	1.6	10.52	0.25	0.59
	1.6	1.8	14.2	1.2	1.0	1.6	1.8	10.62	0.27	0.56
	1.8	2.0	12.33	0.91	0.78	1.8	2.0	10.83	0.27	0.53
	2.0	2.2	12.70	0.88	0.77	2.0	2.2	9.96	0.26	0.47
	2.2	2.4	12.74	0.87	0.76	2.2	2.4	9.74	0.24	0.43
	2.4	2.6	12.02	0.87	0.71	2.4	2.6	9.32	0.23	0.40
	2.6	2.8	9.72	0.54	0.57	2.6	2.8	8.46	0.22	0.35
	2.8	3.0	9.21	0.55	0.54	2.8	3.0	7.87	0.22	0.32
	3.0	3.2	9.26	0.54	0.55	3.0	3.2	7.39	0.23	0.40
	3.2	3.4	8.04	0.49	0.47	3.2	3.4	6.18	0.21	0.31
	3.4	3.6	7.73	0.49	0.45	3.4	3.6	6.02	0.21	0.31
	3.6	3.8	6.77	0.43	0.40	3.6	3.8	5.00	0.19	0.26
	3.8	4.0	5.46	0.38	0.32	3.8	4.0	4.74	0.18	0.24
	4.0	4.2	5.47	0.41	0.32	4.0	4.2	4.27	0.18	0.22
	4.2	4.4	5.35	0.40	0.31	4.2	4.4	3.86	0.17	0.19
	4.4	4.6	3.88	0.34	0.23	4.4	4.6	3.39	0.16	0.17
	4.6	4.8	3.87	0.35	0.23	4.6	4.8	3.13	0.15	0.15
	4.8	5.0	3.81	0.35	0.22	4.8	5.0	2.65	0.14	0.13
	5.0	5.2	3.32	0.32	0.20	5.0	5.2	2.46	0.13	0.12
	5.2	5.6	2.54	0.19	0.15	5.2	5.6	2.05	0.09	0.10
	5.6	6.0	2.64	0.19	0.16	5.6	6.0	1.645	0.077	0.081
	6.0	6.4	1.83	0.17	0.11	6.0	6.4	1.321	0.068	0.065
	6.4	6.8	1.15	0.14	0.07	6.4	6.8	1.061	0.062	0.053
	6.8	7.2	1.14	0.14	0.07	6.8	7.2	0.746	0.052	0.037
	7.2	7.6	0.86	0.12	0.05	7.2	7.6	0.593	0.048	0.029
	7.6	8.0	0.63	0.11	0.04	7.6	8.0	0.472	0.042	0.023
	8.0	8.4	0.533	0.099	0.033	8.0	8.4	0.369	0.038	0.018
	8.4	8.8	0.39	0.12	0.02	8.4	8.8	0.218	0.029	0.011
						8.8	9.2	0.188	0.029	0.009
						9.2	9.6	0.205	0.029	0.010
140 180	0.2	0.3	3.56	0.35	0.29	0.2	0.3	3.02	0.30	0.41
	0.3	0.4	6.05	0.39	0.37	0.3	0.4	4.51	0.34	0.50
	0.4	0.5	8.57	0.42	0.45	0.4	0.5	6.59	0.37	0.58
	0.5	0.6	8.91	0.42	0.45	0.5	0.6	7.72	0.39	0.62
	0.6	0.7	11.31	0.45	0.55	0.6	0.7	9.58	0.42	0.65
	0.7	0.8	13.37	0.51	0.64	0.7	0.8	10.94	0.44	0.67
	0.8	0.9	13.96	0.52	0.72	0.8	0.9	11.20	0.45	0.63
	0.9	1.0	13.34	0.50	0.69	0.9	1.0	10.82	0.43	0.59
	1.0	1.2	12.2	1.0	1.0	1.0	1.2	11.95	0.29	0.63
	1.2	1.4	12.3	1.2	1.0	1.2	1.4	12.44	0.43	0.60
	1.4	1.6	14.0	1.2	0.9	1.4	1.6	12.49	0.31	0.55
	1.6	1.8	13.8	1.2	0.9	1.6	1.8	11.04	0.28	0.42
	1.8	2.0	12.1	1.1	0.8	1.8	2.0	11.27	0.29	0.40
	2.0	2.2	12.7	1.1	0.8	2.0	2.2	9.89	0.27	0.34
	2.2	2.4	9.59	0.98	0.59	2.2	2.4	8.25	0.25	0.29
	2.4	2.6	7.65	0.79	0.48	2.4	2.6	7.46	0.24	0.25
	2.6	2.8	8.27	0.92	0.52	2.6	2.8	6.62	0.22	0.21

Continued on next page

θ_{low} θ_{up} (mrad)	p_{low} (GeV/c)	p_{up}	$\frac{d\sigma}{dp}^{\pi^+}$ (mb/(GeV/c))	Δ_{stat}	Δ_{sys}	p_{low} (GeV/c)	p_{up}	$\frac{d\sigma}{dp}^{\pi^-}$ (mb/(GeV/c))	Δ_{stat}	Δ_{sys}
	2.8	3.0	5.80	0.77	0.36	2.8	3.0	5.74	0.20	0.18
	3.0	3.2	6.04	0.78	0.38	3.0	3.2	5.24	0.19	0.24
	3.2	3.4	3.76	0.63	0.24	3.2	3.4	4.48	0.18	0.20
	3.4	3.6	4.31	0.66	0.28	3.4	3.6	3.80	0.16	0.17
	3.6	3.8	3.58	0.62	0.23	3.6	3.8	3.24	0.15	0.15
	3.8	4.0	3.05	0.57	0.19	3.8	4.0	3.02	0.15	0.14
	4.0	4.2	3.32	0.60	0.21	4.0	4.2	2.40	0.13	0.10
	4.2	4.4	3.37	0.62	0.22	4.2	4.4	2.20	0.13	0.10
	4.4	4.6	1.28	0.41	0.08	4.4	4.6	1.92	0.12	0.08
	4.6	4.8	2.05	0.49	0.13	4.6	4.8	1.58	0.11	0.07
	4.8	5.0	1.34	0.41	0.09	4.8	5.0	1.50	0.10	0.06
	5.0	5.2	1.20	0.39	0.08	5.0	5.2	1.141	0.093	0.050
	5.2	5.6	1.16	0.18	0.08	5.2	5.6	0.748	0.051	0.033
	5.6	6.0	0.83	0.16	0.05	5.6	6.0	0.661	0.049	0.028
						6.0	6.4	0.407	0.037	0.017
						6.4	6.8	0.314	0.035	0.013
						6.8	7.2	0.283	0.031	0.012
						7.2	7.6	0.223	0.030	0.009
180 240	0.2	0.3	6.73	0.38	0.48	0.2	0.3	5.61	0.31	0.71
	0.3	0.4	10.66	0.43	0.58	0.3	0.4	9.3	0.4	1.0
	0.4	0.5	15.58	0.50	0.75	0.4	0.5	13.1	0.4	1.2
	0.5	0.6	17.33	0.52	0.77	0.5	0.6	15.7	0.5	1.2
	0.6	0.7	20.03	0.54	0.84	0.6	0.7	17.7	0.5	1.2
	0.7	0.8	21.01	0.61	0.89	0.7	0.8	18.8	0.5	1.1
	0.8	0.9	22.4	0.7	1.0	0.8	0.9	19.0	0.5	1.1
	0.9	1.0	22.1	0.6	1.0	0.9	1.0	20.0	0.5	1.1
	1.0	1.2	23.0	1.6	1.7	1.0	1.2	19.3	0.4	1.1
	1.2	1.4	21.8	1.5	1.6	1.2	1.4	18.17	0.35	0.97
	1.4	1.6	18.5	1.3	1.3	1.4	1.6	16.74	0.34	0.74
	1.6	1.8	15.8	1.3	1.1	1.6	1.8	14.25	0.32	0.60
	1.8	2.0	15.2	1.2	1.0	1.8	2.0	12.50	0.29	0.50
	2.0	2.2	12.5	1.1	0.8	2.0	2.2	10.46	0.27	0.42
	2.2	2.4	11.6	1.1	0.8	2.2	2.4	9.29	0.26	0.35
	2.4	2.6	7.48	0.86	0.49	2.4	2.6	7.80	0.23	0.29
	2.6	2.8	7.62	0.86	0.49	2.6	2.8	6.63	0.21	0.24
	2.8	3.0	6.51	0.81	0.44	2.8	3.0	5.63	0.20	0.21
	3.0	3.2	5.89	0.75	0.39	3.0	3.2	4.30	0.20	0.22
	3.2	3.4	3.83	0.63	0.24	3.2	3.4	3.47	0.18	0.17
	3.4	3.6	4.95	0.66	0.33	3.4	3.6	2.80	0.16	0.14
	3.6	3.8	3.54	0.62	0.25	3.6	3.8	2.36	0.15	0.12
	3.8	4.0	2.91	0.56	0.19	3.8	4.0	1.93	0.14	0.10
	4.0	4.2	2.31	0.52	0.15	4.0	4.2	1.49	0.12	0.08
	4.2	4.4	1.74	0.46	0.12	4.2	4.4	1.49	0.12	0.07
	4.4	4.6	1.28	0.41	0.09	4.4	4.6	1.26	0.11	0.07
	4.6	4.8	1.72	0.45	0.11	4.6	4.8	1.04	0.10	0.05
						4.8	5.0	0.826	0.092	0.044
						5.0	5.2	0.593	0.076	0.032
						5.2	5.6	0.471	0.047	0.025
						5.6	6.0	0.275	0.037	0.017
						6.0	6.4	0.181	0.033	0.010
240 300	0.2	0.3	8.49	0.44	0.54	0.2	0.3	7.36	0.37	0.87
	0.3	0.4	13.98	0.53	0.66	0.3	0.4	12.4	0.4	1.2
	0.4	0.5	17.89	0.59	0.78	0.4	0.5	15.8	0.5	1.4
	0.5	0.6	20.21	0.61	0.84	0.5	0.6	17.7	0.5	1.3
	0.6	0.7	21.75	0.64	0.84	0.6	0.7	19.7	0.6	1.2
	0.7	0.8	22.60	0.71	0.91	0.7	0.8	19.4	0.6	1.1
	0.8	0.9	22.28	0.74	0.96	0.8	0.9	19.8	0.6	1.1
	0.9	1.0	22.5	1.1	0.9	0.9	1.0	18.4	1.1	0.9
	1.0	1.2	17.1	1.5	1.5	1.0	1.2	17.00	0.40	0.94
	1.2	1.4	16.0	1.5	1.3	1.2	1.4	14.82	0.37	0.77

Continued on next page

θ_{low}	θ_{up} (mrad)	p_{low}	p_{up} (GeV/c)	$\frac{d\sigma}{dp}^{\pi^+}$	Δ_{stat} (mb/(GeV/c))	Δ_{sys}	p_{low}	p_{up} (GeV/c)	$\frac{d\sigma}{dp}^{\pi^-}$	Δ_{stat} (mb/(GeV/c))	Δ_{sys}
		1.4	1.6	14.0	1.3	1.1	1.4	1.6	12.94	0.35	0.66
		1.6	1.8	13.3	1.1	1.0	1.6	1.8	10.20	0.31	0.51
		1.8	2.0	11.7	1.4	1.0	1.8	2.0	8.32	0.28	0.41
							2.0	2.2	6.28	0.25	0.31
							2.2	2.4	5.32	0.22	0.20
							2.4	2.6	3.96	0.19	0.15
							2.6	2.8	3.15	0.17	0.12
							2.8	3.0	2.63	0.16	0.10
							3.0	3.2	2.02	0.14	0.12
							3.2	3.4	1.42	0.12	0.09
							3.4	3.6	0.963	0.095	0.057
							3.6	3.8	1.00	0.10	0.06
							3.8	4.0	0.731	0.085	0.044
							4.0	4.2	0.484	0.070	0.031
							4.2	4.4	0.368	0.060	0.023
300	360	0.2	0.3	10.16	0.69	0.52	0.2	0.3	8.29	0.56	0.98
		0.3	0.4	15.46	0.70	0.70	0.3	0.4	13.6	0.6	1.4
		0.4	0.5	18.86	0.71	0.83	0.4	0.5	16.6	0.6	1.5
		0.5	0.6	21.44	0.73	0.87	0.5	0.6	18.8	0.6	1.5
		0.6	0.7	21.50	0.73	0.82	0.6	0.7	20.0	0.7	1.5
		0.7	0.8	21.32	0.81	0.79	0.7	0.8	20.0	0.7	1.4
		0.8	0.9	20.47	0.79	0.74	0.8	0.9	17.2	0.6	1.2
		0.9	1.0	19.18	0.78	0.73	0.9	1.0	16.6	0.6	1.1
							1.0	1.2	14.02	0.41	0.89
							1.2	1.4	11.09	0.40	0.72
							1.4	1.6	7.89	0.34	0.49
							1.6	1.8	6.53	0.31	0.39
							1.8	2.0	4.25	0.24	0.26
							2.0	2.2	3.43	0.22	0.21
							2.2	2.4	2.81	0.19	0.17
							2.4	2.6	1.81	0.15	0.11
							2.6	2.8	1.31	0.13	0.08
							2.8	3.0	1.06	0.12	0.06
							3.0	3.2	0.68	0.10	0.05
							3.2	3.4	0.512	0.093	0.036
360	420	0.2	0.3	11.81	0.80	0.91	0.2	0.3	10.5	0.7	1.2
		0.3	0.4	18.3	1.0	1.3	0.3	0.4	14.1	0.8	1.5
		0.4	0.5	19.6	0.9	1.4	0.4	0.5	16.9	0.8	1.6
		0.5	0.6	18.0	0.8	1.2	0.5	0.6	18.0	0.8	1.6
		0.6	0.7	19.2	0.8	1.3	0.6	0.7	16.6	0.7	1.4
		0.7	0.8	18.1	0.9	1.2	0.7	0.8	15.7	0.7	1.3
		0.8	0.9	16.7	0.8	1.2	0.8	0.9	14.8	0.7	1.2
		0.9	1.0	15.1	0.8	1.1	0.9	1.0	11.97	0.58	0.92
							1.0	1.2	11.07	0.39	0.84
							1.2	1.4	7.76	0.36	0.60
							1.4	1.6	5.22	0.26	0.39
							1.6	1.8	4.30	0.24	0.33
							1.8	2.0	2.71	0.19	0.22
							2.0	2.2	1.80	0.16	0.13
							2.2	2.4	1.38	0.14	0.10
							2.4	2.6	0.96	0.11	0.07
							2.6	2.8	0.82	0.11	0.06
							2.8	3.0	0.636	0.096	0.049

Appendix III

The final K^0_S production cross sections in polar angle intervals with systematic errors.

θ_{low} (mrad)	θ_{high} (mrad)	p_{low} (GeV/c)	p_{high} (GeV/c)	$d\sigma^{K^0_S}/dp$ (mb/GeV/c)	Δ_{stat} (mb/GeV/c)	Δ_{stat} [%]	Δ_{sys} (mb/GeV/c)	Δ_{sys} [%]
0	20	0.4	7.2	0.066	0.010	15.4	0.004	7.0
20	140	0.4	2.4	1.371	0.284	20.7	0.101	
		2.4	3.2	2.017	0.298	14.8	0.149	
		3.2	4.0	1.748	0.196	11.2	0.129	
		4.0	4.8	1.256	0.165	13.1	0.093	
		4.8	5.6	1.293	0.153	11.8	0.095	7.4
		5.6	7.2	0.899	0.101	11.3	0.066	
		7.2	8.8	0,393	0.071	18.2	0.029	
		8.8	10.8	0.416	0.054	13	0.031	
		10.8	20.0	0.101	0.015	15.2	0.007	
140	240	0.4	2.4	1.734	0.27	15.6	0.117	
		2.4	4.0	1.36	0.111	8.2	0.092	6.7
		4.0	5.6	0,446	0.045	10.2	0.03	
		5.6	10.8	0.076	0,01	13.7	0.005	
240	420	0.4	5.6	0.815	0.227	27.9	0.061	7.5

Table I: The NA61/SHINE preliminary results for the differential K^0_S production cross section in the laboratory system, $d\sigma/dp$ for p+C interactions at 31 GeV/c. Each row refers to a different ($p_{low} \leq p < p_{up}, \theta_{low} \leq \theta < \theta_{up}$) bin, where p and θ are the kaon momentum and polar angle in the laboratory frame. The central value as well as the statistical (Δ_{stat}) and systematic (Δ_{sys}) errors of the cross section are given. The overall uncertainty due to the normalization procedure is not included.